WAVE-CURRENT INERACTIONS IN THE EASTERN CANADIAN WATERS

by

Pengcheng Wang

Submitted in partial fulfilment of the requirements
for the degree of Doctor of Philosophy

at

Dalhousie University
Halifax, Nova Scotia
November 2018

TABLE OF CONTENTS

LIST OF TABLES

LIST OF FIGURES

ABSTRACT

This thesis examines effects of wave-current interactions (WCIs) on surface gravity waves and ocean currents over the eastern Canadian coastal and shelf waters using a coupled wave-circulation numerical model. The coupled model consists of a three-dimensional (3D) circulation model and a third-generation wave model. Comparisons of model results with in-situ oceanographic observations made with buoys and ADCPs and remote sensing measurements from satellites and high frequency (HF) radars demonstrate that the inclusion of WCIs in the coupled model significantly improves the model performance in simulating ocean waves, currents and hydrography over coastal and shelf waters, particularly during extreme weather events.

The important WCI mechanisms on the 3D ocean currents examined in this study include the 3D wave force, breaking wave-induced mixing, and wave-induced vertical Reynolds stress. The research results demonstrate that the vortex force formulation, with a separation of the 3D wave force into conservative (vortex force and Bernoulli head) and non-conservative (breaking wave-induced acceleration) contributions, performs better than the radiation stress formulation in simulating the wave-induced 3D ocean currents over coastal waters under hurricane conditions. Furthermore, the 3D wave force and breaking wave-induced mixing are found to improve the model performance in simulating the storm-induced sea surface temperature changes. The research results also demonstrate that the wave-induced vertical Reynolds stress is an important process for transferring the wind momentum to the water column in addition to the turbulent Reynolds stress.

The important WCI mechanisms on surface gravity waves during storm events include the relative wind effect, current-induced convergence and refraction, which collectively result in different wave responses on the two sides of the storm track. Significant wave modulations by the hurricane-induced near-inertial currents and semidiurnal tidal currents are also demonstrated based on analyses of both observations and numerical model results. Tidal modulations in the Gulf of Maine are mainly due to the strong horizontal gradients of tidal currents near the mouth of the Gulf, resulting in great effects of current-induced convergence, refraction and wavenumber shift. In addition, the current-enhanced dissipation becomes important during high winds by reducing the magnitude of the tidal modulation.

LIST OF ABBREVIATIONS AND SYMBOLS USED

Abbreviation	Definition
2D	two-dimensional
3D	three-dimensional
ADCP	Acoustic Doppler Current Profiler
ATCF	Automated Tropical Cyclone Forecasting
BoF	Bay of Fundy
CC	Corkum's Channel
CFSv2	Climate Forecast System Version 2
CFSR	Climate Forecast System Reanalysis
CODAR	Coastal Ocean Dynamics Applications Radar
DIA	discrete interaction approximation
DWR	directional wave rider
ECS	eastern Canadian shelf
EOF	Empirical Orthogonal Function
ERS	Evolving Rotary Spectrum
ETOPO2	2-min Gridded Global Relief Data
GDOP	Geometric Dilution of Precision
GEBCO	General Bathymetric Chart of the Oceans
GB	Georges Bank
GoM	Gulf of Maine
GoMSS	Gulf of Maine and Scotian Shelf regional model
GSC	Great South Channel
GSL	Gulf of St. Lawrence
HF	high frequency
HFRNet	HFRadar Network
HURDAT	HURricane DATabase

Abbreviation	Definition
JONSWAP	Joint North Sea Wave Atmosphere Program
LB	Lunenburg Bay
LHS	left-hand side
LSC	Lower South Cove
MATLAB	MATrix LABoratory
MEOPAR	Marine Environmental Observation Prediction and Response Network
ML	mixed layer
NARR	North American Regional Reanalysis
NDBC	National Data Buoy Center
NEC	Northeast Channel
NEMO	Nucleus for European Models of the Ocean
NERACOOS	Northeastern Regional Association of Coastal Ocean Observing Systems
NHC	National Hurricane Center
NIO	near-inertial oscillation
NSC	Nova Scotia Current
OSU	Oregon State University
OTIS	OSU Tidal Inversion System
OTN	Ocean Tracking Network
PALM	Projet d'Assimilation par Logiciel Multimethodes
POM	Princeton Ocean Model
RHS	right-hand side
RS	radiation stress
SLP	sea level pressure
ScS	Scotian Shelf
SST	sea surface temperature
SWAN	Simulating WAves Nearshore

Abbreviation	Definition
TC	tropical cyclone
TKE	turbulent kinetic energy
USC	Upper South Cove
VF	vortex force
VRS	vertical radiation stress
WCI	wave-current interaction
WW3	WAVEWATCH III

Symbol	Description	Unites
A^{-1}	inverse wave age	m
B	hurricane shape parameter	
C_b	bottom drag coefficient	
C_d	air-sea drag coefficient	
C_g	group velocity	m s^{-1}
C_p	phase speed at the spectral peak	m s^{-1}
$d\ (D)$	total water depth	m
E	wave variance spectrum	m^2
f	Coriolis parameter	s^{-1}
f_e	effective inertial frequency	s^{-1}
f_p	inertial peak frequency	s^{-1}
$F_{SS}, F_{SS}, F_{SS}, F_{SS}$	vertical profile functions	
g	acceleration due to gravity	m s^{-2}
h	water depth	m
H_s	significant wave height	m
H_s^{max}	maximum significant wave height	m

k=(k_x, k_y)	wave number vector	m^{-1}
K_q	mixing coefficient	$m^2\ s^{-1}$
l_0	length scale at the sea surface	m
L	mean wave length	m
M	simulated variables	
N	wave action density	m^2 s
O	observed variables	
p	hydrostatic pressure	kg $m^{-1}\ s^{-2}$
p_c	central pressure	kg $m^{-1}\ s^{-2}$
p_n	ambient pressure	kg $m^{-1}\ s^{-2}$
q^2	twice the turbulent kinetic energy	$m^2\ s^{-2}$
r	radius	m
R_m	radius of maximum wind	m
(S_{xx}, S_{xy}, S_{yy})	horizontal radiation stress components	kg $m^{-1}\ s^{-2}$
(S_{px}, S_{py})	vertical radiation stress components	kg $m^{-1}\ s^{-2}$
t	time	s
T_p	peak period	s
u_*	friction velocity	m s^{-1}
$\mathbf{U_b}$	near bottom current vector	m s^{-1}
U_{10}	wind velocity at 10 m	m s^{-1}
U_G	geostrophic wind	m s^{-1}
U_t	translation speed	m s^{-1}
V_g	gradient wind	m s^{-1}
(u, v, w)	mean Lagrangian velocity	m s^{-1}
$(\hat{u}, \hat{v}, \hat{w})$	quasi-Eulerian velocity vector	m s^{-1}
(U_s, V_s, W_s)	Stokes drift velocity vector	m s^{-1}
(x, y, z)	spatial coordinates	m
z_0	surface roughness length	m

θ	mean wave direction	^{o}
ρ_o	reference water density	kg m^{-3}
η	surface elevation	m
σ	relative radian frequency	s^{-1}
$\beta(z)$	vertical distribution function	
κ	von Karman's constant	
ϕ_{oc}	wave to ocean energy flux	W m^{-2}
γ^2	measure of fit	
τ	wind stress	kg m^{-1} s^{-2}
τ_b	bottom stress	kg m^{-1} s^{-2}
ζ	relative vorticity	s^{-1}
λ	wave length	m

ACKNOWLEDGEMENTS

Foremost, I would like to thank my supervisor, Dr. Jinyu Sheng, for giving me the opportunity to work on my doctoral research program that was scientifically very interesting but technically very challenging. I would like to thank him for many helpful discussions and for the freedom he allowed me in pursuing new ideas. Without his continued support and encouragement, this thesis research would hardly have been completed. It was a real honour to have him as my supervisor.

I would also like to thank other members of my supervisory committee, Drs. William Perrie, David Barclay, and Li Zhai, for their helpful and constructive comments and contributions on my thesis work. Many thanks to Dr. Lie-Yauw Oey, my external examiner, for taking his busy time to read my thesis. His detailed and constructive comments have helped improve the thesis greatly.

I am particularly grateful to Dr. Keith Thompson for his many constructive and insightful comments on the work based on the high-frequency radar data. It was a real pleasure collaborating with him.

I am thankful to Drs. Bechara Toulany, Li Zhai, and Mathieu Dever for sharing the observational data used in this work. I am also thankful to Drs. Kyoko Ohashi and Lanli Guo for sharing the source code used in this work. Thanks also go to fellow graduate students, to the staff and faculty of the Department of Oceanography. I have benefited a lot from the discussions with members of Jinyu Sheng's regional ocean modelling group.

Finally, I would like to thank my family members for all the love and support they have provided throughout the journey. I am particularly grateful to my girlfriend, Jing Tao, for her companionship throughout. The sweets and bitters of my PhD life shared with her at Dalhousie were unforgettable.

This PhD work was supported in part by the Government of Canada Program World Class Prevention, Preparedness and Response for Oil Spills from Ships Initiative, the Marine Environmental Observation Prediction and Response Network (MEOPAR), Ocean Frontier Institute (OFI), and Lloyd's Register (LR).

CHAPTER 1

INTRODUCTION

1.1 Background

Surface gravity waves are among the most energetic motions in the upper ocean on time scales from seconds to minutes with wavelengths of one to hundreds of meters. Ocean currents (driven by wind, tide, and density), by contrast, are associated with time scales from hours to years and spatial scales of one to thousands of kilometers. Despite their distinctive scales, these two motions can interact with each other.

Reliable knowledge of wave-current interactions (WCIs) in the ocean is of great importance to many scientific and engineering applications, such as weather forecasting (*Chen and Curcic*, 2016), coastal ocean forecasting (*Staneva et al.*, 2016), trajectory forecasting (*Rohrs et al.*, 2012), oil spill analysis (*Guo et al.*, 2014), sediment erosion analysis (*Lettmann et al.*, 2009), site selection for offshore infrastructures (*Hashemi and Neill*, 2014), and de-biasing of remote sensing measurements (*Ardhuin et al.*, 2016). Yet WCIs are not routinely implemented in today's many ocean predicting systems in which ocean wave and circulation models are run separately by assuming the WCIs to be small and thus can be neglected.

Physically, ocean currents can modify the relative speeds of the air above the sea surface known as the relative wind effect and change the absolute frequencies of waves via a process known as the Doppler shift. Spatial variability of currents can modify the relative wave frequencies and cause wave refractions that mimic bathymetric effects. Other indirect effects include enhanced wave breaking due to a rapid steepening of waves when waves encounter opposing currents (*Ardhuin et al.*, 2012). In addition to ocean currents, the sea surface elevation modifies the total water depth experienced by surface waves and thereby

can greatly affect the depth-induced wave refraction and dissipation over coastal waters.

Surface gravity waves, in return, can affect ocean currents through various WCI mechanisms (Fig. 1). At the sea surface, surface waves enhance the wind stress by increasing the surface roughness length (e.g., *Donelan et al.*, 1993) and modify the air-sea momentum flux budget through wave growth and dissipation (*Perrie et al.*, 2003; *Fan et al.*, 2010). At the ocean bottom, the interaction of surface waves with the sea bed can enhance the bottom shear stress experienced by currents (e.g., *Wijesekera et al.*, 2010). In the upper ocean, surface waves can enhance the turbulent mixing through the Langmuir circulation, breaking and nonbreaking waves. The Langmuir circulation arises from an interaction of the Stokes drift with the mean flow (Craik-Leibovich vortex force, *Craik and Leibovich*, 1976). The breaking wave-induced mixing involves a turbulent kinetic energy (TKE) input at the surface (*Craig and Banner*, 1994), and the nonbreaking wave-induced mixing involves an interaction between the wave orbital velocity and the turbulent velocity (*Qiao et al.*, 2004). Furthermore, similar to the turbulent Reynolds stress, the nonlinear feedback of surface waves on ocean currents results in the wave-induced Reynolds stress, which are responsible for generating the wave-induced setup, undertow, longshore currents, and rip currents in the surf zone (*Longuet-Higgins and Stewart*, 1964). The three-dimensional (3D) nonlinear feedback of surface waves on ocean currents (3D wave force) can be formulated through the concept of radiation stress (RS) (*Mellor*, 2003) or vortex force (VF) (*McWilliams*, 2004; *Ardhuin et al.*, 2008b). It is noted that these two methods incorporate the material advection by the Stokes drift and the wave-induced vertical Reynolds stress component $\overline{\tilde{v}\tilde{w}}$ ($\tilde{u}$, $\tilde{v}$, and $\tilde{w}$ are the wave orbital velocities). Here, $\overline{\tilde{v}\tilde{w}}$ is equivalent to an interaction between the Coriolis force and the Stokes drift $\mathbf{f} \times \mathbf{U}_{\boldsymbol{S}}$, known as the Coriolis-Stokes force (e.g., *Polton et al.*, 2005). Another wave-induced vertical Reynolds stress component $\overline{\tilde{u}\tilde{w}}$, however, is not incorporated in these two methods, and it is recently found to be equivalent to a subsurface projection of the wind pressure correlated with the wave slope (*Mellor*, 2013).

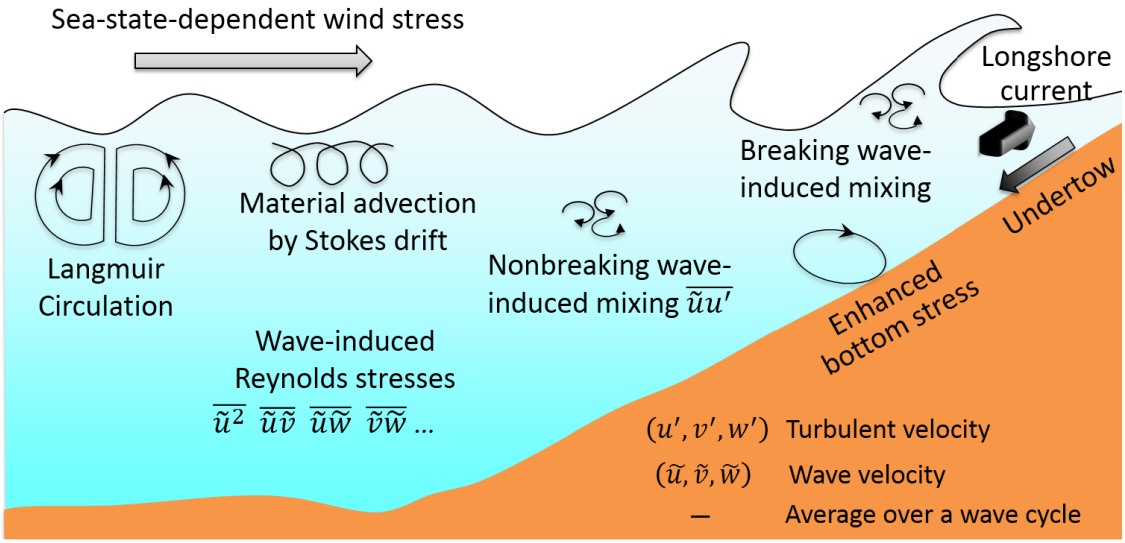

Figure 1.1: Schematic showing important wave-current processes on the three-dimensional ocean circulation.

With the rapid development of computational technology and state-of-the-art numerical circulation models and surface gravity wave models, great efforts have been made in the last decade to study the potential effects of WCIs on the atmosphere-ocean-wave system over different ocean waters around the world using newly developed coupled modelling systems. For example, off the U.S. east coast, *Olabarrieta et al.* (2012) showed that the combined wave age- and steepness-based sea surface roughness parameterization provided the best results for wind and wave growth prediction during storm events. On the southwest Western Australian continental shelf, *Wandres et al.* (2017) found that the simulated surface waves can be greatly modulated (up to 25%) by the Leeuwin Current, a strong poleward-flowing boundary current. In the Adriatic Sea (*Sikiric et al.*, 2012) and the German Bight (*Staneva et al.*, 2016), a model-observation comparison showed improved modelling skills in simulating the surface waves and upper ocean currents when the effects of WCIs were taken into account. In a semi-enclosed bay known as Jiaozhou Bay, China, *Gao et al.* (2018) demonstrated that the inclusion of WCIs is crucial to accurately simulate the suspended-sediment dynamics.

The eastern Canadian shelf (ECS) (Fig. 1.2) considered in this thesis consists of coastal and shelf waters of the Labrador and Newfoundland Shelves, Grand Banks, the Gulf of St. Lawrence, the Scotian Shelf, and the Gulf of Maine. The ECS is socially and economically important since it supports commercial and recreational fisheries, offshore oil and gas exploration and production, marine recreation and tourism, aquaculture, shipping and transportation, and other economic activities that directly contribute to the Canadian economy. The WCIs can be expected to be significant over this region, particularly during extreme weather conditions, since the ECS is affected frequently by winter storms and occasionally by hurricanes. Hurricane Juan, as an example, was an intense tropical cyclone and caused heavy damage in Nova Scotia and Prince Edward Island in late September 2003. Hurricane Juan reached category 2 strength on the Saffir-Simpson hurricane scale on 27 September 2003 and made landfall on the south coast of Nova Scotia near Halifax early on 29 September, with maximum sustained winds of about 158 km h^{-1}. This storm generated about 2 m storm surge in Halifax Harbor, and huge surface waves with maximum significant wave height of about 10 m and maximum wave height of about 20 m observed at Buoy 44258 at Chebucto Head outside of the Harbor (*Fogarty*, 2003). The other example is "White Juan", which was a hurricane-strength nor'easter blizzard and affected most of Atlantic Canada in February 2004. White Juan had an average snowfall rate of 5 cm h^{-1} for 12 h, and winds blew at up to 124 km h^{-1}. White Juan produced hurricane-strength winds at sea with 10-15 m swells, prompting a special marine warning. Although the storm-induced ocean currents and ocean waves over the ECS during Hurricane Juan were studied previously by *Sheng et al.* (2006) and *Xu et al.* (2007), the WCIs on the ECS during extreme weather conditions such as Hurricane Juan and White Juan remain to be studied.

Three specific sub-regions of interest on the ECS (Fig. 1.2) are further considered in this thesis, including the Lunenburg Bay (LB), the Gulf of Maine (GoM), and the central Scotian Shelf (ScS) adjacent to Halifax. These three sub-regions are selected for my thesis work for many considerations including availability of high-quality observations of ocean currents and surface waves made by various instruments, which are of great importance to assess the performance of the coupled wave-circulation modelling system and examine the significant effects of WCIs based on the observations and model results over these sub-regions.

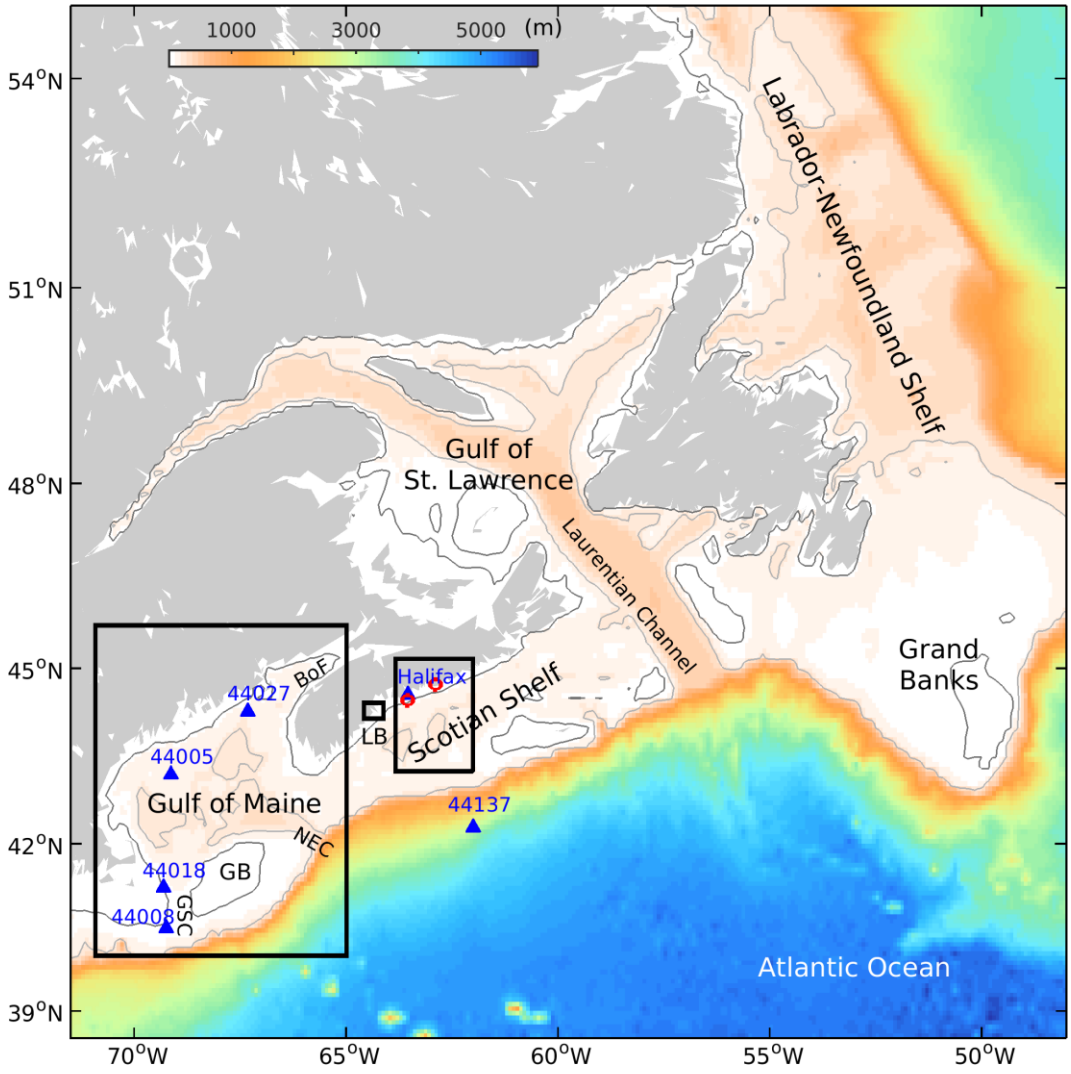

Figure 1.2: Major topographic features over the Labrador-Newfoundland Shelves, Grand Banks, Gulf of St. Lawrence, Scotian Shelf, and Gulf of Maine. The rectangles (from left to right) outline the Gulf of Maine, Lunenburg Bay, and central Scotian Shelf adjacent to Halifax, respectively. The blue triangles denote wave buoy locations, and the red circles denote the high frequency (HF) radar stations. The black and gray contour lines represent respectively the 60 m and 200 m isobaths. Abbreviations are used for the Bay of Fundy (BoF), Northeast Channel (NEC), Georges Bank (GB), Great South Channel (GSC).

The LB (Fig. 1.2) is a semi-enclosed bay located on the south coast of Nova Scotia. The nonlinear feedback of surface gravity waves on ocean currents is expected to be significant over this coastal region where depth-limited wave breaking takes place. In 2001-06, a multiagency research initiative was undertaken to develop a relocatable marine environmental observation and prediction system, using data-assimilative and coupled

models guided directly by real-time observations, for interdisciplinary research in LB. High-quality current and wave observations were made in LB when Hurricane Juan made a landfall within 50 km of the site in September 2003 (*Wang et al.*, 2007). Previous studies of ocean currents and surface gravity waves in LB during Hurricane Juan were made by using a circulation-only model without inclusion of the surface wave force (*Wang et al.*, 2007; *Sheng et al.*, 2009) or using a depth-integrated (2D) surface wave force (*Mulligan et al.*, 2008). Simulations of 3D coastal currents in LB with the effect of the 3D surface wave force on currents were not made.

The GoM (Fig. 1.2) is a semi-enclosed coastal basin bordered by the northeastern United States and the Canadian Maritime Provinces. The GoM is characterized by large semidiurnal M_2 tidal currents, with the world's largest tidal range of ~16 m in the upper reaches of the Bay of Fundy (Greenberg 1983; Hasegawa et al. 2011). The semidiurnal tidal currents are also strong and up to 1.0 m/s over the mouth of the GoM. Since the mouth of the GoM is exposed to large swell waves coming from the North Atlantic Ocean, strong tidal modulations in surface waves are expected to occur. The scientific issues on tidal modulations of surface waves in the GoM, however, were not addressed until recently. Sun et al. (2013) showed that effects of ocean currents on waves were insignificant at buoys located in the inner GoM during a hurricane event. On the contrary, Xie and Zou (2017) demonstrated large impacts of ocean currents on wave heights on Georges Bank during a storm event based on numerical results. It is noted that these two studies focused mainly on short time-scales associated with a single storm event. The relevant physical processes controlling the wave modulation by tidal currents in the GoM were not fully addressed.

The central ScS adjacent to Halifax (Fig. 1.2) is part of the continental shelf, located southwest of Nova Scotia. The ScS is dynamically connected with geographic areas of the Gulf of St. Lawrence and the GoM. The general mean circulation on the ScS is characterized by a persistent southwestward coastal jet (known as the Nova Scotia Current) centered at approximately 45 km off the coast. Temporal variability in the circulation over this region features highly intermittent storm-induced near-inertial oscillations with maximum speeds of order 0.20 m/s (*Anderson and Smith*, 1989). As part of the Marine Environmental Observation, Prediction and Response (MEOPAR) network, a high

frequency (HF) radar system (CODAR) with two long-range HF radars was deployed off Halifax Harbour, Nova Scotia in 2015 to monitor surface ocean currents over this region. This new system produces high-frequency (hourly) and high spatial resolution (~7 km) maps of surface ocean currents, providing a rich database for the study of the surface ocean circulation over this region. Furthermore, it provides a source of observation to assess the model performance, especially with the inclusion of WCIs, in simulating ocean currents over this sub-region.

1.2 Objectives of the Thesis

The main objective of my doctoral research was to examine the effects of WCIs, as well as contributions from different WCI mechanisms, on surface gravity waves and 3D ocean circulation in the eastern Canadian waters using observations and numerical models. The important WCI mechanisms on surface waves considered in this thesis include the relative wind effect, current-induced convergence, refraction, and wavenumber shift. The important WCI mechanisms on the 3D ocean circulation examined in this thesis include the 3D wave force, the breaking wave-induced mixing, and the wave-induced vertical Reynolds stress.

Specifically, my thesis research was carried out for three specific regional ocean waters of the ECS including: (1) LB, (2) GoM, and (3) central ScS adjacent to Halifax. On the ECS, my thesis work focused on the study of effects of WCIs on the surface gravity waves and 3D ocean circulation under extreme weather conditions. In LB, my thesis work focused on the performance assessment of two major different formulations (i.e., RS and VF) for the nonlinear feedback of surface gravity waves on 3D ocean currents. In the GoM, my thesis work explored the semidiurnal tidal modulation in surface gravity waves over this region. On the central ScS adjacent to Halifax, my thesis work first examined the newly HF radar-derived surface circulation features, with a focus on the modulation of the near-inertial oscillations by low frequency current variations. Then the HF-radar data during a particular winter storm were used to further study the effects of surface waves on the storm-induced 3D currents, with a special emphasis on the wave-induced vertical Reynolds stress.

To achieve the above objectives, a two-way coupled wave-circulation modelling

system was developed, as part of my thesis work. The coupled modelling system (Fig. 1.3) consists of a 3D circulation model based on the Princeton Ocean Model (POM) and a third-generation wave model based on WAVEWATCH III (WW3) or Simulating WAves Nearshore (SWAN). The circulation model and the wave model communicate with each other via a dynamic coupling software known as OpenPALM (Fig. 1.4).

1.3 Outline of the Thesis

The structure of this thesis is as follows. In Chapter 2, a two-way coupled wave-circulation modelling system is discussed, with a special emphasis on the implementation of two major different formulations (i.e., VF and RS) for the nonlinear feedback of surface gravity waves on the 3D ocean currents. The performances of the coupled modelling system using the two different formulations are assessed in two idealized test cases and in a realistic application in LB during Hurricane Juan.

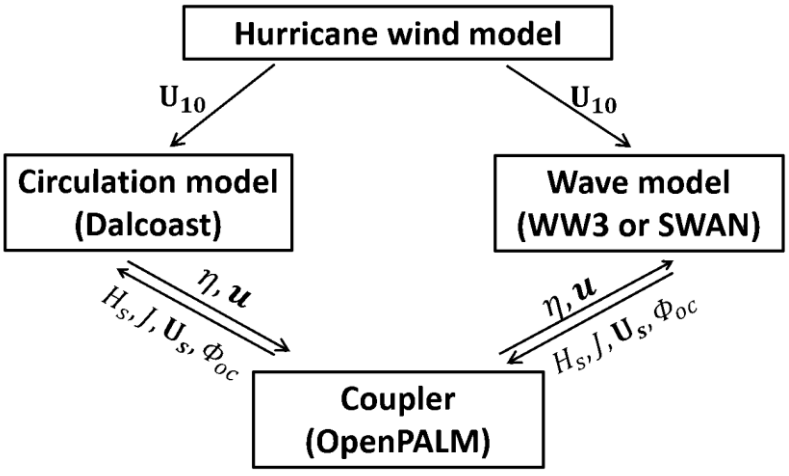

Figure 1.3: Two-way coupled wave-current modelling system based on an ocean circulation model (POM) and an ocean wave model (WW3 or SWAN). An external coupler known as Open PALM is used to exchange information between the circulation and wave models.

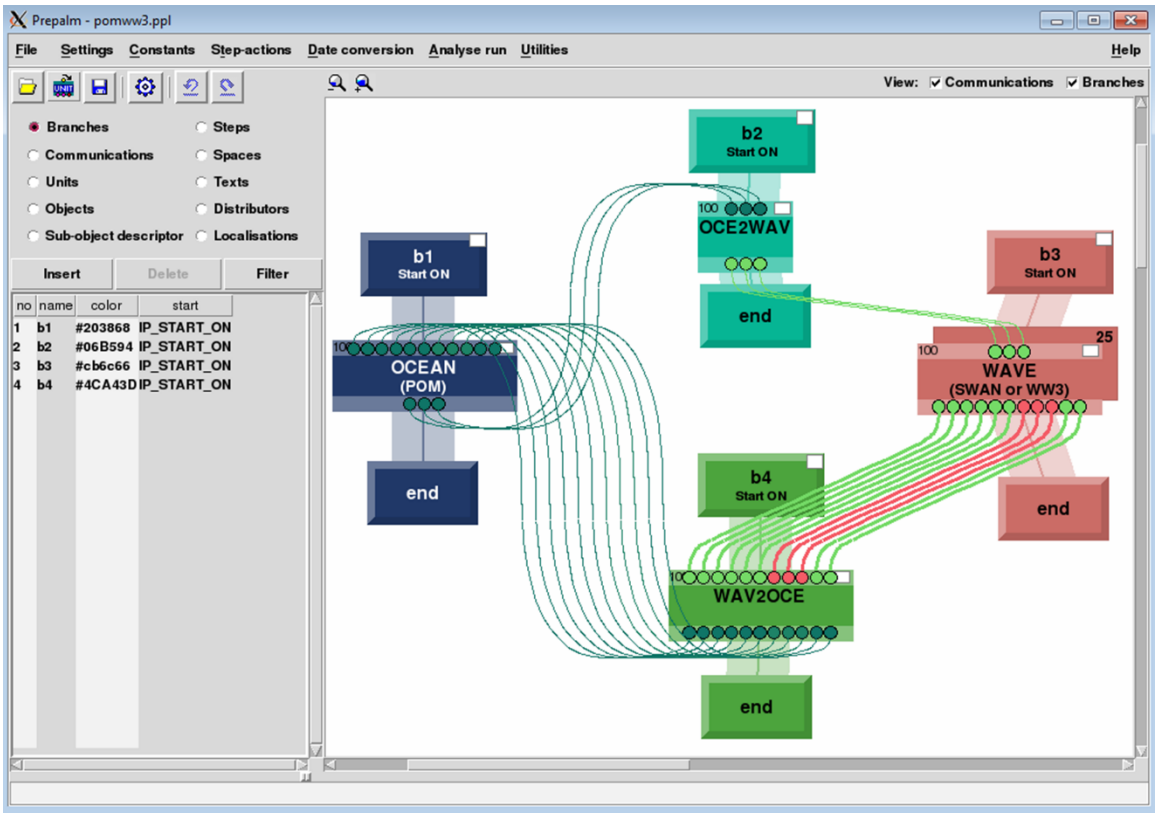

Figure 1.4: The graphical user interface (GUI) of the OpenPALM coupler. OpenPALM allows the concurrent execution and the intercommunication of programs not having been especially designed for that.

In Chapter 3, the coupled wave-circulation modelling system is applied to the ECS and adjacent deep waters to examine the effects of WCIs on surface waves and 3D ocean circulation under three severe storm events: (a) Hurricane Juan, (b) Hurricane Bill and (c) a severe winter storm known as "White Juan". Contributions from different WCI mechanisms are further investigated through process-oriented numerical experiments.

In Chapter 4, the in-situ oceanographic measurements made with operational wave buoys in the GoM are analyzed to investigate the semidiurnal tidal modulation in surface gravity waves. The coupled modelling system used in Chapter 3 is applied to examine the relevant physical processes controlling the tidal modulation over this region.

In Chapter 5, the HF-radar measurements on the central ScS adjacent to Halifax during three winter months are analyzed to examine the observed surface circulation features, with

a special focus on the modulation of the near-inertial oscillations by low frequency current variations over this sub-region. Two advanced shelf circulation models with different strengths are further used to examine these newly observed circulation features and relevant physical processes.

In Chapter 6, the HF-radar measurements described in Chapter 5 during a particular winter storm are used to study the effects of surface gravity waves on ocean currents, with a special emphasis on the wave-induced vertical Reynolds stress. The same coupled modelling system in Chapter 3 updated with the implementation of the wave-induced vertical Reynolds stress is used for this study.

An overall summary and conclusion is given in Chapter 7.

Chapters 2-6 are based on five separate papers. Therefore, some similar background material can be found in these Chapters. In particular, text describing the WCI physics, as well as the model setup are similar in several chapters. Chapter 2 was published in Continental Shelf Research under the title of "Assessing the performance of formulations for nonlinear feedback of surface gravity waves on ocean currents over coastal waters" (*Wang et al.*, 2017). Chapter 3 was published in the Journal of Geophysical Research-Oceans under the title of "A comparative study of wave-current interactions over the eastern Canadian shelf under severe weather conditions using a coupled wave-circulation model" (*Wang and Sheng*, 2016). Chapter 4 was published in the Journal of Physical Oceanography under the title of "Tidal modulation of surface gravity waves in the Gulf of Maine" (*Wang and Sheng*, 2018). Chapter 5 was submitted to the Journal of Physical Oceanography under the title of "Modulation of near-inertial oscillations by low frequency current variations on the inner Scotian Shelf". Chapter 6 has been submitted to the Journal of Geophysical Research-Oceans under the title of "Effects of wave-induced vertical Reynolds stress on ocean currents over the Scotian Shelf during a winter storm". Copyright permission letters for Chapters 2, 3 and 4 are provided in Appendix F.

CHAPTER 2

ASSESSING THE PERFORMANCE OF FORMULATIONS FOR NONLINEAR FEEDBACK OF SURFACE GRAVITY WAVES ON OCEAN CURRENTS OVER COASTAL WATERS[1]

2.1 Introduction

Interactions between ocean surface gravity waves and three-dimensional (3D) ocean currents are an important research topic in the ocean science community, especially for the nonlinear feedback of surface waves on the 3D ocean currents. A good understanding of the wave-current interactions (WCIs) is of great importance for accurate predictions of ocean currents and waves over coastal and shelf waters. The effect of ocean surface waves on ocean currents is usually specified in terms of a "vortex force" (VF) formulation or a "radiation stress" (RS) formulation in the 3D Reynolds-averaged Navier-Stokes equations for the 3D ocean currents. The RS formulation was first introduced by *Longuet-Higgins and Stewart* (1964, hereinafter LS64) as a depth-integrated (2D) version defined as an excess momentum flux in the presence of ocean surface gravity waves. *Mellor* (2003, hereinafter M03) extended the LS64's 2D RS formulation to a depth-dependent (3D) version using a wave-following vertical coordinate. Since then, Mellor's RS formulation has undergone several modifications following scientific debates in the community. *Ardhuin et al.* (2008a) pointed out that the estimation of a vertical flux of wave momentum (vertical radiation stress terms, hereinafter VRS) based on the linear wave theory in M03

[1] Wang, P. J. Sheng, and C. G. Hannah, 2017. Assessing the performance of formulations for nonlinear feedback of surface gravity waves on ocean currents over coastal waters. *Continental Shelf Research*, 146, 102-107.

is insufficient for its application to a sloping bottom. Consequently, *Mellor* (2008, 2011 hereinafter M08-11) modified M03's RS formulation by introducing a surface concentrated Delta function. More recently, *Mellor* (2015, M15) found an error in the expression of the pressure term in LS64 as well as in M03, which led to the erroneous surface singular term in M08-11. The latest version of RS in M15 is identical to that in M03 except that the VRS term is dropped out, which is contrary to *Ardhuin et al.* (2008a, 2008b)'s argument that this term should be given a consistent estimation using a more complex wave theory. In equations based on the RS formulation, the prognostic dependent variable is the Lagrangian mean velocity, namely the combined Eulerian velocity and Stokes drift, which satisfies the non-divergent continuity equation. The vertical component of the Stokes drift is nil, and in general, the Eulerian velocity and Stokes drift are separately divergent.

The VF formulation contains a vortex force term, which is a function of Stokes drift and current vorticity. The vortex force term was first introduced by *Craik and Leibovich* (1976) for describing Langmuir circulations. *McWilliams et al.* (2004) extended the work of *Craik and Leibovich* (1976) and presented a set of 3D wave-averaged equations with the Eulerian mean theory. These equations were obtained by a multiple asymptotic scale analysis, in which waves and currents are separated in amplitude and horizontal space and time scales. In these equations, the wave-averaged effects on currents are represented as a combination of VF formulation and a modified pressure which is theoretically equivalent to the RS representation (*Lane et al.*, 2007). With the generalized Lagrangian theory (*Andrews and McIntyre*, 1978), *Ardhuin et al.* (2008b) derived a different set of wave-averaged equations that is generally consistent with those of *McWilliams et al.* (2004) for cases of weak vertical current shears. The equations presented by *Ardhuin et al.* (2008b) describe the evolution of the quasi-Eulerian velocity (*Andrews and McIntyre*, 1978), which differs from the Eulerian velocity only due to the current vertical shear. Thus, for the case of weak current vertical shear, the quasi-Eulerian velocity for the VF formulation and the Eulerian velocity for the RS formulation are comparable. The vertical Stokes drift in equations based on the VF formulation is non-trivial, and the quasi-Eulerian velocity and Stokes drift are separately non-divergent.

The performance of previous versions of Mellor's RS formulation (i.e., M03 and M08-

11) over the surf zone was assessed by *Haas and Warner* (2009), *Bennis et al.* (2011), *Kumar et al.* (2011), and *Moghimi et al.* (2013) in idealized test cases and field experiments. *Bennis et al.* (2011) found that M03's RS formulation produces very large spurious velocities over a sloping bottom due to its insufficient estimation of the VRS term. *Kumar et al.* (2011) and *Moghimi et al.* (2013) found that M08-11's RS formulation creates unrealistic flows in the wave shoaling region. Despite its known limitation, Mellor's RS formulation has been widely implemented in various coastal ocean models and found to be able to improve the model performance. For example, *Bolaños et al.* (2014) found that the inclusion of M03's RS formulation improves the modeled depth-mean currents and the long-term residual circulation in a tide dominated estuary. *Staneva et al.* (2016) found that both the simulated sea level and currents in the German Bight are improved during an extreme event by implementing M08-11's RS formulation in their coastal ocean circulation model. On the other hand, the VF formulation of *McWilliams et al.* (2004) was validated by *Uchiyama et al.* (2010) and *Kumar et al.* (2012), and the VF formulation of *Bennis et al.* (2011, hereinafter BAD11), which is a simplified form of the VF formulation of *Ardhuin et al.* (2008b), was validated by *Michaud et al.* (2012) and *Moghimi et al.* (2013). The VF formulation was found to be able to produce reasonable 3D nearshore circulations. More recently, however, *Mellor* (2016) questioned existences of the vortex force term and the non-zero vertical Stokes drift term in *McWilliams et al.* (2004), and argued that equations of *McWilliams et al.* (2004), upon vertical integration, disagree with those of LS64, which are deemed to be correct in the 2D case. Apart from the applicability of *Mellor*'s approach to a sloping bottom, *Lane et al.* (2007) showed that the lowest-order RS formulation suffers from being asymptotically inconsistent, since it cannot encompass the vortex force effects, which could affect the currents evolution at a higher order, unless currents are strong compared to wave orbital velocities. It is foreseen, therefore, that scientific debates about these two formulations will continue. It should be noted that the latest version of RS formulation suggested by M15 has not been assessed and compared with the VF formulation over coastal waters in the literature.

In this study, we conduct numerical experiments to assess performances of BAD11's VF formulation and M15's RS formulation in two idealized cases and a realistic application. The first idealized test case was suggested originally by *Haas and Warner* (2009), which

consists of spectral waves obliquely approaching a mildly sloping planar beach. The second case was initially designed by *Haller et al.* (2002) in the wave basin at the University of Delaware, which consists of the generation of the rip current over a barred beach with normally incident waves. These two test cases were used previously in the community for assessing performances of coupled wave-circulation models (*Haas and Warner,* 2009; *Kumar et al.*, 2011; *Michaud et al.*, 2012). The realistic application consists of simulating the storm-induced 3D circulation during the landfall of a hurricane in Lunenburg Bay, which is a semi-closed bay located to the south coast of Nova Scotia.

The coupled wave-circulation modelling system implemented with VF and RS formulations is described in section 2.2. Performance assessments of two formulations with two idealized test cases are given in section 2.3. Applications of the coupled system with the use of these two formulations in Lunenburg Bay during Hurricane Juan are discussed in section 2.4. The summary and discussion are provided in section 2.5.

2.2 The Coupled Wave-Circulation Modelling System

The two-way coupled wave-circulation modelling system consists of a 3D ocean circulation model based on the Princeton Ocean Model (POM), and a third-generation wave model known as Simulating WAves Nearshore (SWAN). An automatic coupler is used to exchange information between the circulation and wave models at a selected coupling time interval.

2.2.1 Ocean Circulation Model

POM (*Mellor*, 2004) is a 3D, sigma coordinate, primitive-equation ocean circulation model. The wave effects on the 3D circulation are specified in POM using the 3D surface wave forces specified in terms of the VF and RS formulations, and breaking wave-induced mixing.

2.2.1a The Vortex Force Formulation

Equations based on the VF formulation describe the evolution of the quasi-Eulerian velocity vector $(\hat{u}, \hat{v}, \hat{w})$ given as,

$$(\hat{u}, \hat{v}, \hat{w}) = (u, v, w) - (U_s, V_s, W_s) \tag{2.1}$$

where (U_s, V_s, W_s) are components of the Stokes drift velocity and (u, v, w) are components of the mean Lagrangian velocity in the horizontal (x, y) and vertical (z) directions, respectively. Following BAD11, the flux form of momentum equations is written as:

$$\frac{\partial \hat{u}}{\partial t} + \frac{\partial (\hat{u}+U_s)\hat{u}}{\partial x} + \frac{\partial (\hat{v}+V_s)\hat{u}}{\partial y} + \frac{\partial (\hat{w}+W_s)\hat{u}}{\partial \mathrm{z}} - f\hat{v} = -\frac{1}{\rho_o}\frac{\partial p}{\partial x} + fV_s$$

$$+ \frac{\partial \hat{u}}{\partial x}U_s + \frac{\partial \hat{v}}{\partial x}V_s - \frac{\partial J}{\partial x} + F_{d,x} + F_{m,x} \tag{2.2}$$

$$\frac{\partial \hat{v}}{\partial t} + \frac{\partial (\hat{u}+U_s)\hat{v}}{\partial x} + \frac{\partial (\hat{v}+V_s)\hat{v}}{\partial y} + \frac{\partial (\hat{w}+W_s)\hat{v}}{\partial \mathrm{z}} + f\hat{u} = -\frac{1}{\rho_o}\frac{\partial p}{\partial y} - fU_s$$

$$+ \frac{\partial \hat{u}}{\partial y}U_s + \frac{\partial \hat{v}}{\partial y}V_s - \frac{\partial J}{\partial y} + F_{d,y} + F_{m,y} \tag{2.3}$$

and the continuity equation is expressed as

$$\frac{\partial \hat{u}}{\partial x} + \frac{\partial \hat{v}}{\partial y} + \frac{\partial \hat{w}}{\partial z} = 0 \tag{2.4}$$

where f is the Coriolis parameter, ρ_o is a reference density, p is the hydrostatic pressure, $(F_{m,x}, F_{m,y})$ represents the mixing effects for exchanging or redistributing the momentum vertically, $(F_{d,x}, F_{d,y})$ represents the non-conservative force of dissipation due to wave breaking, and J is the Bernoulli-head (or wave-induced mean pressure) given as

$$J = \iint g \frac{kE(\sigma,\theta)}{\sinh(2kd)} d\sigma d\theta \tag{2.5}$$

where $E(\sigma, \theta)$ is the frequency-direction variance spectrum computed from SWAN, k is the wavenumber, $\sigma = \sqrt{gktanh(kd)}$ is the relative radian frequency, $d = h + \eta$ is the total water depth. It should be mentioned that in the flux forms of Eqs. (2.2) and (2.3), the vortex force terms do not appear explicitly and their contributions are incorporated in the advection terms.

With the mode splitting, the equation for the surface elevation η can be expressed as

$$\frac{\partial \eta}{\partial t} + (\hat{u} + U_s)\frac{\partial \eta}{\partial x} + (\hat{v} + V_s)\frac{\partial \eta}{\partial y} = \hat{w} + W_s \tag{2.6}$$

Using the flux form formulation, the term $(\hat{w} + W_s)$ can be treated as one variable, and the calculation of W_s is not needed. The horizontal Stokes drift velocity vector must be known and it is defined as

$$(U_s, V_s) = \iint \sigma \boldsymbol{k} E(\sigma, \theta) \frac{\cosh(2k(z+h))}{\sinh^2(kd)} d\sigma d\theta \tag{2.7}$$

where $\boldsymbol{k}$ is the wavenumber vector. In the deep ocean $kd \to \infty$, the hyperbolic function terms in (2.4) and (2.7) approach to $\exp(2kd)$.

Expressions for $(F_{d,x}, F_{d,y})$ are given as

$$(F_{d,x}, F_{d,y}) = \frac{\boldsymbol{k}}{\rho\sigma}\phi_{oc}\beta(z) \quad \text{with } \beta(z) \propto \cosh(\frac{z+h}{a_b H_s}) \tag{2.8}$$

where ϕ_{oc} is the dissipation function of a spectral wave model, $\beta(z)$ is a vertical distribution function suggested by *Uchiyama et al.* (2010) following the vertical distribution of the Stokes drift in (2.7), H_s is the significant wave height, and $a_b = 0.2$ is a constant.

2.2.1b The Radiation Stress Formulation

Equations based on M15's RS formulation describe the evolution of the Lagrangian mean velocity vector (u, v, w) defined as:

$$\frac{\partial u}{\partial x} + \frac{\partial v}{\partial y} + \frac{\partial w}{\partial z} = 0 \tag{2.9}$$

$$\frac{\partial u}{\partial t} + \frac{\partial uu}{\partial x} + \frac{\partial vu}{\partial y} + \frac{\partial wu}{\partial z} - fv = -\frac{1}{\rho_o}\frac{\partial p}{\partial x} - \frac{\partial S_{xx}}{\partial x} - \frac{\partial S_{xy}}{\partial y} + F_{m,x} \tag{2.10}$$

$$\frac{\partial v}{\partial t} + \frac{\partial uv}{\partial x} + \frac{\partial vv}{\partial y} + \frac{\partial wv}{\partial z} + fu = -\frac{1}{\rho_o}\frac{\partial p}{\partial y} - \frac{\partial S_{yx}}{\partial x} - \frac{\partial S_{yy}}{\partial y} + F_{m,y} \tag{2.11}$$

where the radiation terms (S_{xx}, S_{xy}, S_{yy}) are given by:

$$S_{xx} = g \iint kE(\sigma,\theta)(\frac{k_x k_x}{k^2} F_{CS}F_{CC} + F_{CS}F_{CC} - F_{SS}F_{CS})d\sigma d\theta \quad (2.12a)$$

$$S_{xy} = S_{yx} = g \iint kE(\sigma,\theta)(\frac{k_x k_y}{k^2} F_{CS}F_{CC})d\sigma d\theta \quad (2.12b)$$

$$S_{yy} = g \iint kE(\sigma,\theta)(\frac{k_y k_y}{k^2} F_{CS}F_{CC} + F_{CS}F_{CC} - F_{SS}F_{CS})d\sigma d\theta \quad (2.12c)$$

where k_x and k_y are the wavenumber components in the x and y direction, and the vertical structure functions are:

$$F_{SS} = \frac{\sinh(k(z+h))}{\sinh kd}; \quad F_{SC} = \frac{\sinh(k(z+h))}{\cosh kd} \quad (2.13a)$$

$$F_{CS} = \frac{\cosh(k(z+h))}{\sinh kd}; \quad F_{CC} = \frac{\cosh(k(z+h))}{\cosh kd} \quad (2.13b)$$

As $kd \to \infty$, all the F terms in (2.13a) and (2.13b) approach to $\exp(k(z-\eta))$. In M03, the vertical radiation stress (VRS) terms (ie, $\partial S_{px}/\partial z$ and $\partial S_{py}/\partial z$) appear on the right side of (2.10) and (2.11), which are omitted in M15 to be consistent with assumptions made in the linear wave theory. It should be noted that that the VRS terms have zero values of their depth integrations, and their role is to redistribute the wave momentum in the vertical direction.

2.2.1c The Breaking-Wave Induced Mixing

The *Mellor-Yamada* (MY) vertical mixing scheme (*Mellor and Yamada*, 1982) is used in calculating the vertical eddy viscosity coefficient in the POM, in which the surface boundary condition without surface gravity waves is expressed as

$$(q^2, q^2 l_0) = (B_1^{2/3} u_*^2, 0) \quad at\ z = 0 \quad (2.14)$$

where q^2 is twice the turbulent kinetic energy (TKE), l_0 is the length scale at the sea surface, $B_1 = 16.6$ is one of constants for the turbulence closure, and u_* is the friction velocity. *Craig and Banner* (1994) suggested that within a few meters from the sea surface the vertical eddy mixing is enhanced by the action of surface gravity waves. They incorporated the effect of breaking waves via an enhanced flux of the TKE at the sea surface. The surface boundary condition for the turbulent equation in the coupled model is

expressed by

$$K_q \frac{\partial(q^2/2)}{\partial z} = \phi_{oc} \quad at\ z = 0 \tag{2.15}$$

where K_q is the mixing coefficient. In addition, the surface length scale is set as $l_0 = \kappa z_0$, where $\kappa = 0.4$ is the von Karman's constant. The surface roughness length z_0 is related to H_s and defined as $z_0 = 1.6H_s$ according to *Terray et al.* (1996, 1999).

2.2.2 Ocean Wave Model

SWAN (*Booij et al.*, 1999) is a third-generation wave model that solves the wave action ($N(\sigma,\theta) = \frac{E(\sigma,\theta)}{\sigma}$) balance equation which accounts for the WCIs,

$$\frac{\partial N}{\partial t} + \frac{\partial}{\partial x}(c_x + u)N + \frac{\partial}{\partial y}(c_y + v)N + \frac{\partial}{\partial \sigma}c_\sigma N + \frac{\partial}{\partial \theta}c_\theta N = \frac{S_{tot}}{\sigma} \tag{2.16}$$

The first term on the left-hand side of (2.16) represents the local rate of change of action density in time, the second and third terms represent the wave propagation in spatial space (with propagation velocities $c_x + u$ and $c_y + v$ in x and y space, respectively) which accounts for horizontal advection of waves by currents, and (u, v) represents ocean currents at depth of $\mathrm{L}/4\pi$ (*Fan et al.*, 2009; *Stewart and Joy*, 1974), where L is the mean wave length. The fourth term represents depth- and current-induced relative frequency shifting (with propagation velocity c_σ in σ space). The fifth term represents depth- and current-induced wave refraction (with propagation velocity c_θ in θ space). The right-hand side of (2.16) contains the net source term S_{tot}, which includes all physical processes that generate, dissipate and redistribute the wave energy. In the source term, the surface wind velocity vector $\boldsymbol{U_{10}}$ used to calculate the wave growth due to winds is replaced by ($\boldsymbol{U_{10}} - \alpha\boldsymbol{U}$), which is the vector difference between the surface wind velocity and surface ocean current. Here α is a tuning coefficient. It should be pointed out that the use of the full ocean surface current ($\alpha = 1$) will exaggerate the relative wind effect since the relevant level at which the wind should be taken is the top of the atmospheric surface layer where the winds do not adjust to the presence of currents (*Ardhuin et al.*, 2012). In this study, we set $\alpha = 0.7$ according to *Wang and Sheng* (2016). In addition to currents, the sea surface

elevation modifies the total water depth used in the wave model, which is expected to be large in the very shallow water regions where surface waves could feel the ocean bottom.

2.2.3 Coupling Procedure

The dynamic coupling software known as OpenPALM (Fig. 1.4) is used to exchange information between POM and SWAN. OpenPALM is an open source code coupler for massively parallel multi-physics/multi-components applications and dynamics algorithm (http://www.cerfacs.fr/globc/PALM_WEB/index.html). One of the important features in OpenPALM is facilities for scheduling of different coupling components execution either sequentially or concurrently. At a user-specific coupling interval, the sea surface currents and water level fields produced by POM are transferred to SWAN to account for the WCIs. In return, fields of wave parameters calculated in SWAN are transferred to POM to calculate the wave-averaged effects on the 3D currents.

2.3 Two Idealized Test Cases

2.3.1 Test Case 1: Spectral Waves Obliquely Incident on a Planar Beach

The dimension of the planar beach is 1000 m in the cross-shore direction (defined as the x-axis) and 200 m in the longshore direction (the y-axis), with a maximum depth of 12 m and a constant slope of 1:80. The model grid has a resolution of 20 m in the horizontal direction, and 20 equally distributed sigma levels in the vertical. In both the test cases, we put the shoreline and offshore open boundary at the west and east ends of the model domain, respectively. A quadratic bottom stress formulation is used in the POM with a constant drag coefficient of 1.5×10^{-3}. A radiation boundary condition is specified at the offshore open boundary of the circulation model. The lateral open boundary conditions in the y direction are cyclic. The Earth's rotation is excluded since the barotropic Rossby radius is very large in this case, in comparison with the dimension of the study region. The wave field is computed using SWAN by specifying a JONSWAP spectrum with a significant wave height (H_s) of 2 m, a peak period of 10 s and an incident angle of 10^o at the offshore boundary. The spectral domain consists of 90 directional bins and 30 frequencies between 0.04 and 0.5 Hz. To be consistent with previous studies, the coupling in this test case is one-way in

which the simulated wave fields produced by SWAN are used in specifying the VF (or RS) formulation in the POM, without any feedback from the circulation model to the wave model. It should be noted that for this test case only we conducted an additional experiment for M03's RS formulation to discuss the role of the VRS term.

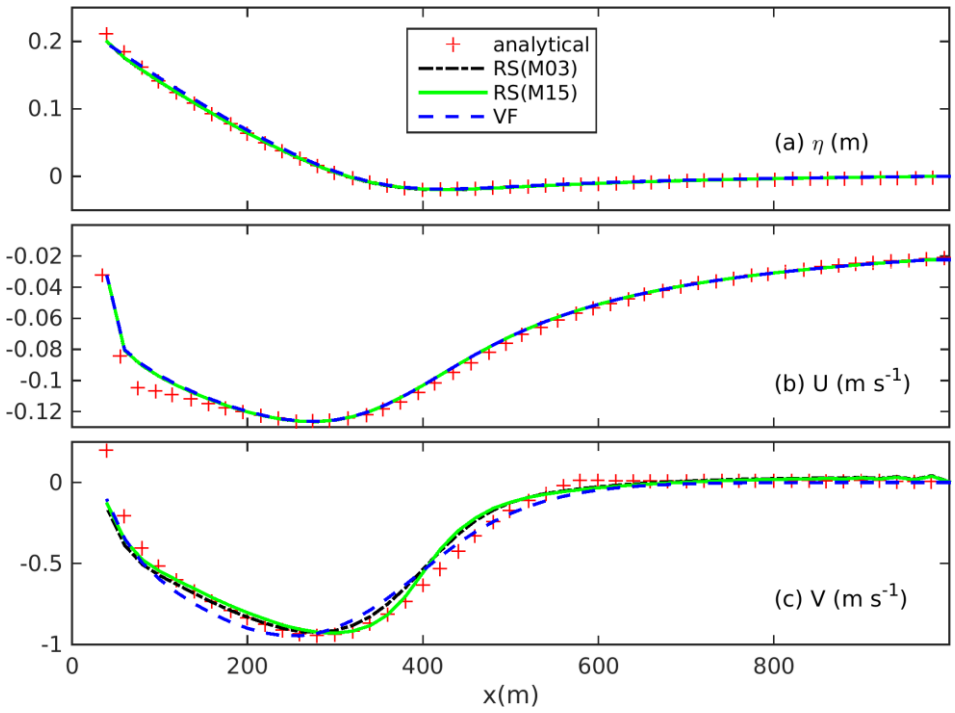

Figure 2.1: Cross-shore distributions of (a) surface elevations, (b) depth-mean cross-shore currents and (c) depth-mean along-shore currents in the planar beach test case produced by the circulation model of the coupled wave-circulation modelling system using the VF (blue dashed lines) and RS (green solid lines) formulations. Red cross symbols represent analytical solutions.

The surface gravity waves shoal after entering the model domain from the offshore open boundary and start to break around 400 m from the shoreline, at which the depth-limited breaking criterion is reached. The coupled wave-circulation modelling system is integrated for one hour by which a steady-state of the circulation is reached. It should be mentioned that an analytical solution for the surface elevation and barotropic velocities in this test case is given by *Uchiyama et al.* (2010). As shown in Figure 2.1a, inside the surf zone (the region of breaking waves), the sea level rises up to 0.2 m to balance the variation

of surface wave forces in the cross-shore direction due to wave breaking. Meanwhile, an off-shore flow is generated to compensate the wave-induced onshore mass transport (Fig. 2.1b). In the along-shore direction, strong longshore currents up to 1 m s^{-1} are generated due to the angle of wave approaching on the shoreline (Fig. 2.1c). The use of the VF and RS (M03 or M15) formulations in the coupled wave-circulation modelling system leads to highly similar sea surface elevations, depth-mean cross-shore and along-shore currents in this test case, which agree fairly well with the analytical solution produced by *Uchiyama et al.* (2010).

Figures 2.2d-f demonstrate that the longshore currents produced by the circulation model using the VF and RS (M03 or M15) formulations have similar vertical structures inside the surf zone. Significant differences occur, however, in vertical structures of cross-shore currents between these two formulations (Figs. 2.2a-c). For the VF formulation, the cross-shore currents have a two-layer circulation feature inside the surf zone, with a weak onshore flow near the sea surface and a strong undertow (up to 0.25 m s^{-1}) near the bottom (Fig. 2.2a), which is mainly driven by the sum of the pressure gradient induced by the surface slope, the Bernoulli-head and the breaking acceleration (Fig. 2.2g). Outside the surf zone, the cross-shore flow is nearly uniform and offshore directed. The model results using the VF formulation are consistent with previous numerical experiments (*Uchiyama et al.*, 2010; *Michaud et al.*, 2012) and laboratory observations (*Ting and Kirby*, 1994) over a planar beach. For M15's RS formulation, the flow is offshore directed at the surface and decreases with depth inside the surf zone, and has a two-layer circulation feature with strong onshore flow in the top few meters and seaward flow in the lower layer outside the surf zone (Fig. 2.2b). The net force excluding mixing or friction is the sum of the pressure gradient and the radiation stress gradient, which has opposite vertical structure inside and outside the surf zone (Fig. 2.2h). In comparison, for M03's RS formulation, the sign of the net force inside the surf zone is completely reversed vertically by the inclusion of the VRS (Fig. 2.2i), and correspondingly the flow is reversed with a weak undertow near the bottom (Fig. 2c). Outside the surf zone, the effect of the VRS on the net force is negligible. Therefore, the omission of the VRS seems to be justified outside the surf zone but not inside the surf zone where the linear wave theory assumptions are violated. However, *Ardhuin et al.* (2008a) showed that, even outside the surf zone, M03's estimation of the

VRS based on the linear wave theory is inadequate over a slopping bottom. They proposed a method to correct for M03's estimation of the VRS, which brings the net force to be nearly uniform over the vertical, but it is computational expensive. This highly non-uniform net force under non-breaking wave conditions induces a recirculation similar to that found in an adiabatic test case using M03's RS formulation by BAD11, and it might have some consequences for applications with complex topography as we will show in the realistic application.

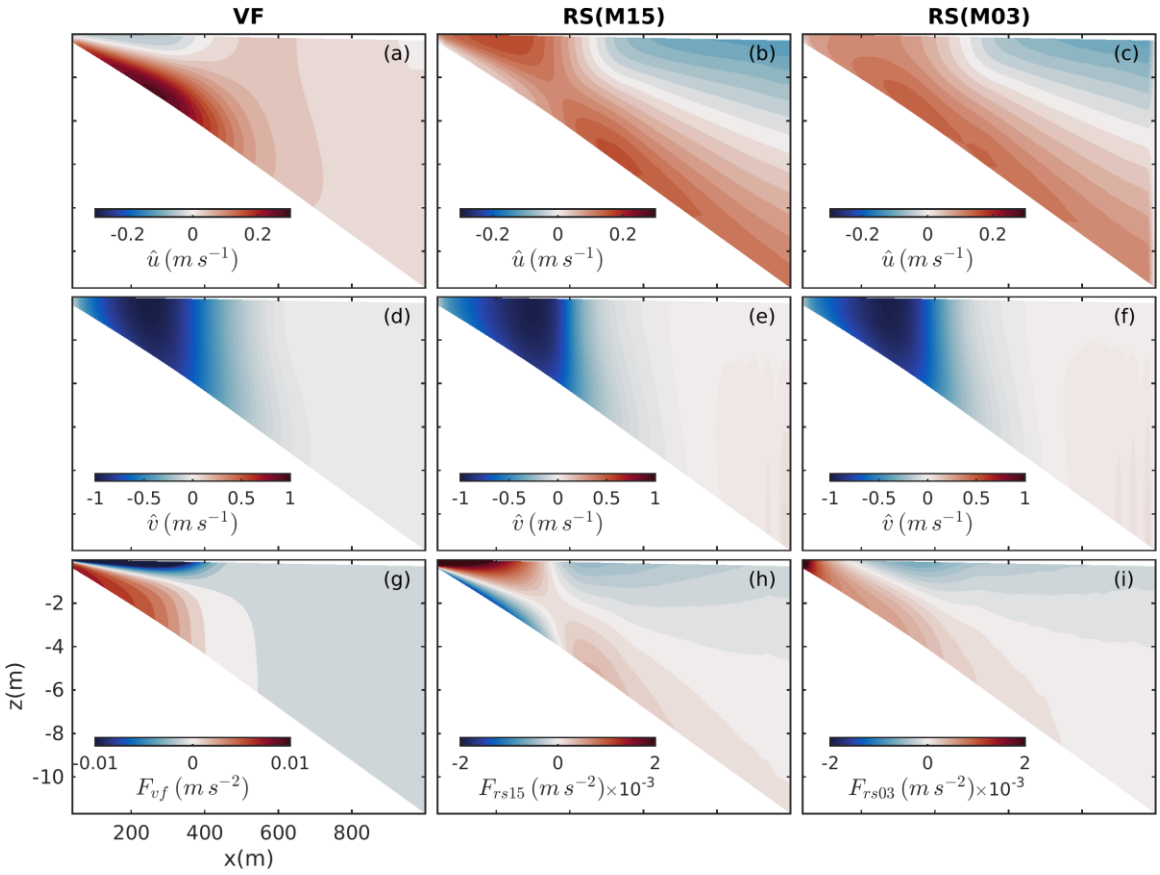

Figure 2.2: Vertical distributions of cross-shore (upper panels), along-shore (middle panels) Eulerian currents, and cross-shore net force (lower panels) in the planar beach test case produced by the circulation model of the coupled wave-circulation modelling system using the VF (left panels), RS (M15) (middle panels), and RS (M03) (right panels) formulations. The net force is defined as $\mathrm{F_{vf}} = -\frac{1}{\rho_0}\frac{\partial p}{\partial x} + \frac{\partial J}{\partial x} + F_{d,x}$, $\mathrm{F_{rs15}} = -\frac{1}{\rho_0}\frac{\partial p}{\partial x} - \frac{\partial S_{xx}}{\partial x} - \frac{\partial S_{xy}}{\partial y}$, and $\mathrm{F_{rs03}} = -\frac{1}{\rho_0}\frac{\partial p}{\partial x} - \frac{\partial S_{xx}}{\partial x} - \frac{\partial S_{xy}}{\partial y} + \frac{\partial S_{px}}{\partial z}$. Positive cross-shore currents are off-shore directed, and negative along-shore currents point out of the page.

2.3.2 Test Case 2: Rip Current over a Barred Beach

The bathymetry used in this test case is a scaled version of the bathymetry of *Haller et al.* (2002) by a factor of 10 (Fig. 2.3a). The model domain has a horizontal dimension of 146 m by 262 m in the cross-shore (defined again as the x-axis) and along-shore (y-axis) directions respectively, with a horizontal resolution of 2 m. The circulation component of the coupled model has 8 sigma levels in the vertical direction. No-slip boundary conditions are used at the coast, offshore and lateral boundaries. A quadratic bottom friction parameterization with a bottom roughness height of 0.015 m is used. The Coriolis effect is excluded for the same reason in the first test case. At the offshore open boundary, SWAN is forced by a JONSWAP wave spectrum with a H_s of 0.5 m, and a peak period of 3.16 s, perpendicular to the coast. The spectral resolution is 36 directional bins and 20 frequency bins between 0.05 and 1 Hz. The coupling interval between POM and SWAN is set to be 10 s.

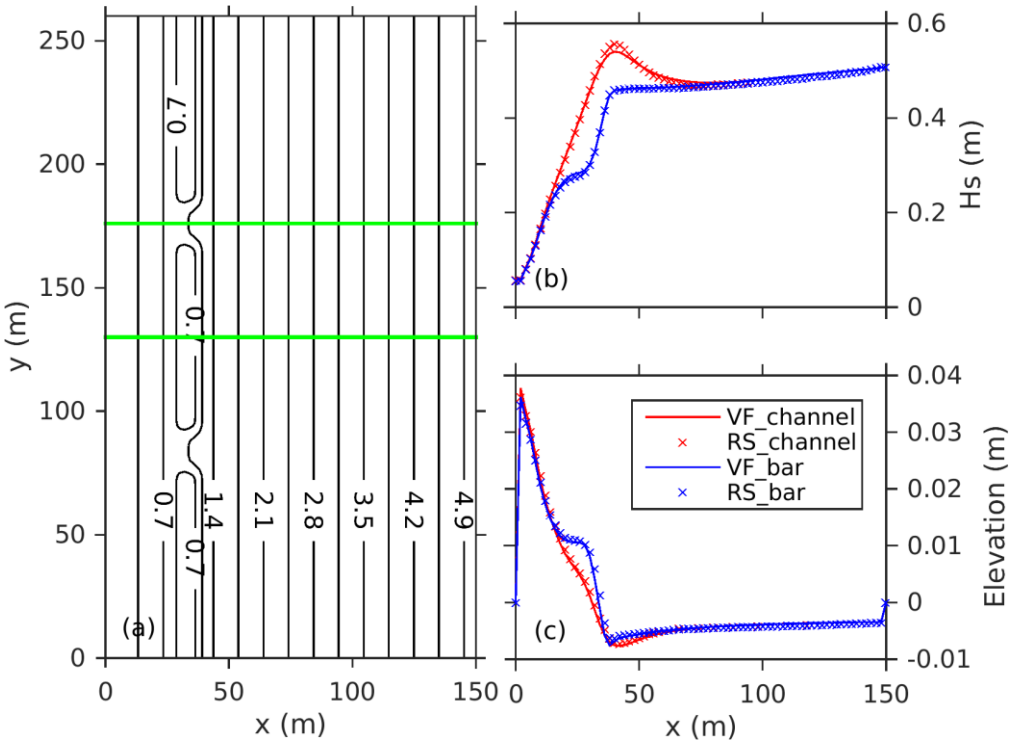

Figure 2.3: (a) Bathymetry for the barred beach test case. Model results along the green lines are presented in (b), (c), and Figure 2.5. Cross-shore distributions of (b) significant wave heights and (c) sea surface elevations through the channel at y = 176 m and over the bar at y = 130 m for the VF and RS formulations.

We follow *Kumar et al.* (2011) and *Michaud et al.* (2012) and use a relatively large horizontal diffusion coefficient (0.20 m^2 s^{-1}) in the circulation model in order to reach a stable circulation quickly for direct comparisons of our results using two different feedback formulations with previous studies. Figures 2.3b and 2.3c present the cross-shore profiles of H_s and sea surface elevations, respectively, over the rip channel and the bar. The simulated H_s and sea surface elevations produced by the circulation model are very similar in both the cases of using the VF and RS formulations. Through the rip channel, significant wave shoaling occurs due to the interaction between the onshore directed waves and offshore directed currents. The surface gravity waves propagate shoreward through the rip channel and start to break at about 38 m from the coast. Over the bar, wave breaking starts at about 36 m from the coast and then takes place again close to the shoreline at about 18 m (Fig. 2.3b). Different wave breaking patterns through the channel and over the bar lead to different sea levels (i.e. wave-induced set-up) inside the bar location (Fig. 2.3c). Through the channel, the surface elevations first decrease due to the wave-induced set-down and then increase almost linearly towards the shoreline (Fig. 2.3c). Over the bar, the surface elevations also increase towards the shoreline, but there is a sharp increase just behind the bar location. Different sea level distributions at the channel and over the bar lead to a large horizontal pressure gradient in the along-shore direction that causes water flow from high surface elevations to low surface elevations. The convergence of longshore currents at the channel generates the rip current and transports the excess of water brought by waves offshore (Fig. 2.4).

The depth-mean current fields produced by the circulation model using VF and RS formulations are also highly similar in terms of the general pattern and intensity (Fig. 2.4). The depth-mean currents in both the cases feature narrow strong currents running out through rip channels and recirculation cells developed both inside and outside the bar. The model calculated depth-mean currents in both cases are in a very good agreement with previous laboratory experiments (*Haller*, 2002) and numerical studies (*Kumar et al.*, 2011; *Michaud et al.*, 2012). Large differences occur, however, in the vertical structure of cross-shore currents through the rip channel and over the bar (Fig. 2.5a-d). In the case of the VF formulation (Fig. 2.5a), the flow over the inshore of the rip channel is onshore directed near the surface and decreases in magnitude with depth, with weak and offshore directed

flow near the bottom. In the case of the RS formulation (Fig. 2.5c), the onshore directed flow over the inshore region is almost uniformly distributed throughout the water column. Within the rip channel and further offshore, a strong offshore-directed flow is developed and the flow structures produced by the model with the use of both formulations are similar: the current velocity reaches a maximum of ~0.3 m s^{-1} in the middle of the water column and decreases in magnitude towards the surface and bottom. Inshore of the bar location, the flow structures produced by the model differ between the two different formulations. For the VF formulation (Fig. 2.5b), the flow is shoreward near the surface and offshoreward near the bottom due to wave breaking in the surf zone. For the RS formulation (Fig. 2.5d), however, the flow is offshoreward in the vertical with the offshore speeds decreasing with depth, which is similar to the results inside the surf zone in the planar beach test case. Further offshore, both feedback formulations give similar results with onshoreward flow near the surface and offshoreward flow near the bottom.

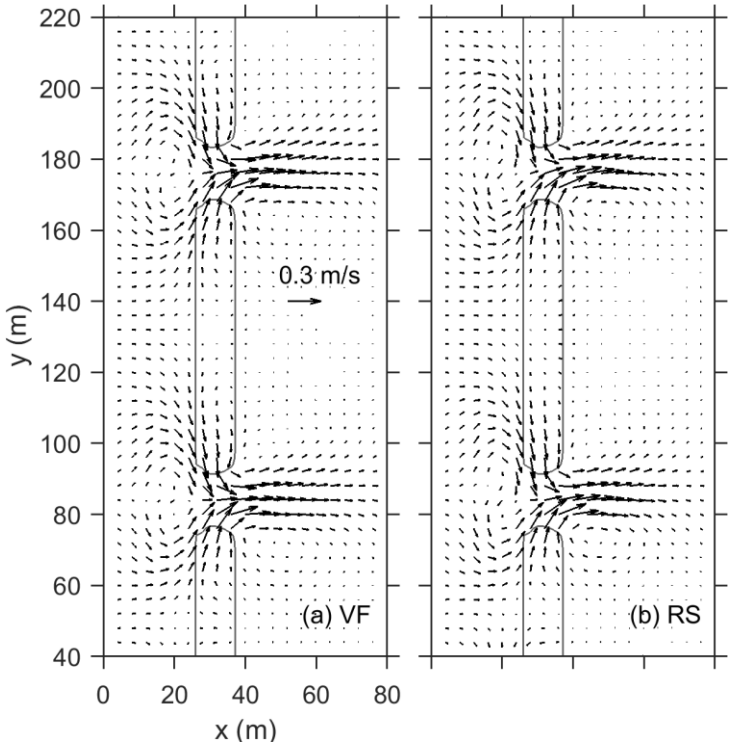

Figure 2.4: Depth averaged fields of (a) quasi-Eulerian velocity produced by the coupled system using the VF formulation and (b) Eulerian velocity produced by the coupled system using the RS formulation.

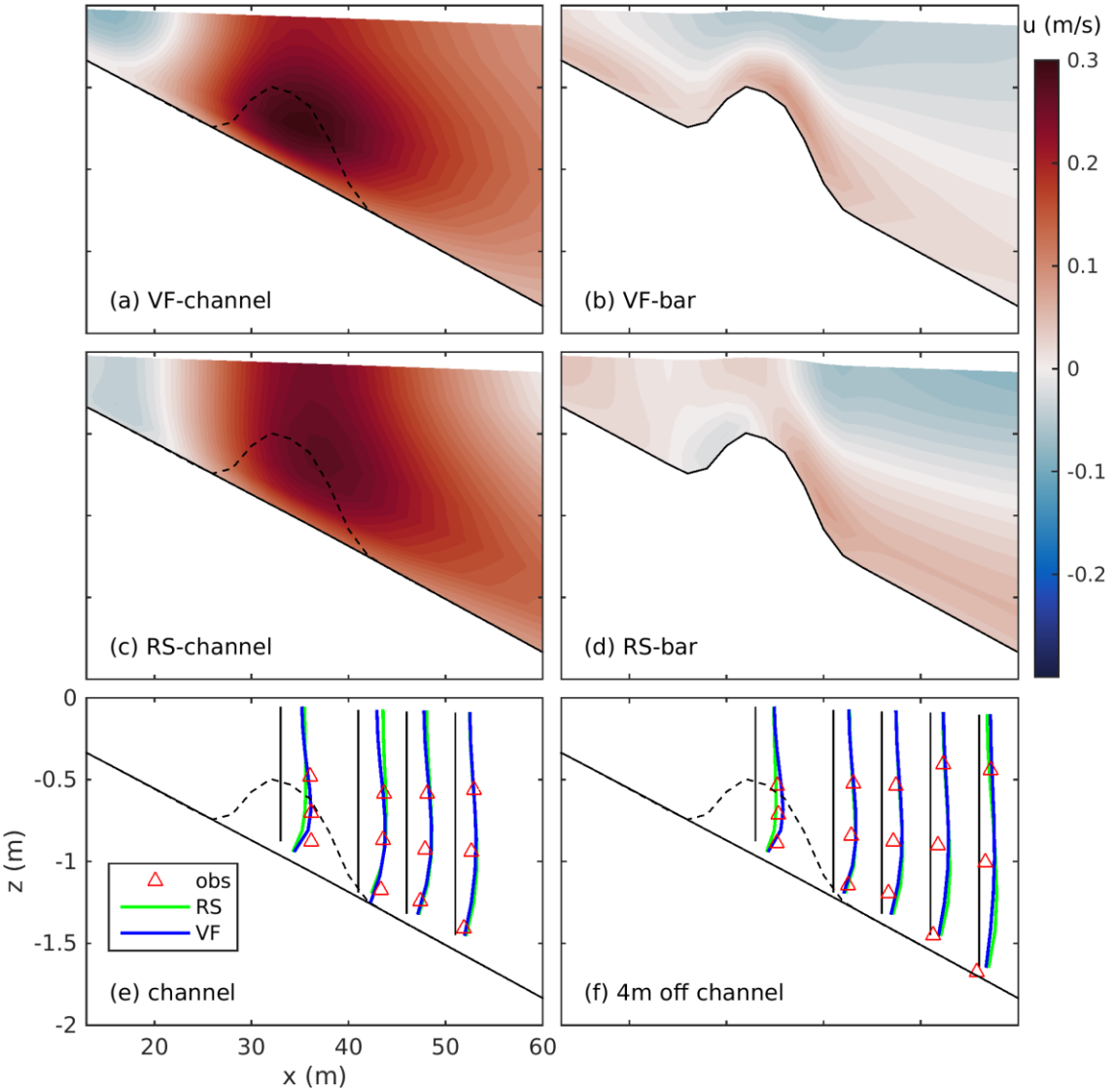

Figure 2.5: Vertical distributions of cross-shore quasi-Eulerian velocity produced by the circulation model using the VF formulation (a) through the rip channel at y = 176 m and (b) over the bar at y = 130 m, and Eulerian velocity produced by the circulation model using the RS formulation (c) through the channel and (d) over the bar. Comparison of normalized model derived cross-shore velocity with normalized observations from Haas and Svendsen (2002) at (e) the channel and (f) 4 m off the channel. Vertical black lines in (e) and (f) indicate locations of measurements and zero value for each profile.

We follow Kumar et al. (2011, 2012) and conduct a semi-quantitative comparison between the observed and modeled vertical structure of the cross-shore currents within the rip channel and further offshore. The observed velocity profiles were obtained from the bin averaged velocities of Test R in *Haas and Svendsen* (2002, HS2002) at all reported

locations (Figs. 2.5e and 2.5f). The observed and modeled velocities are normalized by the corresponding maximum cross-shore velocities at the bar crest (x = 33 m), respectively. As shown in Figure 2.5e and 2.5f, the normalized cross-shore velocity profiles produced by the model using both feedback formulations agree reasonably well with measurements of HS2002 at their observation locations.

Analyses of model results with two different formulations for WCIs in the above-mentioned two test cases indicate that, after the omission of the VRS term, the latest version of RS formulation in M15 performs even worse in reproducing the observed vertical structure of the cross-shore currents inside the surf zone. By comparison, the VF formulation, which separates the 3D wave force into conservative force (vortex force and Bernoulli head) and non-conservative force due to wave breaking, performs reasonably well in simulating the wave-forced currents inside the surf zone. The satisfactory model results in the two test cases indicate that these two different formulations are implemented correctly in the coupled wave-circulation modelling system. The latter will be applied to simulate waves and 3D currents over a coastal embayment to be discussed in the next section.

2.4 A Realistic Application in Lunenburg Bay during Hurricane Juan

In years 2001-06, a multiagency research initiative was undertaken to develop a relocatable marine environmental observation and prediction system, using data-assimilative and coupled models guided directly by real-time observations in Lunenburg Bay (LB, Fig. 2.6). High-quality current and wave observations were made in LB when Hurricane Juan made a landfall within 50 km of the site in September 2003 (*Wang et al.*, 2007).

Hurricane Juan was an intense tropical cyclone and caused heavy damage in Nova Scotia and Prince Edward Island in late September 2003. Hurricane Juan reached category 2 strength on the Saffir-Simpson hurricane scale on 27 September and made landfall on the south coast of Nova Scotia near Halifax early on 29 September (Fig. 2.6), with maximum sustained winds of about 158 km h^{-1} and a rapid translation speed of about 20 m s^{-1}. The storm-induced 3D circulation in LB during Hurricane Juan was previously examined by *Wang et al.* (2007) using a 3D fine-resolution (60 m) coastal circulation model, and re-

examined by *Sheng et al.* (2009) using a more advanced nested-grid circulation model. Both studies reproduced reasonably well the observed currents under normal conditions, but less well during extreme weather conditions (Fig. 9 in *Wang et al.*, 2007), which may be due mostly to the omission of surface gravity wave forces in their circulation models. *Mulligan et al.* (2008) considered the surface wave forces by using LS64's 2D RS formulation in a study of the wave-driven flow in LB during Hurricane Juan, but their coupled model was not able to reproduce the 3D structure of the circulation in the Bay. This motivates us to apply the newly-developed coupled wave-circulation modelling with 3D surface wave forces in terms of VF and RS formulations to LB to simulate ocean surface gravity waves and currents in the Bay.

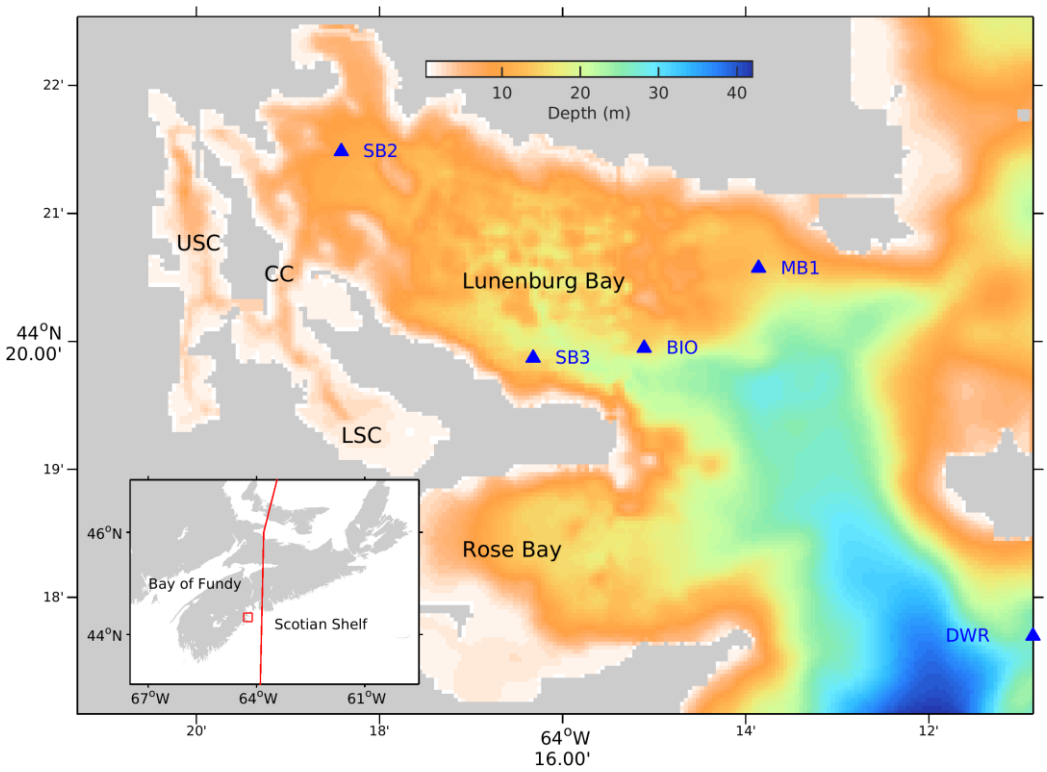

Figure 2.6: Selected bathymetric features within the model domain of the Lunenburg Bay model. The filled triangles denote the observation locations. Abbreviations are used for Corkum's Channel (CC), Upper South Cove (USC), and Lower South Cove (LSC). The inset map shows the location of the study area (red square) and the storm track of Hurricane Juan (red line).

2.4.1 Model Setup

The circulation model for LB is constructed as a single-domain coastal ocean model based on the POM (Fig. 2.6). Previous studies demonstrated that, with proper open boundary conditions and reliable atmospheric forcing, a single-domain model has reasonable skills in simulating the tidal and wind-driven circulations in LB under an extreme weather event known as Hurricane Juan (*Wang et al.*, 2007). *Sheng et al.* (2009) demonstrated that a nested-grid coastal circulation model for LB during this event has similar performances as the single-domain model. Considering that the focus of this section is on the coastal ocean circulation inside the Bay, a single-domain model is considered here. Since the vertical stratification is very weak in LB during Hurricane Juan (*Zhai et al.*, 2007), the model is run in barotropic mode with temperature and salinity held fixed. Along the model open boundaries, the following radiation condition (*Davies and Flather*, 1987) is used:

$$U_B = U_p + \frac{c}{h}(\eta_B - \eta_t - \eta_r) \tag{2.17}$$

where U_B and η_B are the model calculated normal flow and surface elevation at the open boundaries, U_p is a specified normal flow and set to be the normal flow at grid points closest to the open boundaries U_{B-1} for simplicity, c is the external gravity phase speed. η_t and η_r are surface elevations associated with tides and remotely generated waves, respectively. We follow *Wang et al.* (2007) and specify η_t at the open boundary using the simplified incremental approach from the tidal sea level prediction at Lunenburg Harbor, which was made by the Canadian Hydrographic Service using more than 60 tidal constituents determined from the historical sea level observations at the harbor, and η_r is determined from the observed non-tidal sea level at site SB2 using the same approach.

The wave model constructed from SWAN shares the same horizontal model grid as the circulation model. The spectral domain consists of 36 directional bins with 10° of resolution and 23 logarithmic frequency bins ranging from 0.04 to 1.00 Hz ($\frac{\Delta\sigma}{\sigma} = 0.15$). Similar to *Mulligan et al.* (2008), the observed time series of wave spectra at site DWR are applied uniformly along the open boundaries. Since observed winds at sites SB2 and SB3 are highly similar (*Wang et al.*, 2007), for simplicity, we assume winds used to drive the coupled model are spatially uniform and equal to winds at site SB3. It should be noted that

spatial variability occurs in the wind forcing in LB, which will affect the small-scale circulation feature in the Bay, as discussed in *Wang et al.* (2007).

Four basic numerical experiments are conducted in this case to examine effects of WCIs on the surface wave field and the 3D ocean currents: the coupled model run for the VF formulation (Run_VF), the coupled model run for the RS formulation (Run_RS), the wave-only model run (Run_WaveOnly), and the circulation-only model run (Run_CirOnly). Each model run is integrated for three days from 27 September (day 269) to 30 September (day 272) 2003, and the coupling interval between the POM and SWAN is set to be 6 min.

2.4.2 Wave Model Results

Figure 2.7 presents time series of observed and simulated H_s, peak wave periods, and dominate wave directions at site BIO. In comparison with observations, the wave-only model run (Run_WaveOnly) performs reasonably well before and after the storm, but underestimates the maximum observed H_s by ~1 m during the storm, which is consistent with the previous finding made by *Xu et al.* (2007) using a nested wave-only model (Fig. 4a in *Xu et al.*, 2007). The use of the VF and RS formulations (Run_VF and Run_RS) in the coupled wave-circulation modelling system improves the simulated maximum H_s by ~0.5 m due to the inclusion of the effect of strong opposing surface currents in the wave model. The coupled system also reproduces reasonably well the observed peak wave periods and dominate wave directions, with relatively small differences among these three model runs (Figs. 2.7b and 2.7c). The peak wave periods are around 10 s and the dominate wave directions are around 150^o before and after Hurricane Juan at site BIO, indicating the wave field in the Bay is dominated by swells propagating from the southeast direction during this hurricane period.

Figure 2.8a presents the instantaneous wave field produced by the coupled modelling system using the VF formulation at the time of the maximum H_s (at year day of 271.17) at site BIO. Large hurricane-generated waves propagate from the model open boundary into the Bay (Fig. 2.8a) and break along the north coast, over the submerged shoal near the mouth of the Bay, and around the south headland (Fig. 2.8b). These intense breaking waves

are responsible for the strong wave-driven circulation in the Bay as we will discuss later.

We next examine the effects of WCIs on the H_s in the case of the VF formulation at day 271.17. Figure 2.8c shows that H_s at the mouth of the Bay are significantly increased by 0.5-1.0 m due to the strong opposite surface outflow (Fig. 2.11a). The wave heights along the north coast and around the south headland are also significantly increased by ~1.0 m, but due to the feedback of sea levels to the total water depth. The total sea level including the wave setup is about 0.9 m around these regions at this moment (not shown), which decreases the intensity of depth-limited wave breaking. The spatial distributions of H_s changes in the case of the RS formulation (Fig. 2.8d) are generally similar to, but not as smooth as, those in the case of the VF formulation due to different surface current features as we will discuss later.

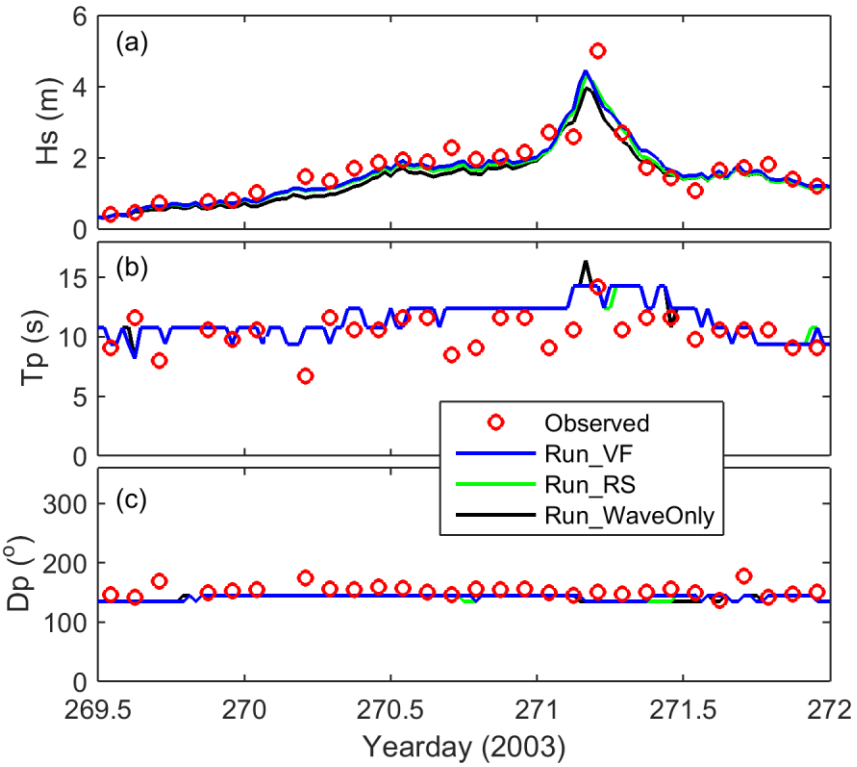

Figure 2.7: Time series of observed and simulated (a) significant wave heights (Hs), (b) peak wave periods (Tp), and (c) dominant wave directions (Dp) at site BIO. Model results in three cases (Run_VF, Run_RS and Run_WaveOnly) are compared with observations.

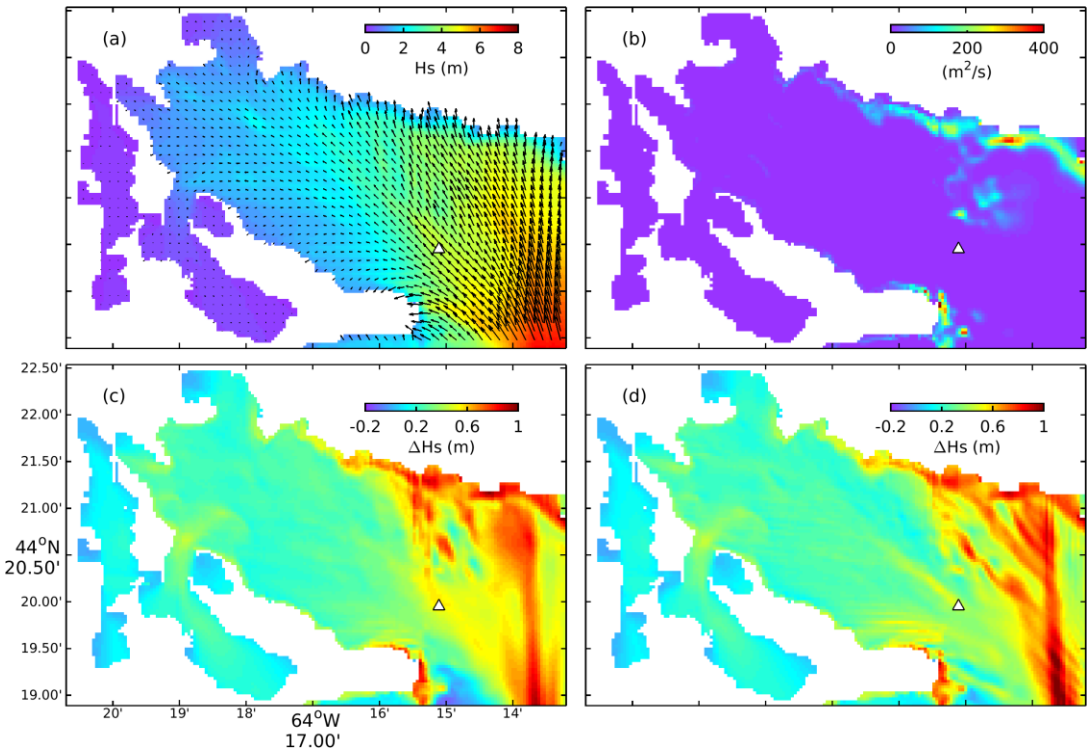

Figure 2.8: (a) Simulated H_s (image) and wave directions and (b) simulated wave energy dissipation produced by the coupled modelling system using the VF formulation, and differences in H_s (c) between Run_VF and Run_WaveOnly and (d) between Run_RS and Run_WaveOnly at 0430Z Sep 29 (day 271.19). Triangles indicate instrument locations.

2.4.3 Circulation Model Results

Figures 2.9a and 2.9b present time series of observed and simulated sea levels at sites SB2 and SB3, respectively. The simulated sea levels produced by the coupled wave-circulation modelling system with the use of the VF formulation (Run_VF) are in a very good agreement with the observations at these two sites, particularly between day 271.0 and 271.4. During this period hydrodynamics over coastal waters of the central Scotian Shelf were impacted significantly by Hurricane Juan (*Sheng et al.,* 2006; *Wang et al.,* 2007; *Xu et al.,* 2007; *Mulligan et al.,* 2008). Figures 2.9a and 2.9b also demonstrate that the model calculated sea levels at these two sites (SB2 and SB3) are highly similar in three model runs (Run_VF, Run_RS, Run_CirOnly), indicating that sea levels at these two sites are not significantly affected by WCIs. This can be explained by the fact that these two sites are located outside the surf zone (positions of these two sites are marked in Figs. 2.9c and 2.9d).

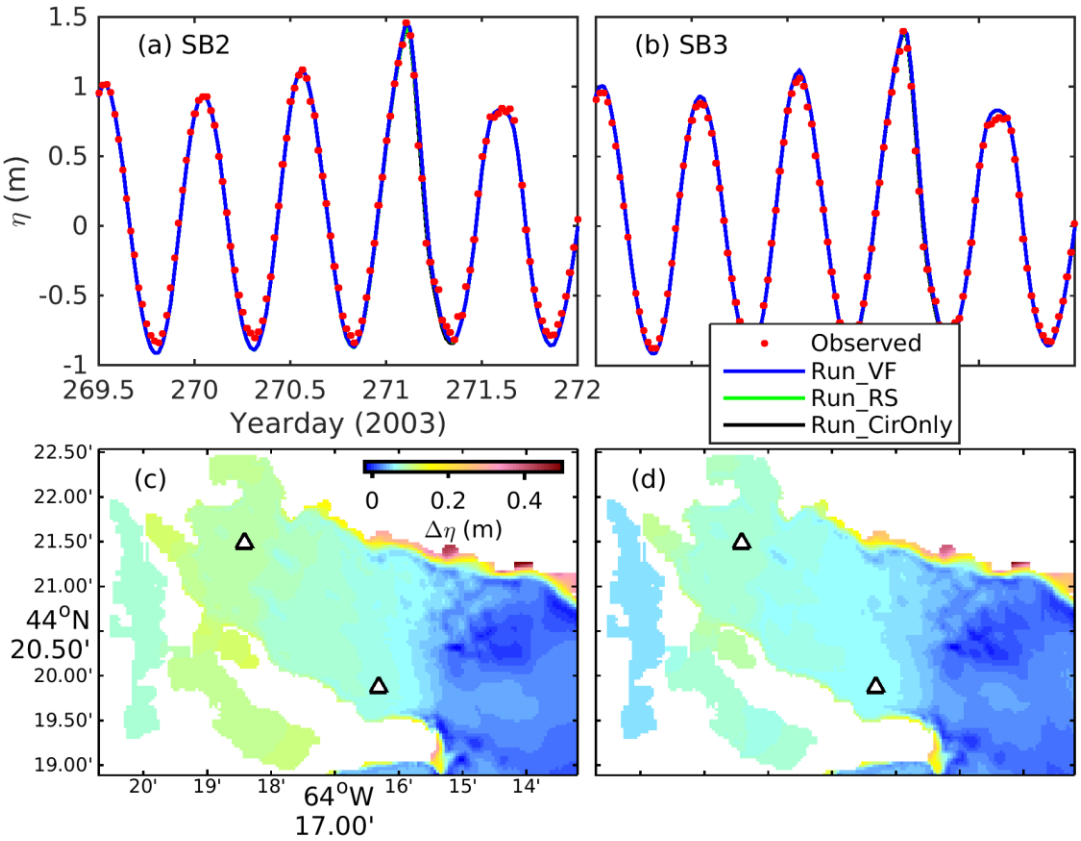

Figure 2.9: Time series of observed and simulated sea levels at sites (a) SB2 and (b) SB3, and differences in sea levels (c) between Run_VF and Run_CirOnly, and (d) between Run_RS and Run_CirOnly at 0430Z Sep 29 (day 271.19). Triangles indicate instrument locations.

To examine the wave-induced sea level changes associated mainly with wave breaking and wave-driven flow, we calculate the differences in model calculated sea levels at day 271.17 between Run_VF and Run_CirOnly. Figure 2.9c demonstrates that wave breaking leads to a significant sea level rise (or wave setup) of 0.3-0.5 m along the north coast and around the south headland in Run_VF. There is also a slight sea level rise (~0.1 m) in the west end of the Bay due to the wave-driven inflow. The wave-induced sea level changes in the case of the RS formulation (Fig. 2.9d) have similar features as those in the case of the VF formulation, except for relatively smaller magnitudes.

Figure 2.10 presents time series of observed and simulated horizontal currents at three different depths of three observation sites MB1, BIO, and SB3 located near the mouth of the Bay. Same as previous studies (*Wang and et al.*, 2007; *Sheng et al.*, 2009), the

circulation-only model run (Run_CirOnly) does not reproduce the observed strong coastal ocean currents around day 271.19. By comparison, the coupled wave-circulation modelling system with the use of the VF formulation (Run_VF) performs much better in simulating 3D currents at all the three sites, indicating that the surface wave forces played a more important role than other forces in driving the coastal currents in the Bay during the passage of Hurricane Juan. The use of the RS formulation in Run_RS also performs well at site BIO with similar model results as those in Run_VF, but it performs less well than the VF formulation at sites MB1 and SB3 located near the shore.

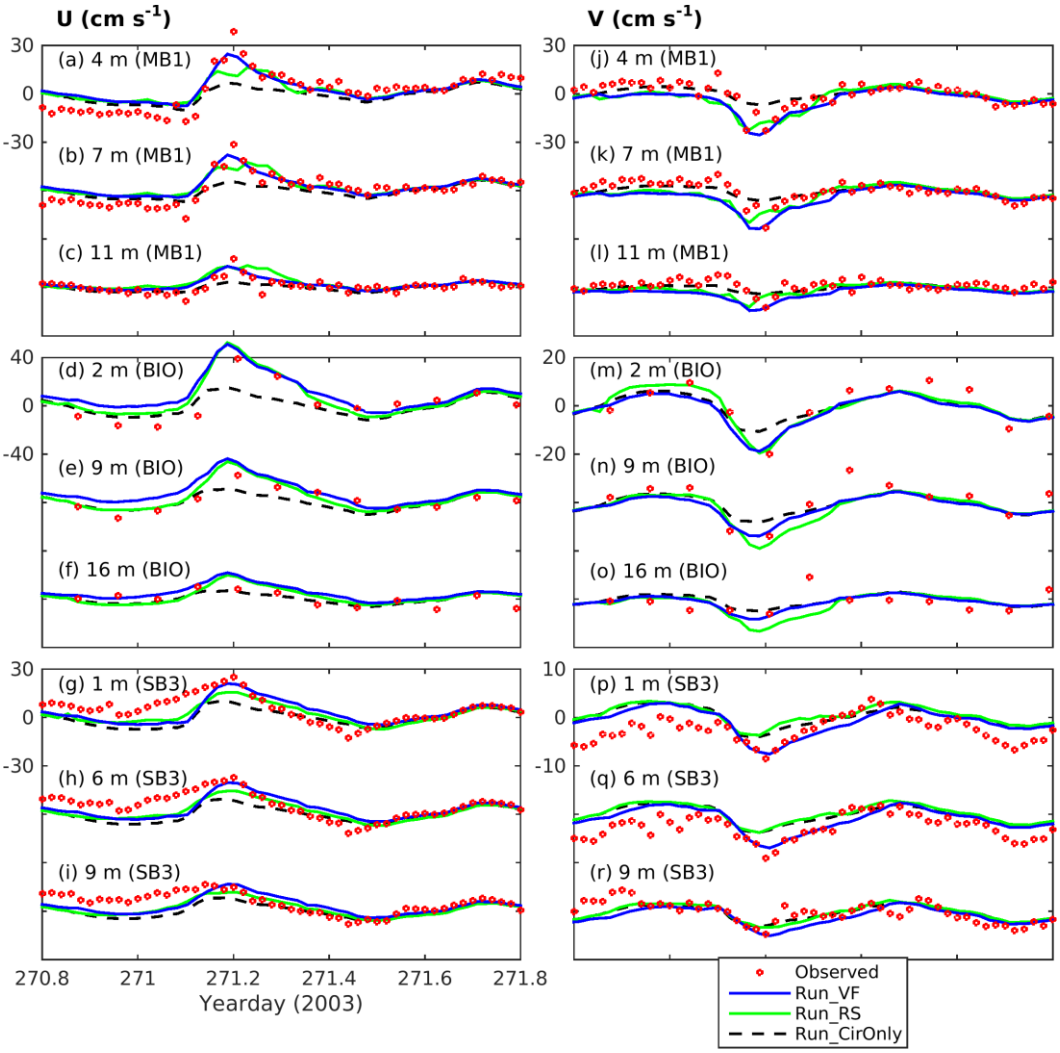

Figure 2.10: Time series of eastward (left panels) and northward (right panels) components of observed and simulated currents at depths of (upper) 4, 7, and 11 m for site MB1; (middle) 2, 9, and 16 m for site BIO, and (lower) 1, 6, and 9 m for site SB3. Model results in three cases (Run_VF, Run_RS and Run_CirOnly) are compared with observations.

To quantify the performance of the coupled model with the use of two different formulations in simulating currents at three sites, we follow *Thompson and Sheng* (1997) and use γ^2, which is defined as the variance of model errors normalized by the observed variance:

$$\gamma^2 = \frac{Var(O-M)}{Var(O)} \tag{2.18}$$

where Var stands for variance, and O and M denote respectively the observed and simulated values of a variable. A smaller value of γ^2 denotes a better agreement between the observed and simulated values. Values of γ^2 less than unity indicate that the observed variance is reduced by the subtraction of the hindcasts from the observations. Values of γ^2 greater than or equal to unity can occur if the model is deficient in some important way or the observations are dominated by measurement noises. In this study, we use $\gamma^2 = 1$ as a threshold to assess the model performance.

For the case of Run_VF, the γ^2 values (Table 2.1) are about 0.15-0.89 for the eastward (u) and northward (v) components of currents at the three sites, particularly with small values of less than 0.40 for the currents at 4 m and 7 m of site MB1 and at 2 m and 9 m of site BIO. This indicates that the coupled wave-circulation modelling system in Run_VF performs reasonably well in simulating currents at these three sites, particularly at sites MB1 and BIO. By comparison, the γ^2 values in Run_RS are larger than the γ^2 values in Run_VF at three sites, except for the u-components at 2 m and 9 m of site BIO and at 9 m of site SB3, and v-components at 2 m of site BIO and at 9 m of site SB3. This indicates that the VF formulation performs better than the RS formulation for reconstructing the currents measurements at site MB1, for currents at the upper and middle depths at site SB3, and for the bottom currents at site BIO. It should be noted that the γ^2 values in Run_CirOnly (Table 2.1) are largest or the second largest in three model runs at three depths of three different sites, which indicates the important role of the WCIs in driving the 3D currents over the coastal embayment. It should also be noted that the γ^2 values in Run_VF are slightly larger than the values in Run_RS for u-components at 2 m and 9 m at site BIO and 9 m at site SB and for v-components at 2 m at site BIO and 9 m at site SB3,

for which exact reasons are unknown.

Figure 2.11c presents the simulated surface currents at the time of maximum currents at site BIO (day 271.19) in Run_CirOnly. The circulation-only model produces a strong jet-like flow (~1 m s^{-1}) over a narrow channel known as Corkum's Channel (CC) and its adjacent waters in LB, with relatively weak currents over other areas of the Bay. The jet-like flow is associated mainly with large differences in sea levels associated with tides between LB and two coves known as Upper South Cove (USC) and Lower South Cove (LSC). These large-scale circulation features produced by the circulation-only model are consistent with previous simulations of *Wang et al.* (2007). By comparison, the coupled wave-circulation modelling system with the use of VF and RS formulations generates much stronger surface currents in LB, in addition to the jet-like flow in the CC and its adjacent waters (Figs. 2.11a and b). Intense wave breaking (Fig. 2.8b) induces strong wave-driven inflows (~1 m s^{-1}) along the north coast, over the submerged shoal at the mouth of LB, and around the south headland. These inflows then drive a strong outflow (~0.5 m s^{-1}) in the deep channel of the Bay due to mass balance, which is captured by the instrument at site BIO. The flow captured at site MB1 is also an outflow due to the wave-driven inflows, but less strong than that at site BIO. Nonetheless, some differences between the two model runs occur over the shallow areas near the north and south shores. Moreover, inside the Bay with complex topography, the circulation in Run_RS is not as smooth as the counterpart in Run_VF (see the color shading in Fig. 2.11b).

Figures 2.12a and b present distributions of wave-induced surface and bottom currents (WICs) defined as differences in current vectors between the coupled model run using the VF formulation (Run_VF) and the circulation-only model run (Run_CirOnly) near the north shore of LB where the Bay is exposed to large waves. At the sea surface, the wave-induced circulation over this area features strong longshore currents along the north coast and two intense recirculation cells on the right and left sides of the submerged shoal. In comparison with the surface currents, near the coast, the bottom currents are more offshore directed consistent with model results in our idealized test cases over the surf zone. Over the submerged shoal area, the bottom currents have similar structures as the surface currents due to a lack of coastal wall. In comparison with WICs in Run_VF, the structure of WICs in Run_RS (Figs. 2.12c and d) is less coherent with some very unphysical currents

generated over areas outside the wave breaking zone (surf zone) (water depth greater than ~5 m), which directly degrades the model skill in simulating currents at site MB1. Furthermore, in a two-way coupled modelling system, the feedback of these less coherent currents to the wave model introduces some unrealistic features to the wave fields (e.g. Fig. 2.8d). In order to examine the origin of these unphysical currents generated in Run_RS, we conducted an additional experiments for the RS formulation with only one-way coupling (Run_RS_oneway). That is, in Run_RS_oneway, there are no feedbacks from the circulation model to the wave model, so that the wave model results and calculated wave forcing terms will not be contaminated by the unexpected less reasonable currents. The results show that the current fields with one-way coupling (Figs. 2.12e and f) are smoother than those with two-way coupling. However, some weak unphysical currents can still be seen over areas with steep topography.

Table 2.1: Values of γ^2 for three different model runs (Run_VF, Run_RS and Run_CirOnly) at three different depths of three sites (MB1, BIO and SB3) from day 271.0 to 271.4 in 2003.

Site (depth)	U component			V component		
	Run_VF	Run_RS	Run_CirOnly	Run_VF	Run_RS	Run_CirOnly
MB1 (4 m)	0.19	0.36	0.48	0.27	0.46	0.52
MB1 (7 m)	0.20	0.33	0.48	0.31	0.53	0.48
MB1 (11 m)	0.33	0.53	0.57	0.66	0.71	0.64
BIO (2 m)	0.28	0.26	0.63	0.15	0.11	0.42
BIO (9 m)	0.33	0.30	0.45	0.30	0.31	0.55
BIO (16 m)	0.40	0.68	0.34	0.69	1.07	0.84
SB3 (1 m)	0.77	0.80	0.84	0.71	0.77	0.75
SB3 (6 m)	0.74	0.75	0.78	0.37	0.45	0.43
SB3 (9 m)	0.89	0.85	0.93	0.71	0.67	0.66

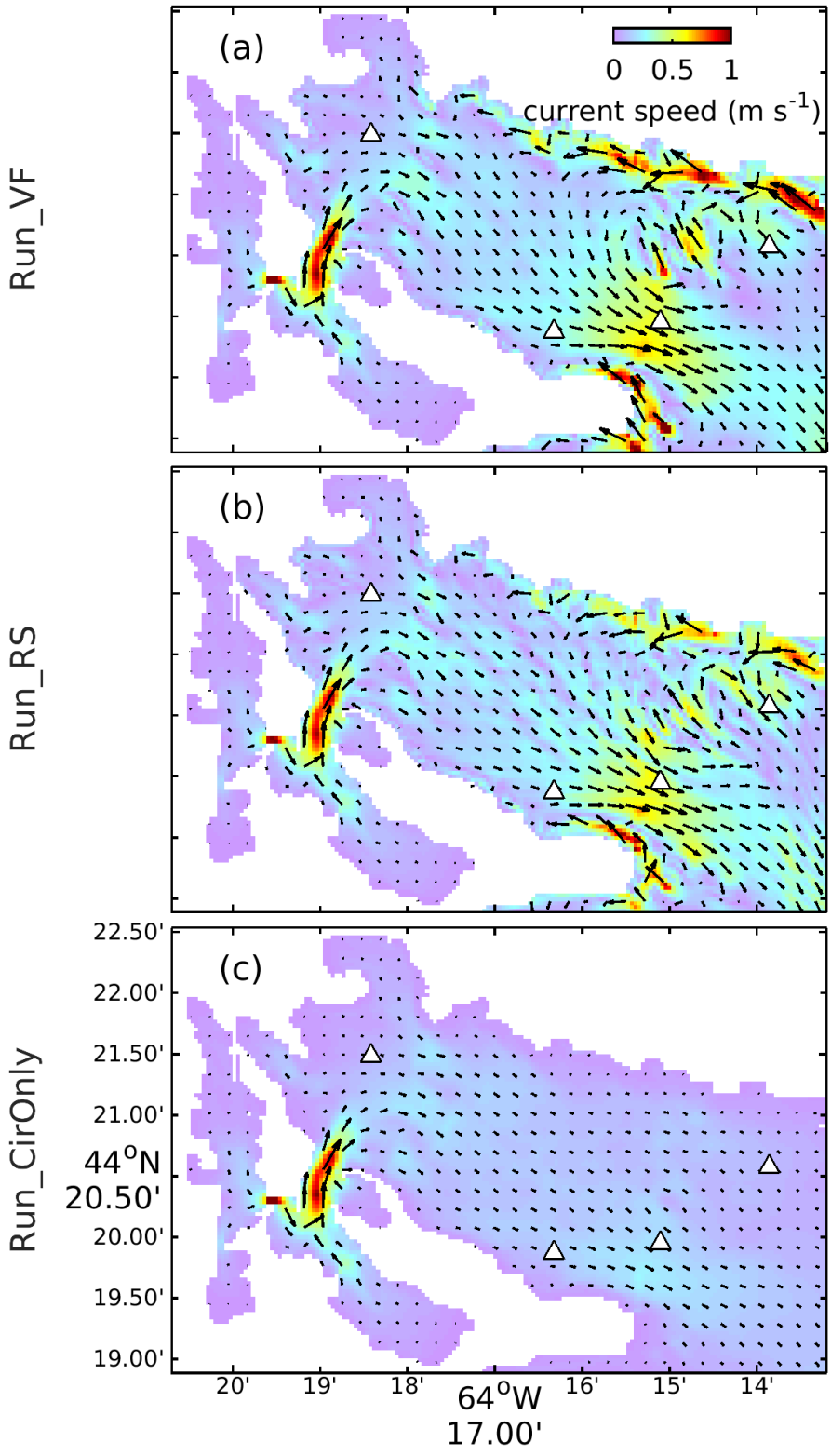

Figure 2.11: Model calculated surface currents in LB at 0430Z Sep 29 (day 271.19) in (a) Run_VF, (b) Run_RS, and (c) Run_CirOnly. Triangles indicate instrument locations.

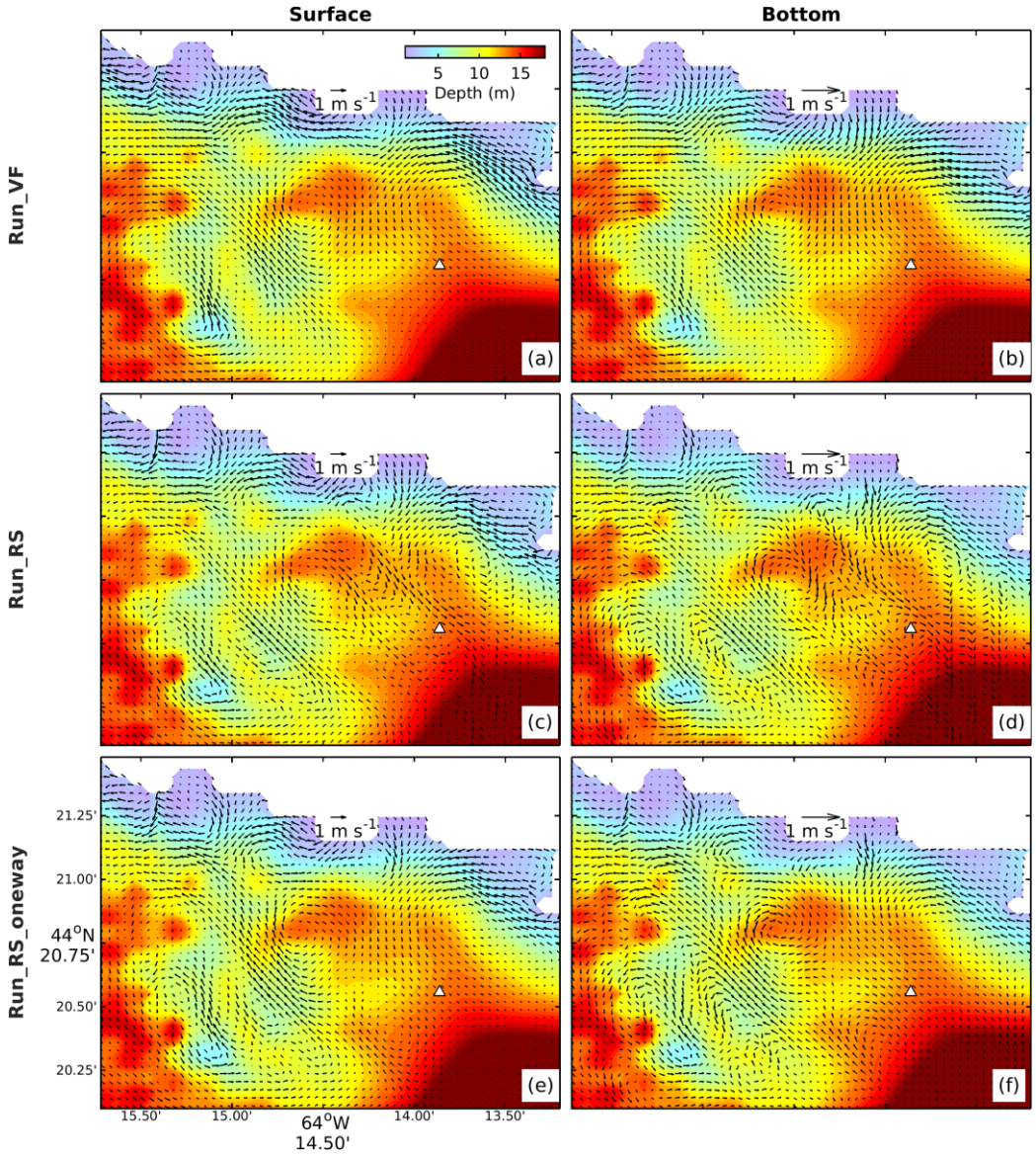

Figure 2.12: Differences in surface and bottom currents (a and b) between Run_VF and Run_CirOnly, (c and d) between Run_RS and Run_CirOnly, and (e and f) between Run_RS_oneway and Run_CirOnly in LB at 0430Z Sep 29 (day 271.19). Color images indicate water depth. Triangles indicate instrument locations.

We next examine the spatial distribution of the depth-averaged dominate forcing terms for the y momentum equation in Run_VF and Run_RS_oneway. As shown in Figures 2.13a and b, the spatial patterns of the pressure gradients mainly due to wave setup in both model runs are similar. For the RS formulation, the RS gradients tend to cancel the pressure gradients (Figs. 2.13b and d). For the VF formulation, the wave effects are separated into two major terms: a Bernoulli-head term and a breaking acceleration term. Outside the surf

zone, the Bernoulli-head and pressure gradients cancel each other, while inside the surf zone, the combination of the Bernoulli-head and breaking acceleration tend to cancel the pressure gradients (Figs. 2.13a, c, and e). It should be mentioned that the so-called VF term is a higher order term that has very minor effects on the model results in this case (not shown).

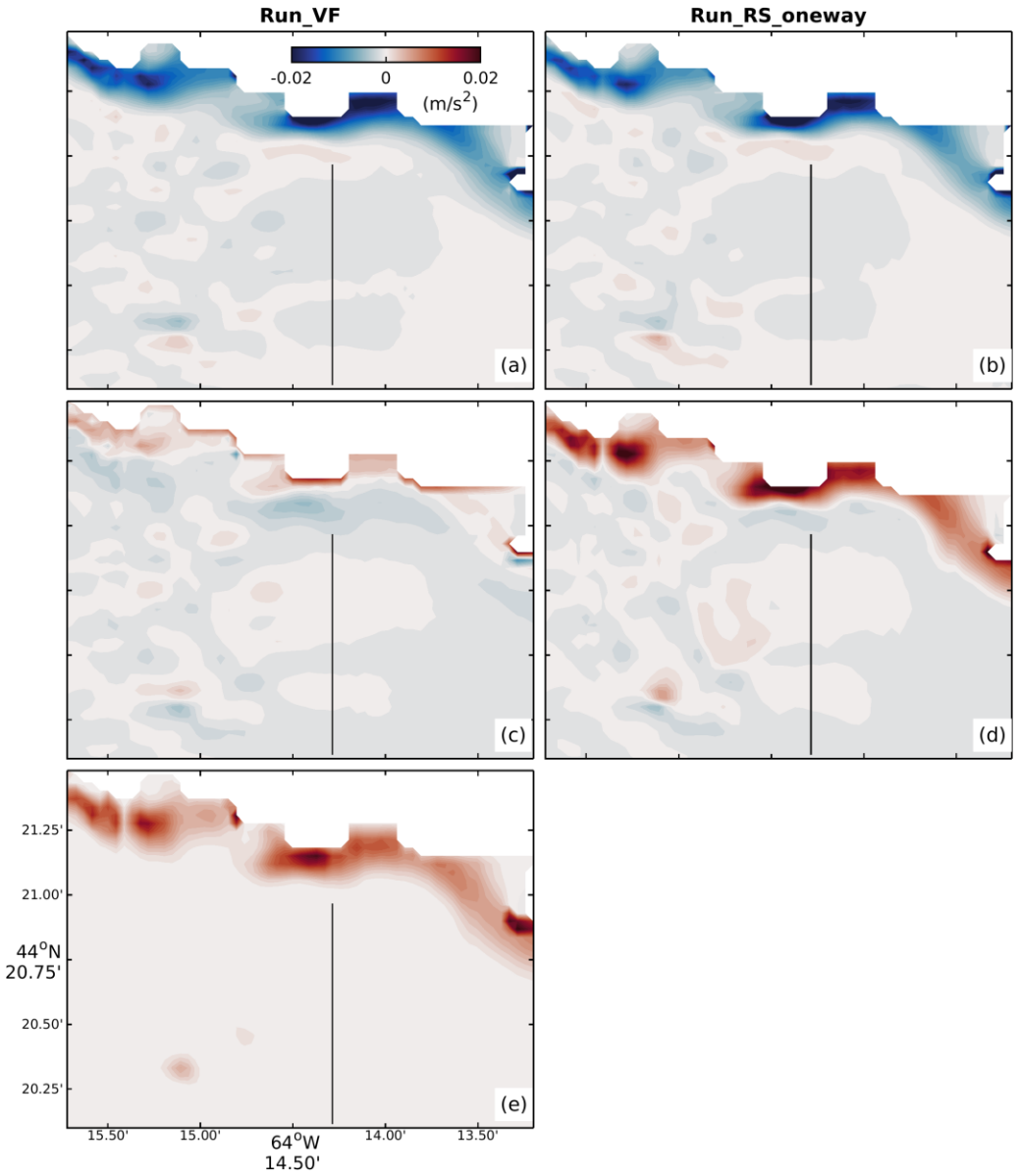

Figure 2.13: Depth-averaged dominate forcing terms for (a) $-\frac{1}{\rho_0}\frac{\partial p}{\partial y}$, (c) $-\frac{\partial J}{\partial y}$, (e) $F_{d,y}$ in Run_VF and (b) $-\frac{1}{\rho_0}\frac{\partial p}{\partial y}$, (d) $-\frac{\partial S_{yx}}{\partial x}-\frac{\partial S_{yy}}{\partial y}$ in Run_RS_oneway at 0430Z Sep 29 (day 271.19). The black straight line in Figure 2.13a-2.13e marks a cross-shore transect at which model results are shown in Figure 2.14.

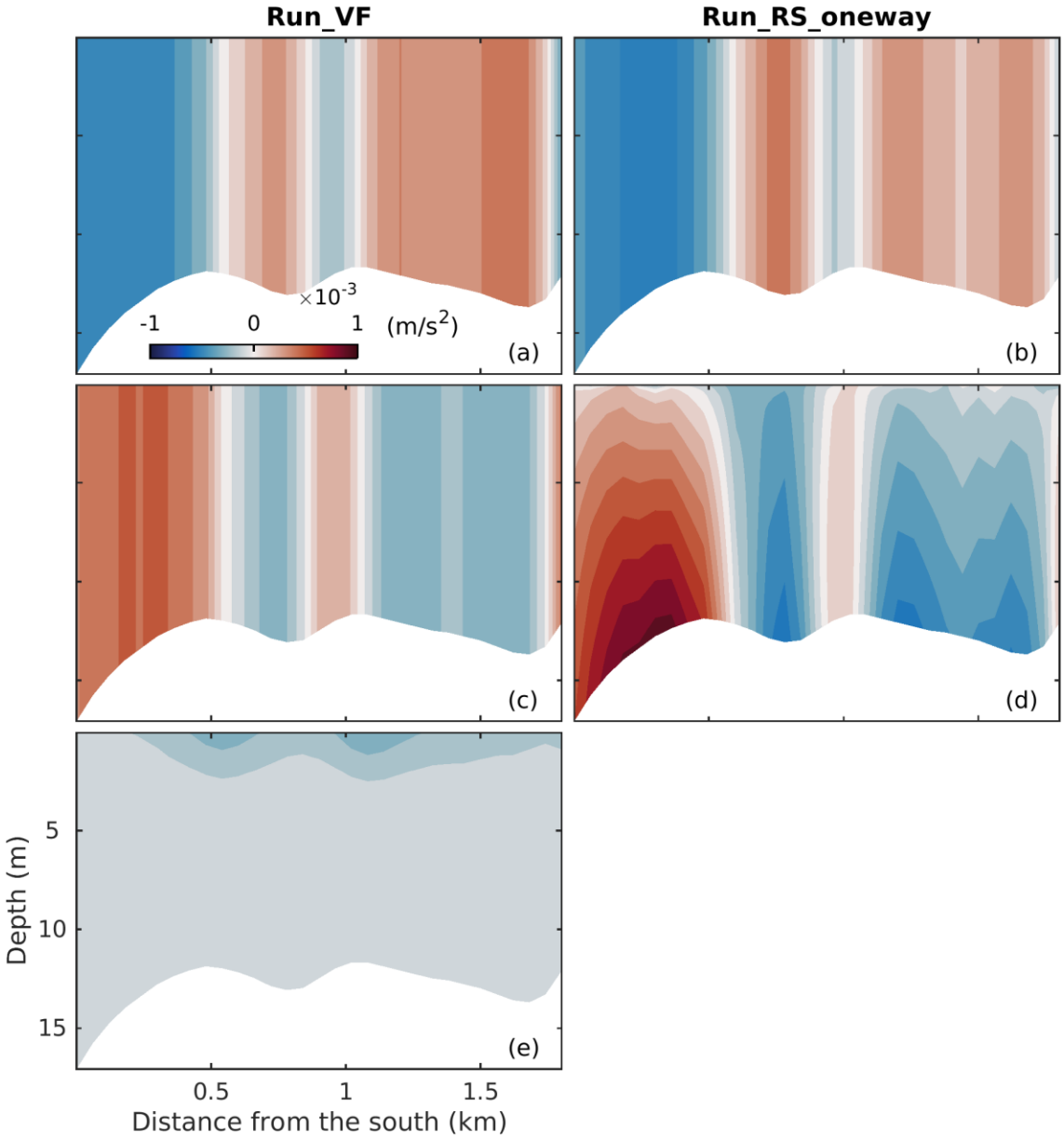

Figure 2.14: Vertical distributions of dominate forcing terms for (a) $-\frac{1}{\rho_0}\frac{\partial p}{\partial y}$, (c) $-\frac{\partial J}{\partial y}$, (e) $F_{d,y}$ in Run_VF and (b) $-\frac{1}{\rho_0}\frac{\partial p}{\partial y}$, (d) $-\frac{\partial S_{yx}}{\partial x}-\frac{\partial S_{yy}}{\partial y}$ in Run_RS_oneway in the cross-shore transect shown in Figure 2.13 at 0430Z Sep 29 (day 271.19).

We next select a cross-shore transect over the area outside the wave breaking zone (Fig. 2.13) to further examine the vertical structure of dominate forcing terms in Run_VF and Run_RS_oneway. Again, vertical structures of the pressure gradients for both model runs are similar (Figs. 2.14a and b). For the VF formulation, the Bernoulli-head is depth-uniform

(Fig. 2.14c) and the breaking acceleration due to whitecapping decreases exponentially with depth (Fig. 2.14e). For the RS formulation, the RS gradients increase with depth even the bottom slope is not very steep (Fig. 2.14d). This is counterintuitive as wave effects are expected to be concentrated near the surface. As a result, some weak unphysical currents are generated wherever there is a bottom slope, and this problem could be significantly amplified in a two-way coupled modelling system when interacting with large surface waves. As discussed in the first test case, the missed VRS term, which redistributes the wave momentum over the vertical, could help solve this problem, but the approximation of this term using the linear wave theory by M15 is simply inadequate.

2.5 Summary and Discussion

A two-way coupled wave-circulation modelling system was used in this study to assess performances of two formulations for the nonlinear feedback of ocean surface gravity waves on three-dimensional (3D) coastal currents. These two formulations are (a) a vortex force formulation (VF) suggested by *Bennis et al.* (2011) and (b) a latest version of radiation stress formulation (RS) suggested by *Mellor* (2015). Model results using the two formulations were compared with observations in two idealized test cases and one realistic application. This was the first time that the RS formulation suggested by *Mellor* (2015, M15) was validated directly with the VF formulation in the two test cases and over realistic coastal waters.

In the two idealized test cases, model results for the VF formulation are consistent with previous numerical simulations, laboratory experiments over a planar beach (*Ting and Kirby*, 1994) and field experiments over a barred beach (*Kumar et al.*, 2012). The RS formulation suggested by M15, however, has difficulties in producing a reasonable vertical structure for the cross-shore currents inside the surf zone. Outside the surf zone, the RS formulation also produces a recirculation over the vertical, which was suggested to be unrealistic. Both problems for the RS formulation are linked to an inappropriate treatment of a vertical radiation stress (VRS) term.

In the realistic application in Lunenburg Bay (LB) of Nova Scotia during the passage of Hurricane Juan in 2003, the simulated significant wave heights (H_s) and sea levels

produced by the coupled wave-circulation modelling system using VF and RS formulations are similar. A comparison of model results with wave observations demonstrated that the simulated maximum H_s is improved by ~0.5 m due to the feedback of strong opposing surface currents at the mouth of LB. Near the north and south shores in LB, the feedback of the local sea level to the total water depth significantly increases H_s (~1.0 m) by decreasing the intensity of depth-limited wave breaking. In return, the depth-limited wave breaking produces a pronounced sea level rise (0.3–0.5 m) over these nearshore regions, which highlights the importance of two-way coupling between waves and currents. Results presented in this study also demonstrated that the surface wave force plays a very important role for the storm-induced intense circulation in LB. It was shown that, by implementing the VF formulation in the circulation model, the large discrepancy between simulated and observed currents at site MB1 in previous studies (*Wang et al.*, 2007 and *Sheng et al.*, 2009) is significantly reduced. In contrast, the RS formulation produces some weak unphysical currents wherever there is a bottom slope, which are significantly magnified in a two-way coupled system, deteriorating the model performance in simulating currents at observation site MB1. These unphysical currents were found to be caused by an unreasonable representation for the vertical distribution of the RS gradients over sloping bottoms, which increases with water depth and reaches the maximum value near the bottom.

Overall, the results presented in this chapter demonstrated that the VF formulation is superior to the RS formulation in simulating the wave-induced 3D currents from the surf zone to the open shelf waters. The fundamental problem concerning the RS formulation in the community is an explicit description of the complex vertical flux of wave momentum (i.e., the VRS term) (*Ardhuin et al.*, 2008, 2017; *Bennis et al.*, 2011), which requires knowledge of a complex wave theory instead of the simple linear wave theory. Nonetheless, the VRS term is completely neglected in M15 based on the linear wave theory assumptions. The omission of this term was found to be responsible for the unrealistic vertical distribution of the RS gradients associated with unphysical currents over slopping bottoms. Furthermore, the 2D version of the RS (LS64) contains the wave force due to wave breaking. The 3D RS of M15, however, has difficulties in giving a reasonable vertical distribution of the wave force due to wave breaking as demonstrated in this study. How to properly account for wave breaking in the 3D RS remains to be studied. By comparison,

the VF formulation applying to the Eulerian velocity circumvents the difficulty with the evaluation of the VRS term, which is only required for the RS formulation applying to the Lagrangian velocity. Furthermore, the VF formulation separates the 3D wave force into conservative (vortex force and Bernoulli head) and non-conservative (breaking wave-induced acceleration) contributions. The former has an analytical vertical distribution. The latter is unknown but it can be approximated with an empirical vertical profile. This separation of conservative and non-conservative forces allows the VF formulation to be successfully applied from the surf zone to the open shelf waters.

CHAPTER 3

A COMPARATIVE STUDY OF WAVE-CURRENT INTERACTIONS OVER THE EASTERN CANADIAN SHELF UNDER SERVER WEATHER CONDITIONS[1]

3.1 Introduction

Reliable knowledge on surface gravity waves, currents and their interactions in the ocean is of great importance to many applications, such as weather forecasting, search and rescue, beach erosion, and site selections for offshore infrastructures (*Hashemi and Neill,* 2014). Physically, ocean currents can modify the relative speed of the air above the sea surface (i.e., relative wind effect) and change the absolute frequency of waves known as the Doppler shift. Spatial variability of currents can modify the relative wave frequency and cause wave refraction, shoaling and breaking that mimic bathymetric effects. The surface gravity waves, in return, can affect vertical mixing, surface and bottom stresses experienced by ocean currents. The surface waves and currents can also exchange energy through the concept of radiation stress (RS) (*Longuet-Higgins and Stewart,* 1964; *Mellor,* 2003) or vortex force (VF) (*McWilliams,* 2004; *Ardhuin et al.,* 2008).

Various studies were carried out on the examination of above-mentioned processes of the wave-current interaction (WCI) in the ocean. *Ardhuin et al.* (2012) demonstrated that the relative wind effect could explain about 20-40% of the modulation in wave heights due

[1] Wang, P., and J. Sheng, 2016. A comparative study of wave-current interactions over the eastern Canadian shelf under severe weather conditions using a coupled wave-circulation model, *Journal Geophysical Research-Oceans*, 121, 5252-5281.

to strong tidal currents. *Holthuusen and Tolman* (1991) found that the current-induced wave refraction due to the strong current shear of the Gulf Stream could induce a considerable variation on wave heights. By using a wave refraction model, *Wang et al*. (1994) showed that the focusing of wave rays by the Gulf Stream meander causes changes in wave direction/energy and directional spreading observed by in-situ measurements. *Liu et al*. (1994) also showed that mesoscale eddies can be detected from the synthetic aperture radar images via the influence of eddy currents on the surface wave fields. In the ocean upper layer, the Coriolis-Stokes force, Langmuir circulation, breaking and nonbreaking wave-induced mixing all contribute to the upper-ocean mixing (*Wu et al.,* 2015). For example, *Zhang et al.* (2011) suggested the surface wave breaking is an important factor in determining the surface boundary depth of temperature in the Yellow Sea in summer. *Deng et al.* (2009) demonstrated that the inclusion of the Coriolis-Stokes force into a global ocean model improves the comparison of the sea surface temperature (SST) with buoy observations.

These WCI mechanisms are expected to be more pronounced under severe weather events such as a tropical cyclone (TC) or hurricane than under the normal weather conditions. *Fan et al.* (2009a, b) found that an inclusion of ocean currents in an ocean wave model significantly reduced the simulated significant wave heights (H_s) under slow-moving TC conditions. By using a simplified one-dimensional wave action equation, they suggested that the reduction of H_s was mainly due to the horizontal current advection of waves, but the contribution of spatial variability of currents was not able to be quantified in that analysis. *Fan et al.* (2009a, b) also found that the contribution from the relative wind effect was very small. However, the ocean model they used did not include the three-dimensional (3D) wave forces (RS or VF), and the contribution of Stokes drift (a residual current averaged over a wave cycle) to ocean currents was not considered. In a realistic simulation of Hurricane Juan, *Xu et al.* (2007) found that an inclusion of the relative wind effect in the feedback from Stokes drift improved the accuracy of simulated wave fields. The other WCI mechanisms were not included in the study by *Xu et al.* (2007). In addition to strong ocean currents and large surface waves, another important feature under a TC is the remarkable right-biased SST cooling relative to the storm track, which is responsible to the decrease of TC intensity. The main physical processes affecting the right-biased SST

cooling include storm-induced vertical mixing, upwelling (*Price,* 1981), and the resonance Reynolds stresses of the near-inertial internal waves (*Huang and Oey,* 2015). It was also found that the maximum H_s appear on the right side of the TC due to both the asymmetry of the hurricane winds and the hurricane translation (*Chen et al.,* 2010). Thus, it is a very important scientific question to be addressed how the right-biased large wave fields could affect the right-biased SST cooling.

The main objective of this chapter is to examine the roles of different WCI mechanisms on the response of circulation and surface wave fields to three severe weather events using a two-way coupled wave-circulation modelling system. The study region of this paper is the eastern Canadian shelf (ECS), which is socially and economically important since it supports commercial and recreational fisheries, offshore oil and gas exploration and production, marine recreation and tourism, aquaculture, shipping and transportation, and other economic activities that directly contribute to the Canadian economy. This region is affected occasionally by extreme weather events such as tropical or extra-tropical cyclones and winter storms. Hurricane Juan, as an example, was an intense tropical cyclone and caused heavy damage in Nova Scotia and Prince Edward Island in late September 2003. Hurricane Juan reached Category-2 strength on the Saffir-Simpson hurricane scale on September 27 and made landfall on the south coast of Nova Scotia near Halifax early on September 29, with maximum sustained winds of about 158 km h^{-1}. This storm generated about 2-m storm surge in Halifax Harbor, and huge surface waves with the maximum H_s of about 10 m and tallest wave height of about 20 m observed at a marine buoy outside of the Harbor (*Fogarty,* 2003). The other example is "White Juan", which was a hurricane-strength northeaster blizzard and affected most of Atlantic Canada in February 2004. White Juan had a snowfall at a rate of 5 cm $hour^{-1}$ for 12 hours, and winds blew at up to 124 km h^{-1}. White Juan produced hurricane-strength winds at sea with 10 to 15 meter swells, prompting a special marine warning. Although the storm-induced ocean currents and ocean waves over the ECS during Hurricane Juan were studied previously by *Sheng et al.* (2006) and *Xu et al.* (2007), the WCIs over the ECS during extreme weather conditions such as Hurricane Juan and White Juan remain to be studied.

The structure of this chapter is organized as below: the coupled wave-circulation

modelling system is described in section 3.2. Applications of this model for three storms mentioned above are used to examine the role of different WCI mechanisms under severe weather conditions in section 3.3. The summary and discussion are provided in section 3.4.

3.2 The Coupled Wave-Circulation Modelling System

The coupled model (Fig. 1.3) uses two-way coupling between a 3D ocean circulation model for the ECS known as DalCoast and a third-generation wave model known as WAVEWATCH III (WW3). The wave effects on the 3D circulation is specified in the circulation model using the VF formalism (*McWilliams,* 2004; *Ardhuin et al.,* 2008) and the breaking wave-induced mixing (*Craig and Banner,* 1994). In the wave model, the effects of currents on waves are implemented through the wave action equation. These effects include the relative wind effect, current-induced convergence, wavenumber shift and refraction. An automatic coupler is used to exchange information between the circulation and wave models at a selected coupling time interval.

3.2.1 Ocean Circulation Model

DalCoast was constructed from the Princeton Ocean Model (POM; *Mellor,* 2004). The latter is a 3D, sigma coordinate, primitive-equation ocean circulation model. DalCoast uses the spectral nudging technique (*Thompson et al.,* 2007) and the semi-prognostic method (*Sheng et al.,* 2001) to reduce the seasonal bias in the model circulation and hydrography. DalCoast has been validated extensively in the past using observations of hydrography, sea level, and currents (*Thompson et al.,* 2007; *Ohashi and Sheng,* 2013, 2015; *Ohashi et al.,* 2009a, 2009b).

Four major modifications were made recently to DalCoast for this study. Firstly, the 2-min Gridded Global Relief Data (ETOPO2) used previously in the model topography was replaced by the General Bathymetric Chart of the Oceans (GEBCO) bathymetry data (http://www.gebco.net/). The latter has a finer resolution (30 arc-seconds) than ETOPO2. The GEBCO dataset also represents the local bathymetry over the study region better than ETOPO. Secondly, the tides specified on the lateral open boundaries of the circulation model are based on the tidal elevations and tidal currents produced by the OSU Tidal

Inversion System (OTIS), which is a tidal prediction system developed at the Oregon State University (OSU). Thirdly, the VF formalism was incorporated into the governing equations for circulation, which includes the wave-averaged vortex and Bernoulli-head forces, sink of the wave momentum due to wave breaking, and advection of material tracers by Stokes drift. We refer these additional wave force terms as the 3D wave forces. Lastly, the breaking wave-induced mixing was implemented in the turbulent module for the circulation model. A reader is referred to Chapter 2 for more information on the implementation of the VF formalism and the breaking wave-induced mixing in the circulation model.

3.2.2 Ocean Wave Model

WW3 is an operational wave model developed at the NOAA/National Centers for Environmental Prediction, which has been widely applied in the global- and regional-scale areas of the world ocean. It should be mentioned that both SWAN and WW3 are the third generation ocean wave models and solve the wave action balance equation. The difference in the wave action balance equation between the two models is that the wave action density spectrum $N = E/\sigma$ is defined as a function of (k, σ) in SWAN (Eq. (2.16)) and a function of (k, θ) in WW3. In a Cartesian grid, the wave action balance equation in WW3 can be written as,

$$\frac{\partial N}{\partial t} + \nabla_x \cdot \dot{X} N + \frac{\partial}{\partial k}\dot{k} N + \frac{\partial}{\partial \theta}\dot{\theta} N = \frac{S_{tot}}{\sigma} \tag{3.1}$$

$$\dot{X} = C_g + \mathbf{U} \tag{3.2}$$

$$\dot{k} = -\frac{\partial \sigma}{\partial D}\frac{\partial D}{\partial s} - \boldsymbol{k} \cdot \frac{\partial \mathbf{U}}{\partial s} \tag{3.3}$$

$$\dot{\theta} = -\frac{1}{k}\left(\frac{\partial \sigma}{\partial D}\frac{\partial D}{\partial m} + \boldsymbol{k} \cdot \frac{\partial \mathbf{U}}{\partial m}\right) \tag{3.4}$$

where C_g is the group velocity of waves, $\mathbf{U}$ is the surface ocean current vector, s is a coordinate in the direction θ, and m is a coordinate perpendicular to s. It is noted that Eq. 3.2 is the vector form of $(c_x + u,\ c_y + v)$ in Eq. (2.16). The left-hand side (LHS) of (3.1) represents the local rate of change of the action density (the first term), the wave

propagation in spatial (second term) and spectral (third and fourth terms) space. The right-hand side (RHS) of (3.1) contains the net source term S_{tot}, which includes all physical processes that generate, dissipate and redistribute the wave energy:

$$S_{tot} = S_{in} + S_{nl} + S_{ds} + S_{bot} + S_{db} + S_{tr} \tag{3.5}$$

The RHS of (3.5) consists of both deep water processes (i.e., wind input S_{in}, quadruplets nonlinear interactions S_{nl}, and white capping S_{ds}) and shallow water processes (i.e. bottom friction S_{bot}, depth-induced breaking S_{db}, and triad wave-wave interactions S_{tr}).

Equations (3.1-3.5) indicate that ocean circulation affects the wave action density spectrum in four ways. Firstly, the horizontal variation of ocean currents causes the convergence of wave action flux in the spatial space. Secondly, in the spectral space, the horizontal variation of ocean currents induces the wavenumber shift and wave refraction in the way similar to effects of the bathymetry variation. Thirdly, in the source term, the surface wind velocity vector $\boldsymbol{U_{10}}$ used to calculate the wave growth due to winds is replaced by $(\boldsymbol{U_{10}} - \alpha \boldsymbol{U})$, which is the vector difference between the surface wind velocity and surface ocean current. Here α is a tuning coefficient for the ocean surface current in the relative wind effect in WW3. It should be pointed out that the use of the full ocean surface current ($\alpha = 1$) will exaggerate the relative wind effect since the relevant level at which the wind should be taken is the top of the atmospheric surface layer where the winds do not adjust to the presence of currents (*Ardhuin et al.,* 2012). In this study we set $\alpha = 0.7$ based on conversions between the geostrophic winds at the top of the atmospheric surface layer and 10 m height winds (see Appendix B). Lastly, the sea surface elevation modifies the total water depth used in the wave model, although this effect is only large in the very shallow water regions where waves could feel the ocean bottom.

3.2.3 Coupling Procedure

The dynamic coupling software known as OpenPALM (Fig. 1.4) is used to exchange information between DalCoast and WW3. At a user-specific coupling interval, the sea surface currents and water level fields produced by DalCoast are transferred to the wave

model to modify the effective wind fields and the wave action equation. In return, fields of wave heights, Stokes drift velocity, Bernoulli-head, and wave dissipation source term calculated in the wave model are transferred to DalCoast to calculate the wave-averaged effects on the 3D circulation.

3.2.3 Model External Forcing, Setup and Operation

3.3.3a Model External Forcing

The external forcing to drive the coupled wave-circulation modelling system of the ECS includes 6 hourly surface winds and atmospheric pressures at the sea level (SLP) extracted from the Climate Forecast System Reanalysis (CFSR, *Saha et al.,* 2010). The CFSR winds and SLP have horizontal resolutions of 0.3º and 0.5º respectively, which are reasonable for large-scale atmospheric forcing but not fine enough to represent atmospheric forcing associated with a hurricane or tropical storm. Reliable wind forcing is essential to have accurate simulations of surface gravity waves and ocean currents. For example, a 10% bias in surface winds may result in ~20% error in wave heights. As a result, an idealized asymmetric vortex suggested by *Hu et al.* (2012), which was modified from the parametric hurricane model (*Holland,* 1980), is inserted into the large-scale CFSR wind and SLP fields based on

$$p(r) = p_c + (p_n - p_c)e^{-\left(\frac{R_m}{r}\right)^B} \tag{3.6}$$

$$V_g(r) = \sqrt{\frac{B}{\rho_a}\left(\frac{R_m}{r}\right)^B (p_n - p_c)e^{-\left(\frac{R_m}{r}\right)^B} + \left(\frac{rf}{2}\right)^2} - \frac{rf}{2} \tag{3.7}$$

where $p(r)$ and $V_g(r)$ are respectively the pressure and the gradient wind at radius r, p_c is the central pressure, p_n is the ambient pressure, R_m is the radius of maximum wind, ρ_a is the air density, f is the Coriolis parameter, and B is the hurricane shape parameter. The Coriolis effect, translation speed of the storm, and all available wind parameters extracted from the datasets produced by the National Hurricane Center (NHC) and the Automated Tropical Cyclone Forecasting (ATCF) are used in constructing the wind fields associated with a tropical storm or hurricane at each model time step. The detailed

procedures can be found in *Hu et al.* (2012). The modified CFSR winds (W_{all}) are obtained by blending the wind field produced by the parametric hurricane winds (W_{vortex}) with the CFSR wind field (W_{CFSR}) using exponential distance weights:

$$W_{all}(r) = (e^{-(r/r_0)^2})W_{vortex} + (1 - e^{-(r/r_0)^2})W_{CFSR} \tag{3.8}$$

where r_0 is the search radius around the center of the storm. We set $r_0 = 300$ km.

From the modified (or original) wind fields, wind stress at each model grid is calculated using a quadratic formula given as

$$\tau_a = \rho_a C_d |\mathbf{U_{10}}| \mathbf{U_{10}} \tag{3.9}$$

where ρ_a is the air density, $\mathbf{U_{10}}$ is the 10 m wind velocity vector in units of m s^{-1}, and the drag coefficient C_d at the air-sea surface is given by the bulk formula of *Large and Pond* (1981) and *Powell et al.* (2003):

$$C_d \times 10^3 = \begin{cases} 1.2 & (|\mathbf{U_{10}}| \leq 11) \\ 0.49 + 0.065|\mathbf{U_{10}}| & (11 \leq |\mathbf{U_{10}}| \leq 25) \\ 2.115 & (|\mathbf{U_{10}}| \geq 25) \end{cases} \tag{3.10}$$

The bottom stress is parameterized in terms of bottom currents based on

$$\tau_b = \rho C_b |\mathbf{U_b}| \mathbf{U_b} \tag{3.11}$$

$$C_b = MAX\left[\frac{\kappa^2}{[\ln\{(1+\sigma_{kb-1})h/z_0\}]^2},\ 0.0025\right] \tag{3.12}$$

where $\boldsymbol{U_b}$ is the near bottom current vector, C_b is the bottom drag coefficient, $\kappa = 0.04$ is the von Karman constant, σ_{kb-1} is the sigma level just above the bottom, and z_0 is a roughness parameter which is set to be 0.01 m in this study.

The blended wind fields discussed above and sea ice concentrations from the CFSR dataset are used by the ocean wave model. The blended SLP and wind stress fields are used to drive DalCoast. In addition, DalCoast is driven by tides, the net heat and freshwater fluxes at the sea surface and the freshwater runoff from major rivers in the region.

3.2.3b Circulation Model Setup

The model domain of DalCoast covers the Gulf of St. Lawrence, the Scotian Shelf (ScS), and the Gulf of Maine and adjacent deep waters (71.5°W-56°W, 38.5°N-52°N, Fig. 2), with a horizontal resolution of (1/16)° (~7 km) for both the longitudinal and latitudinal directions. It should be noted that Langmuir cells (with a length scale of ~5-100 m) cannot be resolved with this horizontal resolution. Incorporating the impact of Langmuir cells on the ocean mixing requires an additional parameterization (*Wu et al.,* 2015), which is a topic of future studies. There are 40 sigma levels in the vertical which are concentrated near the surface and bottom, and are equally distributed in the interior. At the model open boundaries, the model is driven by (a) storm-induced hourly sea level and depth averaged currents simulated by a barotropic model covering the northwest Atlantic Ocean (72°W-42°W, 38°N-60°N) with a resolution of (1/12)°; (b) tidal forcing specified in terms of hourly sea levels and depth averaged currents predicted by OTIS (8 tidal constituents: M_2, S_2, N_2, K_2, K_1, O_1, P_1, and Q_1); and (c) daily values of the 3D temperature, salinity and large-scale density-driven currents provided by an ocean-ice numerical model of the northwest Atlantic (*Urrego-Blanco and Sheng,* 2012). DalCoast uses the mode splitting technique with an external mode time step of 9 s and an internal mode time step of 180 s.

3.2.3c Ocean Wave Setup

WW3 uses the same horizontal model grid (with a horizontal resolution of 1/16^o) and bathymetry as DalCoast. To account for the effect of swells generated outside of the study area, a coarser-resolution wave model based also on WW3 is applied to a larger domain (84°W-10°W, 10°N-65°N) with a horizontal resolution of (1/4)°. The wave model results over this larger domain are used to provide boundary conditions for the wave model of the ECS. The spectral domain consists of 36 directional bins with 10° of resolution and 29 frequencies f_n ranging from 0.04 to 0.6 Hz with a logarithmic increment of $f_{n+1} = 1.1 f_n$. The discrete interaction approximation (DIA) is used to calculate the nonlinear wave-wave interactions. The source package known as ST6 (*Tolman et al.,* 2014) is applied to compute the wave input and dissipation source terms. A linear JONSWAP Bottom friction parameterization and depth-induced wave breaking are also used in the model.

3.2.3d Design of Numerical Experiments

Numerical simulations of surface gravity waves and 3D ocean currents and hydrography during three severe weather events are considered in this study. For each weather event, three basic numerical experiments are designed to examine the effects of the WCIs on ocean currents and surface gravity waves over the ECS and adjacent deep waters, which include the coupled wave-circulation model run (Run_WaveCir), the wave-only model run (Run_WaveOnly) without the feedback from currents, and the circulation-only model run (Run_CirOnly) without the feedback from waves. Furthermore, six additional process-oriented experiments are designed to quantify major WCI mechanisms that affect the ocean waves and currents in the study region. Six specific WCI mechanisms are considered in this study, which include (a) the relative wind effect, (b) current-induced convergence, (c) current-induced wavenumber shift, (d) current-induced wave refraction, (e) 3D wave forces on currents, and (f) breaking wave-induced mixing on the circulation. Model configurations for 9 numerical experiments are summarized in Table 3.1.

Table 3.1: Model configurations for nine numerical experiments.

Experiment	**Relative wind effect** $\boldsymbol{\alpha U}$ in $(\boldsymbol{U_{10}} - \boldsymbol{\alpha U})$	**Current-induced convergence** $\boldsymbol{U}$ in Eq. 3.2	**Current-induced k shift** $\boldsymbol{k} \cdot \frac{\partial \boldsymbol{U}}{\partial \boldsymbol{s}}$ in Eq. 3.3	**Current-induced refraction** $\boldsymbol{k} \cdot \frac{\partial \boldsymbol{U}}{\partial \boldsymbol{m}}$ in Eq. 3.4	**3D wave forces** $\boldsymbol{U_s, V_s, W_s}$ related terms in Eqs.2.2-2.3; $\frac{\partial \boldsymbol{J}}{\partial \boldsymbol{x}}, \boldsymbol{F_{d,x}}$ in Eq. 2.2; $\frac{\partial \boldsymbol{J}}{\partial \boldsymbol{y}}, \boldsymbol{F_{d,y}}$ in Eq. 2.3	**Breaking wave-induced mixing** Eq. 2.15
Run_WaveCir	On	On	On	On	On	On
Run_WaveOnly	Wave-only model run					
Run_CirOnly	Circulation-only model run					
Run_WaveU_{10}	On	Off	Off	Off	On	On
Run_WaveC_g	Off	On	Off	Off	On	On
Run_Wavek	Off	Off	On	Off	On	On
Run_Waveθ	Off	Off	Off	On	On	On
Run_CirVF	On	On	On	On	On	Off
Run_CirTKE	On	On	On	On	Off	On

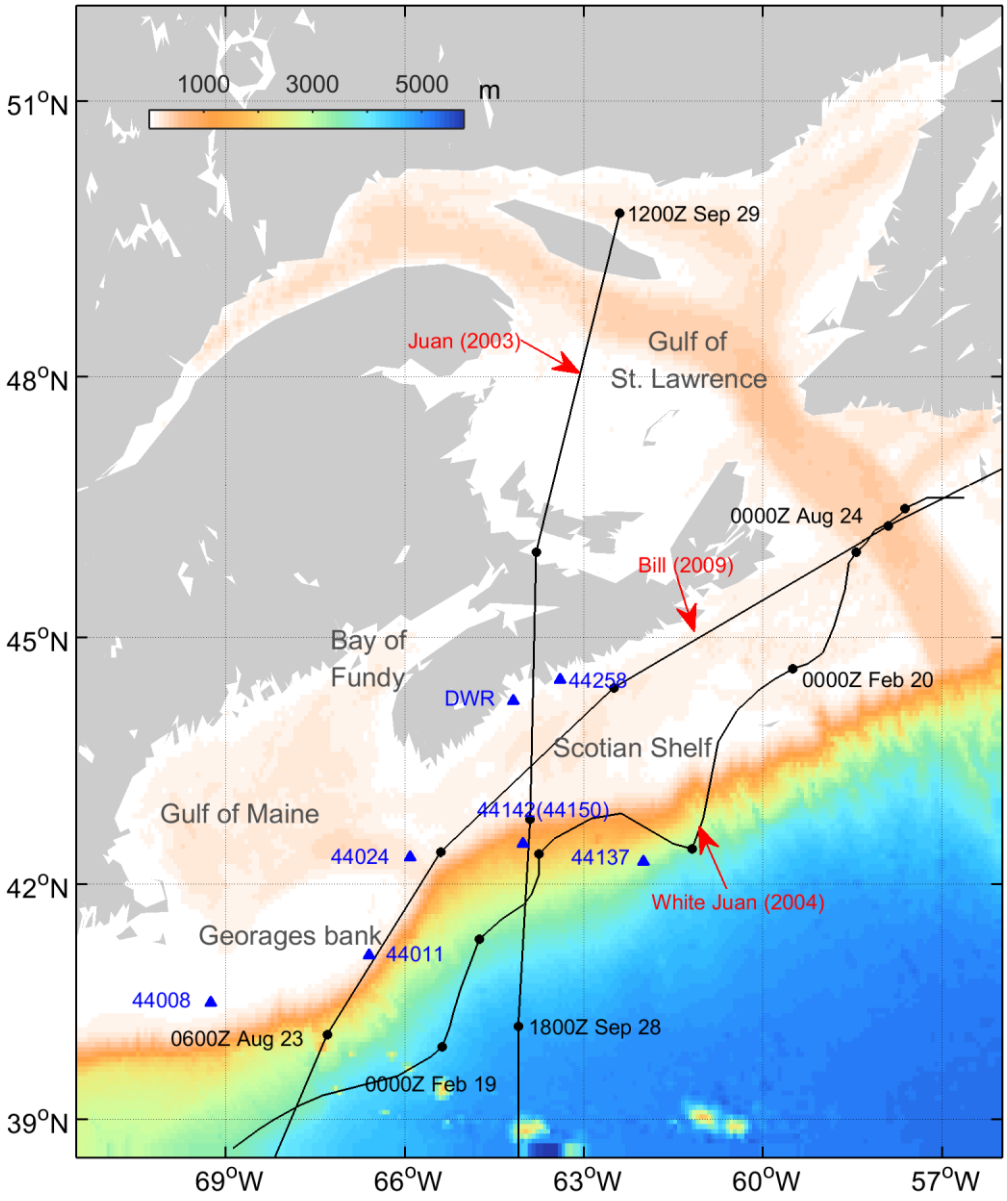

Figure 3.1: Major topographic features of the model domain over the eastern Canadian shelf, buoy stations, and tracks of three storms considered in this study.

3.3 Model Results during Three Storm Events

Three severe weather events considered in this study are (a) Hurricane Juan, (b) Hurricane Bill and (c) a severe winter storm known as “White Juan”. As mentioned earlier, Hurricane Juan swept the central ScS as a category-2 storm and made landfall on the south coast of

Nova Scotia near Halifax early on September 29, 2003. Hurricane Bill came to the ScS as a category-1 storm in late August 2009. The tracks of these two hurricanes, based on the best track data set taken from the Atlantic HURricane DATabase (HURDAT) (http://www.nhc.noaa.gov/data/#hurdat), are very different. Hurricane Juan passed over the southern coast of Nova Scotia directly, while Hurricane Bill travelled along the south coast of Nova Scotia (Fig. 3.1). Different from Hurricanes Juan and Bill, "White Juan" was a hurricane-strength northeaster blizzard that occurred in February 2004. Since the HURDAT database does not provide information on the storm track for any winter storm, the storm track of "White Juan" was approximated by positions of minimum winds of the CFSR wind fields over the region covered by the storm. The reason for using minimum winds instead of minimum pressure is because the CFSR wind field has a higher resolution (0.3^{o}) than the SLP field (0.5^{o}). Figure 3.2 shows that "White Juan" swept the ScS in the pathway very similar to Hurricane Bill, except that "White Juan" had a more complicated storm track and stayed longer on the ScS than Hurricane Bill. Furthermore, "White Juan" was a typical winter storm, and had a diameter of 3-4 times larger with weaker winds than normal hurricanes over the study region.

In-situ wind and wave observations at seven operational buoys and a wave rider buoy on the ScS and in the Gulf of Maine (Fig. 3.1) are used in this study to validate model results. Buoy 44024 has been operated by the Northeastern Regional Association of Coastal Ocean Observing Systems (NERACOOS). Buoys 44008 and 44011 have been operated by the National Data Buoy Center. Buoys 44137, 44142, 44150, 44258, and a directional wave rider (DWR) buoy have been operated by Environmental Canada.

3.3.1 Hurricane Juan

As mentioned above, Hurricane Juan is a category-2 hurricane that translated northward and passed through the central ScS in late September 2003 (Fig. 3.1). In-situ wind observations during Hurricane Juan are available at three operational buoy stations (44137, 44258 and 44142). The anemometer heights of these buoys are 5 m above the sea level. The buoy wind speeds were converted to the 10 m winds by a multiplicative factor of 1.08 suggested by *Boutin et al.* (2009). Figure 3.2 presents a comparison of the original and

modified CFSR winds with observed winds during a period of about 4 days in late September 2003 at buoys 44137, 44142 and 44258. Among these three buoys, buoys 44137 and 44258 are on the right-hand side (RHS) and buoy 44142 on the LHS of the storm track, with buoy 44142 to be the closest to the center of the storm and buoy 44137 to be the farthest. The original CFSR winds agree reasonably well with the in-situ wind observations at low wind speeds, but less well with the observations at high wind speeds during Hurricane Juan (Fig. 3.2). In particular, the original CFSR winds do not reproduce the observed peak winds at buoys 44258 and 44142 during Hurricane Juan. By comparison, the modified CFSR winds agree better with the in-situ wind observations at three buoy stations at high wind speeds during Hurricane Juan. At low wind speeds the modified CFSR winds are highly similar to the original CFSR winds. This is expected since the modified CFSR winds are same as the original CFSR winds in areas far from the storm center. It should be noted that the parametric hurricane model still has some deficiencies in reproducing the observed peak winds at buoy 44142 (Figs. 3.2e and f) located very close to the storm center. This could be attributed to the coarse time interval (6-hourly) of the storm center position taken from HURDAT. The exact positions of the storm center between these 6-hourly intervals are unknown and they can only be approximated with a simple linear interpolation, which can lead to inevitable errors. Figure 3.3 presents a comparison between the original and modified CFSR wind vectors at a specific time for Hurricane Juan. Clearly, the modified CFSR winds significantly improve the original CFSR winds during the storm.

Figure 3.4 presents time series of observed and simulated H_s and peak wave periods at four buoys during Hurricane Juan. The coupled model in Run_WaveCir reproduces reasonably well the observed H_s at these four buoys, particularly at buoys 44258, 44142 and DWR. The maximum H_s (H_s^{max}) at these buoys produced by the coupled model in Run_WaveCir occur roughly during the peak winds of Hurricane Juan and are ~10.7 m at buoy 44258, 11.2 m at buoy 44142, ~8.6 m at buoy 44137, and ~8.5 m at buoy DWR, which are in a good agreement with in-situ wave observations. The simulated peak wave periods are about 8-15 s at these four buoys, with relatively longer peak periods during the peak winds of Hurricane Juan, which are also in general agreement with the in-situ observations. The longer peak period during the peak winds indicates the maximum waves

during Juan are swell-dominated. After the peak winds, the simulated H_s at buoys close to the hurricane track (e.g. 44142, 44258 and DWR) exhibit an oscillation pattern with a period of ~18 hours, which is consistent with observations. Further examination of the instantaneous current field (Fig. 3.8c) indicates that these oscillations are caused by the strong near-inertial currents in the wake of the hurricane.

In comparison with results in Run_WaveCir discussed above, model results in Run_WaveOnly overestimate the H_s^{max} by about 0.8 m and 2.2 m respectively at buoys 44137 and 44258 (Fig. 3.4). The model results in Run_WaveOnly also overestimate the H_s and slightly overestimate the peak wave periods after the maximum winds of the Hurricane. This indicates the importance of the WCIs. Overestimations of the H_s^{max} at buoy 44137 and 44258 during Hurricane Juan by the wave-only model were also found by *Xu et al.* (2007), who managed to reduce the model errors by setting an upper bound for the drag coefficient and modifying the effective wind through subtracting the swell orbital velocities and Stokes drift. They did not consider, however, other contributions from ocean currents except for the Stokes drift. In our wave-only model, the selected parameterization of the drag coefficient (*Hwang,* 2001) already accounts for saturation, and the drag coefficient reaches a maximum with wind speeds of 30 m s^{-1} and decreases with higher winds. It should be noted that the circulation model (see Eq. (3.9)) and the wave model use different drag coefficient parameterizations.

We next examine the effect of WCIs in the wave spectra in the frequency domain during Hurricane Juan (Fig. 3.5). In comparison with model results in Run_WaveOnly, the simulated wave spectra at three buoys in Run_WaveCir agree better with the observations. At buoys located to the RHS of the storm track (44258 and 44137), the model results in Run_WaveOnly overestimate the spectral peaks by up to 33% at buoy 44137. At buoys located to the LHS of the storm track (44142), the simulated wave spectra in these two numerical experiments (Run_WaveCir and Run_WaveOnly) are similar, indicating that the overall influences of ocean currents on the wave spectra peaks are weak on the LHS of the storm. In addition, both model runs underestimate the observed spectral peak at buoy 44142, which could be due in part to the less accurate parametric winds at this location (Figs. 3.23 and f). Furthermore, the underestimation of the spectral peak in Run_WaveCir could also

be due in part to the imperfect parameterization for the enhanced wave dissipation when facing opposing currents (*Ardhuin et al.*, 2012).

Figure 3.6a presents the swath map for Hurricane Juan calculated from simulated H_s (every 15 minutes) in the coupled model run (Run_WaveCir). A swath map depicts the horizontal distribution of H_s^{max} at each location during a storm period. The simulated swath in Run_WaveCir is biased to the right side of the storm track, with H_s^{max} of about 12-15 m appearing over areas within 10-100 km to the right of the storm track (as facing the direction taken by the storm). This rightward swath bias is due to the stronger winds and trapped wave resonance (*Bowyer and MacAfee*, 2005). The trapped wave resonance can be explained by comparing the wave group velocity with the hurricane translation speed. The calculated group velocity of the dominant swell waves under Hurricane Juan is 9-10 m/s, which is very similar to Juan's translation speed (9-15 m/s) over the study region. Thus, surface waves on the right side of the storm track experience a longer trapped fetch, resulting in larger H_s^{max}. In the wave-only model run (Run_WaveOnly) shown in Fig. 3.6b, the swath is also biased to the right side of the storm track, but with much larger magnitudes. Figure 3.6c presents the normalized differences in H_s^{max} (ΔH_s^{max}) which is defined as differences in the swath between Run_WaveCir and Run_WaveOnly (Run_WaveCir minus Run_WaveOnly) normalized by the swath in Run_WaveOnly. A significant reduction of H_s^{max} (11-15%) due to effects of currents on waves occurs on the RHS of the hurricane track. On the LHS of the storm track, however, there is a slight increase of H_s^{max} by about 4-7%. This is a result of combination of the four major WCI mechanisms of currents on waves to be discussed as follows.

Distributions of ΔH_s^{max} between Run_WaveU_{10} and Run_WaveOnly (Fig. 3.7a) indicate that the relative wind effect reduces H_s^{max} by up to 7% on both sides of the storm track. This is due to the fact that hurricane winds and storm-generated strong surface currents are approximately in the same direction on the both sides of the track (Fig. 3.8a,c), which efficiently reduces the energy transferred from surface winds to ocean waves. Distributions of ΔH_s^{max} between Run_WaveC_g and Run_WaveOnly (Fig. 3.7b) demonstrate that the current-induced convergence significantly increases H_s^{max} by 11-18% on the LHS of the storm track and decreases H_s^{max} by 5-7% on the RHS. The effects of

this process depend mostly on the spatial gradients of currents (see Eqs. (3.1) and (3.2)), which can lead to wave energy convergence and divergence in the spatial space. Fig. 3.8c shows that the strong divergence (convergence) of surface currents on the RHS (LHS) of the hurricane center is responsible for the decrease (increase) of H_s^{max}.

The current-induced wavenumber shift depends on the spatial gradients of currents in the propagation directions of surface waves (see Eq. (3.3)). The effect of this process is to decrease (increase) for the case of waves propagating into spatially accelerating (deaccelerating) currents. Figure 3.7c shows the effects of this process are limited to the ScS region with an increase of H_s^{max} (5-7%) along the storm track. The current-induced wave refraction depends on the gradients of currents along the wave crest direction (see Eq. (3.4)). The basic effect of this process is to turn surface waves towards the area with lower absolute propagation speeds. Figure 3.7d shows that this process significantly reduces H_s^{max} (up to 10%) along the RHS at ~25 km off the hurricane track. This reduction of H_s^{max} coincides with the maximum northward current on the RHS of the hurricane track: the vorticity is cyclonic (anticyclonic) on the left (right) side of this maximum speed line. As surface waves also propagate northward, these tend to refract wave energy away from the line of maximum current speed and reduces H_s^{max}.

It is noted that the energy-weighted mean wave directions are approximately northward on both sides of the storm track (Fig. 3.8b), indicating that the waves fields contain a large fraction of remotely generated swells moving in harmony with the hurricane as discussed above. It should be noted that, however, the dominate wave directions at the spectral peak are mostly determined by locally generated wind-sea (i.e., cyclonic relative to the storm center) as shown in *Xu et al.* (Fig. 6, 2007).

Hurricane Juan also generated significant temperature changes in the upper ocean in the vicinity of the storm track. Figure 3.9a presents differences in the SST between September 27 and October 1, 2003 computed from the satellite-derived SST generated every 48 hours for North America. The satellite data were extracted from the dataset known as the SST14NA (http://www.class.ncdc.noaa.gov/saa/products/welcome). Here we only show the satellite SST data in regions covered with a value of "reliability" greater than 75

("reliability" values are in the range of 0~150 in SST14NA), since reliable SST data are not available over the cloud cover regions. Figure 3.9a demonstrate that there was systematic SST cooling centered about 60 km to the right side of the storm track over the region from the deep water near the shelf break of the ScS to the Gulf of St. Lawrence. The simulated SST changes during the same period in Run_WaveCir (Fig. 3.9b) feature a similar highly right-biased SST cooling pattern relative to the hurricane track with a maximum SST change of -4.2^{o}C, which is, in general, consistent with the satellite-derived SST changes. The discrepancy between observations and model results over areas south of ~41^{o}N could be attributed to baroclinic processes associated with the movement of Gulf Stream Meanders that are not simulated correctly due to inadequate model resolutions and imperfect model physics. In comparison with Run_WaveCir, the modeled SST change in Run_CirOnly is smaller with a maximum SST change of only about -3.0^{o}C. This demonstrates the important role of WCIs in enhancing the vertical mixing in the ocean upper layer.

A cross-shore transect over the ScS (Fig. 3.9c) is selected to show the vertical structure of temperature. As shown in Fig. 3.10a, the ocean upper layer is highly stratified and the initial mixed layer (ML) depth is ~40 m before Hurricane Juan. Hurricane Juan reduced the vertical stratification as shown in Fig. 3.10b. Figure 3.10c demonstrates that the 3D wave forces enhance the vertical mixing almost throughout the whole water column along this transect by decreasing the temperature in the upper 50 m depth layer and increase the temperature just below it. The temperature changes are up to ~1^{o}C. The effect of breaking wave-induced mixing, however, is limited only to the top ML. The magnitude of temperature changes induced by this mechanism is about a half of that induced by the 3D wave forces. It should be mentioned that in addition to the 3D wave forces and breaking wave-induced mixing, another important WCI process on the circulation is the nonbreaking wave-induced vertical mixing (*Qiao*, 2004), which has not been implemented in the couple model. It is expected that the effects of waves on the vertical mixing would be stronger when this process is included.

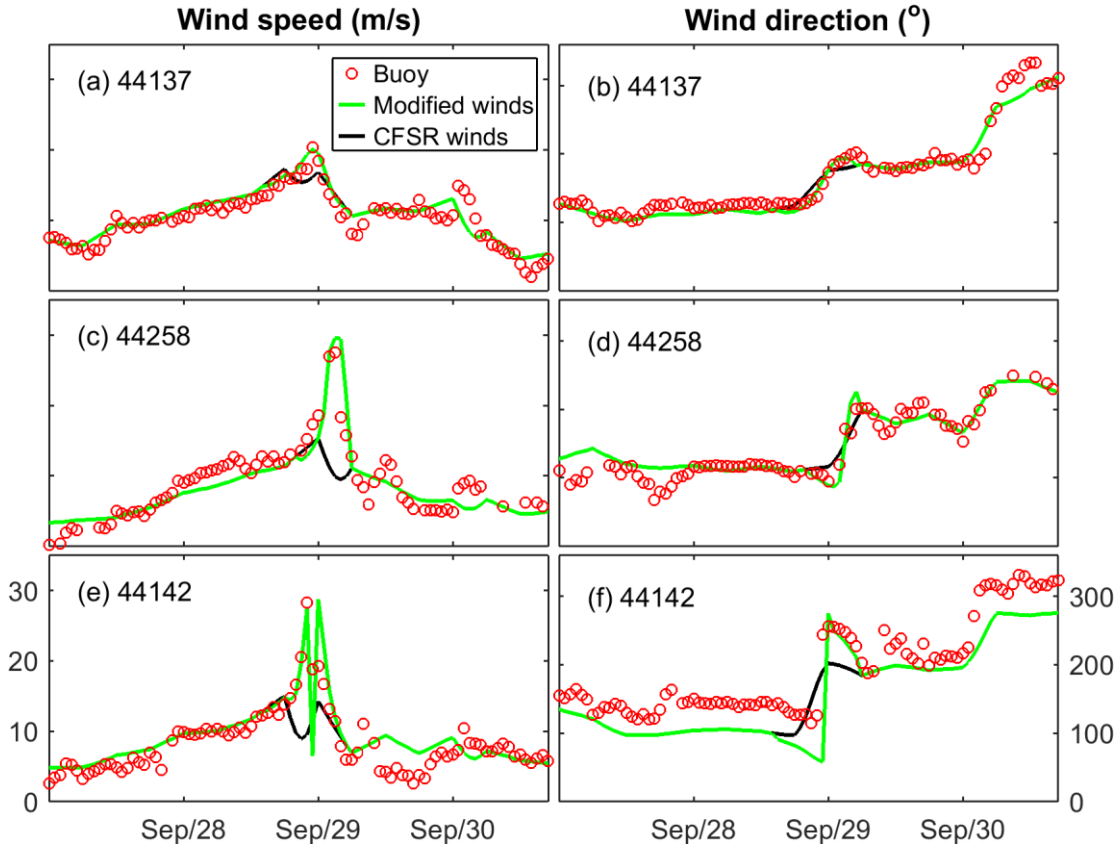

Figure 3.2: Time series of observed wind speeds (left) and directions (right) in comparison with the original and modified CFSR winds at three buoys over the Scotian Shelf and adjacent continental slope during a period of ~4 days in late September 2003. Hurricane Juan occurred on late September 28 and early September 29.

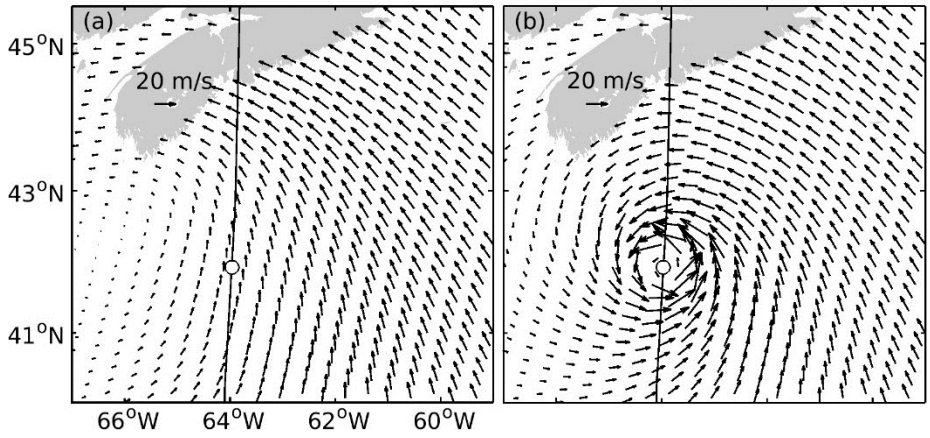

Figure 3.3: Distributions of instantaneous wind vectors for the (a) CFSR winds and (b) Modified winds during Hurricane Juan at 22:00 September 28, 2003.

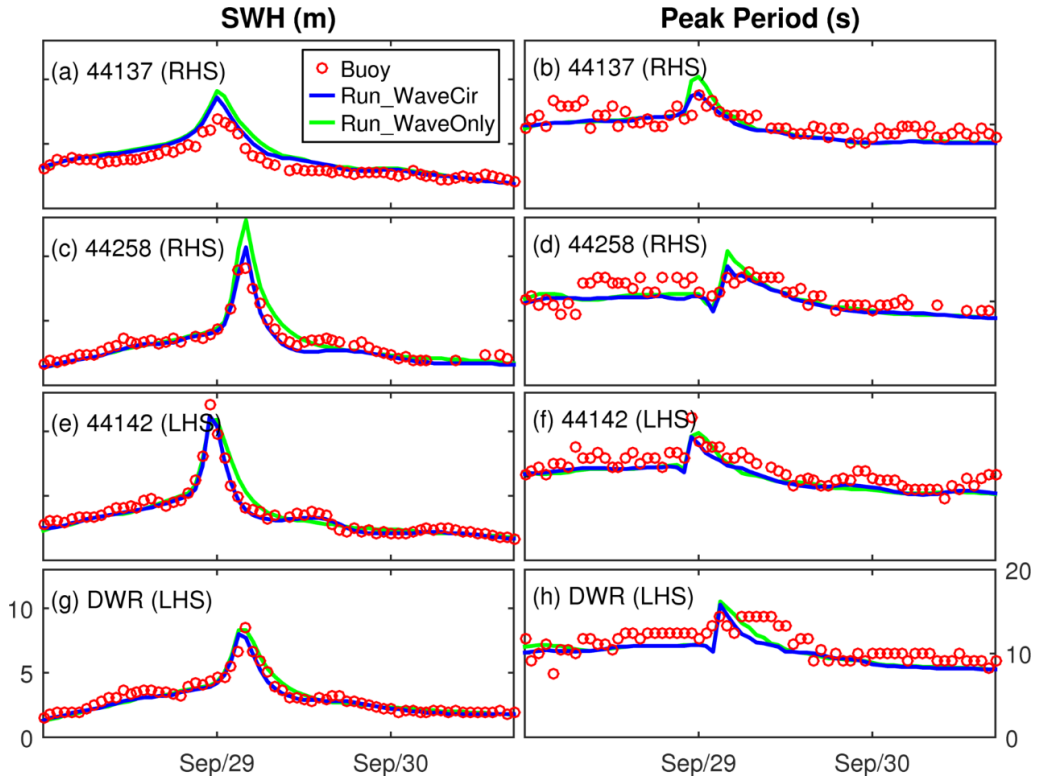

Figure 3.4: Comparison of observed and simulated significant wave heights and peak periods during Hurricane Juan in late September 2003. Abbreviations are used for the right hand side (RHS) and left hand side (LHS) of the storm track.

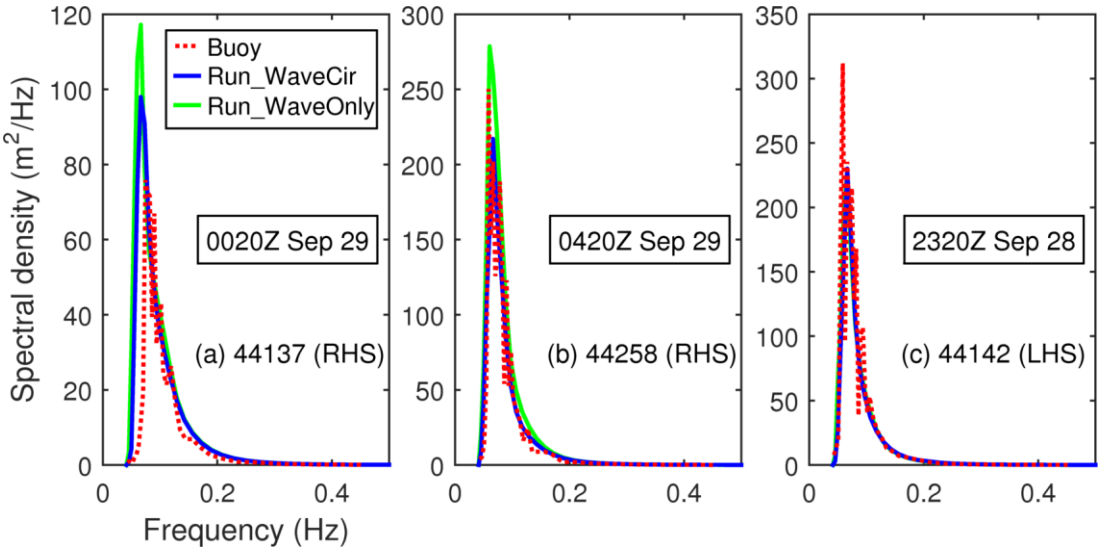

Figure 3.5: Comparison of simulated and observed wave spectral in one dimension during Hurricane Juan.

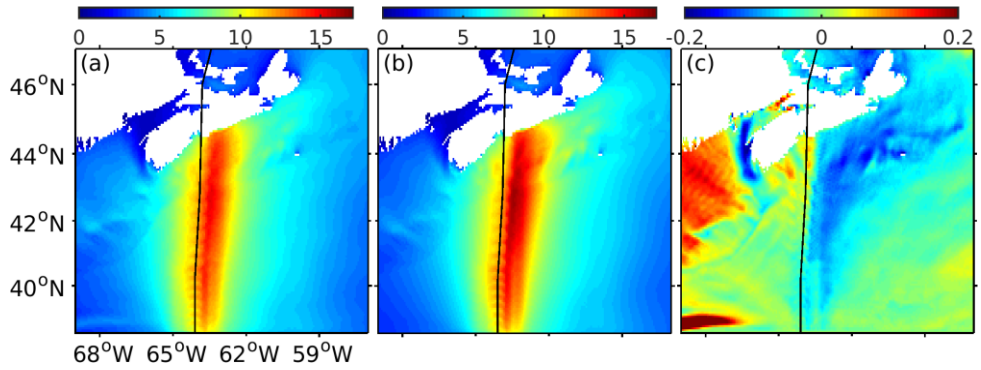

Figure 3.6: Swath maps of (a) significant wave heights (H_s) in Run_WaveCir, (b) H_s in Run_WaveOnly, and (c) normalized differences in maximum H_s between Run_WaveCir and Run_WaveOnly during Hurricane Juan. The black line in each panel represents the storm track of Hurricane Juan.

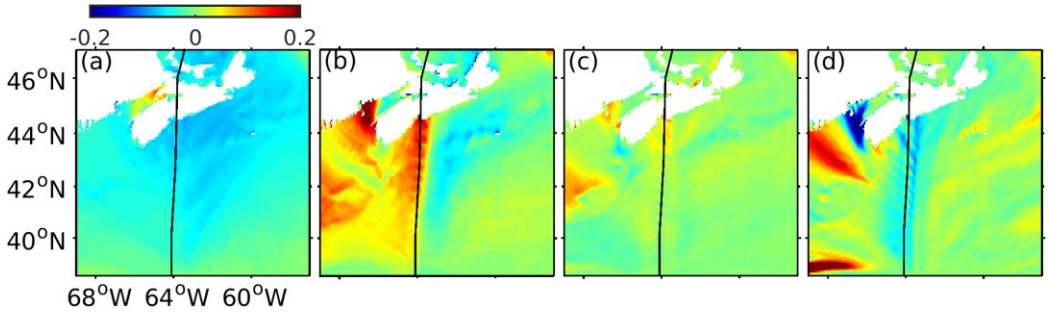

Figure 3.7: Normalized differences in maximum H_s (ΔH_s^{max}) (a) between Run_WaveU_{10} and Run_WaveOnly, (b) between Run_WaveC_g and Run_WaveOnly, (c) between Run_Wavek and Run_WaveOnly, and (d) between Run_Waveθ and Run_WaveOnly during Hurricane Juan. The black line in each panel represents the storm track of Hurricane Juan.

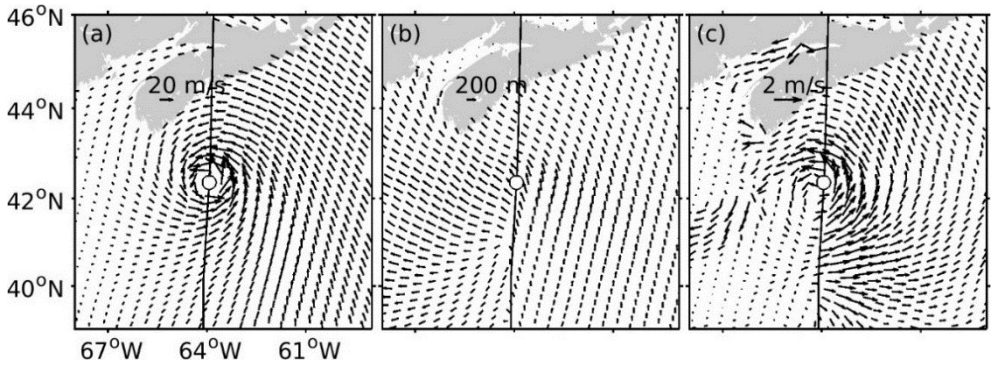

Figure 3.8: Distributions of instantaneous (a) wind velocities, (b) wave vectors, and (c) surface current velocities. The black line in each panel represents the storm track of Hurricane Juan. The open circle at the storm track represents the current position of the storm center at 22:00 September 28, 2003.

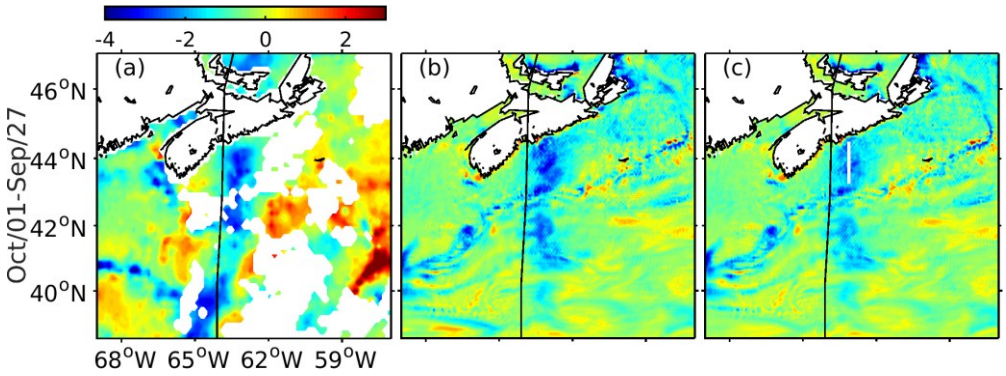

Figure 3.9: Comparison of SST cooling from (a) satellite data and model results in (b) Run_WaveCir and (c) Run_CirOnly during Hurricane Juan. The black line in each panel represents the storm track of Hurricane Juan. In (a) the satellite SST data are missing over white areas in the waters due mainly to the cloud cover. The white straight line (c) marks a cross-shore transect at which model results are shown in Fig. 3.10.

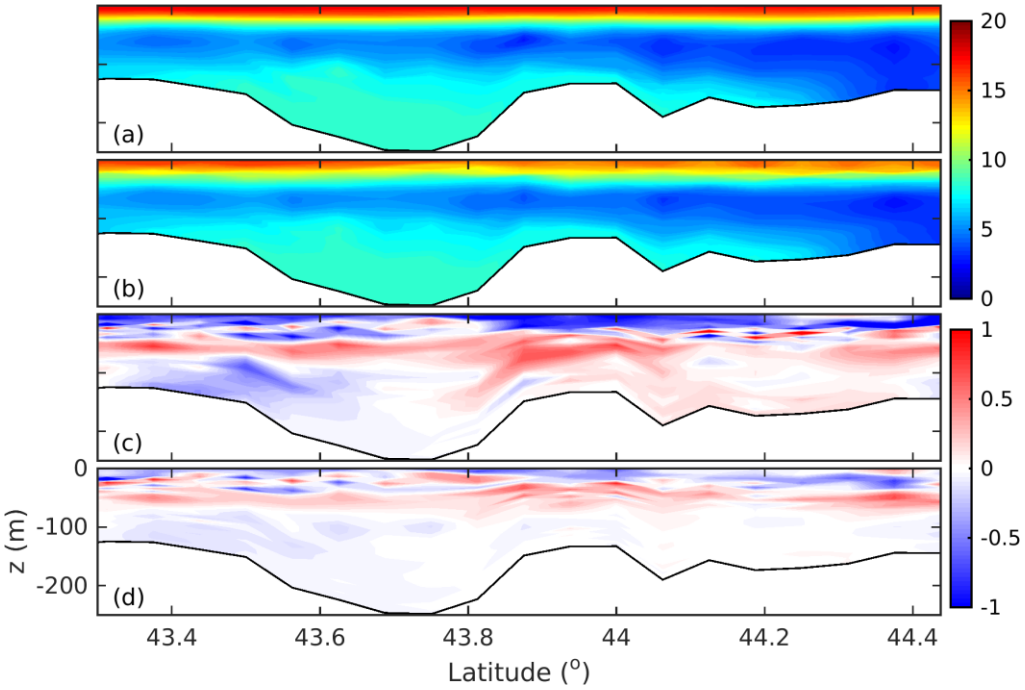

Figure 3.10: Daily averaged temperature distribution in the cross-shore transect shown in Fig. 3.9 (a) before and (b) after Hurricane Juan based on results in Run_WaveCir. Temperature differences in the cross-section between model results in (c) Run_CirVF, (d) Run_CirTKE and those in Run_CirOnly after Hurricane Juan passed by.

3.3.2 Hurricane Bill

Hurricane Bill was a category-1 hurricane that swept the inner ScS in late August 2009 (Fig. 3.1). Figure 3.11 presents time series of original and modified CFSR winds and in-situ wind observations at four buoy stations. Buoys 44011, 44024 and 44258 are located to the LHS and buoy 44150 is located to the RHS of the storm track. Similar to Hurricane Juan, the original CFSR winds agree reasonably well with the in-situ wind observations before and after Hurricane Bill, but do not resolve the peak winds during the storm. By comparison, the modified CFSR wind fields are in better agreement with the observed peak winds during Hurricane Bill in terms of both speeds and directions. In comparison with the original CFSR winds, the instantaneous wind vector maps in the modified CFSR winds (Fig. 3.12) have significant enhancements of winds around the hurricane center. This demonstrates again the effectiveness of the parametric hurricane model for improving the original CFSR winds during a tropical storm or hurricane.

Figure 3.13 presents time series of observed H_s and peak wave periods and simulated values in numerical experiments Run_WaveCir and Run_WaveOnly at four buoys during Hurricane Bill. The coupled model run (Run_WaveCir) reproduces reasonably well the observed H_s with simulated H_s^{max} of ~13.7 m at buoys 44150, ~12.6 m at buoy 44011, ~10.9 m at buoy 44024, and ~9.7 m at buoy 44258. The simulated peak wave periods are about 10-19 s at these four buoys, which are also in general agreement with the in-situ wave observations. After the peak winds, the simulated H_s at four buoys exhibit similar near-inertial oscillation features as previously found in the case of Hurricane Juan, which is also consistent with in-situ wave observations. By comparison with results in Run_WaveCir, the model results in Run_WaveOnly overestimate the H_s^{max} by ~2.0 m at buoy 44150 (Fig. 3.13), which is located to the RHS of the storm track. This overestimation of H_s on the RHS of the track in Run_WaveOnly is due mainly to the omission of the WCIs, same as the wave-only model results for Hurricane Juan. It should be noted that wave period obtained from buoy 44024 is reported in a small number of discrete steps. There are only two values in the range of 10-20 seconds, which leads to a "stair-stepped" appearance in Fig. 3.13f.

The simulated wave spectra (Fig. 3.14) in Run_WaveCir agree reasonably well with the counterparts estimated from in-situ wave observations at three operational buoys (44150, 44258 and 44011). By comparison, the model results in Run_WaveOnly overestimate the spectral peaks by up to 42% at buoy 44150, due to again the omission of the WCIs. At buoys 44258 and 44011 located to the LHS of the storm track, the simulated wave spectra in Run_WaveCir and Run_WaveOnly are highly similar, indicating the secondary effect of the WCI on this region.

Figure 3.15a presents the swath map calculated from results produced by the coupled model in Run_WaveCir for Hurricane Bill. The swath in Run_WaveCir is also biased to the RHS of the storm track, with similar general features in Hurricane Juan (Fig. 3.6a). The values of H_s^{max} in Run_WaveCir for Hurricane Bill are about 12-15 m appearing over areas within 10-200 km to the RHS of the storm track. A comparison in swath between Run_WaveCir and Run_WaveOnly shown in Fig. 3.15a and b demonstrates that values of H_s^{max} on the RHS of the storm track for Hurricane Bill are overestimated by 11-15% in Run_WaveOnly due to the omission of the WCIs. In comparison with the swath map shown in Fig. 3.6 for Hurricane Juan, the intensities of H_s generated by Hurricane Juan and Bill are comparable, although Bill is a category-1 hurricane and Juan is a category-2 hurricane. It should be noted that Hurricane Bill had a longer trapped fetch (or dynamic fetch) (*Bowyer and MacAfee,* 2005) than Hurricane Juan. In addition, the area affected by large surface gravity waves (H_s greater than 12 m) during hurricane Bill is almost twice as the area during hurricane Juan, since the former has a larger radius of the storm than the latter.

Distributions of ΔH_s^{max} based on model results in Run_WaveU_{10}, Run_WaveC_g, Run_Waveθ demonstrate that the relative wind effect, current-induced convergence, and refraction all influence H_s^{max} during Hurricane Bill in a very similar way as those during Hurricane Juan (Fig. 3.16a,b,d). Different from Hurricane Juan, however, the current-induced wavenumber shift in Hurricane Bill induces a relatively large increase of H_s^{max} (~7%) on the LHS of the storm track (Fig. 3.16c). The increase of H_s^{max} due to this process appears at the left-rear quadrant relative to the hurricane center, where the surface current gradient is large in the mean wave direction (Fig. 3.17b,c)

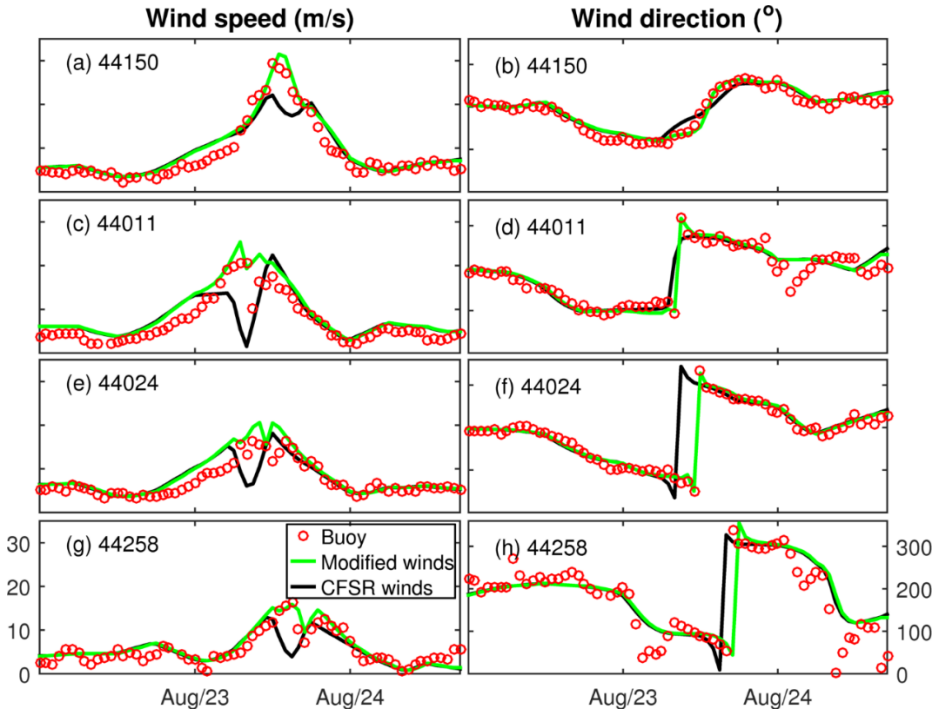

Figure 3.11: Time series of observed wind speeds (left) and directions (right) in comparison with the original and modified CFSR winds at four buoys over the Scotian Shelf and adjacent continental slope during a period of ~4 days in late August 2009. Hurricane Bill occurred on August 23.

Figure 3.18 presents the observed and modeled SST changes during Hurricane Bill, where the SST changes are defined as differences in the SST between August 24 and 22, 2009. Similar to Hurricane Juan, the simulated SST changes in Run_WaveCir (Fig. 3.18b) for Hurricane Bill feature a right-biased pattern of SST cooling (up to -7.4°C) centered at about 100 km to the RHS of the storm track, which agrees well with the satellite-derived SST data. The model results in Run_CirOnly, however, underestimate the SST changes on the RHS of the storm track with a largest cooling of about -6.4°C.

It should be noted that the magnitude of modeled SST change induced by Hurricane Bill (up to -7.4°C) near the shelf break is much larger than that induced by Hurricane Juan (up to -4.2°C) on the ScS. According to *Price* (1981), the SST response is mainly determined by the hurricane strength and translation speed, and the background stratification. In this study, the hurricane strength and translation speed are roughly same for both Hurricane Juan and Bill. But the background stratification before Hurricane Bill

is stronger associated with a shallower initial ML depth and a larger thermocline temperature gradient (Fig. 3.19a) than Hurricane Juan (Fig. 3.10a), which is responsible for the large SST change induced by Hurricane Bill. Similar to Hurricane Juan, the effect of the 3D wave forces on the SST changes can reach up to 200 m, while the penetration depth of the effect of breaking wave-induced mixing is only up to 80 m.

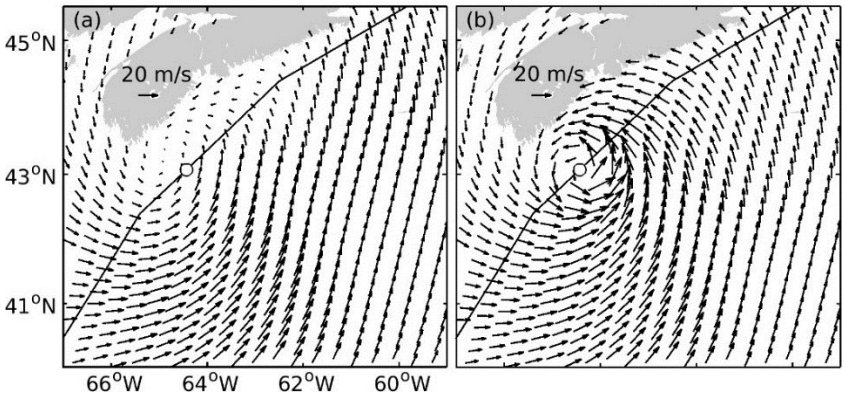

Figure 3.12: Distributions of instantaneous wind vectors for the (a) CFSR winds and (b) Modified winds during Hurricane Bill at 13:00 August 23, 2009.

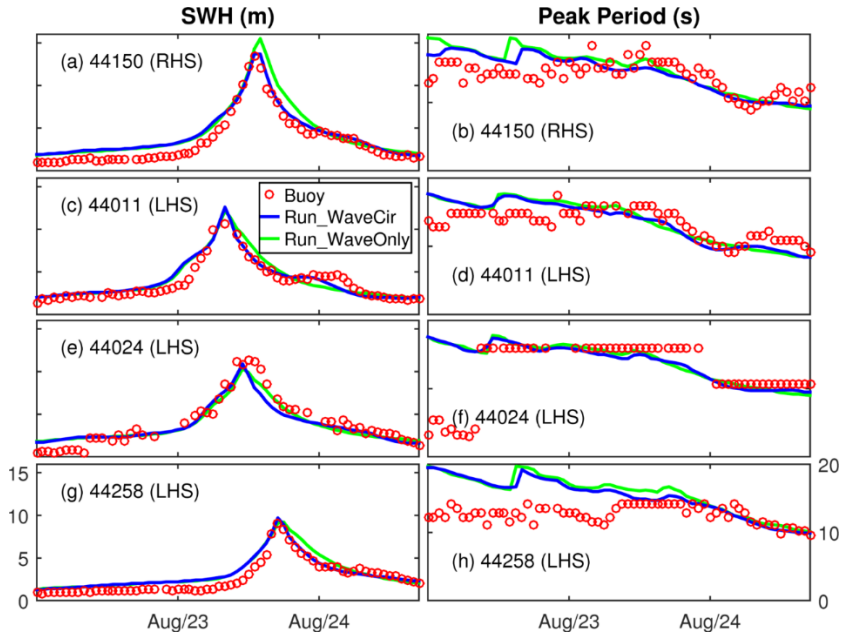

Figure 3.13: Comparison of observed and simulated significant wave heights and peak periods during Hurricane Bill in late August 2009. Abbreviations are used for the right hand side (RHS) and left hand side (LHS) of the storm track.

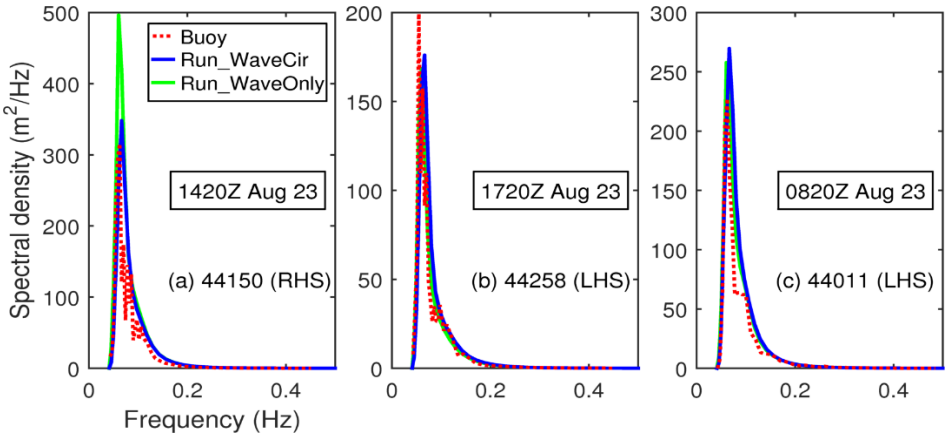

Figure 3.14: Comparison of simulated and observed wave spectral in one dimension during Hurricane Bill.

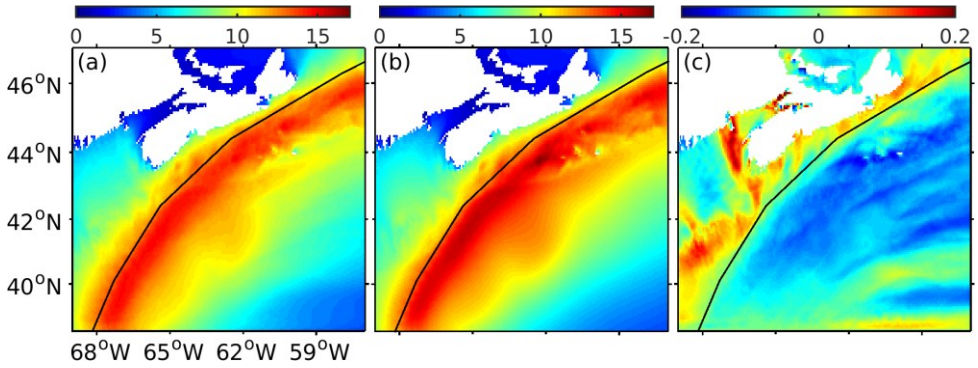

Figure 3.15: Swath maps of (a) significant wave heights (H_s) in Run_WaveCir, (b) H_s in Run_WaveOnly, and (c) normalized differences in maximum H_s between Run_WaveCir and Run_WaveOnly during Hurricane Bill. The black line in each panel represents the storm track of Hurricane Bill.

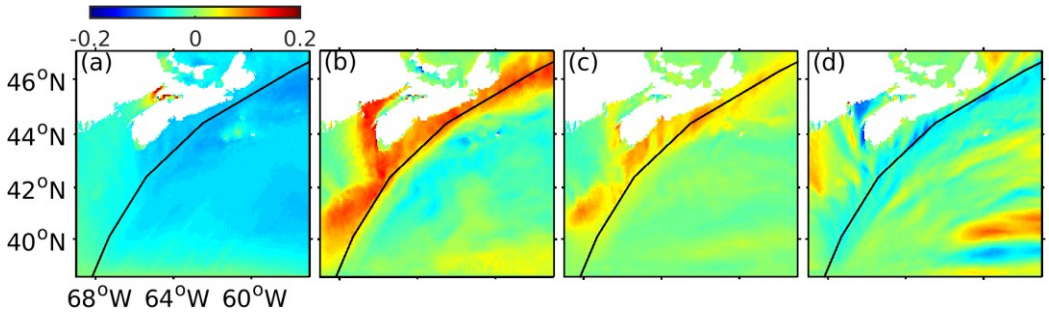

Figure 3.16: Normalized differences in maximum H_s (ΔH_s^{max}) (a) between Run_WaveU_{10} and Run_WaveOnly, (b) between Run_WaveC_g and Run_WaveOnly, (c) between Run_Wavek and Run_WaveOnly, and (d) between Run_Waveθ and Run_WaveOnly during Hurricane Bill. The black line in each panel represents the storm track of Hurricane Bill.

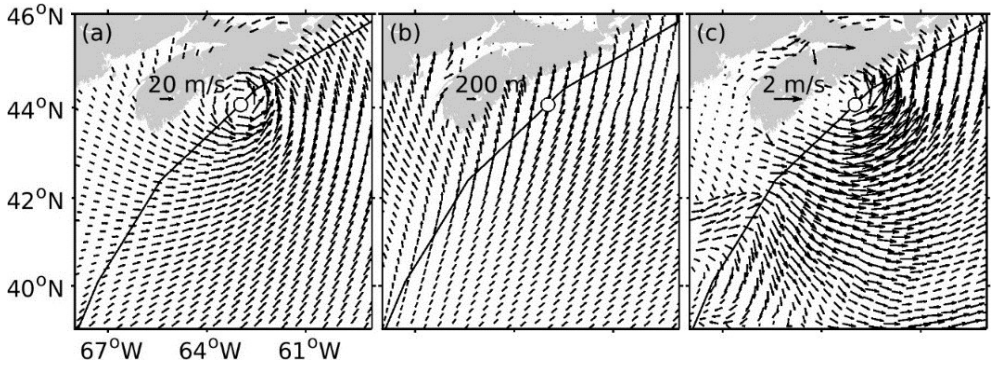

Figure 3.17: Distributions of instantaneous (a) wind velocities, (b) wave vectors, and (c) surface current velocities. The black line in each panel represents the storm track of Hurricane Bill. The open circle at the storm track represents the current position of the storm center.

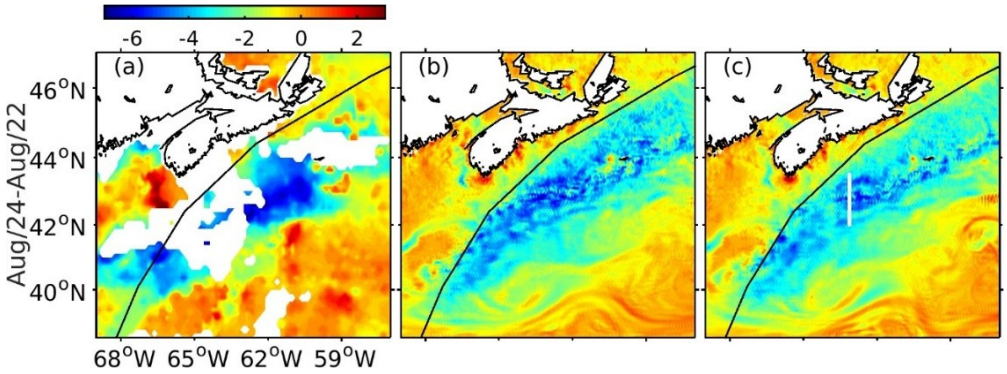

Figure 3.18: Comparison of SST cooling from (a) satellite data and model results in (b) Run_WaveCir and (c) Run_CirOnly during Hurricane Bill. The black line in each panel represents the storm track of Hurricane Bill. In (a) the satellite SST data are missing over white areas in the waters due mainly to the cloud cover.

3.3.3 Winter Storm Known as "White Juan"

White Juan was a hurricane-strength winter storm in February 2004, which was generated by atmospheric processes different from those responsible for hurricanes. White Juan was formed over the northeast coast of the United States when the jet stream dipped far to the south, allowing cold and dry polar air from the north to clash with warm and humid air moving up from the south.

In-situ observations during White Juan were available only at two operational buoy

stations (i.e., buoy 44008 and 44011) in the study region. These two stations were located over the LHS of the storm track, with the shortest distance of about 200 km from the track. Figure 3.20 demonstrates that the original CFSR winds are in good agreement with the observed peak winds during White Juan at both buoy stations. This is because White Juan is a large-size winter storm and the horizontal resolution of the CFSR is reasonable to resolve the general structure of White Juan.

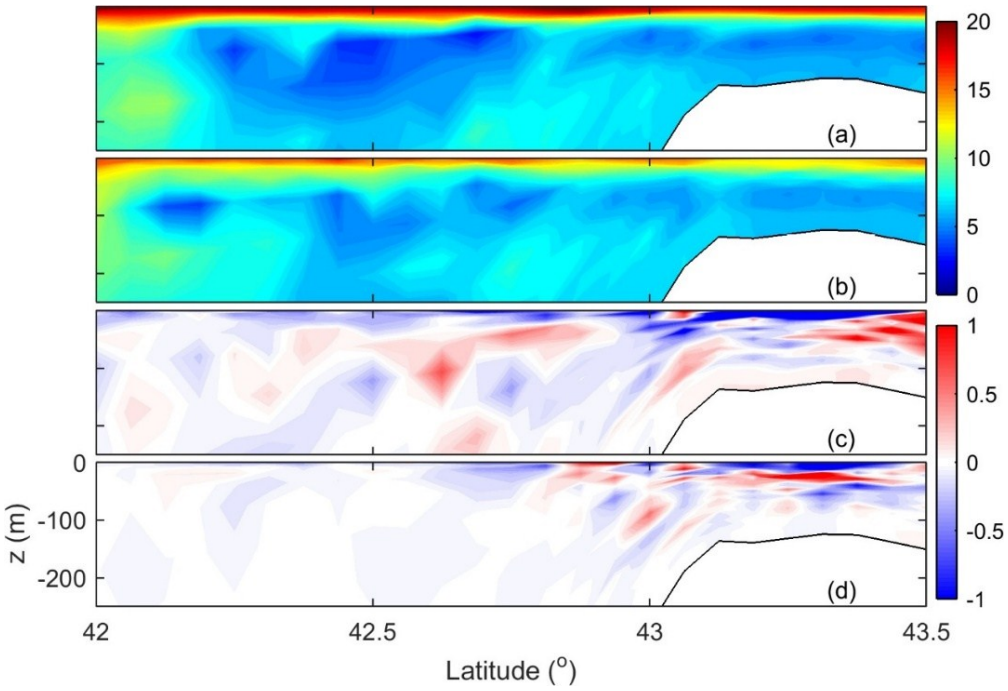

Figure 3.19: Daily averaged temperature distribution in the cross-shore transect shown in Fig. 3.18 (a) before and (b) after Hurricane Bill based on results in Run_WaveCir. Temperature differences in the cross-section between model results in (c) Run_CirVF, (d) Run_CirTKE and results in Run_CirOnly after Bill passed by.

Figure 3.21 presents time series of observed and simulated H_s and peak wave periods during White Juan at two buoy stations (44008 and 44011). The coupled model in Run_WaveCir reproduces reasonably well the observed H_s (with H_s^{max} of ~6.1 m at 44008 and ~8.9 m at 44011) and peak periods at these two stations. Relatively long peak periods (~8 seconds) appearing on February 18 before the peak winds are indicators of swells generated by the storm propagating ahead of the slow-moving storm center. The

duration of large H_s lasts about 2 days during White Juan due to its slow translation speed. Figure 3.22 exhibits that model results in Run_WaveOnly also perform reasonably well in reproducing the observed H_s and peak wave periods at these two stations, indicating that the WCIs on waves are weak over these regions occupied by these two buoys.

The swath map during White Juan in Run_WaveCir (Fig. 3.22a) also features a right-biased pattern relative to the storm track. In comparison with swath maps for Hurricanes Juan and Bill (Figures 6a and 15a), the intensity of H_s^{max} for White Juan is relatively weaker in White Juan, but the area experienced with large waves is much broader owing to the large size of the storm. Figure 3.22b demonstrates that the model in Run_WaveOnly overestimates the intensity of the swath, particularly on the RHS of the storm track for White Juan due to the omission of the WCIs (up to 10%). The reduction of H_s^{max} on both sides of the storm track in White Juan differs from those in the two hurricane cases.

As shown in Fig. 3.23a, the relative wind effect reduces H_s^{max} by ~5% over regions affected by White Juan, which is slightly smaller than the two hurricane cases. The convergence effect induces a significant increase of H_s^{max} on the inner ScS (6-10%) on the LHS of the storm track and a decrease of H_s^{max} (5-7%) around (61°W, 42°N) on the RHS of the storm track (Fig. 3.23b). This is associated with strong convergence and divergence of current over these two areas (Fig. 3.24c). Over other areas there are no significant changes, due to the relatively small spatial current gradients associated with the large-scale structure and slow translation speed of the winter storm. Figures 3.23c and d suggest that the effects of the current-induced wavenumber shift and refraction are relatively small (less than 5%), due again to the relatively small spatial current gradients. It is noted that the mean wave directions during White Juan roughly align with the wind directions (i.e., cyclonic relative to the storm center) (Figs. 3.24a and b), which is different from the two hurricane cases. This is because that, unlike the fast-moving hurricanes, surface waves generated by a slowly-moving storm propagate ahead of the storm. Thus, the wave fields under a slowly-moving storm are mainly affected by locally generated wind-sea.

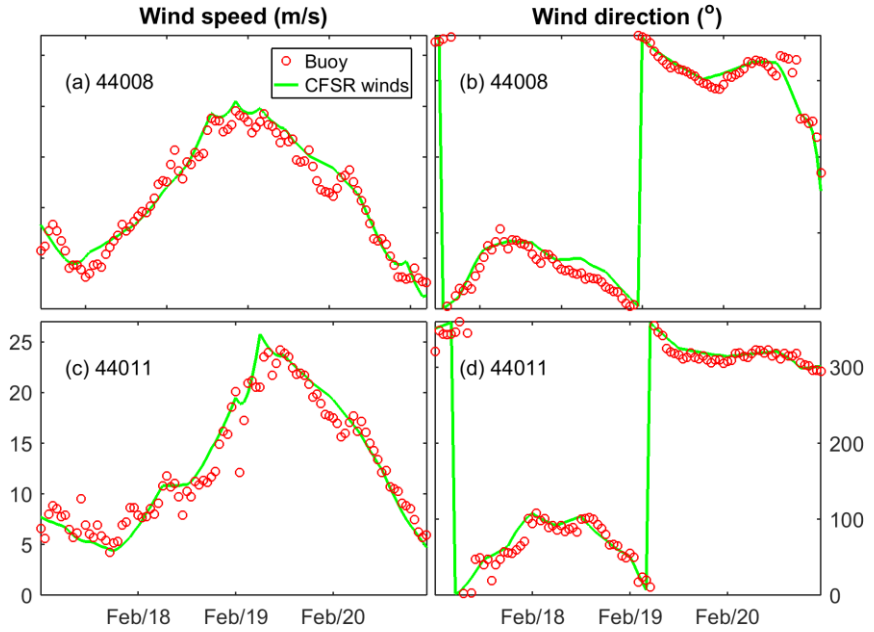

Figure 3.20: Time series of observed wind speeds (left) and directions (right) in comparison with the original CFSR winds at two buoys during a period of ~4 days in February 2004. White Juan occurred from February 17 to February 20.

Figure 3.25 presents the observed and simulated SST changes associated with White Juan, which are defined again as differences in the SST between February 21 and February 17, 2004. Unlike hurricane-induced SST cooling shown in Figures 10 and 19, the observed SST changes during this winter storm feature SST warming of up to a few degrees on the central ScS to the LHS of the storm track. The satellite-derived SST changes are not available on the RHS of the storm track due to the cloud cover during the study period. The model results in Run_WaveCir reproduce large SST warming of ~3.4ºC over the central ScS and much larger SST warming in the deep waters to the south of the ScS. In comparison with results in Run_WaveCir, the SST warming in Run_CirOnly is relatively weaker with the maximum warming of only about 2.4ºC. Figure 3.26a and b present vertical distributions of temperatures before and after White Juan along a cross-shore transect (marked in Fig. 3.25c) based on model results in Run_WaveCir. Before White Juan, water temperature at the transect is relatively cold and uniform in the top 15 m and then increases with depth. After the storm, the water temperature at this transect increases in the ocean upper layer and decreases in the sub-surface layer. Figure 3.26c demonstrates that

the 3D wave forces are experienced by the whole water column (up to 200 m). The magnitude of the temperature changes induced by the 3D wave forces is ~0.6ºC. The effect of the breaking wave-induced mixing is weaker in White Juan than in Hurricane Juan and Bill due most likely to the weaker vertical stratification in the top 50 m in winter months than in summer months.

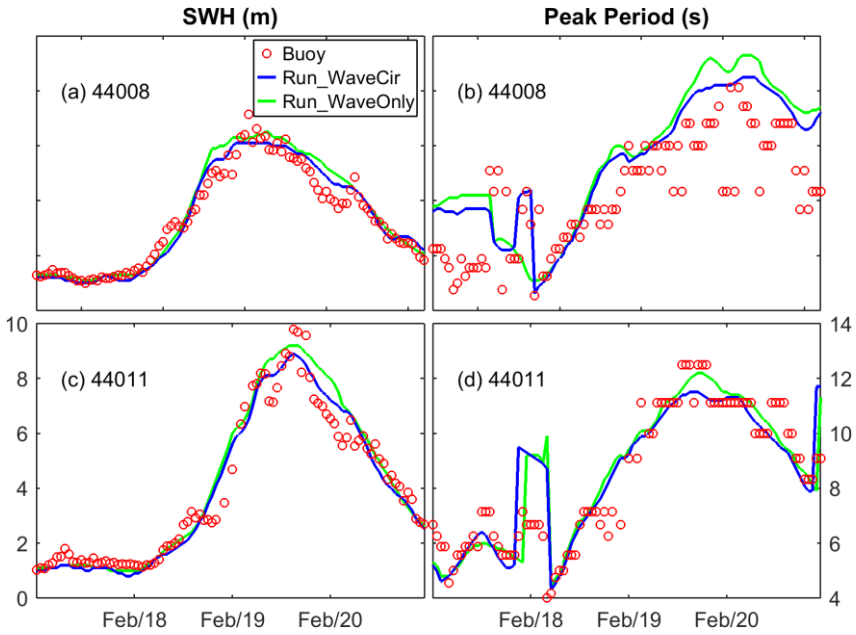

Figure 3.21: Comparison of observed and simulated significant wave heights and peak periods during White Juan in February 2004.

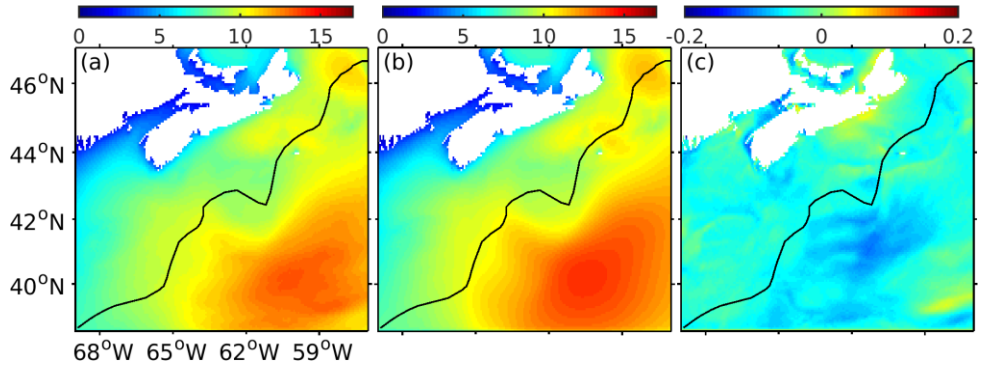

Figure 3.22: Swath maps of (a) significant wave heights (H_s) in Run_WaveCir, (b) H_s in Run_WaveOnly, and (c) normalized differences in maximum H_s between Run_WaveCir and Run_WaveOnly during White Juan. The black line in each panel represents the storm track of White Juan.

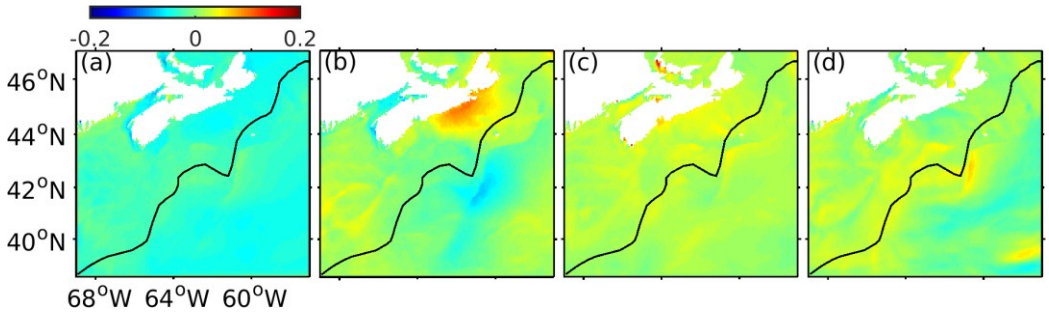

Figure 3.23: Normalized differences in maximum H_s (ΔH_s^{max}) (a) between Run_WaveU$_{10}$ and Run_WaveOnly, (b) between Run_WaveC$_g$ and Run_WaveOnly, (c) between Run_Wavek and Run_WaveOnly, and (d) between Run_Waveθ and Run_WaveOnly during White Juan. The black line in each panel represents the storm track of White Juan.

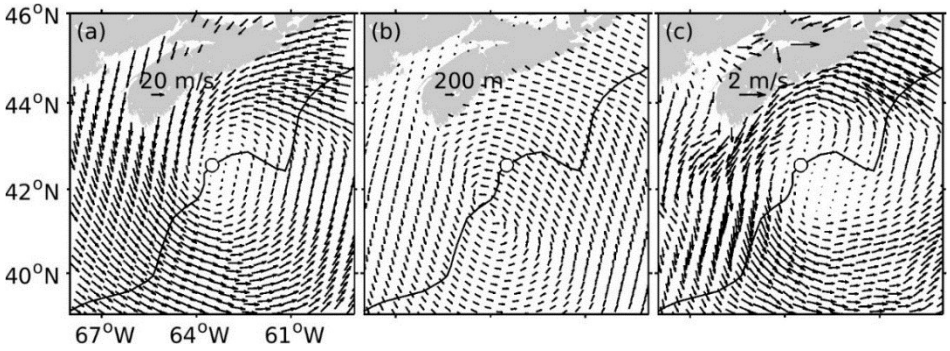

Figure 3.24: Distributions of instantaneous (a) wind velocities, (b) wave vectors, and (c) surface current velocities. The black line in each panel represents the storm track of White Juan. The open circle at the storm track represents the current position of the storm center.

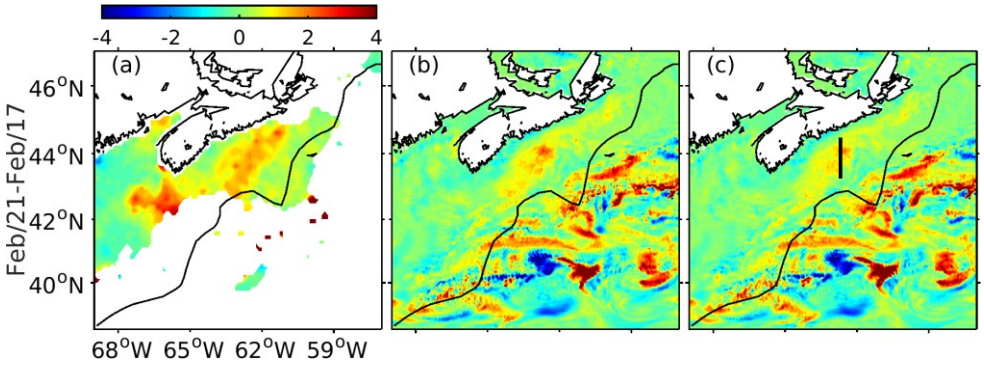

Figure 3.25: Comparison of SST changes from (a) satellite data and model results in (b) Run_WaveCir and (c) Run_CirOnly during White Juan. The black line in each panel represents the storm track of White Juan. In (a) the satellite SST data are missing over white areas in the waters due mainly to the cloud cover. The black straight line in (c) marks a cross-shore transect at which model results are shown in Fig. 3.26.

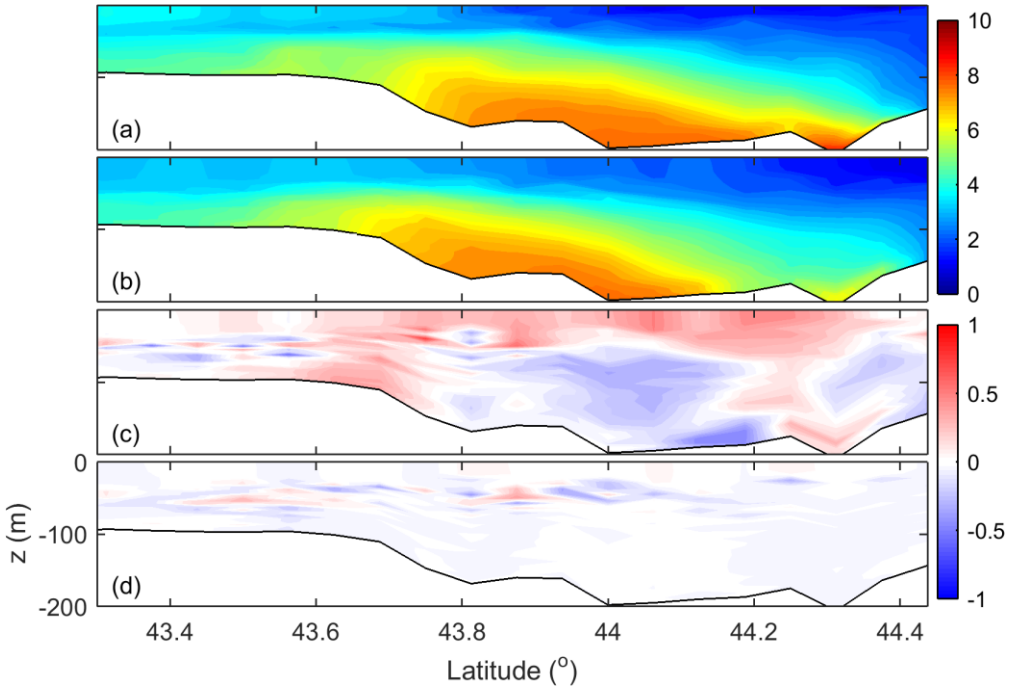

Figure 3.26: Daily averaged temperature distribution in the cross-shore transect shown in Fig. 3.25 (a) before and (b) after White Juan based on results in Run_WaveCir. Temperature differences in the cross-section between model results in (c) Run_CirVF, (d) Run_CirTKE and results in Run_CirOnly after White Juan passed by.

3.4 Summary and Discussion

A two-way coupled wave-circulation modelling system was used in a comparative study of the surface gravity waves, ocean circulation and wave-current interactions (WCIs) over the eastern Canadian shelf (ECS) and adjacent deep waters. The coupled model is based on a three-dimensional ocean circulation model for the ECS (DalCoast) and a third generation wave model (WW3). The coupled model uses OpenPALM to exchange information between the circulation model and the wave model.

Three extreme storms with different sizes, storm tracks, and translation speeds were considered in this study: (a) Hurricane Juan in late September 2003, (b) Hurricane Bill in late August 2009, and (c) a hurricane-strength winter storm known as White Juan in middle February 2004. In comparison with wave-only model results, the coupled wave-circulation modelling system performs better in simulating the observed maximum significant wave heights (H_s^{max}) and peak wave periods during the highest wind occurrences and the near-

inertial oscillation of significant wave heights (H_s) after the highest wind occurrences observed by in-situ wave buoys for the two hurricane cases. By comparison, the values of H_s^{max} are reduced by 11-15% on the right hand side (RHS) of the storm track and increased by 4-7% on the left hand side (LHS) of the storm track due to the WCIs. In the winter storm case, by comparison, H_s^{max} on both sides of the storm track are reduced due to the WCIs.

The contribution of four major WCI mechanisms (i.e., the relative wind effect, the current-induced convergence, wavenumber shift, and refraction) to H_s^{max} changes were examined in process-oriented numerical experiments. The relative wind effect depends on relative directions between winds and surface currents, both of which are roughly parallel to each other beneath a storm. Model results demonstrated that this mechanism reduces H_s^{max} on both sides of the storm track (5-7%) in all three storm cases. The current-induced convergence depends on the spatial gradients of currents. In the two small-scale, fast-moving hurricane cases, this mechanism induces a strong wave energy convergence (divergence) on the LHS (RHS) of the storm track. This corresponds to an increase of H_s^{max} by about 11-18% on the LHS and a decrease of H_s^{max} (5-7%) on the RHS of the storm track. In the large-scale, slow-moving winter storm case, the overall spatial current gradients are relatively small, and the current-induced wave energy convergence (divergence) are only limited to particular areas on the LHS (RHS) of the storm track. The current-induced wavenumber shift and wave refraction depend on the relative directions between waves and surface current gradients. The effect of the wavenumber shift is only pronounced during Hurricane Bill, which introduces an increase of H_s^{max} by 7% on the LHS of the storm track. The current-induced refraction significantly reduced the H_s^{max} by 10% along the storm track in both hurricane cases. Notice that, the relative wind effect is not negligible in this study, which is different from Fan et al., (2009a, b). The difference could be attributed to the inclusion of the feedback of wave fields to ocean currents in this study, which leads to a strong surface Lagrangian mean current field including the contribution from the Stokes drift. Furthermore, in the analysis of the effects of ocean currents in Eqs. (3.1) and (3.2), Fan et al., (Eq. (2), 2009b) considered only the advection of surface waves by a horizontally uniform current and neglected the spatial gradients of ocean currents, which is insufficient. The results in this study indicate that it is the current-

induced wave energy divergence, rather than the advection of surface waves by ocean currents, that contributes mostly to the reduction of H_s^{max} on the right side of the storm track.

Model results also demonstrated that, in addition to locally generated wind-sea, the wave fields under the two fast-moving hurricanes are also strongly affected by remotely generated swells moving in harmony with the storm. This highlights the use of 2D wave spectrum instead of the bulk wave parameters for the estimation of Stokes drift, which is strongly affected by the high-frequency part of the spectrum (see Appendix A).

The response of circulation and hydrography in the ocean upper layer to surface gravity waves was examined in terms of storm-induced circulation and SST changes. Both Hurricane Juan and Bill generated a highly right-biased SST cooling relative to the storm track. In comparison with results produced by the circulation-only model, the SST cooling produced by the coupled wave-circulation modelling system is stronger (up to 1.2^{o}C higher than that in the circulation-only model run), which agrees well with satellite-derived SST changes. In contrast to hurricane-induced SST cooling, White Juan generates a SST warming in the central ScS region to the LHS of the storm track. Compared with the circulation-only model results, the SST warming is enhanced by up to 1.0^{o}C in the coupled wave-circulation model run due to the WCIs.

The process-oriented experiments demonstrated that the effect of 3D wave forces on the vertical mixing and SST changes can reach up to 200 m in all three storm cases. It should be noticed that the effect of breaking wave-induced mixing depends on the initial stratification of the ocean upper layer. This mixed process is negligible under weak background stratification during White Juan, and becomes significant under strong background stratification in two hurricane cases, but its penetration depth is restricted to the surface ML (~70 m).

CHAPTER 4

TIDAL MODULATION OF SURFACE GRAVITY WAVES IN THE GULF OF MAINE[1]

4.1 Introduction

Large tidal currents are known to modulate the behavior of wind-generated surface gravity waves at tidal frequencies (*Vincent*, 1979). With the conventional theory of the wave-current interaction (WCI), one would expect that the tidal modulation in the wave height should reach its maximum in the contra tidal currents. By contrast, however, higher waves were frequently observed in the following tidal currents than those in the contra tidal currents (e.g., *Gemmrich and Garrett*, 2012; *Guillou and Chapalain*, 2012; *Vincent*, 1979). Using a simple analytical model, *Davidson et al*. (2009) demonstrated that wave dissipation due to the opposing tidal currents could be responsible for the unusual timing of the maximum wave height (about 50-60 minutes just after the maximum flooding tidal currents) in the macro-tidal areas. Nonetheless, the important physical processes affecting the unusual timing of the maximum wave height are complex and differ over different areas.

Physically, ocean surface currents can modify the relative wind speeds above the sea surface (the relative wind effect) and change the absolute frequency of surface waves known as the Doppler shift. Spatial variability of surface currents can modify the relative wave frequency and cause wave refraction, shoaling and breaking that mimic bathymetric effects. Furthermore, the variation of sea surface elevations can modify the local water

[1] Wang, P. and J. Sheng. 2018. Tidal modulation of surface gravity waves in the Gulf of Maine. *Journal of Physical Oceanography*, 48, 2305-2323. ©American Meteorological Society. Used with permission.

depth and thus affect the wave propagation and dissipation. Previous studies demonstrated some important effects of these WCI mechanisms on tidal modulations in ocean surface waves. For example, *Ardhuin et al.* (2012) showed that for short wind-generated surface waves the relative wind effect explained about 20-40% of the modulation in wave heights by periodic changes in the effective wind speeds induced by tidal currents. *Bolanos et al.* (2014) demonstrated that in shallow waters of a tidally dominated estuary the tidal modulation in the wave height was mainly controlled by the time-varying water depth. *Masson* (1996) showed that the current-induced refraction affected the phase of the tidal modulation in the wave height off the British Columbia coast. *Tolman* (1990) found that effects of current-induced refraction was negligible in the North Sea. He also found that during strong storm events the effects of surface currents and water level variations approximately balanced each other out, resulting in much smaller tidal modulations of surface waves than in moderate wind cases. *Moon* (2005) demonstrated that tidal modulations in the mean wave variables decreased with increasing severity of winds. Thus, contributions of different WCI mechanisms to tidal modulations in surface waves depend largely on the local bathymetry, winds, waves, and tidal conditions.

The study region of this paper is the Gulf of Maine (GoM), which is a large semi-enclosed coastal basin bordered by the northeastern United States and the Canadian Maritime Provinces. The GoM is recognized as one of the world's richest marine ecosystems with various marine and estuarine habitats (*Johnson et al.*, 2011). Reliable modelling and predictions of marine environmental conditions are needed for effective ecosystem management of natural resources in the region.

The GoM is characterized by large semidiurnal M_2 tidal currents, with the world's largest tidal range of ~16 m in the upper reaches of the Bay of Fundy (BoF) (*Greenberg*, 1983; *Hasegawa et al.*, 2011). The semidiurnal tidal currents are also strong and up to 1.0 m/s over the mouth of the GoM. The general physical oceanography of the GoM can be found elsewhere (*Bigelow et al.*, 1927; *Xue et al.*, 2000; *He et al.*, 2008; *Smith et al.*, 2012; *Li et al.*, 2014).

The main topographic feature over the mouth of the GoM includes the Georges Bank

(GB), Northeast Channel (NEC) and Great South Channel (GSC). The GB is a large shallow submarine bank, and the NEC and GSC are two deep channels in the region (Fig. 1.1). Since the mouth of the GoM is exposed to large swell waves coming from the North Atlantic Ocean, strong tidal modulations in ocean surface waves are expected to occur. In-depth knowledge on tidal modulations of surface waves is important for accurate and reliable surface wave modelling and predictions in the GoM. The scientific issues on tidal modulations of surface waves in the study region, however, were not addressed until recently. *Sun et al.* (2013) showed that effects of ocean currents on waves were insignificant at buoys located in the inner GoM during a hurricane event. On the contrary, *Xie and Zou* (2017) demonstrated large impacts of ocean currents on wave heights on GB during a storm event based on numerical results. It is noted that these two studies focused mainly on short time-scales associated with a single storm event. The relevant mechanisms controlling the wave modulation by tidal currents in the study region have not been fully addressed.

The long-term wave buoy measurements and newly developed coupled wave-circulation modelling system in the GoM provide us a unique opportunity to examine tidal modulations of surface waves, as well as the relevant physical processes controlling them in the region. The analysis of observational data is presented in the following section. The coupled wave-circulation modelling system is described in section 4.3. The comparison of model results with observations is presented in section 4.4. The examination of relevant physical processes controlling the tidal modulation in the region is provided in section 4.5. The summary and discussion are given in section 4.6.

4.2 Analysis of Observational Data

In-situ surface wave observations at four operational wave buoys (44027, 44005, 44018, and 44008) in the GoM (Fig. 1.1) are used in this study. They were 3-meter discus buoys operated by the National Data Buoy Center (NDBC). They were equipped with the AMPS (Advance Modular Payload System) payload (i.e. onboard processor) to acquire and transmit NDBC measurements. (See http://www.ndbc.noaa.gov/rsa.shtml for the system accuracy of the AMPS payload.) The buoy sensors were calibrated by the NDBC prior to deployment and replaced with calibrated instruments every two years. These buoys

reported hourly measurements of non-directional wave variables, i.e., the significant wave height (H_s), the peak wave period (T_p), and the average wave period, derived from the measured spectral wave density over a 20-minute acquisition period. Starting from 2007, buoys 44008 and 44018 have also reported directional wave data from which the mean wave directions θ_m were derived. Automated quality control procedures were used to ensure the accuracy of the NDBC measurements. The transmission parity error, range limit, time continuity and internal consistency checks were performed. See *NDBC* (2009) for more detailed information on the NDBC's quality control technique.

In-situ wind measurements were made at these operational buoys using the 4-blade, impeller-driven, wind-vane sensors (*NDBC*, 2009). Hourly wind vector data were reported based on time series of instantaneous wind samples taken at a minimum rate of 1 Hz measurements over an 8-minute acquisition period. Wind measurements underwent range, consistency, standard deviation, and gust-to-speed ratio checks. In-situ ocean current measurements were also made at buoys 44027 and 44008. However, these current measurements were sparse and only available for a few months, which limit their applicability in our study.

Direct water level measurements at these four buoys are not available. Instead, the tidal elevations predicted by the OSU Tidal Inversion System (OTIS) at these buoy locations are used in this study. The OTIS solutions used an inverse data assimilation approach to incorporate all different types of observed tidal data into a regional finite difference tidal model (*Egbert and Erofeeva*, 2002). Therefore, the OTIS solutions can be considered as a reanalysis of the two-dimensional tidal circulation, which is capable of providing reliable predictions of tidal surface elevations and depth-mean tidal currents in the study region.

Lastly, it should be noted that two buoys (44018 and 44005) underwent several considerable location changes since initial deployments (Table 4.1). In particular, since 2011, buoy 44018 has been relocated from (41.3°N, 69.3°W) to further northwest (42.2°N, 69.8°W). At this latter location, the observed tidal modulations of mean wave variables were found to be weaker than they were before. Considering the location changes of these buoys, the study period in this section is chosen to be the duration between January 2008

and December 2010.

Table 4.1: Location changes of four NDBC buoys.

44018		44008		44005		44027	
Date (mm/yy)	Lat./Lon.	Date (mm/yy)	Lat./Lon.	Date (mm/yy)	Lat./Lon.	Date (mm/yy)	Lat./Lon.
07/02-08/11	41.3/-69.3	08/82-10/08	40.5/-69.4	12/78-03/88	42.7/-68.3	05/03-now	44.3/-67.3
10/11-12/11	42.2/-69.8	11/08-now	40.5/-69.2	06/88-08/91	42.7/-68.6		
02/12-03/12	42.1/-69.6			01/92-01/94	42.6/-68.6		
04/15-now	42.1/-69.7			04/94-03/01	42.9/-68.9		
				03/01-12/10	43.2/-69.2		
				01/11-now	43.2/-69.1		

4.2.1 Spectral Content

Spectral analysis was performed by taking the fast Fourier transform of the demeaned and detrended 3-year H_s and wind speed time series at four buoys (Figs. 4.1a and b). The spectral estimates were smoothed using a Parzen window with a bandwidth of 0.104 cpd (cycles per day). Both the H_s and wind speed spectra at four buoys have large power at low frequencies corresponding to a period of 5-10 d, which is mainly associated with typical time scales of winter storms passing over the GoM. In addition, all the spectra of H_s feature sharp peaks at the semidiurnal tidal frequency (M_2) of 1.93 cpd. Because there are no corresponding peaks in the wind speed spectra, the results in Fig. 2a suggest the influence of tidal currents. The extra semidiurnal variance in the H_s spectrum is about 0.05 m^2 (corresponding to an average H_s modulation of 0.22 m) at buoy 44018, which is much larger than the 0.003 m^2 reported in a tidal channel of Western Canada by *Gemmrich and Garrett* (2012). It is also much larger than the extra semidiurnal variances (less than 0.006 m^2) calculated at the other three buoys in this study. In addition, different from *Gemmrich and Garrett* (2012) who found the signature of inertial currents in offshore wave records, there are no evident inertial peaks in all the spectra of H_s, indicating that inertial

motions are not significant at these buoy locations.

Figures 4.1c and d present the cross-spectra analysis of the H_s and tidal elevation time series. For all four buoys the coherences between these two time series at the semidiurnal frequency exceed 0.4, which are significantly different from zero at the 1% significance level (Fig. 4.1c). This confirms that the semidiurnal H_s peaks are mainly induced by the M_2 tide. The phase relationships between two signals (Fig. 4.2d) show different phase lags at the semidiurnal frequency at four buoys, indicating that the semidiurnal H_s peak could occur at different times (or phases) relative to the local tide. For example, a phase lag of about -50^o at buoy 44018 indicates that the maximum H_s occurred about 1.4 h after the maximum flood current or about 1.7 h before the slack tide. Thus, higher waves occur in the following tidal currents at this particular location, similar to those reported in previous studies (e.g., *Davidson et al.*, 2009; *Gemmrich and Garrett*, 2012). In the later part of the paper, a coupled wave-circulation modelling system is used to further examine this issue.

4.2.2 Temporal Variability

We next examine the observational data at buoy 44018 where the observed semidiurnal tidal modulations were the most significant among the four buoys. Figures 4.2a, c, and e present the 3-year H_s time series at this buoy. These figures demonstrate large seasonal variations of H_s associated with high sea states from October to April and low sea states from May to September. To examine the temporal variability of tidal modulation in H_s, we present in Figs. 4.2b, d, and f the time-evolving spectrum of H_s in the semidiurnal band calculated using Matlab's spectrogram function. Individual spectra were calculated from the H_s time series within 10-day time window with a 2.5-day increment. The semidiurnal power in the time-evolving spectrum changed with time, and strong tidal modulations occurred during high sea states (e.g., March, April, and November 2010). However, the magnitude of tidal modulation was not simply correlated with the H_s magnitude. In many cases the magnitudes of tidal modulation during high sea states were similar to those during low sea states. This suggests that different wave types (i.e., wind-sea and swell) might play an important role in the tidal modulation.

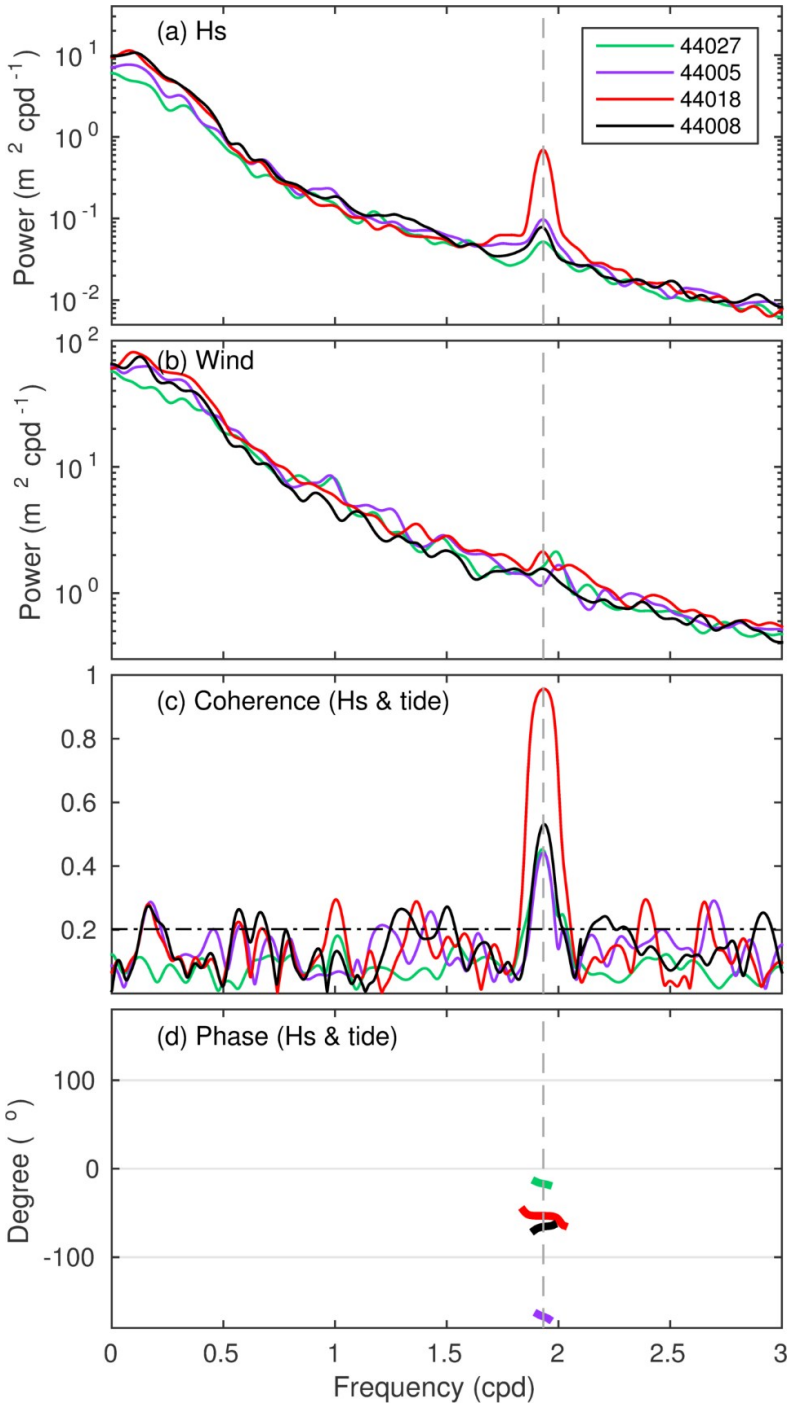

Figure 4.1: (a, b) Power spectra of observed time series of (a) significant wave heights and (b) wind speeds at four buoys in years 2008-2010. Cross-spectra analysis between time series of significant wave heights and tidal levels with (c) coherence (The dash-dotted line is the 1% significant level for zero coherence) and (d) phase (plotted for coherent points only). The vertical dashed lines in the four panels represent the semidiurnal tidal frequency.

We next examine the individual H_s oscillations during a selected low sea state period (August 2010) and a high sea state period (November 2010). To quantitatively distinguish the wind-seas and swells, we follow *Hanley et al.* (2010) and use the criteria based on the inverse wave age defined as:

$$A^{-1} = \frac{U_{10}\cos\theta_r}{C_p} \tag{4.1}$$

where $U_{10}\cos\theta_r$ is the projection of the 10-m wind velocity in the direction of wave propagation, θ_r is the relative angle between the winds and the waves, and C_p is the phase speed at the spectral peak defined as $C_p = gT_p/2\pi$. According to *Hanley et al.* (2010), surface waves start to grow by absorbing momentum from the wind when $A^{-1} > 0.83$, and fast moving waves start to impart momentum to the wind when $A^{-1} < 0.15$. Therefore, three wave types can be identified based on:

$$\begin{cases} Swell: & A^{-1} < 0.15 \\ Intermediate\ waves: & 0.15 < A^{-1} < 0.83 \\ Wind\ sea: & A^{-1} > 0.83 \end{cases} \tag{4.2}$$

Figure 4.3 presents time series of observed wind stress, H_s, T_p, θ_m, and values of A^{-1} calculated from the wave data at buoy 44018 in August and November 2010. The wind stress was converted from the observed wind speed using the bulk formula of Large and Pond (1981). Based on the values of A^{-1} shown in Figs. 4.3i and j, the surface waves were dominated by swells/wind-seas when the local wind was weak/strong. In August 2010 (except for times around 23 August), the local winds were relatively weak at buoy 44018, and the low-frequency (sub-tidal) variabilities at this buoy were characterized by relatively low values of H_s (less than 2.5 m), long wave periods (T_p) (larger than ~7 s), and stable wave propagation directions (70-190°, meteorological convention). These low-frequency variabilities in the surface waves during this period were associated mostly with swells forced by remote wind forcing. Around 23 August, a strong local wind event occurred and wind-sea was dominant with H_s up to 4.0 m and relatively short T_p of ~5.0 s. In November 2010, the low-frequency variabilities of surface wave variables were highly correlated with the local wind. The wave field was generally swell-dominated in the first

half of the month (before 18 November), with relatively longer T_p (larger than ~7 s) and stable wave directions. The wind-sea dominated in the last half of the month with shorter T_p (less than ~7 s) and dramatically changed wave directions.

In addition to the low-frequency variabilities discussed above, the observed surface wave variables shown in Figs. 4.3c-h also feature high-frequency oscillations (or modulations) at periods of nearly half a day during these two months. The amplitudes of the high-frequency (semidiurnal) oscillations in H_s can reach ~0.5 m, which is more than twice the average value (0.22 m) obtained from the spectral estimates of the 3-year H_s record. The amplitudes of the semidiurnal oscillations in T_p and θ_m can reach 3.0 s and 25^o, respectively. One interesting feature in November 2010 is that the semidiurnal oscillations in the observed surface waves were much stronger with swell-dominated surface waves in the first half of the month than those with wind-sea-dominated waves in the last half of the month. It is noted that the semidiurnal oscillations were also weak during the relatively strong wind event around 23 August when the wave field was dominated by wind-seas. This indicates that the semidiurnal oscillations of surface waves depend strongly on the wave type. The swell-dominated surface waves associated with relatively stable wave propagation directions are favorable for the generation of these semidiurnal oscillations induced by tidal currents. This conclusion is also found to be valid for other periods of the 3-year record.

To further examine the relationship between H_s and tides in the time domain, we consider time series of tidal elevation and H_s at buoy 44018 on 03-19 August 2010 shown in Figure 4.4. During this period with swell-dominated waves propagating northeastward to the inner Gulf (see Fig. 4.3g for wave directions), almost every tidal cycle was associated with a modulation of H_s. Moreover, a consistent phase relationship occurs between these two signals, with the maximum H_s modulation occurring during the flood tide (i.e., in the following tidal currents). These results are consistent with the spectral analysis presented in Figs. 4.1c and d.

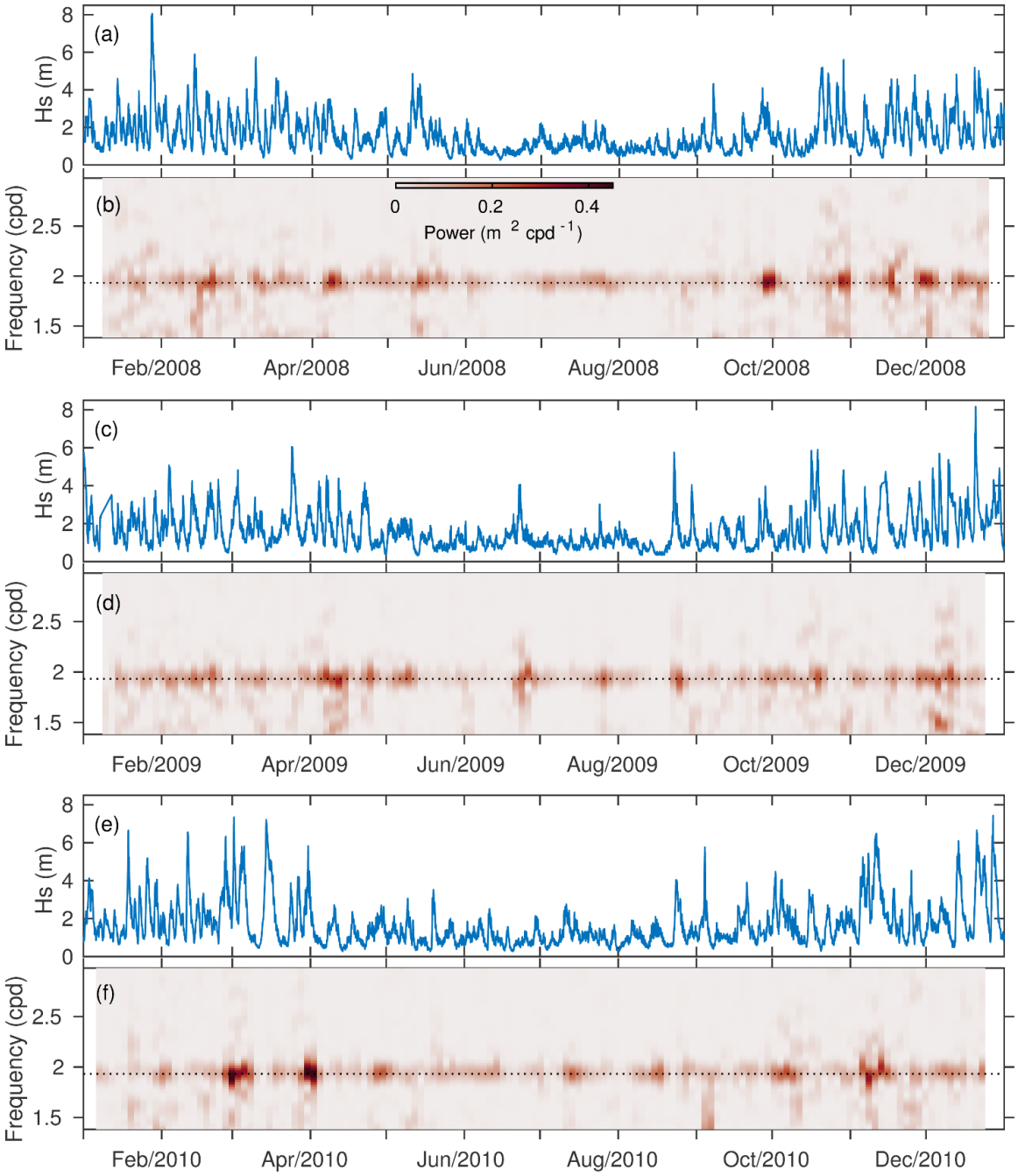

Figure 4.2: (a, c, e) Time series of observed significant wave heights (H_s) at buoy 44018 in years 2008-2010, and (b, d, f) corresponding time-evolving spectra in the semidiurnal band calculated from the H_s time series within 10-day time window with a 2.5-day increment. The dashed lines represent the semidiurnal tidal frequency.

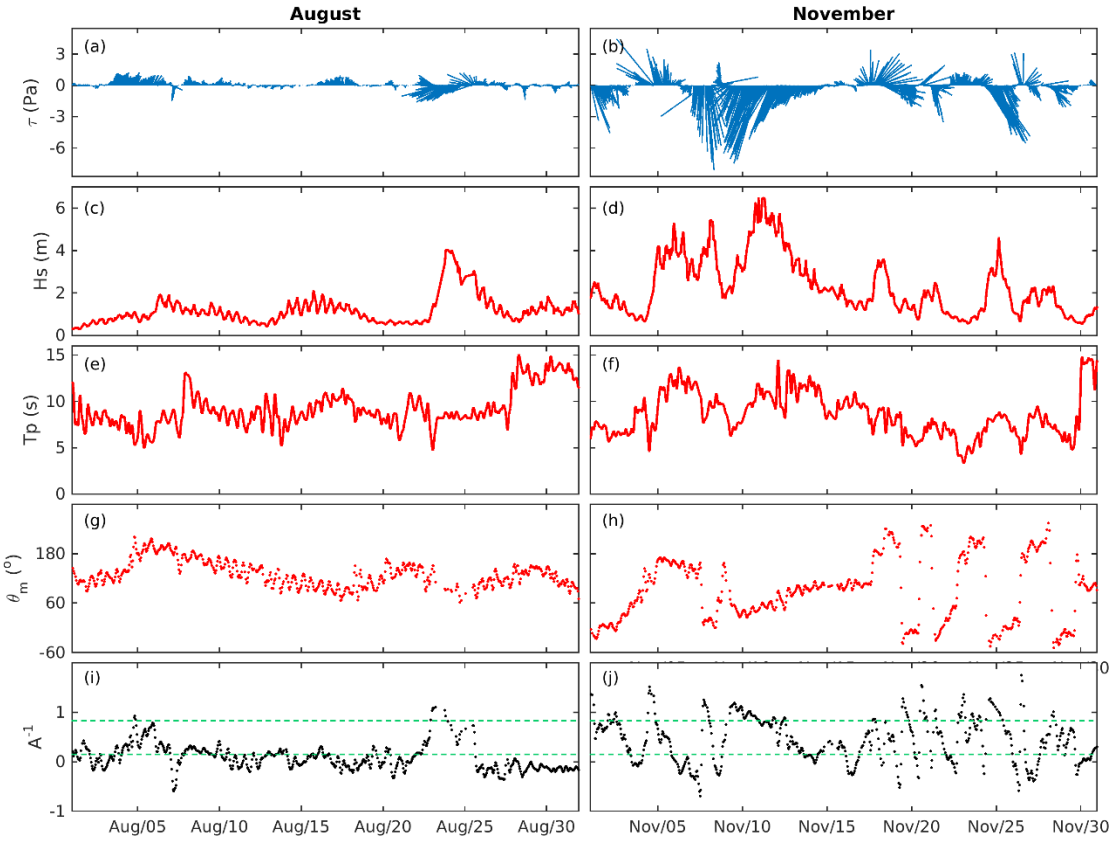

Figure 4.3: Time series of observed (a, b) wind stress, (c, d) significant wave height, (e, f) peak period, (g, h) mean wave direction, and (i, j) calculated inverse wave age at buoy 44018 in August and November 2010, respectively. Green dashed lines in (i) and (j) indicate two selected critical inverse wave age values for wind-seas (0.83) and swells (0.15) (Hanley et al. 2010).

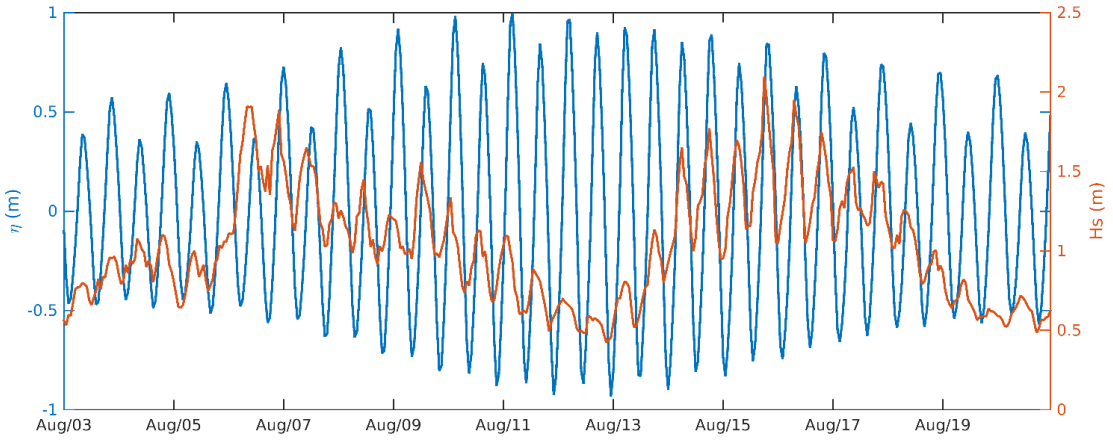

Figure 4.4: Time series of predicted tidal elevation (blue) superimposed time series of observed significant wave height (red) on 3-19 August 2010.

4.3 The Coupled Model and Experimental Design

The two-way coupled wave-circulation modelling system developed for the eastern Canadian shelf in Chapter 3 is used in this study. The coupled model consists of a 3D ocean circulation model known as DalCoast, and a third-generation surface gravity wave model known as WAVEWATCH III (WW3). The wave effects on the 3D circulation is specified in the circulation model using the vortex force formalism (*Bennis et al.*, 2011) and the breaking wave-induced mixing (*Craig and Banner*, 1994). In the wave model, the effects of ocean surface currents on surface waves are implemented through the wave action equation. These effects include the relative wind effect, current-induced convergence, wavenumber shift and refraction. A reader is referred to Chapter 3 for more information about the coupled model and model setup.

Two basic numerical experiments (Table 4.2) were conducted to examine the effects of tidal currents on ocean waves in the GoM, which include the coupled wave-circulation model run (Run_WaveCir, control run) and the wave-only model run (Run_WaveOnly) without the feedback from currents. Furthermore, four additional process-oriented experiments were conducted to quantify major mechanisms that affect the ocean waves in the study region. Four specific WCI mechanisms are considered in this study, which include (a) the relative wind effect, (b) current-induced convergence, (c) current-induced wavenumber shift, and (d) current-induced refraction. Model configurations and model forcing for six numerical experiments are summarized in Table 4.2.

Table 4.2: Model configurations for six numerical experiments.

Experiment	**Relative wind effect** $\boldsymbol{\alpha U}$ in the term of $(\mathbf{U_{10}} - \boldsymbol{\alpha U})$	**Current-induced convergence** $\mathbf{U}$ in Eq. 3.2	**Current-induced k shift** $\boldsymbol{k} \cdot \frac{\partial \mathbf{U}}{\partial s}$ in Eq. 3.3	**Current-induced wave refraction** $\boldsymbol{k} \cdot \frac{\partial \mathbf{U}}{\partial m}$ in Eq. 3.4
Run_WaveCir	On	On	On	On
Run_WaveOnly	Off	Off	Off	Off
Run_WaveU_{10}	On	Off	Off	Off
Run_WaveC_g	Off	On	Off	Off
Run_Wavek	Off	Off	On	Off
Run_Waveθ	Off	Off	Off	On

4.4 Comparison with Observational Data

The performance of the coupled model in simulating the tidal elevations and currents in the GoM has been found to be reasonable through a comparison of model results with the OTIS tidal solutions and ADCP measurements (not shown). The focus in this section is on the performance of the coupled model in simulating the surface waves in the GoM based on the model results in the control run (Run_WaveCir). To quantify the model performance, we follow *Thompson and Sheng* (1997) and use γ^2 defined in Eq. (2.18). Figure 4.5 presents time series of observed and simulated mean wave variables at buoy 44018. The wave-only model (Run_WaveOnly) reproduces reasonably well the observed sub-tidal variations of surface waves, with relatively low values of γ^2 for the H_s (0.19), T_p (0.66), and θ_m (1.02) at buoy 44018. The wave-only model, however, does not reproduce the observed tidal modulations at this buoy. The coupled model (Run_WaveCir, control run), by comparison, successfully reproduces the observed semidiurnal oscillation in the surface waves with smaller values of γ^2 for all mean wave variables (Table 3). The model-observation comparisons at the other three buoys (buoys 44005, 44008, 44027) yield the same conclusion as at 44018. The γ^2 values at the four buoys are listed in Table 4.3.

Figure 4.6 presents observed and simulated power spectra of H_s at the four wave buoys. As expected, the model results in Run_WaveOnly do not have the observed semidiurnal spectral peak at these four buoys. By comparison, the model results in Run_WaveCir reproduce very well the observed semidiurnal peak at four buoys in the two months. It is noted that some of the observed spectra (Figs. 4.6d, f and g) feature spectral peaks between diurnal and semidiurnal frequencies, which were not captured by the two model runs. The similar corresponding peaks were also found in the observed wind speed spectra but not in the spectra of local winds used by the model (not shown). Thus, the above-mentioned discrepancy is largely due to the deficiency in reanalysis winds used by the model.

Figure 4.7 presents observed and simulated directional wave spectra at buoy 44018 at four tidal phases that are maximum ebb at 1000Z, slack tide at 1300Z, maximum flood at

1600Z, and slack tide at 1900Z on 14 August 2010. The corresponding observed and simulated frequency-dependent mean wave direction and directional spread at these four tidal phases are also presented in Fig. 4.8. The observed spectra are relatively broad with large wave energy coming from northeast-southeast directions with frequencies of 0.10-0.15 Hz. From the maximum ebb to the second slack tide, the dominant wave directions first turned to the southeast and then turned to the east, and the dominant wave frequencies first moved to higher frequencies and then moved slightly to lower frequencies. In comparison, the coupled model (Run_WaveCir) reproduces reasonably well the observed movements of the spectrum in the directional-frequency space induced by tidal currents, which are completely missed in Run_WaveOnly. However, the simulated spectra provided by both model runs are relatively narrow, and the mean directional spread is underestimated by 8-30 degrees at frequencies of 0.10-0.15 Hz (Figs. 4.8e-h). This discrepancy is due in part to the deficiency in the reanalysis winds used to drive the model. The remaining discrepancy can be due to the imperfect model physics and observation errors. We note that the observed spectra are too smooth as the buoy only measures the first several components of the Fourier series (*Longuet-Higgins et al.*, 1963). Nevertheless, the inclusion of tidal currents is found to be able to improve the simulated directional spread by ~4 degrees at frequencies of 0.10-0.15 Hz during the ebb tide (Figs. 4.8e and f).

Table 4.3: Values of γ^2 for the wave height (H_s), peak period (T_p), and wave direction (θ) in two different model runs (Run_WaveCir and Run_WaveOnly) at four wave buoy stations in August and November, 2010.

Wave buoy		**44018**			**44008**			**44005**		**44027**	
Wave variables		H_s	T_p	θ	H_s	T_p	θ	H_s	T_p	H_s	T_p
Aug.	**Run_WaveCir**	0.13	0.62	0.90	0.12	0.42	0.47	0.20	0.61	0.28	0.58
	Run_WaveOnly	0.19	0.66	1.02	0.14	0.44	0.51	0.21	0.66	0.29	0.62
Nov.	**Run_WaveCir**	0.09	0.32	0.63	0.09	0.25	0.56	0.07	0.39	N/A	N/A
	Run_WaveOnly	0.11	0.36	0.71	0.10	0.27	0.62	0.08	0.40	N/A	N/A

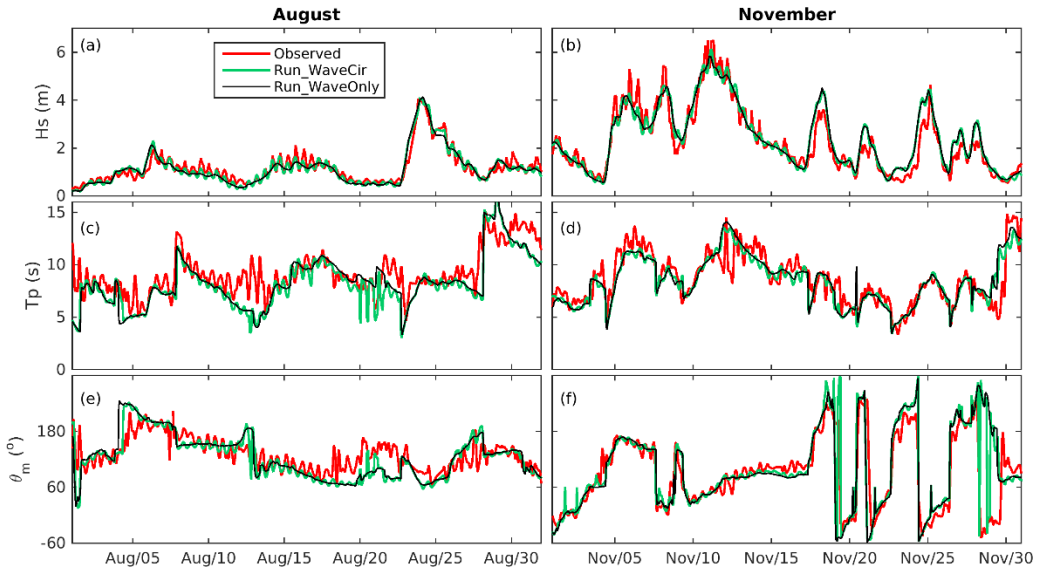

Figure 4.5: Time series of observed (red) and simulated (green and black) (a, b) significant wave heights, (c, d) peak wave periods, and (e, f) mean wave directions at buoy 44018 in August and November 2010, respectively.

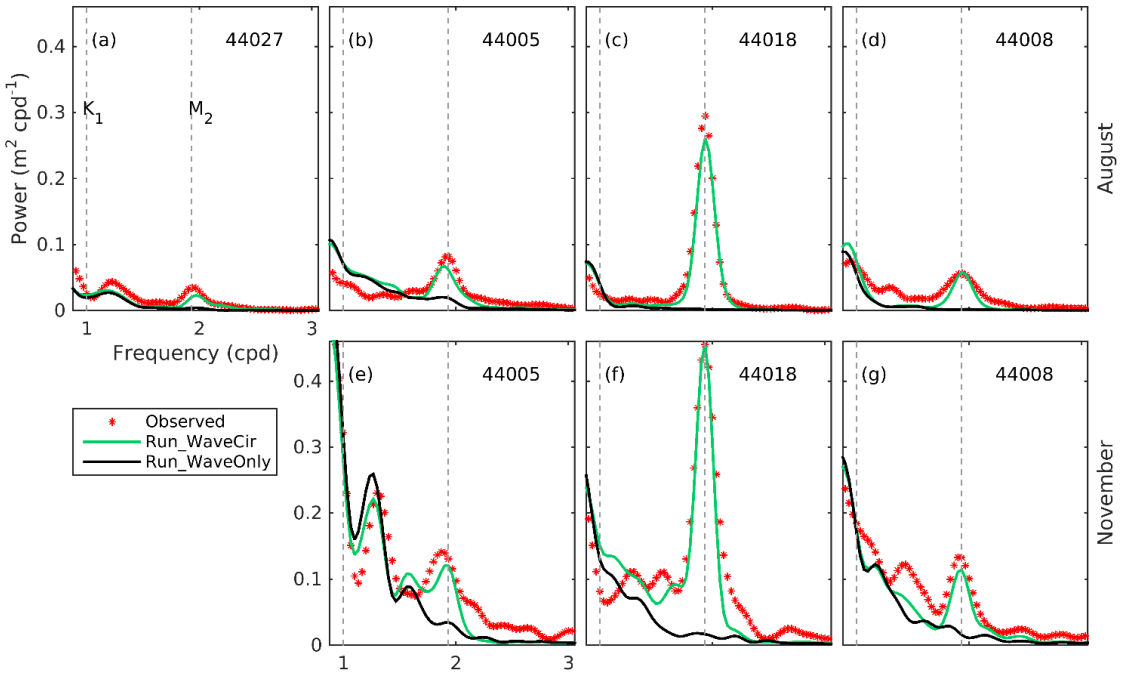

Figure 4.6: Observed (red) and simulated (green and black) power spectra of the wave height time series at four wave buoy sites in (a-d) August and (e-g) November 2010, respectively.

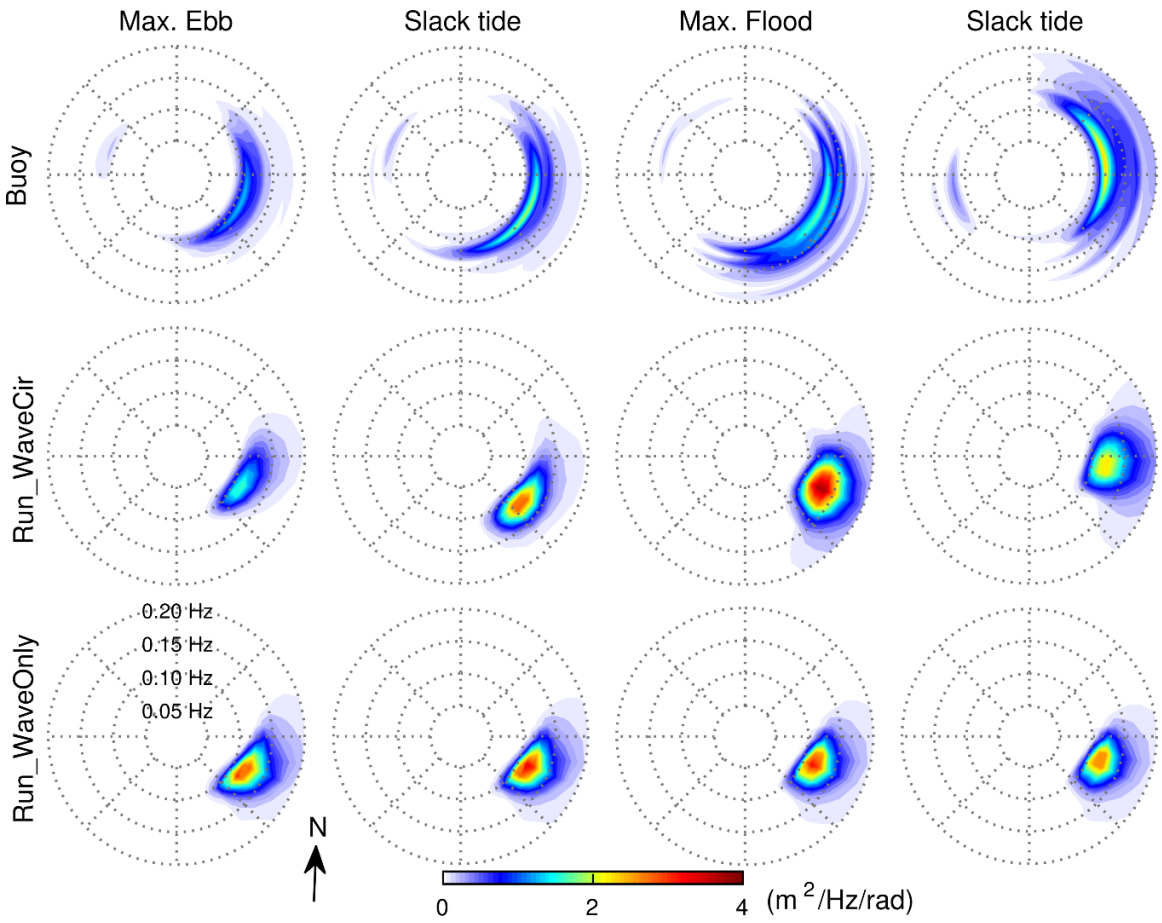

Figure 4.7: Observed (top panel) and simulated (middle and bottom panels) directional wave spectra at four typical tidal phases at buoy 44018 on 14 August 2010. The color scales represent spectral density, and the dashed circles correspond to frequencies of 0.05, 0.10, 0.15, and 0.20 Hz. Wave directions are defined using the meteorological convention that "N" means "coming from north".

4.5 Process-Oriented Studies

The numerical model results in six numerical experiments listed in Table 4.2 (including the control run, wave-only model run, and four process-oriented model runs) are used in this section to examine the major WCI mechanisms controlling the tidal modulations of surface waves in the GoM. Figure 4.9 presents time series of simulated mean wave variables at buoy 44018 on 10-17 August 2010 in five different runs. Three major controlling mechanisms are identified for the tidal modulation in H_s (Fig. 4.9a): current-induced

convergence, refraction, and wavenumber shift. The modulations of H_s induced by the three mechanisms, however, have different amplitudes and phases relative to overall H_s modulation in the control run. Another interesting feature is that the H_s modulation induced by the refraction show noticeable temporal changes from 10-13 to 14-17 August relative to those in the control run. It is noted that during this period the mean wave directions change approximately from the south (140-160^o) to the east (60-100^o). This indicates that the refraction-induced H_s modulation can be strongly affected by the wave propagation direction. The mechanisms controlling the tidal modulations in T_p and θ_m are less complex than those in H_s. A comparison of model results in different runs (Figs. 4.9b and c) demonstrates that the modulation in T_p is mainly due to wavenumber shift as expected in Eq. (3.3), and the modulation in θ_m is mainly due to refraction as expected in Eq. (3.4). It should be mentioned that the relative wind effect is small in this case for swell-dominated waves (not shown). Model results during other periods yield the same conclusion at this buoy location, but contributions of different mechanisms to the tidal modulation in H_s differ over different areas in the GoM as we will show later.

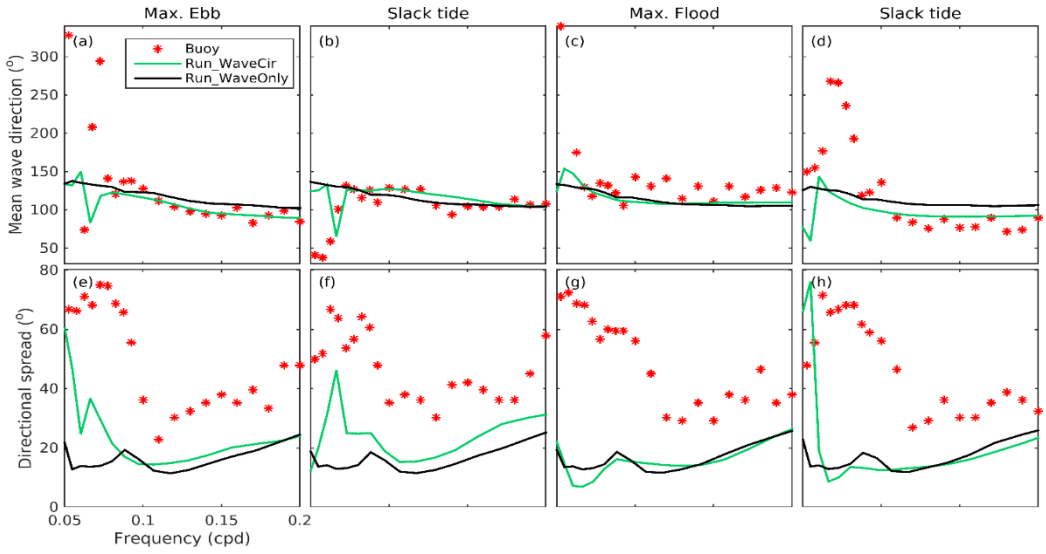

Figure 4.8: Observed and simulated (a-d) frequency-dependent mean wave direction, and (e-h) directional spread at four typical tidal phases at buoy 44018 on 14 August 2010.

Figure 4.10 presents distributions of amplitudes of tidal modulations in H_s in August 2010. The amplitude is calculated as the square root of the differences in semidiurnal H_s variance between Run_WaveCir (or process-oriented model runs) and Run_WaveOnly. The semidiurnal H_s variance is defined as the integral of the spectrum between two cut-off frequencies of the semidiurnal peak. Figure 4.10a shows that the amplitude in the control run reaches its maximum over areas just north of GB where buoy 44018 was located, and decreases towards the inner Gulf. The amplitude is also relatively large over the southern flank of GB and western Scotian Shelf where there are strong current gradients. By comparison, the amplitude is relatively small on GB where the tidal currents are strongest. Process-oriented experiments demonstrate that the convergence effect (Fig. 4.10b) mainly contributes to the H_s modulation over the northern and southern flanks of GB. The distribution of amplitude due to wavenumber shift (Figs. 4.10c) is similar to that due to advection, except for smaller magnitudes. Different from the other two mechanisms, the refraction effect (Fig. 4.10d) mainly contributes to the H_s modulation on GB and over areas just north of GB.

We next investigate how the three major controlling WCI mechanisms contribute to the tidal modulation of H_s by examining distributions of percentage changes in H_s between three process-oriented model runs and Run_WaveOnly in two special events with northward (event A, Fig. 4.11a-b) and westward (event B, Fig. 4.11c-d) propagating surface waves respectively.

4.5.1 Current-Induced Convergence

The current-induced convergence modulates the significant wave height (H_s) by modifying the propagation velocity vector of wave energy (see Eq. (3.2)), and its effect depends on the spatial gradients of currents. During event A at the maximum flood (Fig. 4.11e), the model results associated with this mechanism show significant energy convergence (up to 14%) over the northern flank of GB and western Scotian Shelf, and noticeable energy divergence over the southern flank of GB. These energy convergence/divergence zones are associated with strong spatially deaccelerating/accelerating tidal currents. The convergence effect for this event is similar

to the depth-induced wave shoaling, with surface waves and currents propagating nearly in the same direction. If directions of waves and currents are different (e.g., event B), the convergence effect can also change the propagation direction of wave energy. Figure 4.11g shows that the result in event B at the maximum flood is very similar to that in event A. Additional numerical experiments with southward and eastward propagating waves (not shown) show similar results to those in events A and B. This indicates that the convergence effect is less affected by the wave propagation direction, and it is mainly determined by the spatial structure of currents.

Three hours later (i.e., slack tide), the model results for events A and B (Figs. 4.11f and h) show respectively northward and westward propagations of the tidal modulation in H_s produced at the maximum flood. The propagation distance is ~50 km, and the estimated speed is ~5 m/s. The latter is comparable to the typical magnitude of $\mathbf{c}_g$ for a 6.5-s period wave over this area. This indicates that, during the slack tide, the effects of local tidal currents become relatively weak, and the tidal modulation in the Gulf is mainly a spatial propagation of that generated during flood tide.

To further interpret the model results, we use analytical results for unidirectional, monochromatic linear waves by ignoring wave generations and dissipations. Considering a deep water surface wave propagating from a region 1 with currents of magnitude U_1 to a region 2 with currents of magnitude U_2, the equality of action fluxes gives,

$$\frac{E_1}{\sigma_1}(C_{g1} + U_1) = \frac{E_2}{\sigma_2}(C_{g2} + U_2) \tag{4.3}$$

which gives the change in H_s

$$\frac{H_{s2}}{H_{s1}} = \left(\frac{E_2}{E_1}\right)^{1/2} = \left(\frac{\sigma_2}{\sigma_1}\frac{C_{g1}+U_1}{C_{g2}+U_2}\right)^{1/2} \tag{4.4}$$

Eq. (4.4) is identical to that derived by *Longuet-Higgins and Steward* (1961) based on the wave energy balance equation in the case with the convergence of U balanced vertically. *Longuet-Higgins and Steward* (1961) also considered a second case with the convergence of U balanced laterally, and showed that the solution is (4.4) multiplied by a factor of $\frac{C_{g2}}{C_{g1}}$.

In this study, since the major current gradients occur approximately in the north-south direction over GB and the lateral variation of tidal currents is relatively small, we can use Eq. (4.4) to illustrate our model results. It is noted that the changes in σ and C_g are due to the current-induced wavenumber shift as we will discuss later. Considering only the convergence effect (i.e., $\sigma_2 = \sigma_1$, $C_{g2} = C_{g1}$), Eq. (4.4) gives a factor of $(\frac{C_{g1}+U_1}{C_{g1}+U_2})^{1/2}$. Considering a 6.5-s period wave ($C_{g1} \approx 5$ m/s) propagating from GB ($U_1 \approx 1$ m/s) to the area just north of GB (similar to event A at the maximum flood, $U_2 \approx 0$ m/s), the estimated percentage change in H_s is ~10%, which explains most of those (10-14%) produced by the model over the northern flank of GB (Fig. 4.11e). The differences between the above theoretical estimates and the model results can be due to the unsteadiness of tidal currents. For example, the typical propagation time of surface waves over GB is about 5.5 h, which is not small in comparison with the period of M_2 tidal currents (~12.4 h). Thus, surface waves propagating across GB are subject to subsequent modulations by different current fields at different tidal phases. However, since most of the H_s modulation can be explained by the solution in the steady situation, the time-dependence of tidal currents is expected to play a minor role in the tidal modulation over this region.

4.5.2 Current-Induced Wavenumber Shift

The effect of current-induced wavenumber shift depends on the spatial gradients of currents in the propagation directions of surface waves (see Eq. (3.3)). Since the current-induced wavenumber shift induces change in $\dot{k}$ that is associated with a change in σ and $\mathbf{c}_g$, it can modify H_s through two processes (*Ardhuin et al.*, 2017): an exchange of energy between waves and currents (i.e., the radiation stress effect) due to the change in σ, and energy bunching/stretching (similar to wave shoaling) due to the change in $\mathbf{c}_g$. The effects of both processes decrease (increase) H_s for the case of waves propagating into spatially accelerating (deaccelerating) currents. During event A, the model results at the two tidal phases (Figs. 4.11i-j) show a clear northward propagation of tidal modulations in H_s. The maximum tidal modulation is generated over the northern/southern flanks of GB at the maximum flood, due to strong tidal current gradients in the north-south direction. By comparison, the model results in event B (Figs. 4.11k-l) show a westward propagation of

tidal modulations, with noticeable increases of H_s generated around the mouth of the GoM at the maximum flood due to strong tidal current gradients in the east-west direction. Thus, different from the convergence effect, the current-induced wavenumber shift varies with the wave propagation direction. In particular, in the case of surface waves travelling perpendicular to the direction of tidal currents over GB at the maximum flood, model results show that the effect of the current-induced wavenumber shift becomes negligible (not shown).

We also use the analytical results in section 4.5.2 to interpret the model results. From Eq. (4.4), the factor for the change in H_s due to wavenumber shift is $(\frac{\sigma_2}{\sigma_1}\frac{C_{g1}}{C_{g2}})^{1/2}$, which is approximately equal to σ_2/σ_1 given $C_g = g/2\sigma$. The solution is found to be $\sigma_2/\sigma_1 = (1 + \frac{U}{2C_{g1}})$ (*Ardhuin*, 2018) based on the conservation of the number of wave crests. Using the same example discussed in section 4.5.2 ($C_{g1} \approx 5\ \mathrm{m/s},\ U \approx 1\ \mathrm{m/s}$), the estimated percentage change in H_s due to wavenumber shift is ~10%, which is similar to those (8-10%) produced by the model over the northern flank of GB during event A (Fig. 4.11i). Thus, the tidal modulation in H_s due to wavenumber shift is mostly explained by the spatial variation of currents.

4.5.3 Current-Induced Refraction

The current-induced refraction effect depends on the gradients of currents along the wave crest direction (see Eq. (3.4)). The basic effect of this mechanism is to turn surface waves towards the area with lower absolute propagation speeds (i.e., relative to the fixed bottom). Thus, during event A at the maximum flood (Fig. 4.11m), surface waves propagating over GB are refracted to the east and west parts of GB associated with lower tidal current speeds. While during event B (Fig. 4.11o), surface waves are refracted to the north and south sides of GB, resulting in significant decrease of H_s (up to 20%) on GB and noticeable increase of H_s (~14%) over areas north of GB. It is noted that the current-induced refraction effect is much more significant for event B than event A, because the tidal current gradients in the north-south direction are much larger than those in the east-west direction around GB. It is also noted that, during event B over the western Scotian Shelf, surface waves gradually

turn to northward, and they are refracted to further west due to the strong tidal current gradients in the east-west direction, resulting in significant decrease of H_s on the western Scotian Shelf and noticeable increase of H_s further west. Similar to the other two mechanisms, the refraction-induced H_s modulation during the slack tide (Figs. 4.11n and p) is mainly a spatial propagation of that generated during flood tide (Figs. 4.11m and o).

Overall, the above analyses demonstrate that the significant effects of all three current-induced mechanisms depend on the strong gradients of tidal currents near the mouth of the GoM, particularly around GB. Furthermore, the modulations of H_s due to convergence are less affected by the wave propagation direction, while those due to wavenumber shift and refraction vary with the changes in wave propagation direction. Therefore, the distribution of tidal modulation in H_s over the GoM is not fixed in time and space, and the combined effects of all three mechanisms in the tidal modulation (Fig. 4.11q-t) could reach 25% over areas north of GB. In addition, the above analyses also demonstrated that the observed maximum H_s modulation during the flood tide (i.e., in the following tidal currents) at buoy 44018 can be mostly explained by the tidal current-induced convergence and wavenumber shift associated with wave energy convergence and energy transfer from tidal currents to surface waves in spatially deaccelerating tidal currents (e.g., Figs. 4.11e and i, Figs. 4.11g and k). Although the refraction effect also contributes the overall H_s modulation at this particular location, this effect does not significantly change its phase due to the dominate effects of the other two mechanisms.

4.5.4 Current-Enhanced Wave Dissipation

The effects of current-enhanced wave dissipation on the tidal modulation of H_s is not easily separated from other mechanisms, since the current-enhanced wave dissipation is implicitly implemented in the model (*Tolman et al.,* 2014). For simplicity of discussion, we consider time series of the calculated wave dissipation term S_{ds} in Run_WaveOnly and Run_WaveCir at buoy 44018 in the second half of August 2010 shown in Fig. 4.12a. Wave dissipation is shown to be only significant around 23 August during a strong wind event. In comparison with Run_WaveOnly, model results in Run_WaveCir demonstrate a significant tidal modulation of S_{ds} around 23 August, which correlates with the tidal

modulation of H_s (Fig. 4.12a). Furthermore, distributions of differences in wave dissipation (ΔS_{ds}) between Run_WaveCir and Run_WaveOnly at two selected maximum floods also correlate with those of ΔH_s (comparing Figs. 4.12b with c, and Figs. 4.12d and e), particularly over areas north of GB. The correlation of ΔS_{ds} with ΔH_s in both space and time suggests that the current-enhanced dissipation could reduce the magnitudes of H_s modulation during this strong wind event.

To estimate how much of the tidal modulation in H_s is reduced by the current-enhanced dissipation, we compare the model results between two selected maximum flood tides. Figures 4.12b and d show that the current-enhanced dissipation (ΔS_{ds}) over areas north of GB at the first flood is much more significant than that at the second flood. As a result, the magnitudes of increased H_s (ΔH_s) over areas north of GB at the first flood are only about half of those at the second food (Figs. 4.12c and e). This indicates that at least half of the tidal modulation in H_s is eliminated by the current-enhanced dissipation at the first flood.

4.6 Summary and Discussion

This study examined the tidal modulation of surface gravity waves in the Gulf of Maine (GoM) based on in-situ observations and numerical model results produced by a coupled wave-circulation modelling system. Analysis of observational data demonstrated significant semidiurnal tidal modulations in the mean surface wave variables (i.e., significant wave height H_s, peak wave period T_p, and mean wave direction θ_m) in the region. The amplitudes of tidal modulations in H_s, T_p, and θ_m can reach about 0.5 m, 3.0 s, and 25^o, respectively. The observed tidal modulation features significant spatial-temporal variabilities, with large amplitudes near the mouth of the GoM, particularly during high sea states. The favorable conditions for tidal modulations in the region were found to be swell-dominated surface waves associated with relatively stable wave propagation directions. In addition, the phase relation between tide and H_s demonstrates an unusual timing of the maximum H_s modulation in the following tidal currents at buoy 44108 located north of Georges Bank (GB).

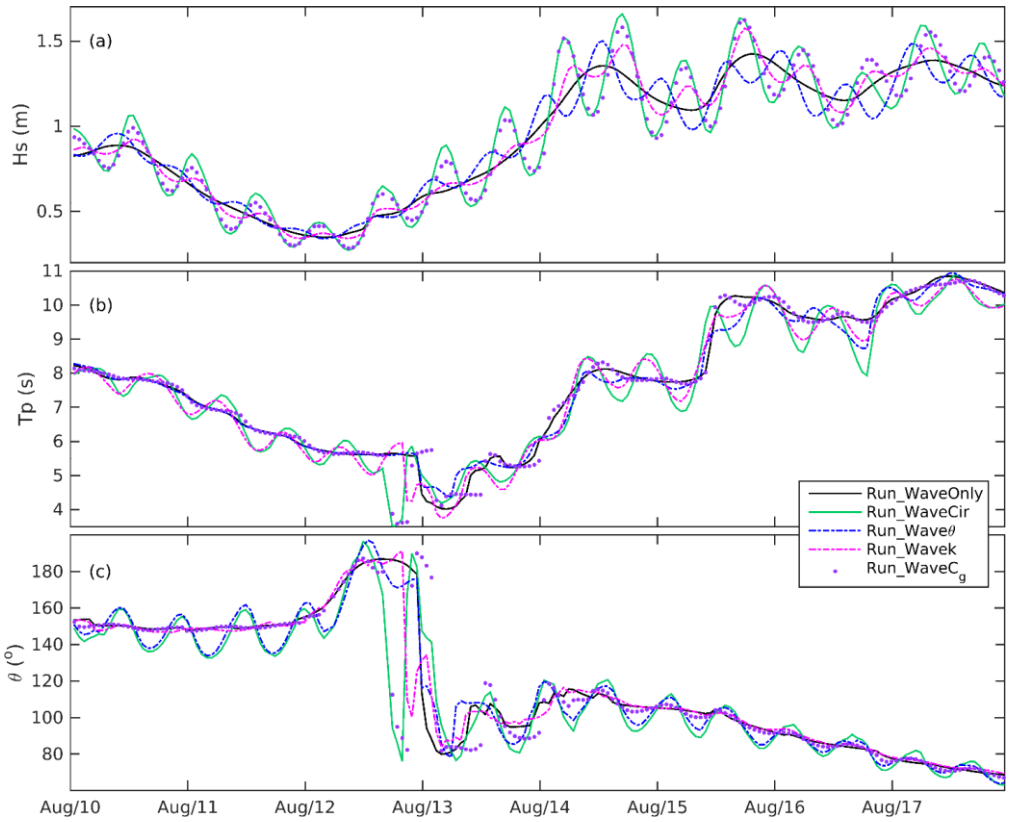

Figure 4.9: Time series of (a) significant wave heights, (c) peak periods, and (d) mean wave directions at buoy 44018 on 10-17 August 2010 in five different numerical experiments.

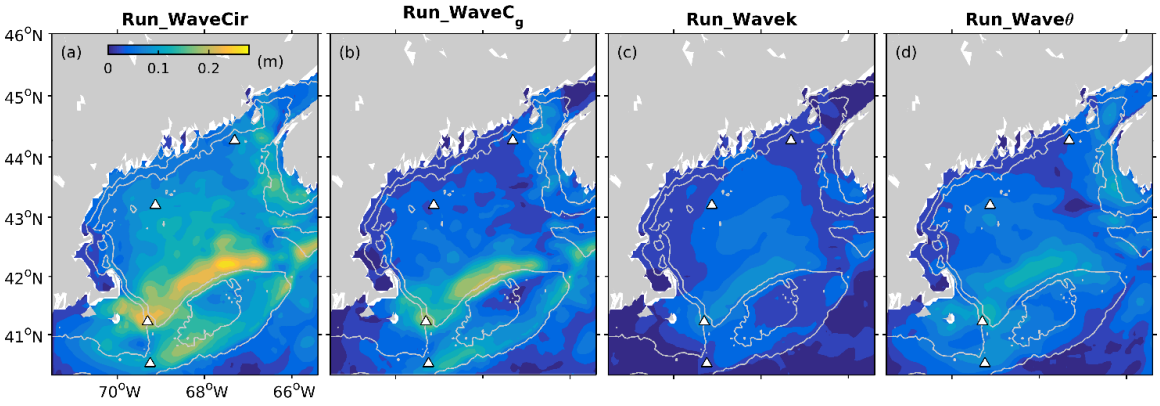

Figure 4.10: Amplitudes of semidiurnal tidal modulations in significant wave heights in four different numerical experiments in August 2010. The contour lines indicate the 50 m and 100 m isobaths. The triangles denote wave buoy locations.

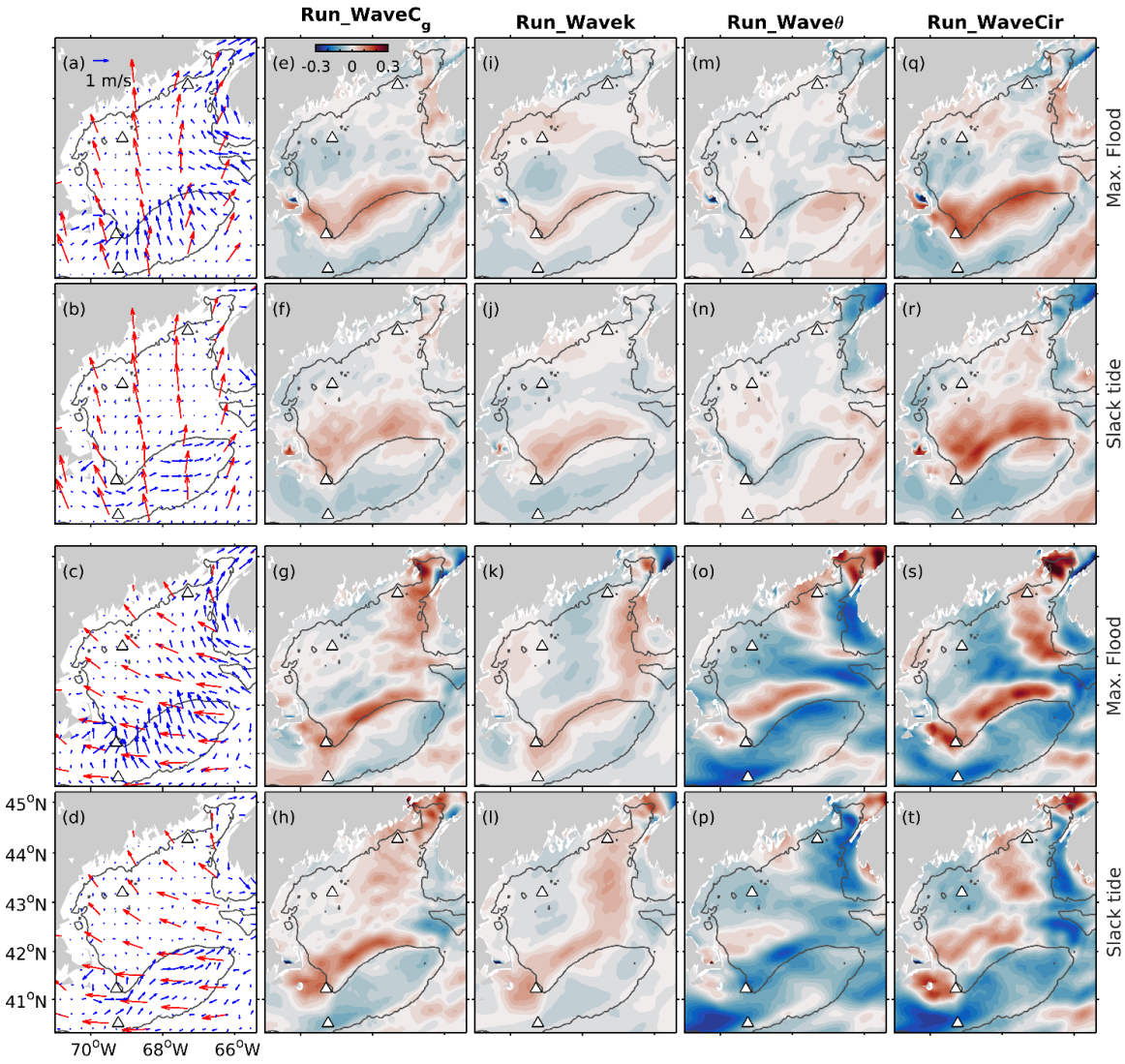

Figure 4.11: The ocean surface current vectors (blue arrows) and surface wave vectors (the length and direction of the wave vectors represent the mean wave length and direction, respectively) (red arrows) produced by Run_WaveCir at (a, c) the maximum flood and (b, d) subsequent slack tide (a, b) during event A with the northward propagating waves and (c, d) during event B with westward propagating waves, respectively. Differences (image) in significant wave heights (e-h) between Run_WaveC_g and Run_WaveOnly, (i-l) between Run_Wavek and Run_WaveOnly, and (m-p) between Run_Waveθ and Run_WaveOnly, (a-t) between Run_WaveCir and Run_WaveOnly at the maximum flood and subsequent slack tide during two events with northward (upper two panels) and westward (lower two panels) propagating waves. The contour lines indicate the 100 m isobaths, and the triangles denote wave buoy locations.

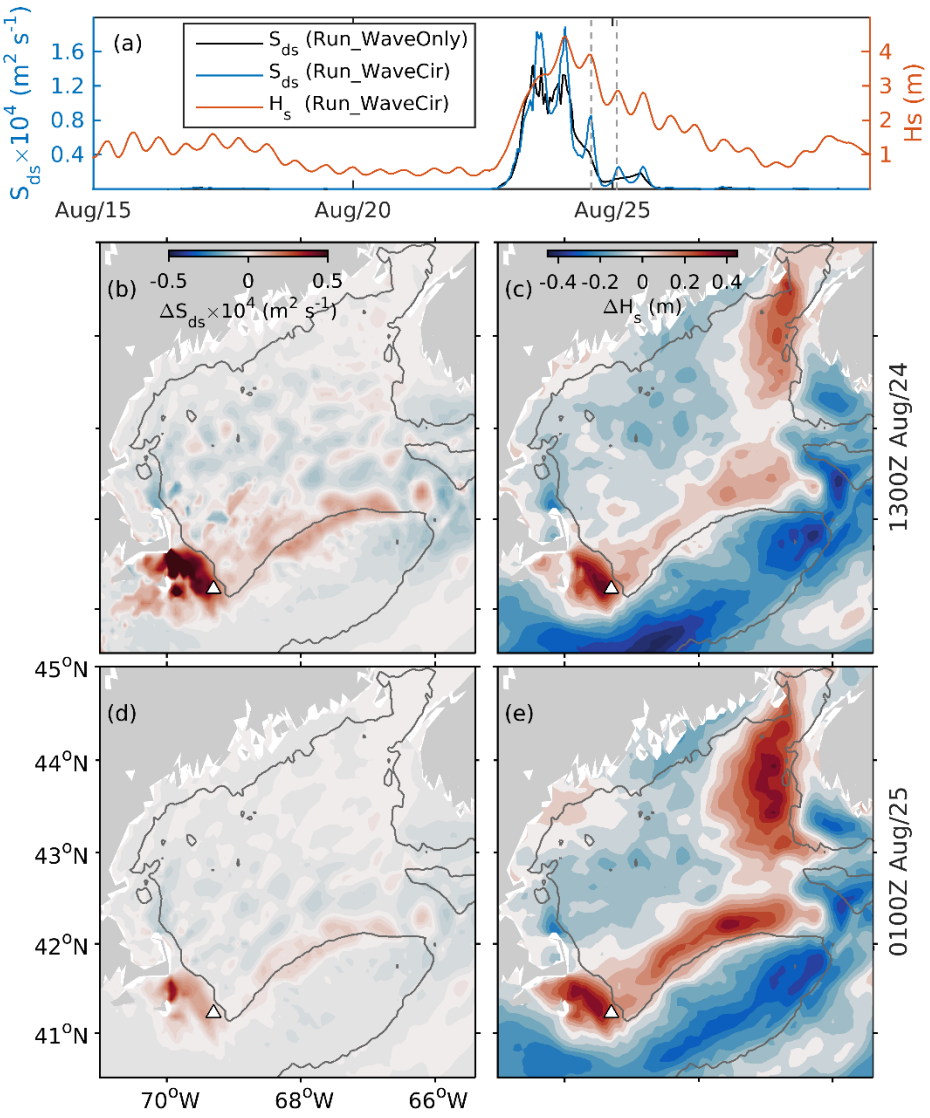

Figure 4.12: (a) Time series of simulated wave dissipations S_{ds} in Run_WaveOnly and Run_WaveCir at buoy 44018 (triangles in (b-e)), overlaid with time series of simulated significant wave height H_s in Run_WaveCir. Differences in (b, d) S_{ds} and (c, e) H_s between Run_WaveCir and Run_WaveOnly at the two selected maximum flood tides marked by two gray dashed lines in (a). The contour lines in (b-e) indicate the 100 m isobaths.

The coupled wave-circulation modelling system successfully reproduces the observed tidal modulation and associated spatial-temporal variabilities in the GoM. Model results demonstrate that tidal modulations in the GoM are mainly due to the strong horizontal

gradients of tidal currents near the mouth of the GoM, particularly around GB and western Scotian Shelf. The maximum tidal modulations in H_s (up to 25%) are first generated during the flood/ebb tide when the gradients of tidal currents are strongest, and then propagate to the inner gulf. Process-oriented numerical experiments demonstrate that the observed tidal modulation is associated with the current-induced convergence, refraction, and wavenumber shift, which contribute differently to the overall tidal modulation in H_s by modifying the propagation velocity vector of surface wave energy, the wavelength, and the wave direction, respectively. The significant effects of all three current-induced mechanisms depend on the strong current gradients near the mouth of the GoM. The tidal modulations of H_s due to convergence are less affected by the wave propagation direction, and feature relatively large effects (10-14%) over the northern/southern flanks of GB. By contrast, the tidal modulations of H_s due to wavenumber shift (7-10%) and refraction (5-20%) vary with the changes in the wave propagation direction. Thus, the distribution of overall tidal modulation in H_s in the GoM is not fixed in space and time depending on the wave propagation direction. In addition, the current-enhanced dissipation was found to become important during high winds, which could reduce at least half the H_s modulation over areas north of GB.

Model results also demonstrate that the observed unusual timing of the maximum tidal modulation in H_s at buoy 44018 in the following tidal flows can be mostly explained by the current-induced convergence and wavenumber shift. This is associated with an energy convergence and an energy transfer from currents to waves in spatially deaccelerating tidal currents during flood tide.

The results presented in this chapter highlight the important role of the spatial structure of currents, which is usually not available in previous analysis of tidal modulation of surface waves at a single wave buoy (e.g., *Gemmrich and Garrett*, 2012; *Vincent*, 1979). The spatial structure of ocean currents can be provided by numerical models, high-frequency radar or satellite observations. Our findings can also be readily applied over other regions with shallow oceanic banks, usually associated with strong tidal currents. For an example, the causes for the observed increase of H_s in the following tidal currents at buoy 46145 in *Gemmrich and Garrett* (2012) can be similar to those at buoy 44018 in this

study. This is because that buoy 46145 located ~30 km east of Learmonth Bank, and spatially deaccelerating tidal currents are expected to occur at this location during flood tide (https://www.ndbc.noaa.gov/station_page.php?station=46145). Furthermore, it is important to include tidal currents as input parameters in the wave model, which is usually neglected in many today's operational wave forecast models. For example, the wave forecasts issued by the Environmental Canada neglect wave-current interactions, and this could lead to large forecast errors over areas with strong spatial variability of tidal currents.

CHAPTER 5

MODULATION OF NEAR-INERTIAL OSCILLATIONS BY LOW FREQUENCY CURRENT VARIATIONS ON THE INNER SCOTIAN SHELF[1]

5.1 Introduction

Near-inertial oscillations (NIOs) are ubiquitous throughout the ocean. They are associated with strong vertical shear and so contribute to upper-ocean mixing (e.g., *Zhai et al.*, 2009; *Jochum et al.*, 2013). The downward flux of near-inertial energy associated with NIOs is also thought to contribute to diapycnal mixing in the deep ocean (*Jing and Wu*, 2014; *Alford et al.*, 2016). The classical mechanism for the generation of wind-driven NIOs includes two stages. During the first (short) stage, a storm passing overhead generates currents in the surface ocean mixed layer. During the second (longer) stage, these currents undergo "Rossby adjustment" and NIOs are generated. *Gill* (1984) used vertical modes method to study the wind-driven NIOs in the ocean with a flat bottom. In this case, the frequency squared of near-inertial waves for mode n is $\omega_n^2 = f^2 + c_n^2 l^2$ (where f is the planetary vorticity, c_n is the eigenvalue for the nth mode, and l is the horizontal wavenumber). As the horizontal extent of the NIOs is limited by the pattern of the wind and the proximity of the coast, the frequency of NIOs is expected to exceed f. At the base of the mixed layer, near-inertial internal gravity waves are generated through the horizontal convergence and divergence of the mixed layer ("inertial pumping", *Gill*, 1984). *Zervakis and Levine* (1995) noted that near-inertial energy can propagate downward into deeper water as low modes

[1] Wang, P., Z. He, K. R. Thompson, and J. Sheng. 2018. Modulation of near-inertial oscillations by low frequency current variations on the inner Scotian Shelf. Submitted to *Journal of Physical Oceanography*.

leave the generation area. The resulting frequency changes at a fixed point are a complicated combination of contributions from each mode. *Zervakis and Levine* (1995) also noted that the typical mixed layer frequency is about 1.005 f and the frequency increases with depth. On a β plane, the near-inertial waves with $\omega > f$ can propagate horizontally poleward until they reach the turning latitude (*Anderson and Gill*, 1979; *Gill*, 1984). Alternatively, the near-inertial waves generated near their turning latitudes can propagate equatorward and vertically downward until they reach the seafloor with their frequencies exceeding the local f (order of 10% of f at midlatitudes, *Garret*, 2001). At the seafloor, these waves can be further reflected equatorward until their frequency becomes $2f$ and decay by parametric subharmonic instability (*Nagasawa et al.*, 2000).

In addition to the β effect, low-frequency flows can influence the generation and propagation of NIOs. In a seminal paper, *Kunze* (1985; see also *Mooers*, 1975) showed that the effective inertial frequency (f_e) of NIOs can be modified by a low-frequency flow as follows:

$$f_e \approx f + \zeta/2 \tag{5.1}$$

where ζ is the relative vorticity. The frequency shift of $\zeta/2$ has been observed to influence the generation of NIOs in regions where the diurnal wind forcing period matches f_e (*Mihanovic et al.*, 2016). Once generated, trapping and amplification of propagating NIOs can occur in regions of negative vorticity (*Kunze*, 1985). This has been confirmed by observations of elevated near-inertial energy in anticyclonic eddies (*Elipot et al.*, 2010). These anticyclonic eddies can transfer the near-inertial energy to the deep ocean through the so-called "inertial chimney" effect (e.g., *Zhai et al.*, 2005, 2007). Horizontal advection of NIOs by large-scale geostrophic flows, such as the Gulf Stream, can also play a role in redistributing near-inertial energy (*Zhai et al.*, 2004), and nonlinear interactions between NIOs and low-frequency flows can lead to an exchange of energy (e.g., *Müller*, 1976; *Whitt and Thomas*, 2015; *Jing et al.*, 2017). For example, in the Kuroshio Extension region, the efficiency of energy exchange in anticyclonic eddies is about twice that of cyclonic eddies due to the frequency shift by the relative vorticity (*Jing et al.*, 2017).

Equation (5.1) has been validated in the Tropical Pacific (*Poulain et al.*, 1992) and the

global ocean (*Elipot et al.*, 2010) based on analyses of observed surface drifter tracks. Both of these open ocean studies focused on frequency modulation of the inertial frequency in regions with energetic mesoscale eddies. Equation (5.1) has also been validated closer to coastal boundaries. For example, *Mihanovic* et al. (2016) showed that changes in the Leeuwin Current off southwest Australia can modulate f_e by more than 50%. *Shearman* (2005) found that the strong relative vorticity associated with the shelf break front off New England can cause a significant reduction in the peak frequency of NIOs. *Bondur et al.* (2013) found that the background currents on the Hawaii Shelf could induce strong variations of f_e, leading to the anomalous counter-clockwise rotation of NIOs in this region.

This study focuses on the inner half of the Scotian Shelf off the east coast of Canada. This region features a persistent southwestward coastal jet (the Nova Scotia Current, NSC), which has peak surface speeds reaching 0.3 m/s centered at approximately 45 km from the coast. The NSC varies on time-scales of days to seasons (*Petrie*, 1987; *Dever et al*., 2016) and occasionally meanders in the alongshore direction with a mean wavelength of ~50 km (*Petrie*, 1987). *Anderson and Smith* (1989) observed strong NIOs with maximum speeds of order 0.20 m/s on the Scotian Shelf using moored current meters located on the 150-m isobaths. The same authors also found that the peak frequency of NIOs was slightly subinertial which might be caused by the mean flow shear induced by the NSC.

The Marine Environmental Observation Prediction and Response network (MEOPAR) deployed a high-frequency (HF) radar system off Halifax Harbour in 2015 to monitor surface ocean currents over the inner Scotian Shelf (Figs. 5.1 and 5.2). The radial currents observed by the two antennas have been processed to give hourly maps of near-surface currents defined on a horizontal grid with a spacing of 6 km. In this study, the HF-radar data are complemented by the observed time-varying, vertical profiles of horizontal currents made by an ADCP located close to the center of the mean NSC and within the region monitored by the HF-radar. These two new observational datasets provide an excellent opportunity to examine the NIOs on the inner Scotian shelf and, in particular, how they are modulated by an meandering coastal boundary current.

To help interpret these new observational datasets, we also take advantage of three

models. The simplest is a slab model that we use to quantify the effect of local wind forcing. We also use two prototype operational shelf circulation models known as DalCoast (*Ohashi et al.*, 2006) and GoMSS (*Katavouta et al.,* 2016). DalCoast is based on the Princeton Ocean model (POM, *Mellor*, 2004), and GoMSS is based on the Nucleus for European Modelling Ocean framework (NEMO, *Molines et al.* 2014). Both DalCoast and GoMSS have been validated extensively and shown to have satisfactory performances on tidal and subtidal circulations. These two models, however, use different numerics and different vertical coordinates. An important scientific question that remains to be addressed is that how well these two operational models simulate the NIOs.

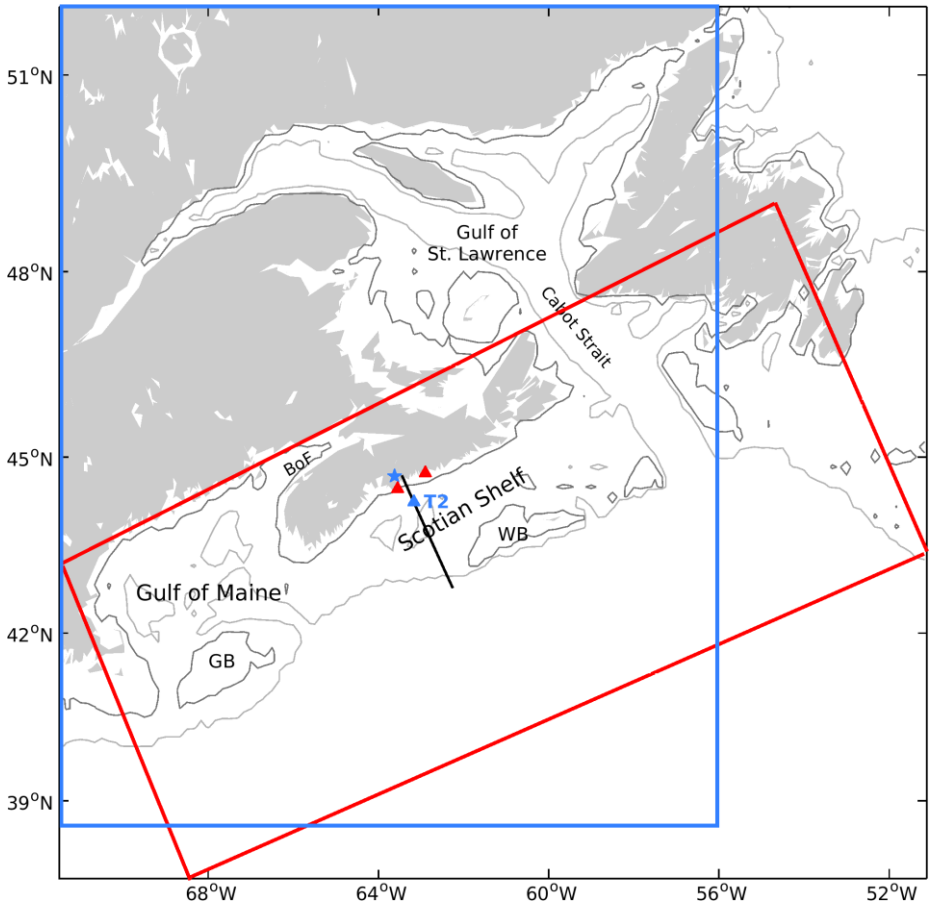

Figure 5.1: (a) Map showing the ocean model domains (blue line is open boundary for DalCoast; red line is open boundary for GoMSS). Also shown are the HF radar stations (red triangles), the ADCP location (blue triangle), tide gauge (blue pentagram), and the Halifax Line (thick black line). The black and gray contour lines represent respectively the 60 m and 200 m isobaths. The following abbreviations are used for the Bay of Fundy (BOF), Georges Bank (GB), and Western Bank (WB).

In this chapter, we first use the new observations made by the HF-radar and the ADCP to describe the intensity, intermittency and, for the first time, the spatial structure of NIOs over the inner Scotian Shelf. We also attempt to explain the observed changes in the frequency of peak near-inertial energy (f_p) using Eq. (5.1) with the changes in ζ estimated from the low-pass filtered HF-radar observations. We then use the above-mentioned three models to help understand how the slowly-varying background circulation influences the NIOs on the Scotian Shelf. We also use the observations to assess the performance of the two operational models in the near-inertial band and identify possible ways of improving the models for practical applications including the forecasting of currents on the inner shelf.

Section 5.2 provides a statistical description of the HF-radar and ADCP observations and compares them to results produced by the simple slab model forced by the local wind. Section 5.3 presents a description of the two operational models. Section 5.4 provides a description of model results produced by the two operational models and their comparison with the observations. Section 5.5 is a summary and discussion.

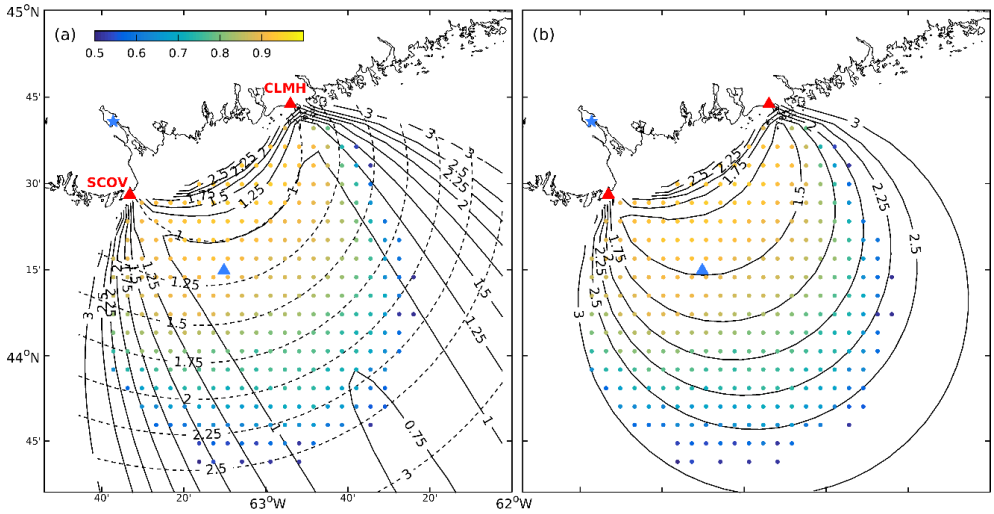

Figure 5.2: Errors associated with HF radar geometry and current data availability. (a) East (solid line) and north (dashed line) GDOP, (b) magnitude of GODP. The color coded dots in (a, b) indicate HF radar data points used in the present study; the color indicates data availability (see color bar in panel (a)). Also shown are the HF radar stations (red triangles), the ADCP location (blue triangle), and tide gauge (blue pentagram). Abbreviations are used for Sandy Cove (SCOV) and Clam Harbour (CLMH).

5.2 Processing and Analysis of Observations

5.2.1 Processing of HF-Radar and ADCP Data

The HF-radar system consists of two long-range CODAR-Seasonde radars located at Sandy Cove and Clam Harbour (Fig. 5.2) off the Atlantic coast of Nova Scotia, Canada. Each radar operates at a central frequency of 4.8 MHz and provides hourly radial surface currents with 6 km resolution and coverage up to 200 km from the coastal radar site. HF-radar measurements correspond to the ocean currents averaged from the surface to a depth of the order of $\lambda/4\pi$ where λ is the Bragg wavelength (*Steward and Joy*, 1974). This depth corresponds to approximately 2.5 m given the system's transmit frequency. We will henceforth refer to the currents observed by the HF-radar as "surface" currents. (For more details on HF-radar technology see *Paduan and Graber* (1997).)

The HF-radar data used in this chapter were processed by the HFRadar Network (HFRNet, http://cordc.ucsd.edu/projects/mapping/) using the following procedure. The data were first mapped onto regional grids defined using an equidistant cylindrical projection with a grid spacing of 6 km. Surface current vectors were then estimated using a least squares fit to at least three radial velocities within a search radius of 10 km from each grid point. As part of the data quality control, a velocity threshold of 3.0 m/s was applied to both the radial and total velocities. One issue associated with this method is that the solution becomes unstable when the radial current components are close to parallel. This occurs near the line connecting the two radar sites and in the far field. Errors associated with the radar geometry are usually quantified by the Geometric Dilution of Precision (GDOP, *Chapman*, 1997). Low GDOP values correspond to a preferred geometric configuration. The GDOP map for the present system is given in Fig. 5.2. Grid points with a GDOP greater than 3 are not used in the present study.

The HF-radar data could have data gaps due to the radio interference experienced by both HF-radar units. The radio interference usually occurs between sunset and sunrise and is often related to changes in the ionosphere. The hourly data at grid points with more than 50% temporal coverage (Fig. 5.2) for three complete winter months (December 2015 to February 2016) are used in this chapter. During this 3-month period, the HF-radar data

coverage is relatively good.

During these three winter months, vertical profiles of currents were measured by a bottom-mounted, upward-looking ADCP at location T2 on the Halifax Line (Fig. 5.1). The water depth at this location is about 160 m. The ADCP was deployed by the Ocean Tracking Network to monitor the NSC. (Two additional ADCP were also deployed in the same general area, but they were not functional during the study period.) The ADCP currents were averaged over 30 min time windows and 4 m vertical bins. The shallowest bin was centered at 20 m from the sea surface and the deepest bin was 10 m off the bottom.

5.2.2 The Slab Model

Slab models have been widely used to simulate wind-driven inertial oscillations of surface current (e.g., *Pollard and Millard*, 1970; *D'Asaro*, 1985; *Paduan and Szoeke*, 1989). The equation for the mixed layer velocity $\mathbf{u} = u + iv$ is assumed to be

$$\frac{\partial \mathbf{u}}{\partial t} + if\mathbf{u} + \lambda\mathbf{u} = \frac{\boldsymbol{\tau}}{\rho h} \tag{5.2}$$

where f is the inertial frequency, $i = \sqrt{-1}$, λ is a linear damping coefficient, $\boldsymbol{\tau} = \tau_x + i\tau_y$ is the wind stress, ρ is water density, and h is the mixed layer depth.

The damping parameter λ represents the decay of NIOs in the mixed layer. Possible mechanisms responsible for this decay include the energy radiation into to the interior of the ocean, local turbulent dissipation, and nonlinear transfer to other frequencies (e.g., *D'Asaro*, 1985; *Park et al.*, 2008). Recent studies showed that the downward energy propagation can play a dominant role in the observed decay of near-inertial mixed layer energy (*Balmforth and Young*, 1999; *Johnston et al.*, 2008).

Assuming $\boldsymbol{u} = 0$ at $t = 0$, the velocity at subsequent times can be written explicitly in term of the history of the wind stress:

$$\mathbf{u}(t) = \frac{1}{\rho h}\int_0^t e^{-(if+\lambda)(t-t')}\boldsymbol{\tau}(t')\,dt' \tag{5.3}$$

The e-folding time of an inertial oscillation forced by a wind impulse is λ^{-1}. If the wind

stress can be modelled as a stationary process with a flat spectrum over the near-inertial band, the rotary spectrum of the current will peak at $\omega = f$. The half-width of the spectral peak, determined in terms of half power points, is λ, thereby providing an alternative interpretation of λ. *D'Asaro* (1985) suggested that typical values of λ^{-1} lie in the range of 2-10 days. In our study, we set λ^{-1} to three inertial periods. This estimate was based on analysis of the observed current time series in both the time and frequency domains. Specifically we visually examined the observed time series at location T2 to estimate the decay of significant NIOs following their generation using the fact that the e-folding decay time is λ^{-1} (Eq. (3)). We also examined the shape of the rotary spectral peak to estimate λ using the fact that the half-width of the spectral peak is λ according to the simple model by a stationary wind process.

5.2.3 Observed Monthly Means

The monthly mean surface currents calculated from the HF-radar observations indicate a persistent southwestward along-shore jet known as the NSC for all three months (Figs. 5.3a-c). The observed NSC generally occurred between the 100 m and 200 m isobaths and had a width of about 30 km. The NSC weakened by about 0.07 m/s over the study period and the center of the NSC migrated offshore by about 11 km between January and February (Table 5.1). The current maps for December and January had small-scale circulation features offshore of the NSC but they were weak and could result from the relatively low data availability in this region (Fig. 5.2).

Dever et al. (2016) analyzed current observations for all three ADCPs deployed by the Ocean Tracking Network and estimated geostrophic currents from glider observations of temperature and salinity for the period 2011 to 2014. They found that location T2 was close to the center of the mean NSC in winter, consistent with the observed means for December 2015 and January 2016 shown in Figs. 5.3a and b.

Figure 5.4 presents the observations of monthly mean currents normal to the Halifax Line (along-shore currents) made by the HF-radar and the ADCP at T2. The HF-radar observations along this section confirm the weakening and offshore migration of the NSC but also suggest that the NSC widened in February. The vertical current profiles from the

ADCP show the NSC was strongest for the shallowest bin centered on 20 m and decreased towards the bottom, consistent with the finding made by *Dever at al.* (2016). The mean currents observed by the ADCP at 20 m were stronger than the shallower surface currents observed by the HF-radar (Table 5.1). This difference can be explained by the mean effect of the wind on the near-surface flow.

Table 5.1: Monthly means of observed and simulated current normal to the Halifax Line. For each cell of the table, the upper left number is the peak mean current (m/s) and the number in parentheses is the distance from shore (km) at which it occurs. The lower value is the mean current (m/s) observed by the ADCP at T2 which is 42 km from shore.

		December 2015	January 2016	February 2016
HF-radar	z=2.5m	0.29 (42)	0.26 (42)	0.22 (53)
ADCP	z=20m	0.32	0.34	0.30
DalCoast	z=2.5m	0.27 (45)	0.25 (45)	0.20 (49)
	z=20m	0.27	0.24	0.20
GoMSS	z=2.5m	0.26 (38)	0.25 (38)	0.21 (34)
	z=20m	0.26	0.25	0.20

5.2.4 Observed Near-Inertial Oscillations at Location T2

Time series of wind stress and observed surface currents at T2 are presented in Fig. 5.5. The intense NIOs in the current time series coincided with strong wind events associated with the passage of winter storms such as on 5 and 16 December. The NIOs typically lasted for three or four inertial periods. Not all winter storms, however, generated strong NIOs, such as the storms on 12-16 January and 9 February. To explain this difference, the simple slab model is used to simulate the NIOs at T2 from the local wind. The simulated currents by the slab model are dominated by NIOs. They are in reasonable agreement with the observed NIOs (Figs. 5.5b-c and 5.5e-f), confirming the important influence of the local wind in generating NIOs in this region. The results produced by the slab model also explain why some wind events were more effective than others in generating NIOs. For example, from 12 to 16 January, the NIOs were partially supressed by the counter-clockwise-rotating wind stress around 13 and 16 January. Similarly, the counter-clockwise-rotating wind stress around 9 February was rotationally unfavourable for the generation of NIOs.

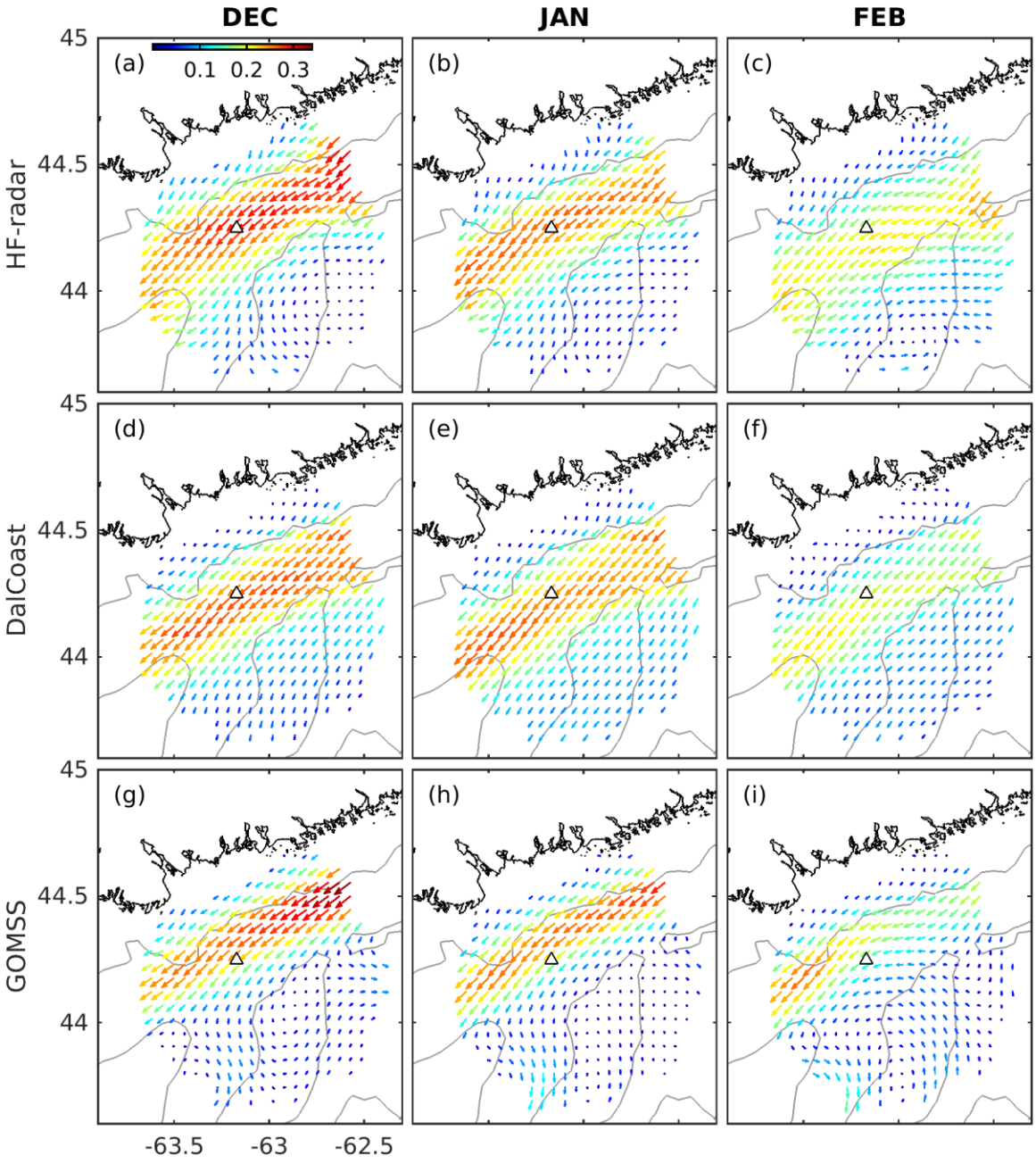

Figure 5.3: Monthly mean surface currents at the HF-radar grid with a spacing of 6 km. The top row is for the HF-radar observations in (a) December 2015, (b) January 2016, and (c) February 2016. The color of the arrows indicates speed (colorbar in panel a). The middle and bottom rows of panels represent the corresponding monthly mean currents simulated by DalCoast and GoMSS respectively. The contour lines represent the smoothed 100 and 200 m depths and the triangle marks the location of the ADCP at location T2.

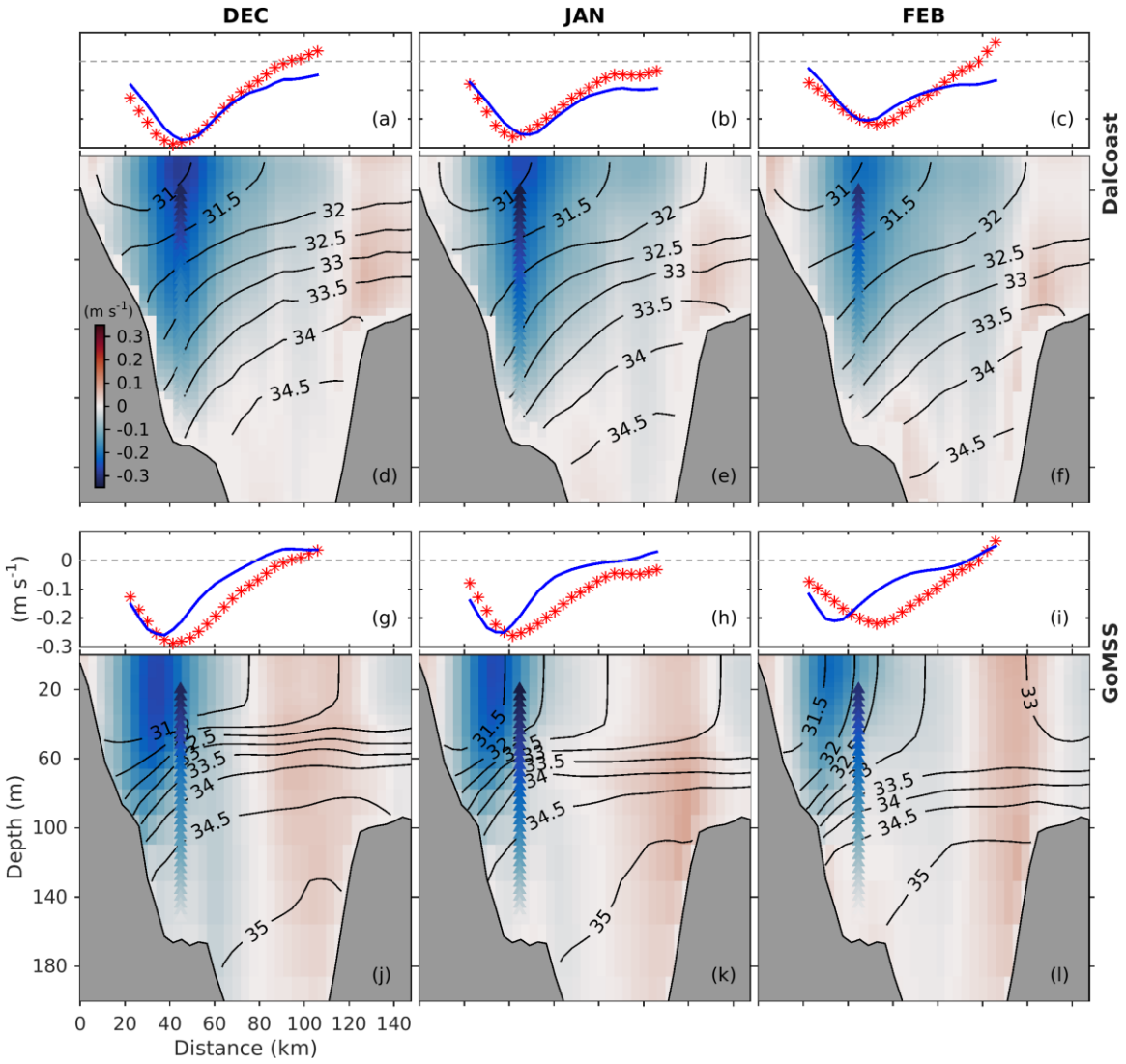

Figure 5.4: Monthly mean currents and salinity along the Halifax Line as a function of offshore distance. The red asterisks in the first and third rows represent the monthly mean currents normal to the Halifax Line observed by the HF-radar, and the blue lines show simulated surface currents by (a-c) DalCoast and (g-i) GoMSS. The vertical stack of colored triangles shows the monthly mean currents observed by the ADCP at location T2. The color shading and black contour lines show the simulations of normal current and salinity made by (d-f) DalCoast and (j-l) GoMSS.

Rotary spectra (*Gonella*, 1972) of the observed current time series made by the HF-radar and the ADCP (Fig. 5.6a) confirm the important contribution of NIOs. It should be mentioned that, for simplicity of discussion in this paper, positive (negative) frequencies denote clockwise (counter-clockwise) rotating motions in the rotary spectra. Both rotary

spectra are very similar in the near-inertial band, even though the observations were made at depths separated by 17.5 m. The K_1 tidal currents were relatively weak and the M_2 tidal currents were insignificant during the study period. Both rotary spectra also indicate a high level of variability at periods longer than about 4 days which we attribute to subtidal variability of the NSC.

The rotary coherence between the HF-radar and ADCP observations exceeds 0.8 at the inertial frequency of 1.39 cpd (Fig. 5.6b). This high coherence is consistent with visual inspection of the two observed current time series (Fig. 5.5), which show good agreement in amplitude and timing during the strong storm-induced NIOs of December 5 and 16, and February 18. During moderate wind events (Fig. 5.5), when the Ekman depth was relatively shallow and vertical shear near the surface was large, discrepancies between the two time series were evident.

As mentioned in the Introduction, *Kunze* (1985) showed that the background flow can modify the effective inertial frequency f_e through changes in relative vorticity ζ according to Eq. (5.1). To estimate the magnitude of this effect, we present in Fig. 5.6c the evolving rotary spectrum (henceforth ERS) of the ADCP time series in the near-inertial band calculated using a sliding window of length 10-day with a one hour overlap. (The HF-radar time series at T2 has too many missing observations to undertake this type of analysis.) It is clear that the peak frequency in the near-inertial band f_p changed with time. For example, the NIO associated with the December 16 storm had a peak frequency $f_p \approx 1.06f$ in contrast to $f_p \approx 0.93f$ around February 18. We also show in Fig. 5.6c the f_e calculated from Eq. (5.1) using ζ at T2 estimated from the HF-radar data averaged in time using the same 10-day sliding window. The similarity of the variability of f_p and f_e during the NIOs in December and February is consistent with the relative vorticity correction given by Eq. (5.1) and thus the idea that changes in the position and intensity of the NSC influence the NIOs over the inner Scotian Shelf. To illustrate, the ~6% shift of f_p in mid-December coincided with an inward excursion of the NSC and the ~7% shift in late February coincided with an offshore excursion of the NSC that changed the sign of ζ at T2 (see Figs. 5.3 and 5.4). We note that the agreement between variations in f_p and f_e is

not perfect. The discrepancy between f_p and f_e during the NIOs in January can be explained in part by local wind forcing as demonstrated by the slab model (Fig. 5.6d). Overall however, adding $\zeta/2$ to the ERS of the slab model (Fig. 5.6e) leads to closer agreement between the ERS of the slab model and the ADCP observations.

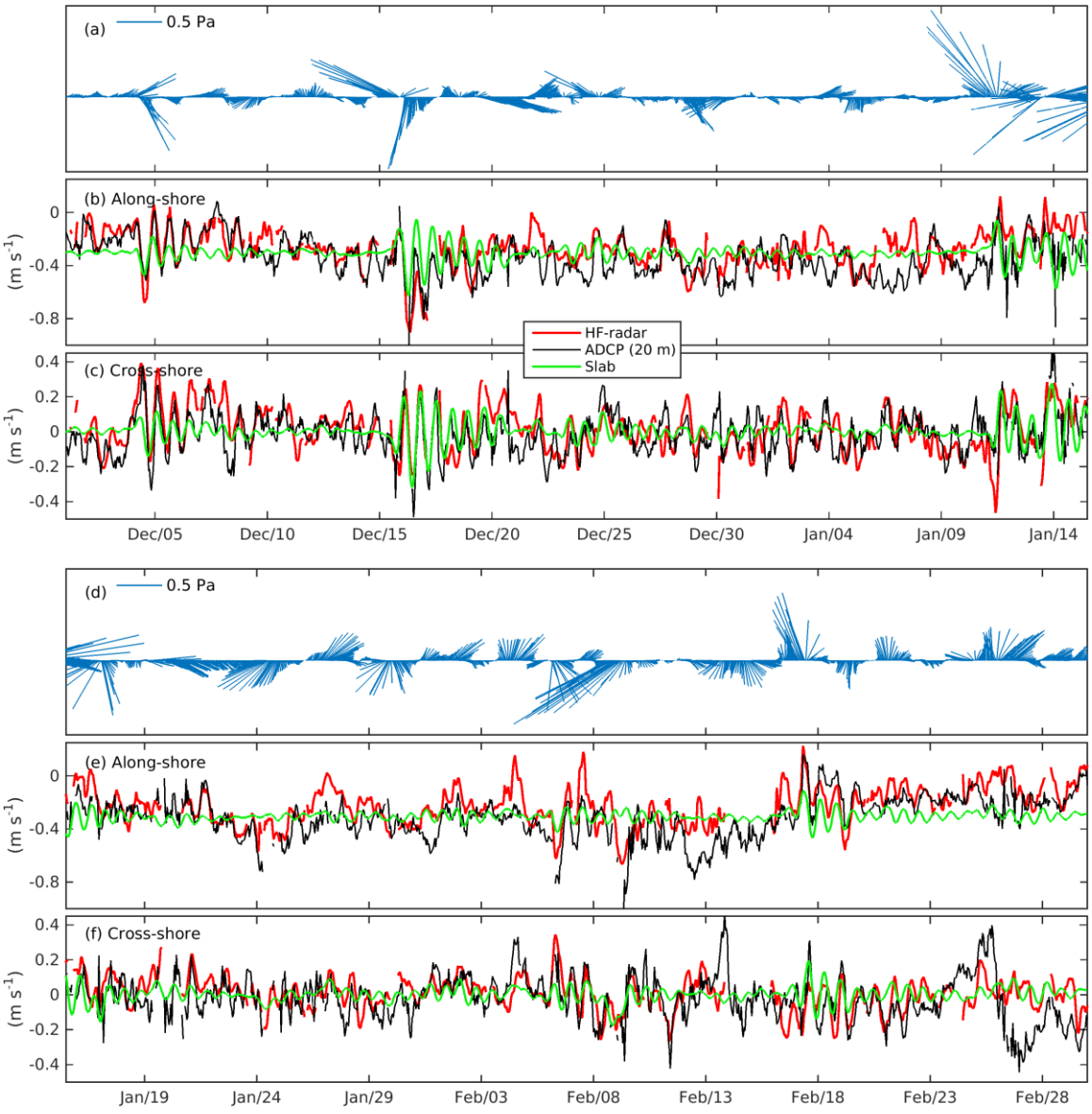

Figure 5.5: Time series of (a, d) wind stress (b, e) along-shore and (c, f) cross-shore currents observed by the HF-radar at 2.5 m (red line) and ADCP at 20 m (black line), and simulated by the slab model (green line) at location T2 (positive offshore). The along-shore currents simulated by the slab model in (b, e) are shifted by -0.3 m/s for comparison with observations.

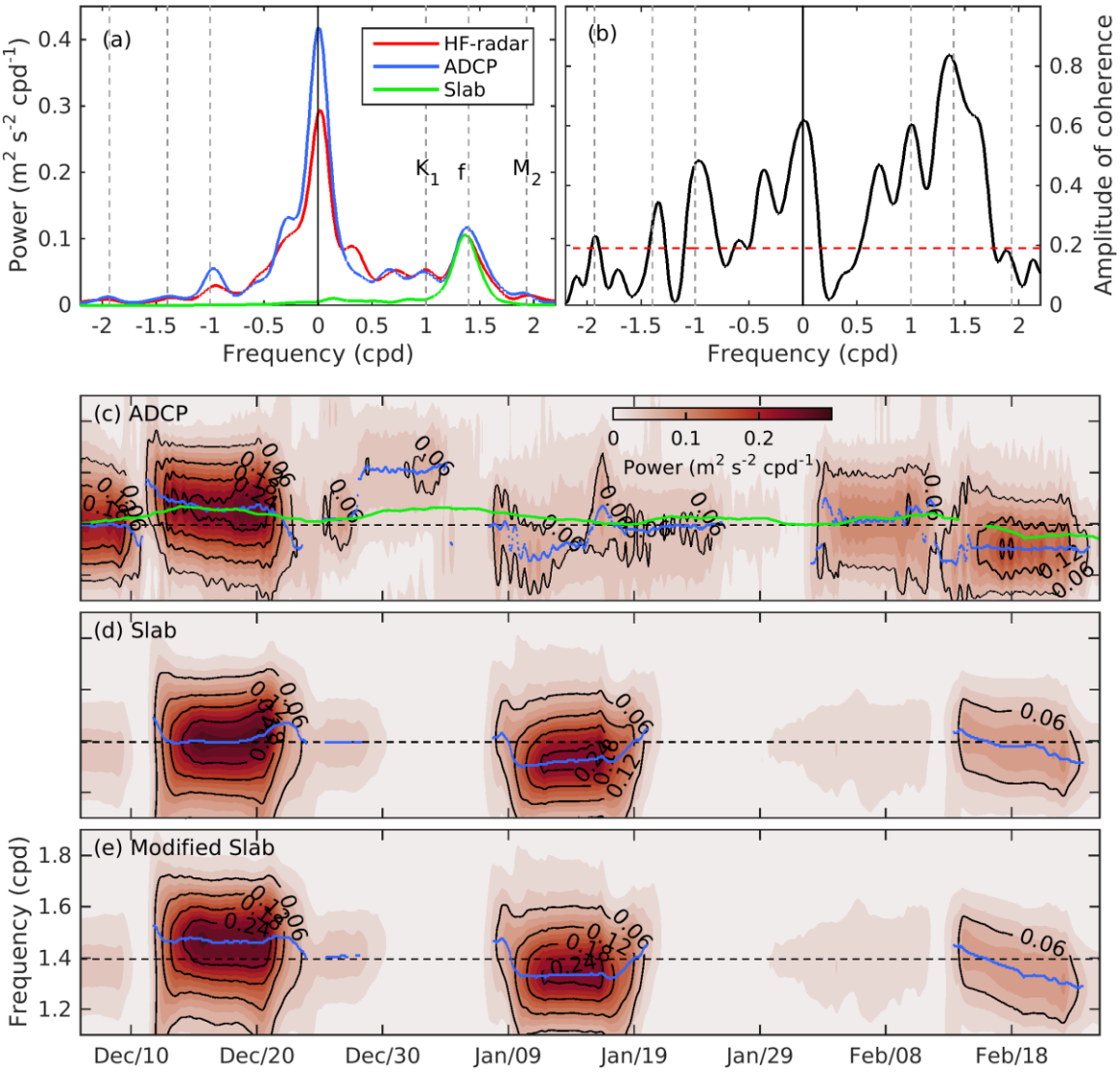

Figure 5.6: Rotary spectral analysis of observed surface currents at T2 and simulations by the slab model. (a) Rotary spectra (b) magnitude of the coherence between the HF-radar and ADCP observations at 20 m. The red dashed line in (b) is the 1% significance level. A Parzen spectral window of width 0.252 cpd was used to estimate (a) and (b). (c) The evolving rotary spectrum (ERS) of the ADCP observations. The green line represents the effective inertial frequency ($f_e = f + \zeta/2$) where ζ was estimated from current fields observed by the HF-radar. (d) ERS of slab model simulations. (e) Same (d) except that the ERS of the slab model simulations has been shifted at each frequency by $\zeta/2$. All ERS were calculated using a 10 d sliding window and a spectral window of width 0.379 cpd. The frequency axis is limited to the near-inertial band. The black dashed lines represent the local inertial frequency ($\omega = f$) and the blue lines show the peak frequency f_p (plotted only for frequencies with relatively high near-inertial energy).

5.2.5 Spatial Structure of the Observed Near-Inertial Oscillations

To quantify the observed current variability in the near-inertial band, an empirical orthogonal function (EOF) analysis described in Appendix C was performed for the band-pass filtered HF-radar observations. About 71% of the total variance can be explained by the first mode. The spatial structure of this mode (Fig. 5.7) was large-scale with lower amplitudes within ~40 km of the coast. The elements of the first mode rotated cyclonically moving from west to east. The mode amplitude (Fig. 5.7b) was dominated by oscillations centered at the inertial frequency with increased amplitudes during storms. The higher order modes are not presented because each of them individually accounts for less than 7% of the total variance of the HF-radar data.

To explain the phase differences of NIOs moving from west to east in Fig. 5.7a, we used the slab model driven by the reanalysis winds to simulate the local current response at each HF radar grid point. The results of an EOF analysis of the slab model simulations are presented in Fig. 5.7b. Note the complex elements of the first EOF rotate cyclonically moving from west to east, in general agreement with the first EOFs of the HF-radar observations (Fig. 5.7a). This indicates that the phase differences moving from west to east are due primarily to the movement of the atmospheric forcing. This is consistent with the fact that storms generally move from west to east in the study region during winter.

To examine the spatial structure of the NIOs in more details, we spectrally analyzed each grid point time series of observed currents and mapped the results across the grid. The amplitudes of the NIOs, defined by the square root of the integral of the rotary spectrum between cut-off frequencies of $0.85\,f_p$ and $1.15\,f_p$, are presented in Fig. 5.8a. The amplitudes were largest (~0.25 m/s) in the offshore region, and decayed rapidly within ~40 km of the coast, consistent with the EOF analysis described above. In the literature, the coastal suppression of NIOs has often been attributed to a "coastal inhibition" of NIOs within one internal Rossby radius from the coast (e.g., *Kim and Kosro*, 2013; *Kundu et al.*, 1983; *Smith*, 1989). The inhibition is explained in terms of the leakage of near-inertial energy both downward and offshore. *Kundu et al.* (1983, Fig. 6) showed that NIOs undergo an exponentially decay over 5 days within one Rossby radius of the coast due to leakage

of energy both horizontally and vertically. The horizontal leakage from the coastal region increases the NIO energy over the same time period offshore.

The internal Rossby radius for the Scotian Shelf is about 15 km (*Dever*, 2017). In agreement with *Kundu et al.* (1983) we found a slight initial increase in NIO amplitude during well-defined NIO events at a distance of approximately one internal Rossby radius from shore (not shown). However, we found that the coastal suppression of NIO amplitude occurred over a scale of ~40 km, well beyond one internal Rossby radius.

To explain this discrepancy with the theory of *Kundu et al.* (1983) we plotted the distribution of near-inertial kinetic energy over the whole model domain (not shown) as predicted by the numerical models described in section 5.3. We found the simulated near-inertial kinetic energy depends strongly on water depth even in regions well away from the coast. For example in the Gulf of Maine, where the offshore gradient of water depth near the coast is relatively small, the coastal suppression of NIOs occurs over larger offshore distances than the Scotian Shelf. Away from the coast, we found that NIOs are effectively suppressed over shallow regions such as Western Bank and Georges Bank (Fig. 1). *Kundu and Thompson* (1985, Eq. (22)) showed that the inertial current amplitude under a fast moving storm is proportional to $\tau_0(1 - \mathrm{h/D})/\mathrm{fh}$ (where τ_0 is the wind stress, D is the water depth, and h is the mixed layer depth). This implies that the amplitude increases with D and decreases with h. Mixed layer depth in shallow water is usually increased due to tidal and wind mixing. We therefore conclude that shallower water depth, and increased mixed layer depth, contribute to the observed suppression of NIOs within ~40 km of the coast in the study area.

The spatial scale of the NIOs was estimated from the rotary coherence between the HF-radar observations at location T2 and all other grid points. The coherence was evaluated at f_p. The coherence amplitude is anisotropic (Fig. 5.8d) which exceeds 0.5 within about 80 km of T2 in the along-shore direction, and about 40 km in the cross-shore direction. The phase of the coherence shown in Fig. 5.8g increases from west to east, consistent with the EOF analysis.

Figure 5.9a presents the horizontal distribution of the relative frequency shift ($\Delta f =$

$f_p - f$). The observed f_p was below f within ~50 km of the coast and slightly above f seaward of this distance. To explain the spatial variation in f_p, the value of $\zeta/2$ was calculated from the mean of the HF-radar observations (Fig. 5.9d). Overall, there is reasonable agreement between the two maps of Δf and $\zeta/2$ thereby providing additional observational evidence for Eq. (5.1) and modification of f_p by the NSC.

To further examine the relevance of the present study to other locations, we also analyzed the HF-radar observations made off the Oregon coast (see Appendix C for details). Overall, the coastal suppression of NIOs and the modulation of f_p by the background vorticity found off the Oregon coast are consistent with our findings for the Scotian Shelf.

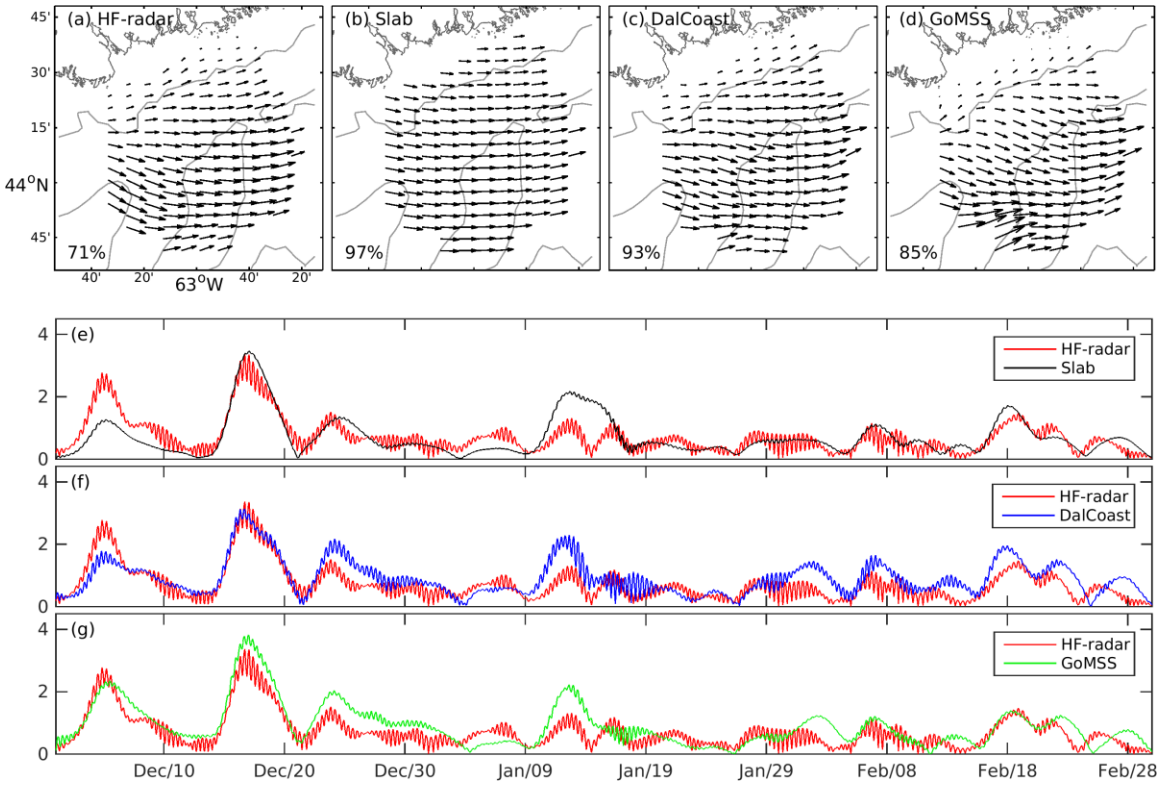

Figure 5.7: The EOF analysis of the HF-radar observations and model simulations after filtering to pass variations in the near-inertial band. The top row of panels shows the spatial structure of the first mode. The number in the lower left corner of each panel in the top row is the proportion of total variance explained by the first mode. The contour lines show the smoothed 100 and 200 m isobaths. The second, third, and fourth rows show the time variation of the amplitude of the first mode calculated from the HF-radar data (red line) and model results produced by the slab model (black line in (e)), DalCoast (blue line in (f)), and GoMSS (green line in (g)).

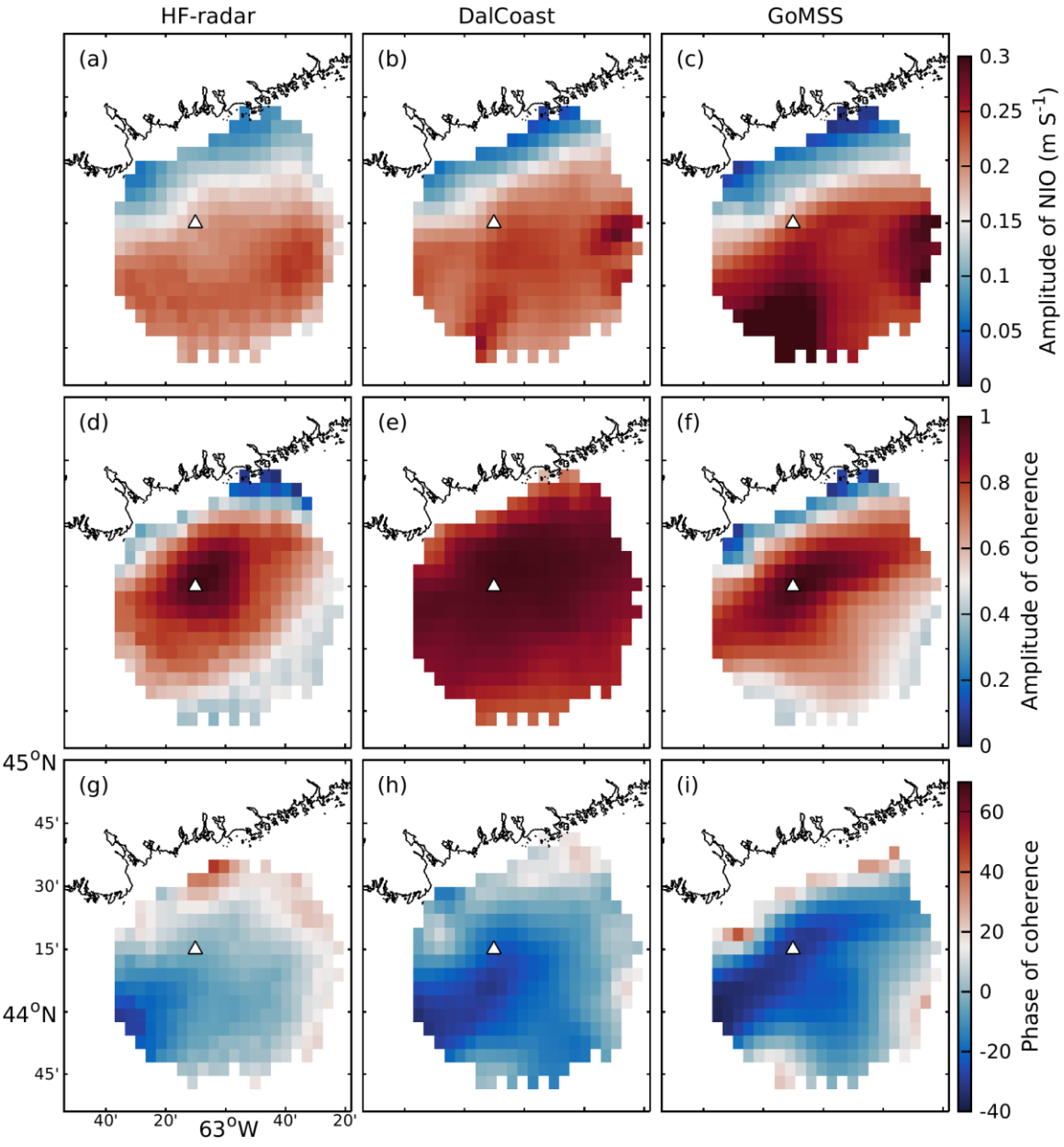

Figure 5.8: Distributions of NIOs observed by the HF-radar and simulated by two models. (a, b, c) amplitudes of NIOs, (d, e, f) amplitudes of rotary coherence, (g, h, i) corresponding phase of rotary coherence. The left, middle and right panels are for the HF-radar observations, DalCoast simulations, and GoMSS simulations respectively. The phase is only plotted for coherences above 0.4. The coherence is relative to location T2 (triangle) and evaluated at the peak frequency in the near-inertial band.

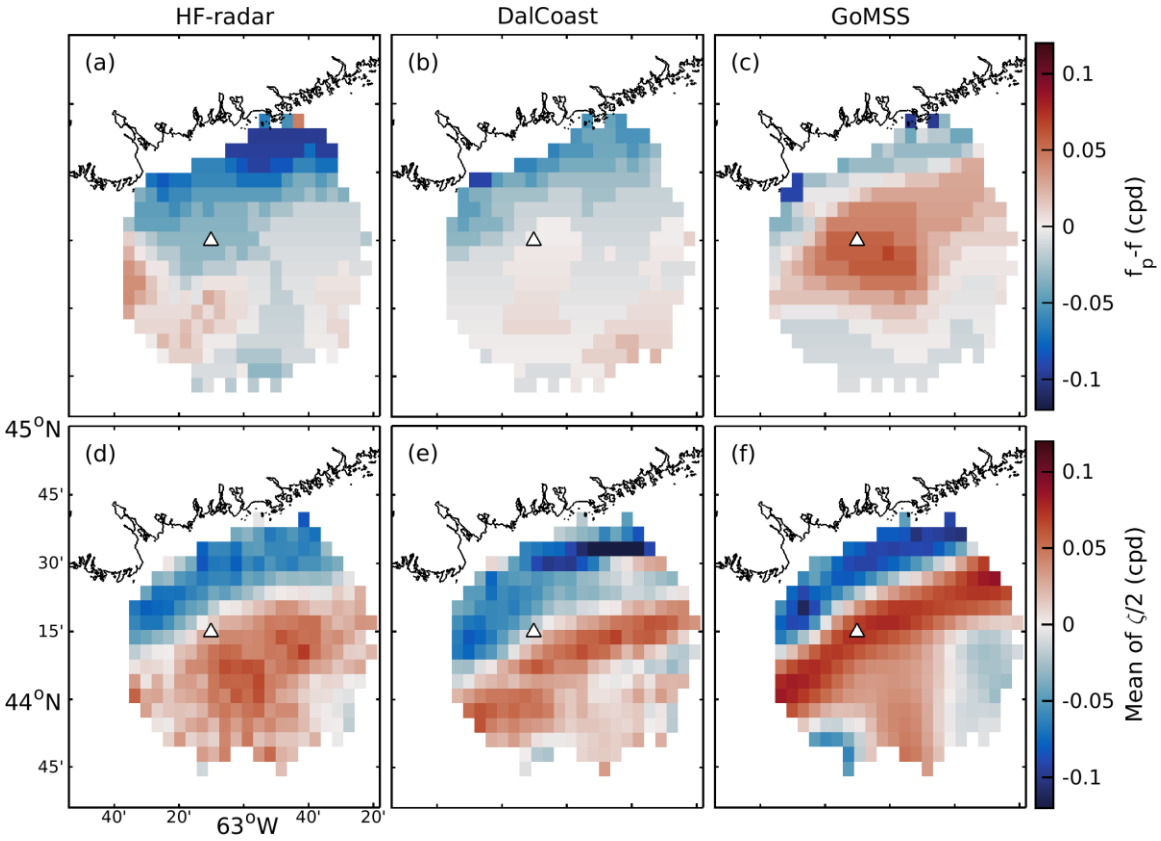

Figure 5.9: Horizontal distributions of (a, b, c) shift in peak frequency relative to inertial frequency, $f_p - f$ and (d, e, f) 3-month mean of $\zeta/2$. The left, middle and right panels are for the HF-radar observations and simulations by DalCoast and GoMSS respectively.

5.3 Two Prototype Operational Shelf Models

5.3.1 DalCoast

As described in Chapter 3, DalCoast is a 3D, sigma-coordinate, primitive-equation ocean circulation model based on the POM (*Mellor*, 2004). The model domain covers the Gulf of St. Lawrence, the Scotian Shelf, and the Gulf of Maine and adjacent deep waters (71.5°-56°W, 38.5°-52°N, Fig. 5.1). The grid spacing is 1/16° (~7 km) in both the longitudinal and latitudinal directions. There are 40 sigma levels in the vertical with the highest concentration near the surface and bottom and approximately equal spacing in the interior. The model topography is based on the General Bathymetric Chart of the Oceans (GEBCO) bathymetric dataset (http://www.gebco.net/).

The external forcing is calculated using hourly surface winds and atmospheric pressures at the sea level both extracted from the Climate Forecast System Version 2 (CFSv2, *Saha et al.*, 2014). Wind stress is calculated using a quadratic formula with the drag coefficient given by the bulk formula of *Large and Pond* (1981) and *Powell et al.*, (2003) (see Eq. 3.10). In addition to forcing by surface winds and atmospheric pressures at the sea level, DalCoast is also driven by the net heat and freshwater fluxes at the sea surface and freshwater runoff from major rivers in the region.

At the model's open boundaries, the model is driven by (a) wind-induced hourly sea level and depth averaged currents produced by a barotropic model covering the northwest Atlantic Ocean (72°-42°W, 38°-60°N) with a resolution of 1/12°, (b) tidal forcing specified in terms of hourly sea levels and depth averaged currents predicted by the OSU Tidal Inversion System (OTIS) for 8 tidal constituents (M_2, S_2, N_2, K_2, K_1, O_1, P_1, and Q_1), and (c) daily values of temperature, salinity and large-scale density-driven currents provided by an ocean-ice numerical model of the northwest Atlantic (*Urrego-Blanco and Sheng,* 2012). Spectral nudging (*Thompson et al.*, 2007, *Wright et al.*, 2006) and the semi-prognostic method (Sheng et al. 2001) are used to reduce bias in temperature and salinity in DalCoast and the model of *Urrego-Blanco and Sheng* (2012). Both models are nudged to the mean and seasonal cycle of the monthly climatology of *Geshelin et al.* (1999).

5.3.2 GoMSS

GoMSS is a 3D, z-coordinate, primitive-equation ocean circulation model based on the NEMO (Molines et al. 2014). Its domain covers the Scotian Shelf, Gulf of Maine and adjacent deep waters (Fig. 5.1). The grid spacing is 1/36° (~2.8 km) in both longitudinal and latitudinal directions. There are 50 z-levels with a spacing that varies from 1 m near the surface to 458 m at the deepest level (5500 m). Partial cells are used to better represent the bathymetry. The use of the ‘‘variable volume level’’ approach (*Levier et al.*, 2007) allows the thickness of the vertical levels to vary with changes in the sea surface elevation. The model bathymetry is based primarily on the 2-arc-min gridded global relief dataset ETOPO2v2 (NOAA, National Geophysical Data Center). Higher-resolution data provided by Richard Karsten (*Acadia University*, 2014, personal communication) were used to

improve the bathymetry in the inner Gulf of Maine.

Momentum and heat fluxes at the ocean surface are calculated using the same hourly atmospheric variables used to force DalCoast. The initial and open boundary conditions (excluding tides) are interpolated from daily temperature, salinity, sea surface height, and horizontal velocity fields from the Mercator global ocean forecast system (Prototype System version 4, nominal horizontal grid spacing of 1/12°). Eight tidal constituents (M2, S2, N2, K2, K1, O1, P1 and Q1) are also used to specify tidal forcing at the model's lateral open boundaries. The tidal elevations and transports were obtained from the FES2004 finite element global tidal model of *Lyard et al.* (2006).

5.3.3 Validation

Both DalCoast and GoMSS have been validated extensively in the tidal, synoptic and seasonal frequency bands. (For DalCoast see *Thompson et al.,* 2007; *Ohashi and Sheng*, 2013 and 2015; *Ohashi et al.*, 2009a and b; *Wang and Sheng*, 2016. For GoMSS see *Katavouta et al.*, 2016 and *Katavouta and Thompson*, 2016.) Further validation of both models in the tidal and synoptic bands, using observations of coastal sea level and current for the present study period, is described in Appendix E along with some typical maps of simulated sea surface temperature. The following section focuses on the near-inertial band.

5.4 Comparison of Ocean Model Simulations and Observations

The simulated monthly mean surface currents by DalCoast and GoMSS are first assessed by comparing them with the HF-radar and ADCP observations. This is followed by an assessment of the model simulations in the near-inertial band.

5.4.1 Monthly Means

Both DalCoast and GoMSS simulate the well-defined southwestward NSC that is strong (0.25-0.27 m/s) in December and January and weakens (~0.20 m/s) in February, consistent with the HF-radar observations (Fig. 5.3, Table 5.1). DalCoast reproduces reasonably well the width (~30 km) and the location of the observed NSC for all three months, while the NSC produced by GoMSS is too narrow (~20 km) and also too close to shore for all three

months (Table 5.1). There is some indication in Fig. 5.3 that GoMSS provides more realistic simulations seaward of the NSC, including some small-scale circulation cells that are evident in the HF-radar observations.

The simulated monthly mean currents normal to the Halifax Line (along-shore currents) produced by DalCoast and GoMSS are presented in Fig. 5.4 as a function of depth and offshore distance. Both models produce the vertical shear and near zero bottom velocities evident in the ADCP observations at T2. The velocity sections also confirm that the NSC simulated by GoMSS is too close to shore for all three months. Both models also produce the mean along-shore flows at 20 m that are weaker than the corresponding ADCP observations by almost 0.1 m/s (Table 5.1). It is speculated that this discrepancy is caused mainly by baroclinic processes associated with the movement of oceanic fronts that are not simulated correctly due to inadequate model resolutions and imperfect model physics.

The vertical distributions of monthly mean salinity along the Halifax Line simulated by the two models are also shown by black contour lines in Fig. 5.4. Both models produce low salinity waters within 20-80 km of shore. There is good agreement between the salinity simulated by DalCoast and the section published by *Dever et al.* (2016, see their Fig. 5.5b) based on glider observations made during the months of January, February and March over the period 2011 to 2014. By comparison, GoMSS produces weaker vertical gradients of salinity in the top 50 m than DalCoast, suggesting a salinity bias error in GoMSS. The reasons for this bias and the incorrect offshore position of the NSC in GoMSS are currently under investigation.

5.4.2 Near-inertial oscillations at location T2

Time series of the simulated surface currents by DalCoast and GoMSS are presented in Fig. 5.10. There is generally good agreement between the simulations and the observations of surface currents made by the HF-radar. Well-defined NIOs, clearly related to the wind forcing, are evident in both the observations and simulations.

The rotary spectra of the simulated current time series in the near-inertial band are qualitatively similar to those of the observed currents made by the HF-radar and ADCP

(Figs. 5.11a and b). The rotary coherence between the observed and simulated currents exceeds 0.7 at the inertial frequency for both models (not shown). These estimates are significantly different from zero at the 1% significance level. In addition, all spectra have peaks in the vicinity of zero frequency, but DalCoast underestimates the observed low-frequency variability of currents at 20 m, indicating its simulated mean flow is less variable in time at this water depth.

Closer inspection of the rotary spectra for GoMSS (Figs. 5.11a and b) reveals that the near-inertial peaks occur at $f_p \approx 1.05f$. To explain this frequency shift, we present the ERS of both model simulations at 20 m in Figs. 5.11d and e. As expected, the ERS of simulations produced by DalCoast and GoMSS reproduce reasonably well the observed bursts of near-inertial energy forced by changes in the surface winds (Figs. 5.10a and d).

The most interesting feature in the ERS of the model simulations is the time variation of f_p shown by the blue lines in Figs. 11d and 11e. For DalCoast, f_p is less variable than observed (Fig. 5.11c). For GoMSS, f_p exhibits more temporal variability that is closer to the observed f_p but there is a difference in the mean (Figs. 5.11c and e). To explain these results, we estimated the time variation of ζ for both models and added the plot of $f_e = f + \zeta/2$ to Figs. 5.11d and e. For DalCoast, ζ is close to zero over the three month period, consistent with the proximity of f_p to the inertial frequency. For GoMSS, in the near-inertial events of December and February, the correlation between the strong positive background vorticity and the positive shift of f_p is consistent with the relative vorticity correction $\zeta/2$ in Eq. (5.1). The calculated f_e does not match f_p exactly. One contributor to the discrepancy is the way f_p was calculated: it is based on an average over a 10-day period. Given NIOs are highly intermittent, the calculated f_p at a specific time is only a smoothed approximation. In mid-January, the slab model simulations show that the negative shift of f_p is due to the sub-inertial wind forcing (Fig. 5.6d).

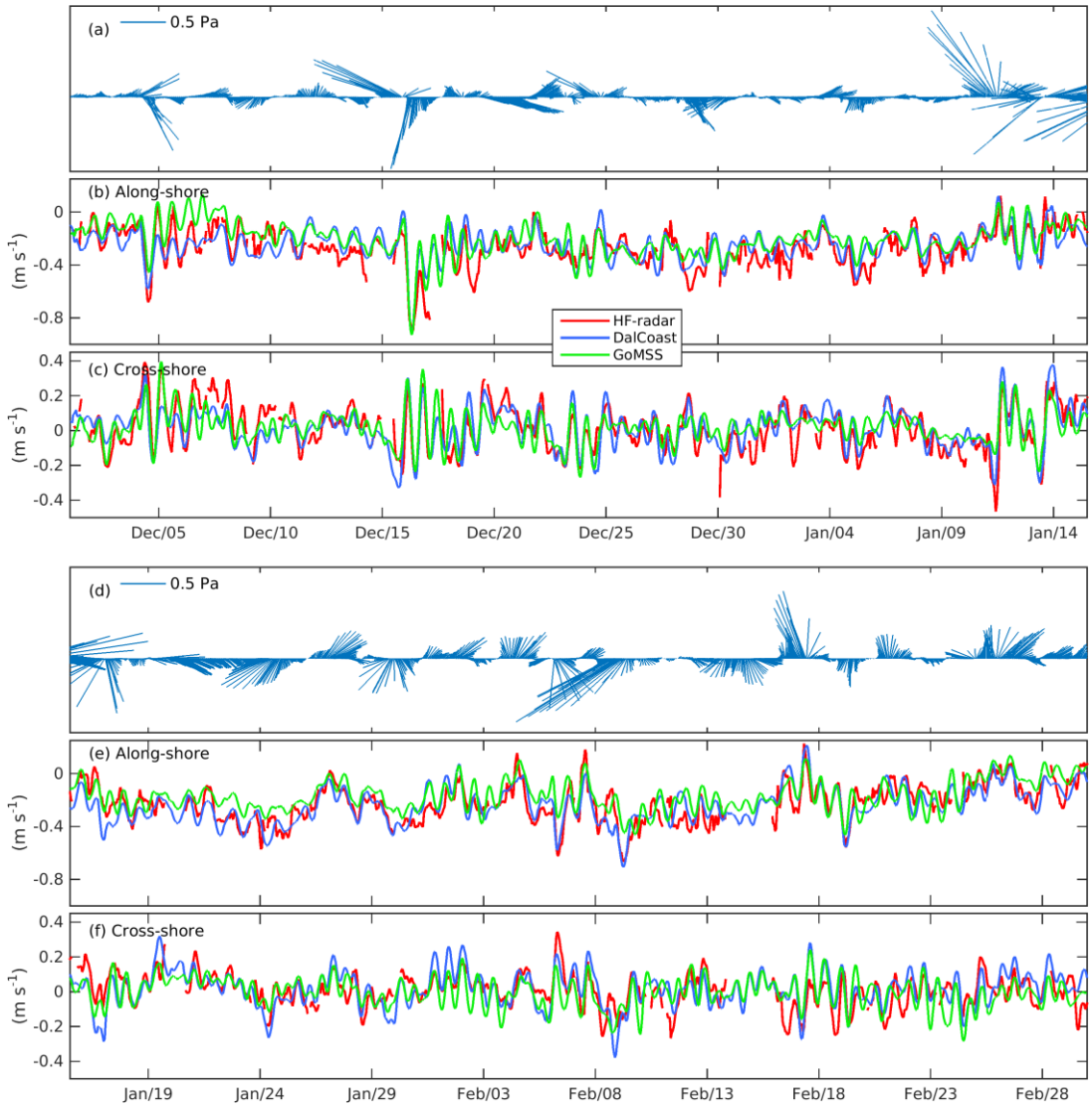

Figure 5.10: Time series of (a, d) wind stress (b, e) along-shore and (c, f) cross-shore currents observed by the HF-radar (red line) and surface currents simulated by DalCoast (blue line) and GoMSS (green line) at location T2.

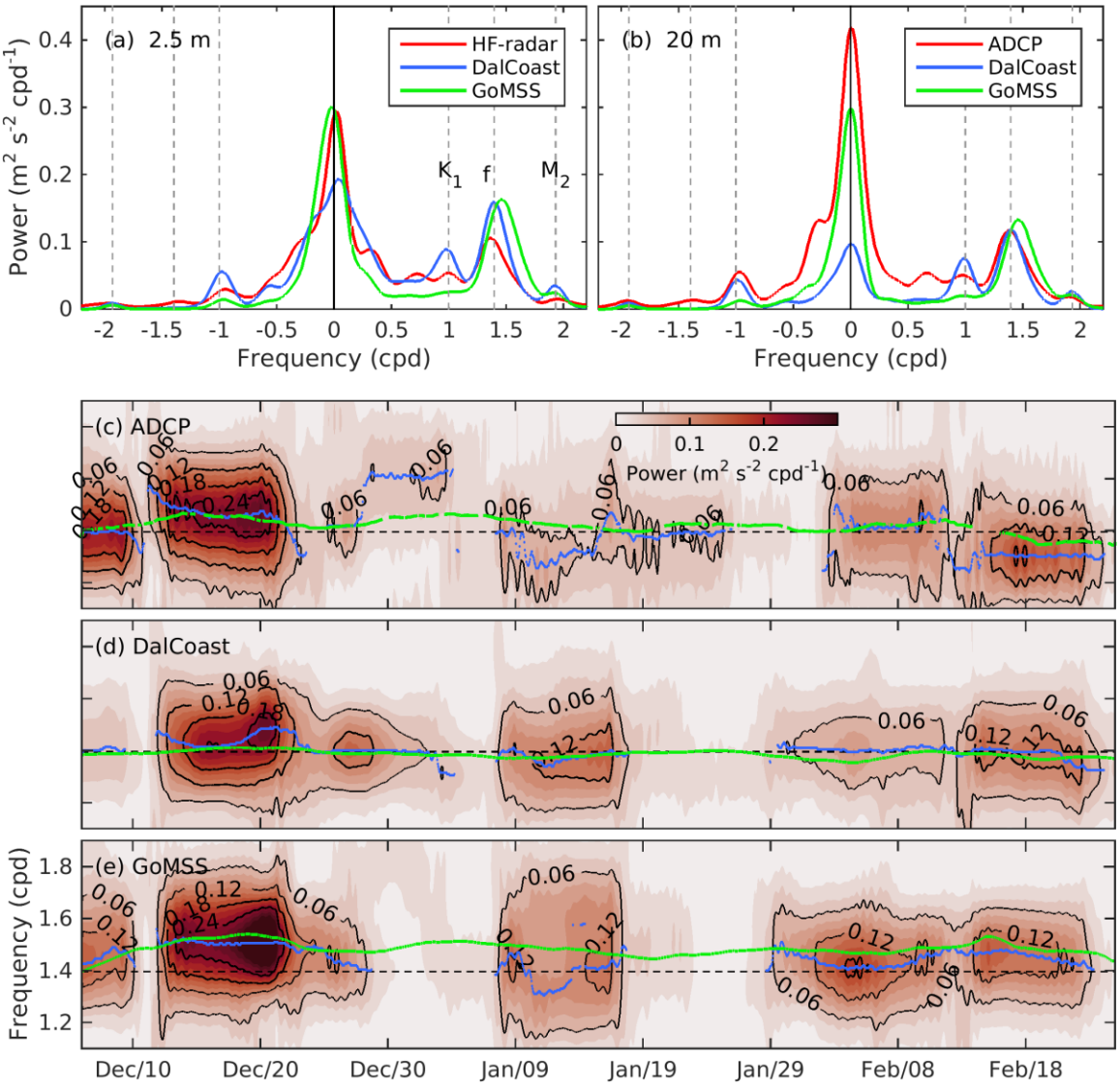

Figure 5.11: The first row shows the rotary spectra of observed and simulated currents at location T2 at depths of (a) 2.5 m and (b) 20 m. The observations at 2.5 m and 20 m were made by the HF-radar and ADCP respectively. The remaining three rows show the evolving rotary spectrum (ERS), based on a 10-day sliding window, of the (c) ADCP observations, and model simulations by (d) DalCoast and (e) GoMSS, all at a depth of 20 m. The frequency axis is limited to the near-inertial band. The dashed lines represent the local inertial frequency ($\omega = f$) and the blue lines show the peak frequency f_p (plotted only for frequencies with relatively high near-inertial energy). The green lines show the effective inertial frequency ($f_e = f + \zeta/2$) where the relative vorticity (ζ) was estimated from (c) near-surface currents at 2.5 m observed by the HF-radar, and simulations made by (d) DalCoast and (e) GoMSS at 20 m.

5.4.3 Spatial Structure of the Near-Inertial Oscillations

To further examine the variability of the model simulations in the near-inertial band, an EOF analysis of the band-pass filtered simulations was conducted in the same way as for the HF-radar observations. The first mode of the DalCoast simulations explains about 93% of the total variance, and the spatial structure of the first mode and the accompanying amplitude are in good agreement with their observed counterparts (Fig. 5.7). The first mode of the GoMSS simulations explains about 85% of the total variance and the amplitude is also in good agreement with its observed counterpart. Overall, DalCoast fits the first mode of the observations more closely than GoMSS. The latter overestimates the intensity of the NIOs in the southwest area of the study region. Both models, particularly DalCoast, account for more of their total variance in the first mode than the observations. This is due in part to missing values in the observed time series made by the HF-radar. More specifically, after treating the simulated currents as missing if they occur at the same time and location as the missing observations, the explained variance of DalCoast and GoMSS are reduced to 88% and 82% respectively, in closer agreement with the 71% obtained for the observations. The remaining discrepancy can be due to observation errors and real small-scale features that are not simulated correctly by the models due to inadequate model resolution and imperfect model physics.

A comparison of Figs. 5.8a and b demonstrates that the amplitudes of the NIOs simulated by DalCoast are in good agreement with their observed counterparts. By comparison, the NIO amplitudes produced by GoMSS are smaller than the observations close to shore (Figs. 5.8c and a). It is speculated that this discrepancy is caused by the unrealistically low vertical stratification and deeper mixed layer in GoMSS in this region, in comparison with DalCoast (see Fig. 5.4).

Furthermore, GoMSS also overestimates the NIO amplitudes in the offshore region. To explain this overestimation, we present in Fig. 5.12 the band-pass filtered along-shore currents as a function of time and depth for the ADCP and the models for four periods with relatively strong NIOs. It should be noted that the mixed layer depth for model results of DalCoast is more constant in time, and the density jump is weaker compared to the results

of GoMSS (Fig. 5.4). (The mixed layer depth can be inferred from the depth of the 180 degree phase difference in current shown in Fig. 5.12.) It is speculated that the stronger density stratification and occasionally shallower mixed layer depth are responsible for the stronger NIOs simulated by GoMSS in the offshore region. Another interesting feature in Fig. 5.12 is the higher mode variability evident in the ADCP observations and GoMSS simulations at depths exceeding 100 m. This is consistent with a more variable density field shown in the results of GoMSS (i.e., density jumps at ~100 m shown in Figs. 5.4j-l) compared to DalCoast (Figs. 5.4d-f). Specifically, the growing strength of the second mode inertial wave in the observations and GoMSS simulations could be attributable to the thick bottom mixed layer over which the bottom stress plays an active role (*Mackinnon and Gregg*, 2005).

The spatial coherence of the NIOs relative to location T2 simulated by GoMSS are in qualitative agreement with the HF-radar observations (Figs. 5.8d and f). Specifically, both maps show strong anisotropy with a more rapid drop in coherence in the on-offshore direction. The coherence of the DalCoast simulations decreases more slowly in all directions, with coherences exceeding 0.8 (Figs. 5.8d and e). This is consistent with the relatively high proportion of total variance of the DalCoast simulations accounted for by the first EOF. The different coherence scales can be explained by the fact that DalCoast's density field is relatively smoother, and less variable in time, due to its use of the spectral nudging method and this reduces the amount of scattering of the NIOs. The phase maps of the simulated NIOs (Figs. 5.8h and i) show that both models reproduce reasonably well the observed NIO phase changes moving from west to east (Fig. 5.8g).

The horizontal distribution of the relative frequency shift $(\Delta f = f_p - f)$ for the simulations produced by DalCoast and GoMSS (Figs. 5.9b and c) are generally similar to the frequency shift of the HF-radar observations (Fig. 5.9a), with negative values of Δf close to shore and positive values with distance from shore. The maps of simulated Δf are also broadly consistent with the corresponding maps of $\zeta/2$ (comparing Figs. 5.9b with e, and Figs. 5.9c and f), thereby providing further evidence for the effect of the NSC on f_p on the inner Scotian Shelf. The model results of DalCoast provide more realistic maps of Δf and $\zeta/2$ than the results of GoMSS, presumably due to its use of the

spectral nudging and semi-prognostic methods that ensure its simulated NSC and background vorticity field remain close to the observed winter mean state in DalCoast.

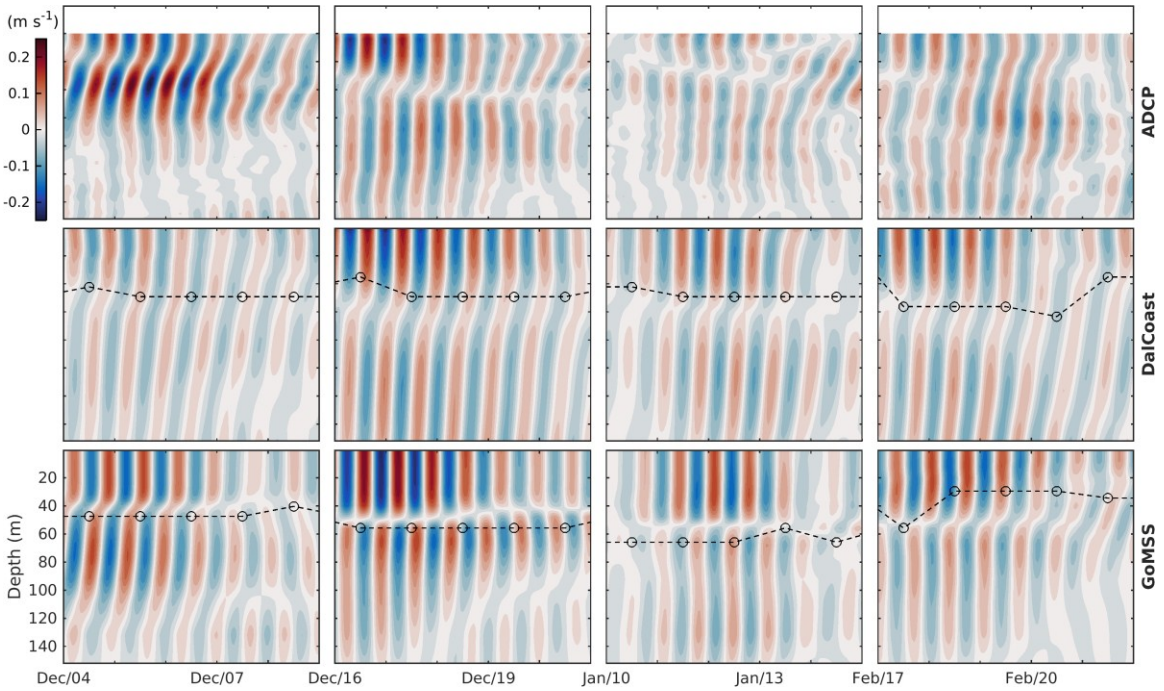

Figure 5.12: Hovmoller plots of band-pass filtered alongshore currents for four periods with relatively strong NIOs at station T2. Each column of 3 panels corresponds to a specific 5 day period defined by the *x*-axis of the bottom panel. The dashed line represents the mixed layer depth estimated from the vertical gradient of density. The top, middle and lower rows are for the ADCP observations, and the DalCoast and GoMSS simulations respectively.

5.5 Summary and Discussion

The near-inertial oscillations (NIOs) on the inner half of the Scotian Shelf were examined using HF-radar and ADCP observations (December 2015 - February 2016), a simple slab model, and two prototype operational shelf circulation models. The most interesting finding is that the observed peak frequency of the NIOs (f_p) varied with time by about 7% of the local inertial frequency (f), as demonstrated in the evolving rotary spectrum (ERS) of the ADCP observations. The variation in f_p can be explained in part by local wind forcing as demonstrated by a simple slab model. The remaining variation of f_p can be

mostly explained by variations in the background vorticity (Eq. (5.1)) associated with changes in the strength and position of the unstable Nova Scotia Current (NSC). The horizontal distribution of f_p estimated from the HF-radar observations shows that it was below f within ~50 km of the coast and slightly above f seaward of this point, consistent with the frequency shifts caused by the changes in background vorticity. This provides additional observational evidence for Eq. (5.1) and modification of f_p by the NSC.

Analysis of the HF-radar and ADCP observations also demonstrated that the NIOs on the inner Scotian Shelf are driven primarily by time variations in wind stress associated with the passage of storms. Individual NIO events typically lasted for three or four inertial periods. NIOs with speeds exceeding 0.25 m/s were observed in the offshore part of the study region but their amplitudes decreased shoreward within ~40 km of the coast, consistent with the effect of decreasing water depth and increasing mixed layer depth as the coast is approached. The observed NIOs during the study period had spatial scales of ~80 km and ~40 km in the along and cross shore directions respectively. The NIO phases varied moving from west to east, consistent with typical movement of winter storms in this region. A relevant study over other locations demonstrates that the coastal suppression of NIOs and the modulation of f_p by the background vorticity found for the Scotian Shelf are consistent with those found off the Oregon coast.

Two prototype operational shelf circulation models (DalCoast and GoMSS) were used to examine the above features in the current observations. These two models use different numerics and different vertical coordinates. Both models reproduce well the spatial structure of the NIOs and, in a qualitative sense, the temporal and spatial variations in f_p. Comparisons of model simulations with the HF-radar and ADCP observations also demonstrated the strengths and weaknesses of the two ocean models. DalCoast benefits from its use of the spectral nudging and semi-prognostic methods. These two methods ensure DalCoast's simulated NSC and background vorticity field remain close to the observed winter mean state in DalCoast. But for the same reason, DalCoast underestimates the low-frequency circulation variability, which further degrades its performance in simulating the time variation of f_p, the spatial scales of the NIOs, and the high mode

variability of the NIOs over the vertical. In contrast, GoMSS allows the model density field to evolve freely and uses more realistic open boundary conditions provided by the Mercator global ocean forecast system. As a result, GoMSS shows a better skill in simulating the low-frequency circulation variability and associated changes in NIOs than DalCoast. However, GoMSS performs less well in simulating the mean circulation and misplaces the position of the NSC, despite the much higher resolution in GoMSS. Reasons for this bias error are currently under investigation.

CHAPTER 6

EFFECTS OF WAVE-INDUCED VERTICAL REYNOLDS STRESS ON OCEAN CURRENTS ON THE SCOTIAN SHELF DURING A WINTER STORM[1]

6.1 Introduction

Surface gravity waves at the air-sea interface play a very important role in transferring momentum and energy from the atmosphere to the ocean. Accurate predictions of ocean currents require proper representations of wave-related processes, which are typically neglected in many numerical simulations of ocean currents. For example, the wind stress (i.e., momentum flux) used in an ocean circulation model is usually parameterized in terms of wind speeds with the wind-dependent drag coefficient C_D (e.g., *Edson et al.*, 2013; *Large and Pond*, 1981). However, the presence of surface waves (sea states) can strongly modify the sea surface roughness and thus C_D (*Donelan et al.*, 2004; *Holthuijsen et al.*, 2012). In addition, surface waves can mediate the momentum flux transferred to the ocean through wave growth and dissipation (e.g., *Perrie et al.*, 2003; *Fan et al.*, 2010). Reductions or enhancements in the momentum transferred from the atmosphere to the ocean due to surface wave growth or dissipation can each reach about 20%-30% (*Perrie et al.*, 2003). The inclusion of the momentum transfer from surface waves to ocean currents due to the wave dissipation was found to significantly improve the simulated nearshore

[1] Wang, P. and J. Sheng. 2018. Effects of wave-induced vertical Reynolds stress on ocean currents on the Scotian Shelf during a winter storm. Submitted to *Journal of Geophysical Research-Oceans*.

currents during extreme weather events such as hurricanes and tropical storms (*Staneva et al.*, 2017; *Wang et al.*, 2017).

From the sea surface to the subsurface water, surface waves can affect the vertical momentum transfer through the wave-enhanced turbulent mixing. For example, the breaking waves can enhance the surface turbulence through the turbulent kinetic energy (TKE) input at the surface (*Craig and Banner*, 1994). The nonbreaking waves can enhance the production of turbulence through an interaction between the wave orbital velocity and the turbulent velocity (e.g., *Qiao et al.*, 2014). The Langmuir circulation, which involves an interaction of the Stokes drift with the mean flow (*Craik and Leibovich*, 1976), is another important wave process that can strongly enhance the mixing of upper ocean (e.g., *Fan and Griffies*, 2014). By accounting for some or all of above-mentioned wave-enhanced mixing processes, numerical circulation models were found to have a better skill in reproducing observed currents and scalar quantities such as temperature and salt (e.g., *Qiao et al.*, 2004; *Wang and Sheng*, 2016; *Wu et al.*, 2015).

Surface waves can also affect the vertical momentum transfer through the wave-induced vertical Reynolds stress components defined as $\overline{\tilde{v}\tilde{w}}$ and $\overline{\tilde{u}\tilde{w}}$ (where $\tilde{u}$, $\tilde{v}$, $\tilde{w}$ are the wave orbital velocities in a Cartesian coordinate system (x, y, z), x is taken to be the direction of wave propagation, y is parallel with wave crests, and z is vertically upward from the mean sea level). Here, $\overline{\tilde{v}\tilde{w}}$ is equivalent to an interaction between the Coriolis force and the Stokes drift ($\mathbf{f} \times \mathbf{U_s}$), known as the Coriolis-Stokes force. *Polton et al.* (2005) showed that the Coriolis-Stokes force can substantially change the mean current profile over the wind-driven surface mixed layer. However, $\overline{\tilde{u}\tilde{w}}$ has usually been neglected in ocean circulation models since $\overline{\tilde{u}\tilde{w}} = 0$ based on the linear wave solution with $\tilde{u}$ and $\tilde{w}$ in quadrature. In practice, however, $\tilde{u}$ and $\tilde{w}$ can be out of quadrature for growing waves (*Mellor*, 2013; *Nielsen et al.*, 2011) and dissipative waves (*Phillips*, 1977; *Deigaard and Fredsoe*, 2011), resulting in non-zero $\overline{\tilde{u}\tilde{w}}$. Recent laboratory experiments made by *Olfateh et al* (2017) also provided reasonable measurements of non-zero $\overline{\tilde{u}\tilde{w}}$ under wind waves. Thus, $\overline{\tilde{u}\tilde{w}}$ is potentially significant since it provides an additional mechanism for the vertical momentum transfer in addition to the turbulent Reynolds stress. *Mellor* (2013) recently found that $\overline{\tilde{u}\tilde{w}}$ is equivalent to a subsurface

projection of the wind pressure correlated with the wave slope. Subsequently, *Mellor* (2013) treated $\overline{\tilde{u}\tilde{w}}$ as a pressure-slope momentum transfer term in an ocean model, and demonstrated improved agreements between simulated and measured temperature in a simple one-dimensional case. *Gao et al.* (2018) adopted the approach of *Mellor* (2013) and found that the inclusion of $\overline{\tilde{u}\tilde{w}}$ can enhance the vertical mixing by 30% in the middle layers in Jiaozhou Bay. Nonetheless, the effects of $\overline{\tilde{u}\tilde{w}}$ on ocean currents remain to be studied.

The main objective of this study is to examine the effects of surface gravity waves on ocean currents, with a special emphasis on the effects of $\overline{\tilde{u}\tilde{w}}$, using a coupled wave-circulation modelling system. The study region is the Scotian Shelf (ScS), which is a rugged open shelf bounded by the Laurentian Channel to the east, the Northeast Channel to the west, and deep waters to the south (Fig. 1.1). The ScS is socially and economically important since it supports commercial and recreational fisheries, marine recreation and tourism, aquaculture, shipping and transportation, and other economic activities that directly contribute to the economic health of the province of Nova Scotia. This region is frequently affected by winter storms associated with high waves and intense ocean currents. A two-way coupled wave-circulation modelling system was recently developed for this region to study the effects of different wave-current interaction mechanisms under extreme weather conditions (*Wang and Sheng*, 2016). For the present study, the wave-induced vertical Reynolds stress $\overline{\tilde{u}\tilde{w}}$ was implemented recently in the coupled wave-circulation modelling system to study its effects on ocean currents over the ScS during Winter Storm "Echo" on 15-16 December 2015. In particular, during this storm, high-quality surface current observations on the inner ScS were collected by the high frequency (HF) radar, which will be used in this chapter to assess the model performance with and without the inclusion of $\overline{\tilde{u}\tilde{w}}$.

The structure of this chapter is organized as below. The observational data provided by the HF-radar and wave buoys are described in section 6.2. The coupled wave-circulation modelling system is described in section 6.3. The model results are presented in section 6.4. The summary and discussion are given in section 6.5.

6.2 Observation

As described in Chapter 5, the HF-radar system consists of two long-range CODAR-Seasonde radars located at Sandy Cove and Clam Harbour off the Atlantic coast of Nova Scotia, Canada. Each radar operates at a central frequency of 4.8 MHz and provides hourly radial surface currents with 6 km resolution and coverage up to 200 km off the coastal radar site. The HF-radar data are generally expected to be accurate to within 0.1 m/s in the current speed and 10^{o} in the current direction. The HF-radar data were found to have relatively good quality in comparison with moored ADCP data. The details on the processing of the HF-radar data can be found in Chapter 5.

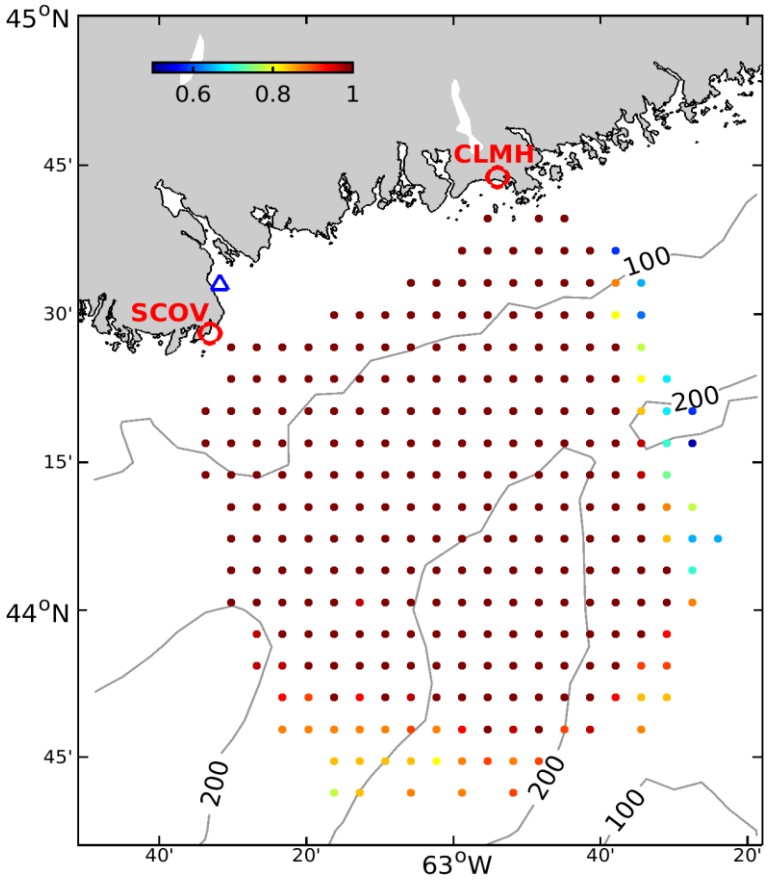

Figure 6.1: Map showing the area covered by the HF-radar on the inner Scotian Shelf. The color coded dots in indicate HF radar data points used in the present study; the color indicates data availability on 15-16 December 2015. Also shown are the HF radar stations (red circles), the Halifax buoy (blue triangle), and water depths (contour lines). Abbreviations are used for Sandy Cove (SCOV) and Clam Harbour (CLMH).

The hourly HF-radar data at grid points with more than 50% temporal coverage (Fig. 6.1) from 1200Z 15 December to 1800Z 16 December 2015 during Winter Storm Echo are used in this chapter. During this period, the HF-radar data coverage is relatively good.

During this storm, hourly surface winds and waves were measured at a shallow water buoy (~35 m) located at the approaches to Halifax Harbor and a deep water buoy 44137 (~4000 m) located at the East Scotia Slope (Fig. 1.1). The Halifax buoy was deployed in 2013 and maintained by the SmartAtlantic (http://www.smartatlantic.ca). Buoy 44137 was maintained by Environment and Climate Change Canada and has been operational since 1988.

6.3 The Coupled Wave-Circulation Modelling System

The two-way coupled wave-circulation modelling system developed for the eastern Canadian shelf in Chapter 3 is used in this chapter. The coupled model consists of a 3D ocean circulation model known as DalCoast, and a third-generation wave model known as WAVEWATCH III (WW3). The wave effects on the 3D circulation are specified in the circulation model using the vortex force formalism (*Bennis et al.*, 2011) and the breaking wave-induced mixing (*Craig and Banner*, 1994). In the wave model, the effects of ocean surface currents on surface waves include the relative wind effect, current-induced convergence, wavenumber shift, and refraction (*Tolman et al.*, 2014). The important effects of these different wave-current interaction mechanisms in the eastern Canadian waters have been demonstrated in previous studies (*Wang and Sheng*, 2016, 2018; *Wang et al.*, 2017). In this study, to examine the effects of the wave-induced vertical Reynolds stress, we follow *Mellor* (2013) and incorporate $\overline{\tilde{u}\tilde{w}}$ in the circulation model through a pressure-slope momentum transfer term associated with a sea-state-dependent wind stress formulation.

6.3.1 Pressure-Slope Momentum Transfer

Eqs. (2.2) and (2.3) are modified to incorporate the pressure-slope momentum transfer term on the right side of the momentum equation,

$$\frac{\partial \hat{u}}{\partial t} + \frac{\partial (\hat{u}+U_s)\hat{u}}{\partial x} + \frac{\partial (\hat{v}+V_s)\hat{u}}{\partial y} + \frac{\partial (\hat{w}+W_s)\hat{u}}{\partial z} - f\hat{v} = -\frac{1}{\rho_o}\frac{\partial p}{\partial x} + fV_s$$

$$+\frac{\partial \hat{u}}{\partial x}U_s + \frac{\partial \hat{v}}{\partial x}V_s - \frac{\partial J}{\partial x} + F_{d,x} + F_{m,x} + \frac{\partial \tau_{P,x}}{\partial z} \tag{6.1}$$

$$\frac{\partial \hat{v}}{\partial t} + \frac{\partial (\hat{u}+U_s)\hat{v}}{\partial x} + \frac{\partial (\hat{v}+V_s)\hat{v}}{\partial y} + \frac{\partial (\hat{w}+W_s)\hat{v}}{\partial z} + f\hat{u} = -\frac{1}{\rho_o}\frac{\partial p}{\partial y} - fU_s$$

$$+\frac{\partial \hat{u}}{\partial y}U_s + \frac{\partial \hat{v}}{\partial y}V_s - \frac{\partial J}{\partial y} + F_{d,y} + F_{m,y} + \frac{\partial \tau_{P,y}}{\partial z} \tag{6.2}$$

where $(F_{m,x}, F_{m,y}) = (\frac{\partial \tau_{T,x}}{\partial z}, \frac{\partial \tau_{T,y}}{\partial z})$, and the turbulent stress $\tau_T = (\tau_{T,x}, \tau_{T,y})$ is

$$\tau_T(z) = (K_M \frac{\partial \hat{u}}{\partial z}, K_M \frac{\partial \hat{v}}{\partial z}) \tag{6.3}$$

where K_M is the mixing coefficient, and $\tau_T(0)$ at the surface is the friction drag which represents the direct molecular interaction at the air-sea interface. The pressure-slope stress $\tau_P = (\tau_{P,x}, \tau_{P,y})$ is,

$$\tau_P(z) = -\overline{\tilde{u}\tilde{w}} = \overline{p_w \frac{\partial \eta}{\partial x}} F_{SS} F_{CC}; \tag{6.4a}$$

$$F_{SS} = \frac{\sinh(k(z+h))}{\sinh kd};\ F_{CC} = \frac{\cosh(k(z+h))}{\cosh kd} \tag{6.4b}$$

where p_w is the surface wind pressure, η is the surface elevation, k is the wavenumber, and $d = h + \eta$ is the total water depth. It is noted that, $F_{SS}F_{CC} = 1$ at the surface, and $\tau_P(0)$ is the correlation of wind pressure and wave slope, known as the wave or "form" drag which arises from a greater integrated pressure on the backward face of a wave than on the forward face (e.g., *Buckles et al.*, 1984). It should be noted that $\frac{\partial \tau_P}{\partial z}$ has the same vertical structure as the Stokes drift velocity (*Mellor*, 2003). *Mellor* (2013) showed that τ_P dominates over τ_T near the surface, while below the surface these two stresses are comparable. In addition, the non-zero value of $\overline{\tilde{u}\tilde{w}}$ leads to a non-zero term $\overline{\tilde{u}\tilde{w}}\frac{\partial \hat{u}}{\partial z}$ in the TKE equation by modifying the shear production term as:

$$S = (\tau_P + \tau_T)\frac{\partial \hat{u}}{\partial z} \tag{6.5}$$

6.3.2 Wind Stress

The surface wind stress has two types, namely: the friction drag $\tau_T(0)$ and the form drag $\tau_P(0)$. Here $\tau_T(0)$ accounts for most of the momentum transfer at wind speeds below 3 m/s, while $\tau_P(0)$ accounts for most of the wind stress at wind speeds above 7.5 m/s (*Donelan*, 1990). By assuming that $\tau_P(0)$ and $\tau_T(0)$ dominate the wind stress at high and low wind speeds respectively, the vertical boundary conditions (*Mellor,* 2013) for (6.1) and (6.2) are given as:

$$\begin{cases} \tau_P(0) = \rho_a C_{DP} |\mathbf{U}_{10r}| U_{10r}, \ \tau_T(0) = 0 & (C_{DP} > C_{DT}) \\ \tau_T(0) = \rho_a C_{DT} |\mathbf{U}_{10r}| U_{10r}, \ \tau_P(0) = 0 & (C_{DP} < C_{DT}) \end{cases} \tag{6.6}$$

where ρ_a is the density of the air, $\mathbf{U}_{10r}$ is the difference between the 10-m wind vector and the surface current vector. The form drag coefficient C_{DP} is defined in terms of the significant wave height H_s and inverse wave age $\frac{\sigma_p U_{10}}{g}$, in which σ_p is the frequency at the peak of the spectrum and $\kappa = 0.41$ is the von Karman constant:

$$C_{DP} = \left[\frac{\kappa}{\ln(z_{10}/z_{0P})}\right]^2, \quad z_{0P} = 1.38 \times 10^{-4} H_s \left(\frac{\sigma_p U_{10}}{g}\right)^{2.66} \tag{6.7}$$

The friction drag coefficient C_{DT} is calculated from the law of the smooth wall, resulting in:

$$C_{DT} = \left[\frac{\kappa}{\ln(z_{10}/z_{0T})}\right]^2, \quad z_{0T} = \gamma \frac{\nu}{u_*} \tag{6.8}$$

where ν is the kinematic viscosity, $u_* = \sqrt{\frac{\tau_a}{\rho_a}}$ is the friction velocity, and $\gamma = 0.11$ (*Edson et al.*, 2013) is the roughness Reynolds number for smooth flow.

6.3.3 Experiment Design and Model Setup

Since the main focus of this study is on the effects of the wave-induced vertical Reynolds stress, model results in three numerical experiments (Table 6.1) are examined. These three experiments include (a) the fully coupled wave-circulation model run (the control run, Run 1), (b) the coupled wave-circulation model run without the inclusion of $\widetilde{\tilde{u}\tilde{w}}$ (i.e., the run

without the pressure-slope momentum transfer) (Run 2), and (c) the circulation-only model run (Run 3). The information about the coupled model setup including the external forcing and open boundary conditions can be found in Chapter 3.

Table 6.1: Model configurations for three numerical experiments.

Experiment	Vortex force formulism	Breaking-wave-induced mixing	Pressure-slope momentum transfer
Run 1	On	On	On
Run 2	On	On	Off
Run 3	Off	Off	Off

6.4 Model Results

6.4.1 Winds and Waves

Figures 6.2a-d present distributions of instantaneous CFSv2 reanalysis winds at four specific times A (1500Z DEC 15), B (2300Z DEC 15), C (0700Z DEC 16) and D (1200Z DEC 16) during Winter Storm Echo. The storm moved from west to east over the Maritimes of Atlantic Canada on 15-16 December 2015, at a translation speed of about 45 km/h. Due to the large-scale structure of the storm, the wind intensity on the ScS was strong (~22 m/s) from about eight hours before (time A, Fig. 6.2a) to eight hours after (time C, Fig. 3c) the passage of the storm. Also shown in Fig. 6.2 are distributions of simulated H_s by WW3 at these four specific times. At times A, B, and C (Figs. 6.2e-g) associated with strong local winds, the distribution of simulated H_s generally follows the wind structure with maximum value of ~7.7 m on the ScS. At time D (Fig. 6.2h) the local winds were weak, but the simulated waves remained strong due to propagations of previously generated swells by the storm. In the later part of the paper, observations and simulations of ocean currents at these four specific times will be further analyzed.

Figures 6.3a-d present time series of observed and reanalyzed winds (speed and direction) at the buoy in Halifax Harbour and buoy 44137 (see Fig. 1.1 for locations). The CFSv2 reanalysis winds at buoy 44137 agree very well with observations, which is

expected since the meteorological observations made at this buoy were assimilated into the model in generating the CFSv2 winds. The reanalysis winds at the Halifax buoy also agree reasonably well with observations except around 23:00 on 15 December, during which the reanalysis winds suggest that the storm's center approximately passed this buoy with rapid changes in speeds and directions, while the observed winds at the Halifax buoy remained strong. It should be noted that wind observations at the Halifax buoy were not used in generating the CFSv2 winds.

Figures 6.3e-h present time series of observed and simulated H_s and peak wave period (T_p) at the two buoys. The observed H_s reached ~4 m at the nearshore location (Halifax buoy) and ~8 m at the offshore location (buoy 44137), and the observed T_p increased from ~3 s to ~11 s during the storm. In comparison, the wave model in the control run (Run 1) reproduces reasonably well the observed H_s and T_p at these two buoys, except that the model underestimates the observed H_s at the Halifax buoy around 00:00 on 16 December due to the underestimated reanalysis winds used by the model.

Figure 6.4 presents calculated $C_D = \max(C_{DP}, C_{DT})$ based on (6.7) and (6.8) sampled over the ScS at 3-h intervals on 15-16 December 2015. For $U_{10} >$ ~7 m/s, the data points at a given U_{10} are highly scattered, indicating the important role of the form drag. For $U_{10} <$ ~3 m/s, by contrast, the data points at a given U_{10} are much less scattered, indicating the dominance of the friction drag. Also shown in Fig. 6.4 is the wind-speed-dependent C_D given by the COARE 3.5 algorithm (Edson et al., 2013), which is a recent comprehensive drag coefficient parameterization fitting well to observations. Thus this algorithm can give a reasonable approximation for the drag coefficient if the sea state is not directly simulated. Figure 6.4 shows that the data points are scattered around the solid line for 3 m/s $< U_{10} <$ 25 m/s, indicating that the mean values of C_D at a given U_{10} produced by the coupled model agree reasonably with those provided by the COARE 3.5 algorithm.

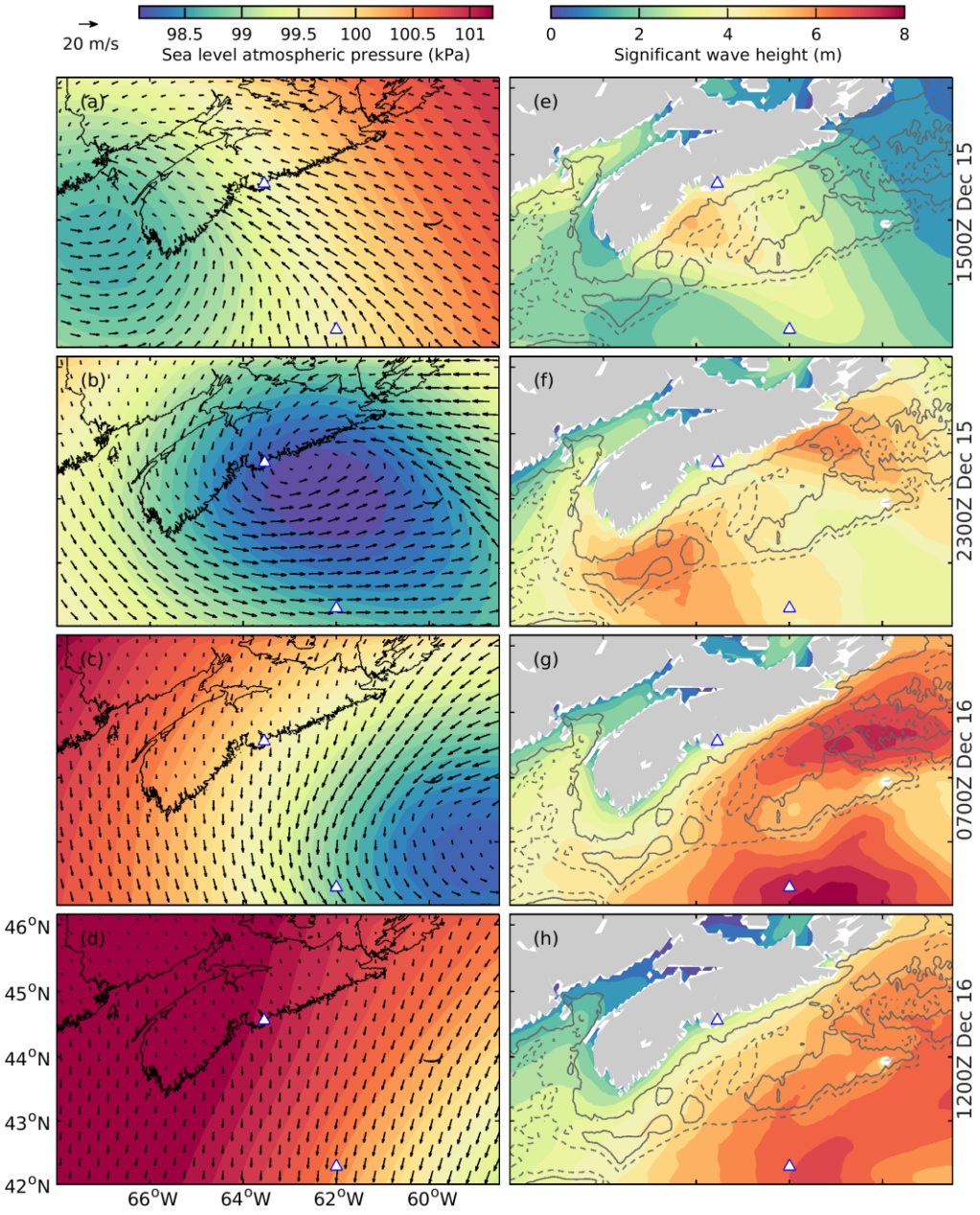

Figure 6.2: Instantaneous distributions of atmospheric forcing (surface winds: vectors; sea level atmospheric pressure: color image) (left) and significant wave heights (right) at four specific times A (1500Z DEC 15), B (2300Z DEC 15), C (0700Z DEC 16) and D (1200Z DEC 16) shown in Figure 4 during Winter Storm Echo. The triangles mark the buoy locations, and the gray solid and dashed contour lines in (e-h) represent the smoothed 100 and 200 m depths, respectively.

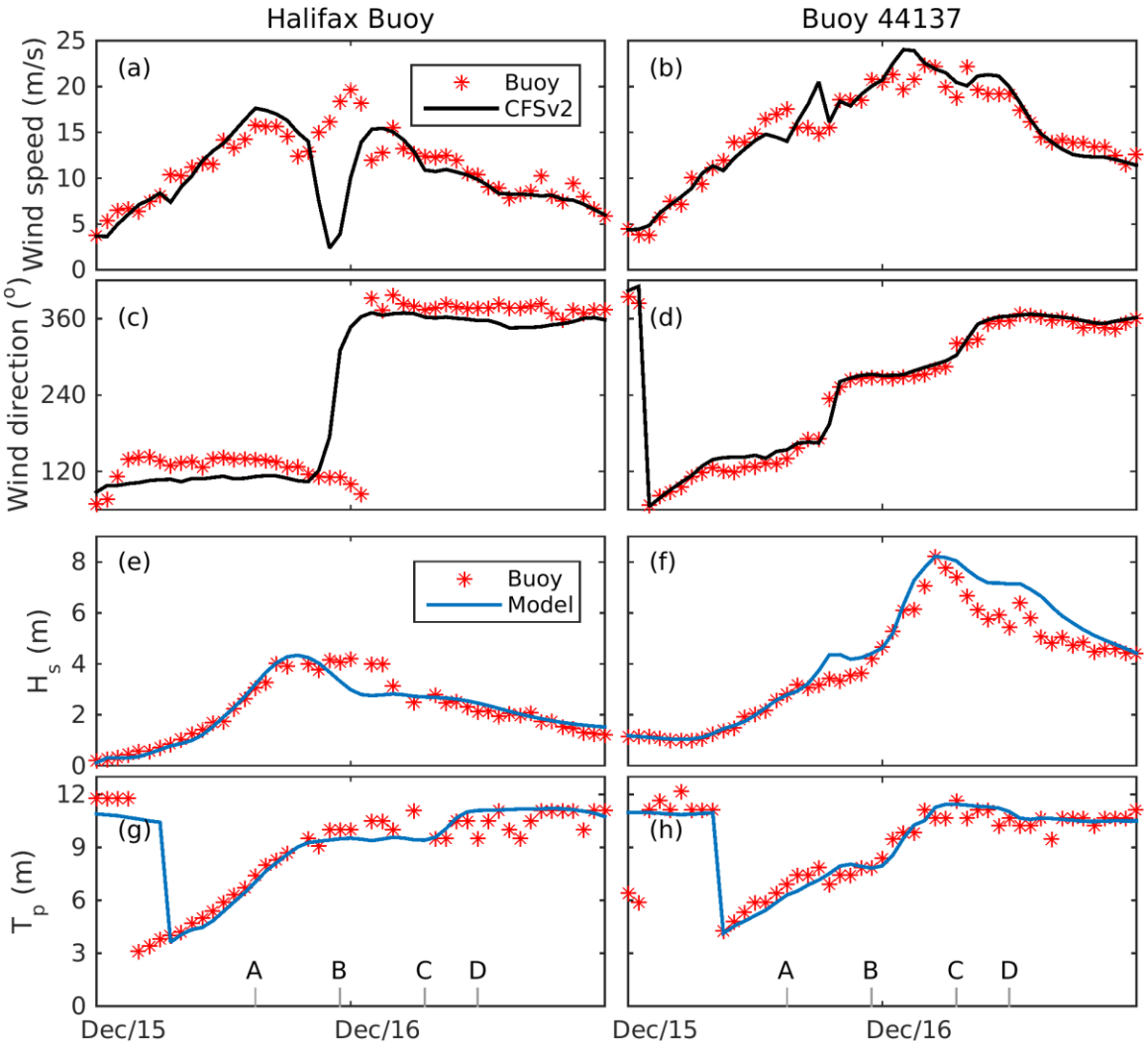

Figure 6.3: Time series of (a-d) observed and reanalyzed wind speed and direction, and (e-h) observed and simulated significant wave height (H_s) and peak period (T_p) in Run 1 at the Halifax buoy and buoy 44137 on 15-16 December 2015. The gray x-axis ticks in (g-h) mark the selected four specific times (A, B, C and D) at which the results are shown in Fig. 6.2.

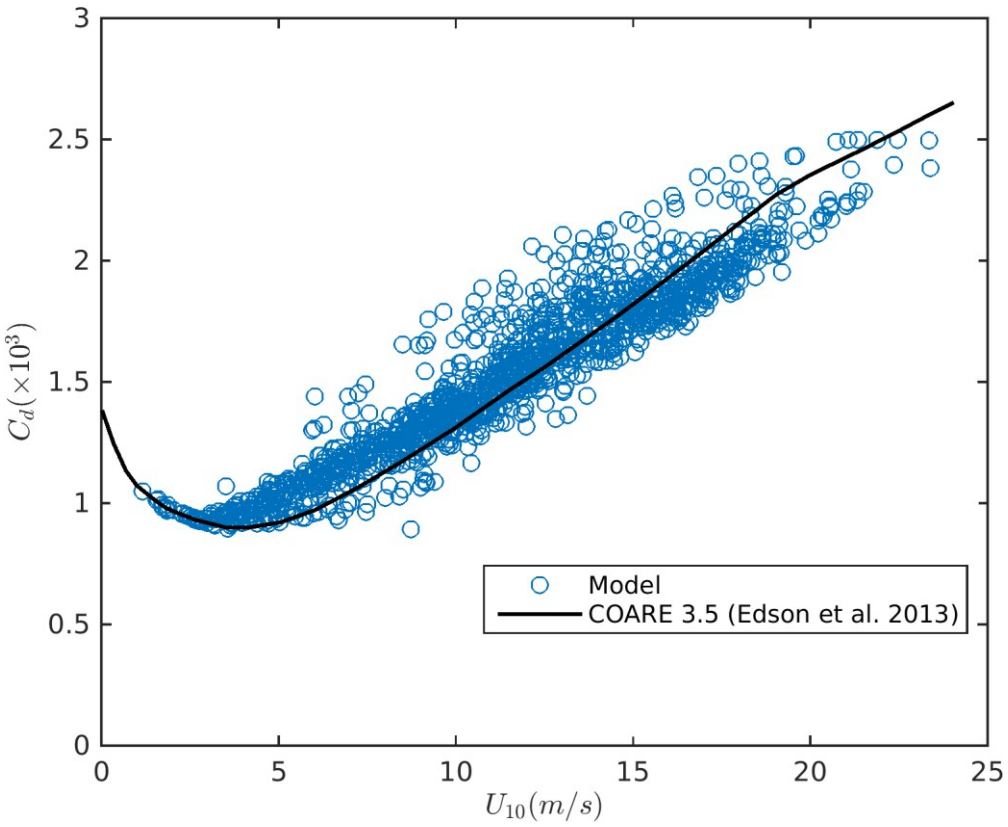

Figure 6.4: The sea-state-dependent drag coefficient ($C_D = max(C_{DT}, C_{DP})$) produced by the coupled model over the study region at 3-h intervals on 15-16 December 2015 (scatter), and wind-speed-dependent C_D given by COARE 3.5 algorithm (Edson et al., 2013).

6.4.2 Currents

We next assess the model performance in simulating surface ocean currents by comparing model results with the HF-radar observations. Figure 6.5 presents time series of wind stress, observed and simulated surface currents spatially-averaged over the HF-radar grid points. Most of the grid points are located on the right side of the storm track (Fig. 6.2) and thus the wind stress shown in Fig. 6.5a rotated clockwise during the storm, which is favorable for generating the clockwise rotating near-inertial oscillations (NIOs) in the North Hemisphere. The observed surface currents (Figs. 6.5b and c) feature an oscillation behavior with a period close to the local inertial period (~17 h), indicating the presence of NIOs. The average amplitude of the NIOs was about 0.27 m/s, which can be roughly estimated from the cross-shore currents that were nearly pure inertial motions. The along-

shore currents, however, are a combination of the wind- and density-driven flow. The density-driven flow is the well-known Nova Scotian current (NSC), a baroclinic alongshore current that runs along the coast to the southwest. The strength of the NSC was strongest in winter and could reach 0.3 m/s (*Dever et al.*, 2016). Because of the effect of the NSC, the intense along-shore currents up to 0.83 m/s were observed at 0700Z on 16 December when the wind-driven flow ran roughly in the same directions as the density-driven flow.

The coupled wave-circulation modelling system in the control run (Run 1) reproduces reasonably well the above observed variations of currents, but the model has deficiencies in reproducing the observed cross-shore currents around 1500Z and 2300Z 15 December due mainly to the less accurate atmospheric forcing used to force the coupled model during this period. By comparison, the coupled model without the inclusion of $\overline{\tilde{u}\tilde{w}}$ (Run 2) and the circulation-only model (Run 3) both overestimate the observed along-shore currents (up to 0.17 m/s) after 0400Z 16 December. To quantify the model performance, we use both the spatial root-mean-square error (RMSE) and the spatial version of the γ^2 statistic defined in Eq. (2.18). Figures 6.5d-g present time series of calculated spatial RMSEs and γ^2 for three model runs. Except around 2300Z 15 December, the RMSE and γ^2 in Run 1 are respectively less than 0.25 m/s and 1.0, indicating that the coupled model has reasonable skill in simulating the storm-induced surface currents. Around 2300Z 15 December when the center of the storm passed the inner ScS, both RMSE and γ^2 for the cross-shore currents in Run 1 are relatively large. This is due mostly to the less accurate reanalysis winds which do not reproduce correctly positions of the storm center during this period, as discussed in Figs. 4a and 4c. In comparison with model results in Run 1, both the RMSEs and γ^2 in Run 2 (i.e., the coupled model run without the effect of $\overline{\tilde{u}\tilde{w}}$) are relatively larger, indicating the importance of $\overline{\tilde{u}\tilde{w}}$. Both the RMSE and γ^2 are the largest in Run 3 (i.e., the circulation-only run) among three model runs, indicating the importance of the effects of surface gravity waves on the currents. It is noted that large reductions in RMSE do not necessarily correspond to large reductions in γ^2, since the RMSE represents the average error and γ^2 (with subtracting the mean) measures the model performance in simulating the spatial variability of currents. Significant reductions of γ^2 from Run 2 to

Run 1 (0600Z-0900Z 16 December for along-shore currents and 0700Z-1500Z 16 December for cross-shore currents) demonstrate the important role of $\overline{\tilde{u}\tilde{w}}$ in improving the simulated spatial variability of currents.

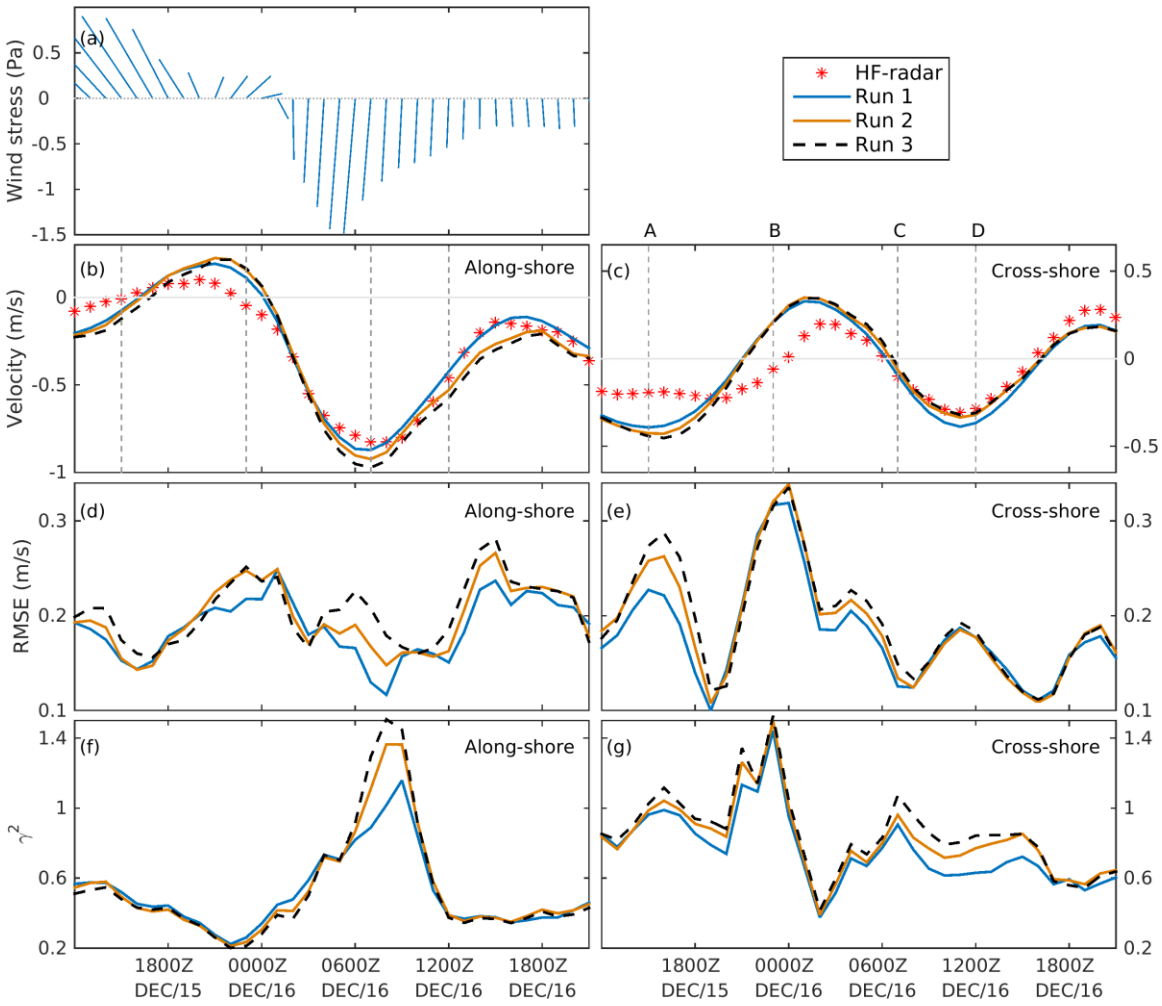

Figure 6.5: Time series of (a) reanalyzed wind stress, (b, c) observed and simulated currents spatially-averaged over the HF-radar grid points, (d, e) spatial RMSEs, and (f, g) spatial γ^2 for three different model runs on 15 and 16 December 2015. The dashed lines in (b-c) mark the selected four specific times (A, B, C and D) at which the results are shown in Fig. 6.6.

6.4.2a Horizontal Distribution

Figure 6.6 presents observed and simulated surface currents on the inner ScS covered by the HF-radar at the above-mentioned four specific times (A, B, C, and D) during the storm.

The winds and simulated H_s during this period are shown in Fig. 6.2. At time A, the eastern periphery of the storm approached the ScS associated with intense onshore winds (up to 22 m/s) (Fig. 6.2a). The HF-radar observations (Fig. 6.6a) feature generally onshore-directed flow but with some small-scale circulation cells near the center of the domain. The coupled model in Run 1 (Fig. 6.6b) reproduces reasonably well the observed onshore-directed flow, but does not reproduce the observed small-scale circulation features, which could be due to the relatively coarse-resolution atmospheric forcing, inadequate model resolution, or imperfect model physics. The model results in Runs 2 and 3 (Figs. 6.6c-d) are similar to those in Run 1, except for overestimated magnitudes by the model in these two runs with the largest overestimation in Run 3.

At time B when the center of the storm passed the inner ScS (Fig. 6.6e), the observed surface currents feature a cyclonic pattern. Model results in all three model runs (Figs. 6.6f-h) also produce a cyclonic circulation pattern but with some deficiencies in simulating its position. This model discrepancy could be mainly caused by the less accurate reanalysis winds used by the model as discussed above.

At time C, the western periphery of the storm approached the ScS associated with strong offshore winds (up to 22 m/s) (Fig. 6.2c). The HF-radar observations feature intense southwestward currents (up to 1.3 m/s), particularly over areas between the 100-200 m isobaths. It should be noted that the observed NSC during this winter month occurred roughly between the 100-200 m isobaths and had a width of about 30 km. Thus, the observed strong surface currents between the 100-200 m isobaths at this time are largely a combination of the wind- and density-driven flow. By comparison, the results in Run 1 (Fig. 6.6j) agree reasonably well with observations, while the results in Run 2 (Fig. 6.6k) overestimate the observed magnitudes of currents, particularly within 60 km of the coast, and the results in Run 3 (Fig. 6.6l) show the largest overestimation among the three model runs.

At time D after the passage of the storm, the local winds were weak (Fig. 6.2d), but the observed surface currents remained relatively strong (0.4-0.8 m/s) (Fig. 6.6m) due to propagations and gradual decay of the storm-induced currents. In comparison with

observations made at the previous time, the currents over the offshore areas (~60 km off the coast) rotated 90°-105° in the clockwise direction (comparing Figs. 6.6m and i), indicating the near-inertial motions. The currents between the 100-200 m isobaths show only a slight rotation (~30 °) due to the presence of the southwestward NSC. Figure 6.6n shows that model results in Run 1 agree reasonably well with observations. By comparison, model results in both Runs 2 and 3 (Figs. 6.6o and p) significantly underestimate the clockwise rotation of currents over the offshore areas, with the largest underestimation by the model in Run 3.

Figure 6.7 further compare the surface current vectors produced by the circulation model in the three runs over a relatively large domain on the ScS at these four specific times. At times A, B, and C (Figs. 6.7a-c), relatively large differences between Runs 1 and 3 are found over areas experiencing strong winds and waves (see Fig. 6.2), indicating the importance effects of surface waves on surface ocean currents. The largest differences occur over shallow banks on the ScS at 0700Z 16 December (Fig. 6.7c) with magnitude changes up to 50% and direction changes up to 40°. By comparison, there are also noticeable differences in model results between Runs 1 and 2, indicating the important effects of $\overline{\tilde{u}\tilde{w}}$. At time D when local winds became weak (Fig. 6.7d), large differences in current directions between Runs 1 and 3 occur over the offshore areas of the ScS where the background mean flow are generally weak. The direction changes are about 20°-30° indicating that the phase of the NIOs in Run 3 lags ~1 h behind those in Run 1. The differences in results between Runs 1 and 2 are also noticeable, indicating again the important effects of $\overline{\tilde{u}\tilde{w}}$ on surface ocean currents.

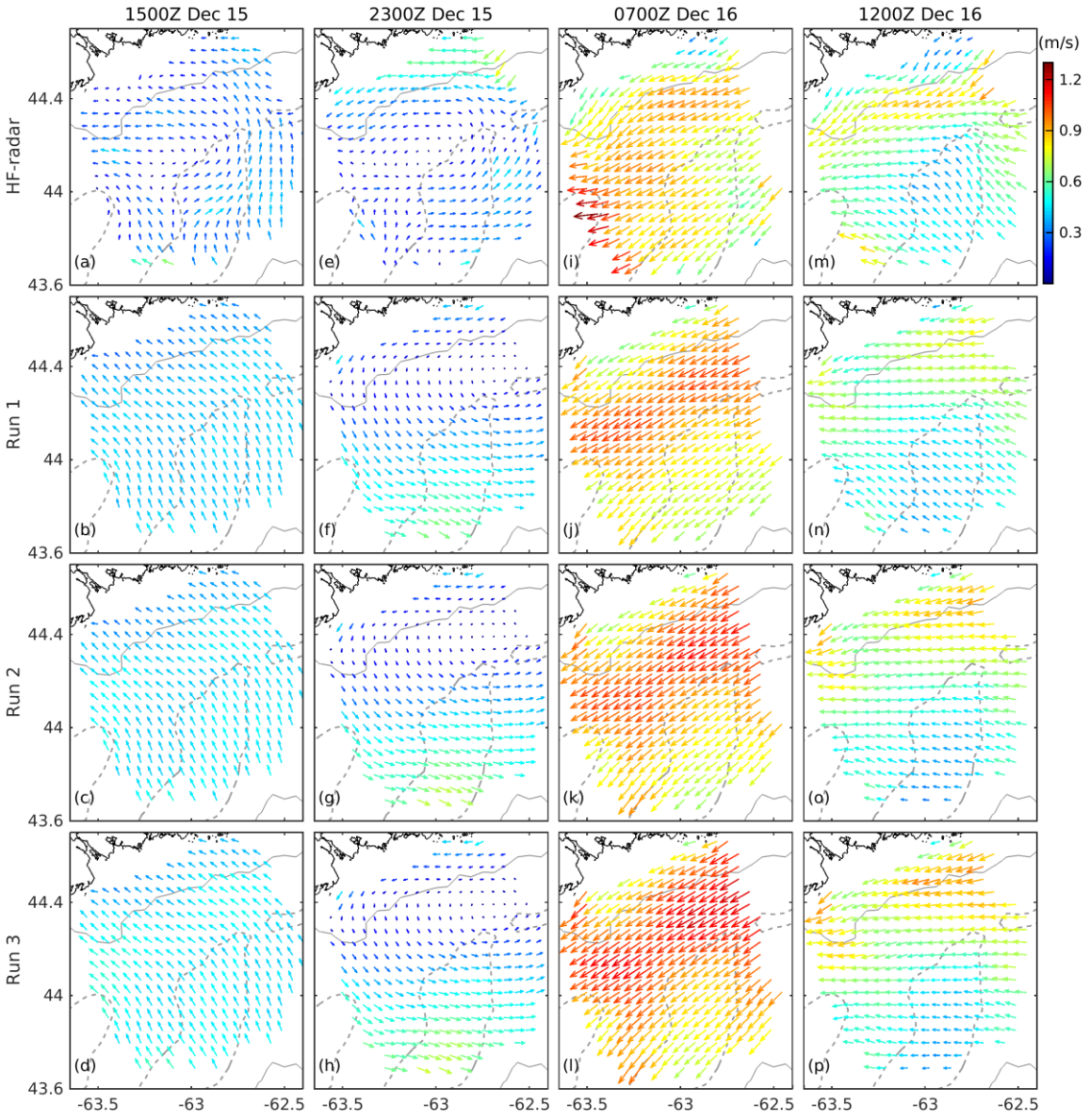

Figure 6.6: Instantaneous distributions of (a-d) observed and (e-p) simulated surface current vectors at four specific times A (1500Z 15 DEC), B (2300Z 15 DEC), C (0700Z 16 DEC) and D (1200Z 16 DEC) shown in Figure 6 during Winter Storm Echo. The gray solid and dashed contour lines represent the smoothed 100 and 200 m depths, respectively.

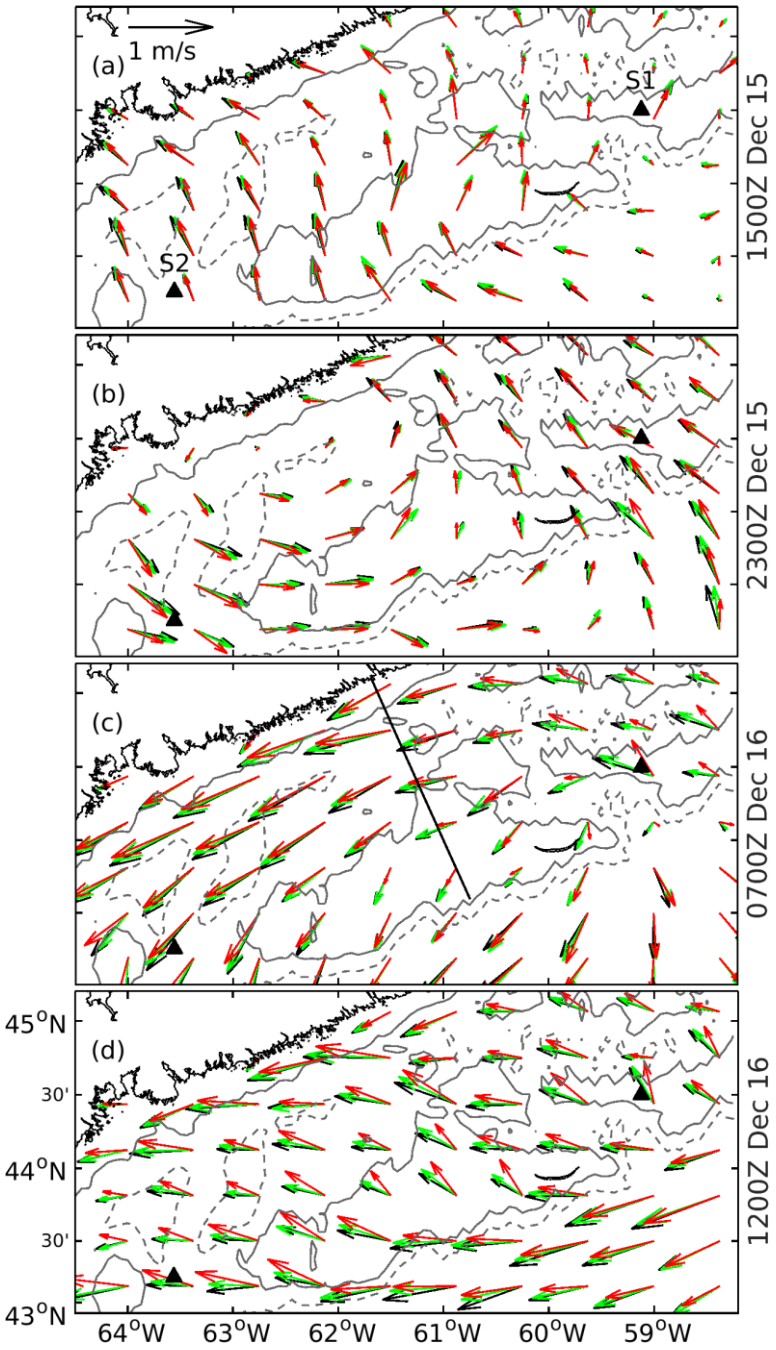

Figure 6.7: Surface current vectors in Run 1 (red), Run 2 (green), and Run 3 (black) at four specific times A (1500Z 15 DEC), B (2300Z 15 DEC), C (0700Z 16 DEC) and D (1200Z 16 DEC) during Winter Storm Echo. The gray solid and dashed contour lines represent the smoothed 100 and 200 m depths, respectively. The black solid line in (c) marks a cross-shore transect where model results are presented in Fig. 6.8, and the black triangles mark two locations (S1 and S2) where model results are presented in Fig. 6.9.

6.4.2b Vertical Distribution

Figures 6.8a-c present vertical distributions of simulated along-shore currents over a cross-shore transect (see Fig. 6.7c for location) on the ScS at 0700Z 16 December when the effects of waves on currents are strongest. Model results in Run 1 (Fig. 6.8a) feature a surface-intensified coastal jet (the NSC) within ~60 km of the coast. Around 100 km off the coast, there is a weak reversal flow near the bottom. Further offshore over the shallow bank, the along-shore currents are weak and nearly uniform in the vertical. By comparison, the simulated along-shore currents in Runs 2 and 3 have stronger near-surface vertical shear than those in Run 1. The differences in the vertical distribution of the along-shore currents between Runs 1 and 2 (Fig. 6.8d) indicate that the effects of $\overline{\tilde{u}\tilde{w}}$ significantly reduce the currents (up to 0.6 m/s) in the near-surface layer. The strongest effects of $\overline{\tilde{u}\tilde{w}}$ occur over the shallow bank, where surface waves significantly modify the currents almost throughout the water column (~37 m water depth). Over the relatively deep waters, the effects of $\overline{\tilde{u}\tilde{w}}$ are mainly confined to the thin surface layer (~5 m). By comparison, the differences in model results between Runs 1 and 3 (Fig. 6.8e) are very similar to those between Runs 1 and 2 (Fig. 6.8d), indicating that, among the wave-related processes considered in this study, $\overline{\tilde{u}\tilde{w}}$ has dominant effects on the vertical distribution of currents.

Figure 6.9 presents the near-inertial band-pass filtered along-shore currents as a function of time and depth at locations with relatively shallow (site S1) and deep water depths (site S2) (see Fig. 6.7 for locations). At site S1, the NIOs in Run 1 (Fig. 6.9a) have magnitudes of ~0.07 m/s, with the downward phase propagation (i.e., upward energy propagation) during the storm. By contrast, results in Runs 2 (Fig. 6.9b) show the upward phase propagation (i.e., downward energy propagation). As a result, the phases of NIOs between Runs 1 and 2 in the upper 20 m water column are very different, resulting in large differences in magnitudes (~0.05 m/s) (Fig. 6.9d). At site S2, the NIOs in Run 1 (Fig. 6.9f) have larger amplitudes (~0.21 m/s) than site S1. By comparing results between Runs 1 and 2 (Figs. 6.9d and e), the inclusion of $\overline{\tilde{u}\tilde{w}}$ in Run 1 enhances the NIOs in the upper water column associated with a deeper pycnocline. (The pycnocline can be inferred from the depth of the 180^o phase difference.) The magnitude changes in NIOs due to $\overline{\tilde{u}\tilde{w}}$ feature a strong near-inertial variation in the upper 100 m water column (Fig. 6.9f). The magnitudes

changes are not in phase with the corresponding NIOs due to the phase lag (~1 h) of NIOs between Runs 1 and 2. Overall, the differences in NIOs between Runs 1 and 3 at the two sites (Figs. 6.9e and i) are very similar to those between Runs 1 and 2 (Figs. 6.9d and h), indicating the dominant effects of $\overline{\tilde{u}\tilde{w}}$ on the vertical distribution of NIOs.

6.5 Summary and Discussion

The effects of surface gravity waves on ocean currents were examined over the Scotian Shelf (ScS) during Winter Storm Echo on 15-16 December 2015 based on numerical model results in this study, with a special emphasis on the wave-induced vertical Reynolds stress $\overline{\tilde{u}\tilde{w}}$. The effects of $\overline{\tilde{u}\tilde{w}}$ were implemented in a coupled wave-circulation modelling system using the pressure-slope momentum transfer derived by *Mellor* (2013). The coupled model performance was assessed by comparing model currents with the observed surface ocean currents made by the high frequency (HF) radar on the inner ScS.

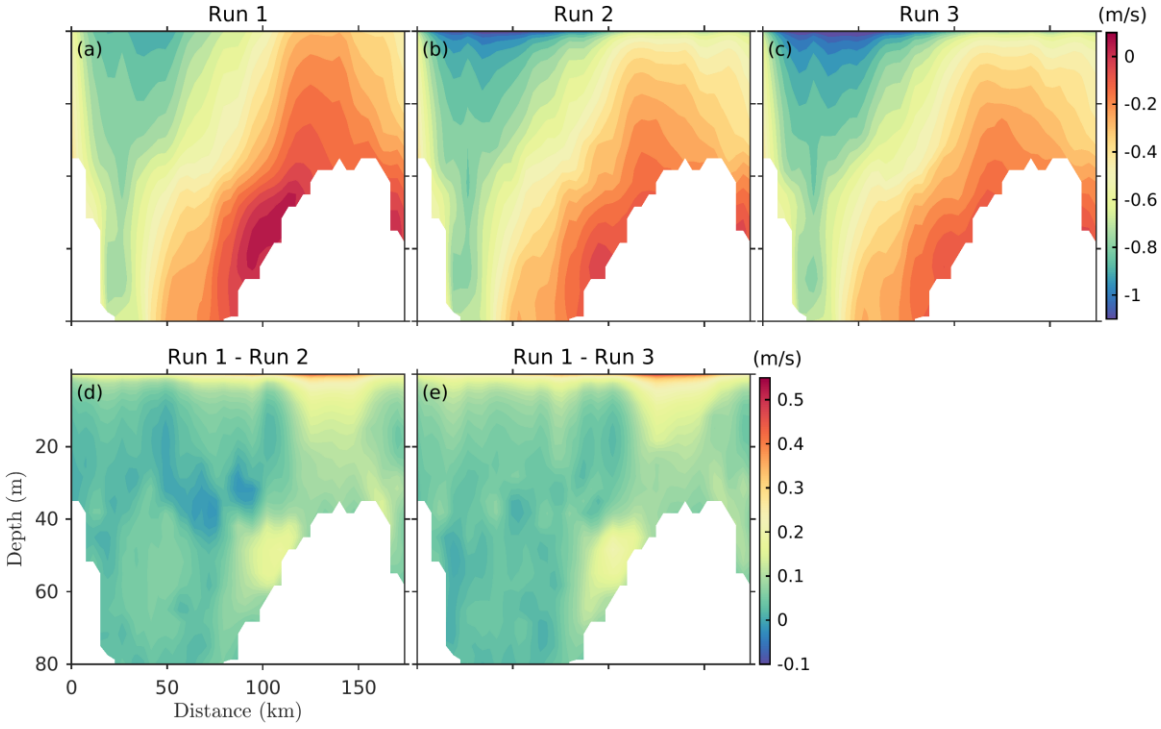

Figure 6.8: Vertical distributions of (a-c) simulated along-shore currents over a cross-shore transect marked in Fig. 6.7c at 0700Z on 16 December 2015, and differences in along-shore currents between (d) Runs 1 and 2, and (e) Runs 1 and 3. In (a-c), negative values indicate southwestward flow and positive values indicate northeastward flow.

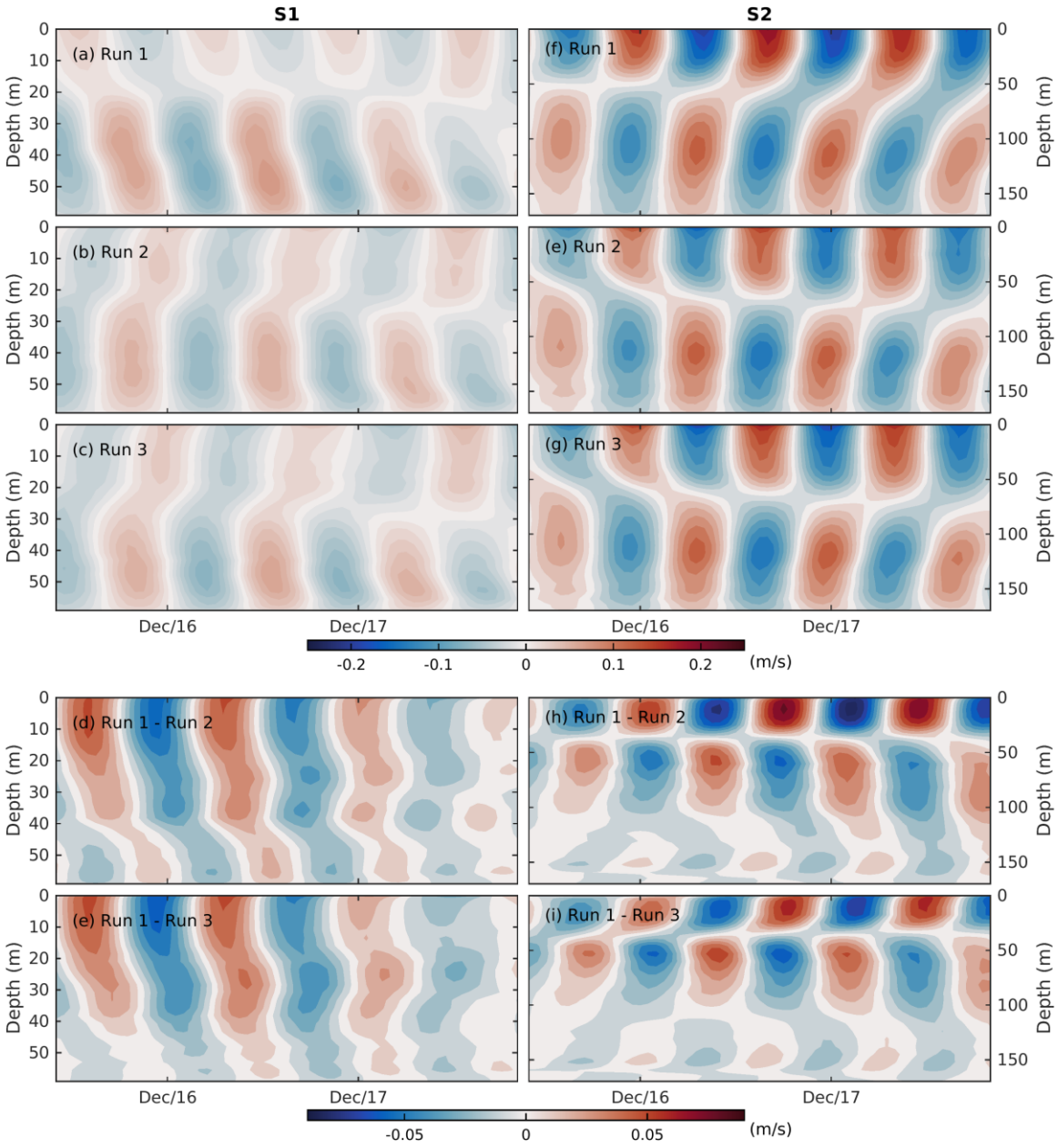

Figure 6.9: Hovmoller plots of near-inertial band-pass filtered along-shore currents in (a, f) Run 1, (b, e) Run 2, (c, g) Run 3, and differences in along-shore currents between (d, h) Runs 1 and 2, and (e, i) Runs 1 and 3 at locations S1 (left) and S2 (right) marked in Fig. 6.7.

The analysis of the HF-radar data demonstrated that the change of wind directions from onshore to offshore during the passage of the storm generated different surface circulations on the inner ScS. Intense surface currents (up to 1.3 m/s) over areas between the 100-200 m isobaths were observed by the HF-radar when strong winds blew offshore and the wind-driven flow ran in nearly the same directions as the density-driven flow (i.e., Nova Scotian Current). By comparison, when strong winds blew onshore, the observed surface currents over the inner half of the ScS were relatively weak (~0.5 m/s). In addition, the HF-radar observations demonstrated intense storm-induced near-inertial oscillations (NIOs) (~0.27 m/s on average), with the wind stress rotating clockwise on the right side of the storm track.

The coupled wave-circulation modelling system reproduced reasonably well the above-mentioned circulation features observed by the HF-radar during Winter Storm Echo. By comparison, the inclusion of the wave-related processes (i.e., vortex force formulism, breaking wave-induced mixing, and $\overline{\tilde{u}\tilde{w}}$) significantly improves the model performance by reducing the surface currents during the passage of the storm and increasing the phase angles of currents over the offshore areas after the passage of the storm. Furthermore, the effects of $\overline{\tilde{u}\tilde{w}}$ were found to play a dominant role among these wave-related processes. The largest effects of $\overline{\tilde{u}\tilde{w}}$ occur over the shallow banks on the ScS, where the inclusion of $\overline{\tilde{u}\tilde{w}}$ substantially reduces the vertical current shear by modifying the currents (up to 0.6 m/s) throughout the water column (~37 m). Over the relatively deep waters, the effects of $\overline{\tilde{u}\tilde{w}}$ are mainly confined to the thin surface layer (~5 m). In addition, the effects of $\overline{\tilde{u}\tilde{w}}$ can strongly modify the storm-induced NIOs in terms of their magnitudes, phases, and vertical propagation. Over the shallow banks, the inclusion of $\overline{\tilde{u}\tilde{w}}$ leads to an upward near-inertial energy propagation which could be attributable to bottom reflection. Over the relatively deep waters, the phase of NIOs shifts forward about one hour due to the inclusion of $\overline{\tilde{u}\tilde{w}}$, resulting in better agreement with the HF-radar observations. The results in this study indicate that, in addition to the turbulent Reynolds stress, the wave-induced vertical Reynolds stress is another important process that transfers wind momentum to the water column. The fact that the wind momentum is partly transferred by the surface wave motion should be acknowledged in future ocean circulation models.

This chapter only examined the important effects of $\overline{\tilde{u}\tilde{w}}$ in the case of a particular

winter storm with moderate wind speeds (i.e., less than 30 m/s). It should be noted that this is our first step toward understanding the role of $\overline{\tilde{u}\tilde{w}}$ on the ocean circulation. A future study will be conducted to examine the effects of $\overline{\tilde{u}\tilde{w}}$ on ocean currents during hurricane conditions with high wind speeds. Another interesting research direction for future work is how the effects of $\overline{\tilde{u}\tilde{w}}$ could affect the oceanic mixed layer development over a longer period.

CHAPTER 7

CONCLUSIONS

My doctoral research was motivated by the growing interest of the ocean science community in the subject of wave-current interactions (WCIs) associated with developments of WCI theories and a coupled wave-circulation modelling system. The main objective of my thesis was to examine the potential effects of WCIs, as well as contributions from different WCI mechanisms, on surface gravity waves and three-dimensional (3D) ocean circulation over the coastal and shelf waters of the eastern Canadian shelf. The methodologies taken in this thesis included the development, validation, and analysis of model results produced by a two-way coupled wave-circulation modelling system. The coupled modelling system consists of a 3D circulation model based on the Princeton Ocean Model (POM) and a third-generation wave model based on WAVEWATCH III (WW3) or Simulating WAves Nearshore (SWAN). The circulation model and the wave model were coupled externally using a dynamic coupling software known as OpenPALM. The WCI mechanisms considered in the wave model include the relative wind effect, current-induced convergence, refraction and wavenumber shift. The WCI mechanisms considered in the circulation model include the 3D surface wave forces (formulated through the concept of vortex force or radiation stress), the breaking wave-induced mixing, and the wave-induced vertical Reynolds stress (formulated through the pressure-slope momentum transfer). The coupled model was used to conduct different numerical experiments to examine (a) the nonlinear feedback of surface waves on ocean currents in Lunenburg Bay during Hurricane Juan, (b) the interaction between surface waves and ocean currents over the eastern Canadian shelf during three severe storm events, (c) the semidiurnal tidal modulation in surface waves in the Gulf of Maine, and (d) the effects of wave-induced vertical Reynolds stress on ocean currents on the central Scotian

Shelf adjacent to Halifax during a winter storm.

7.1 Summary of Main Research Results

The research work conducted for Lunenburg Bay of Nova Scotia focused on applications of a two-way coupled wave-circulation modelling system over coastal waters and the performance assessment of two different methods for the effect of surface gravity waves on 3D ocean currents (EWC). These two methods are the vortex force (VF) formulation suggested by Bennis et al. (2011) and the latest version of radiation stress (RS) formulation suggested by Mellor (2015). For demonstrating the proper implementation of these two methods in the coupled wave-circulation system, the coupled wave-circulation modelling system was first applied in two idealized test cases of surf-zone scales. Model results in the two test cases demonstrated that the latest version of the RS formulation suggested by Mellor (2015) has difficulties in producing the undertow over the surf zone. The coupled system was then applied to Lunenburg Bay of Nova Scotia during Hurricane Juan in 2003. The coupled wave-circulation modelling system using either the VF or RS formulations generated much stronger and more realistic 3D circulation in the Bay during Hurricane Juan than the circulation-only model, demonstrating the importance of surface wave forces to the 3D ocean circulation over coastal waters. By comparison with the VF formulation, the RS formulation was found to generate some weak unphysical currents outside the wave breaking zone due to a less reasonable representation for the vertical distribution of the RS gradients over a slopping bottom. These weak unphysical currents are significantly magnified in a two-way coupled system when interacting with large surface waves, degrading the model performance in simulating currents at one observation site. Our results demonstrated that the VF formulation, with a separation between the conservative and non-conservative 3D wave forces, is able to produce reasonable results for applications over coastal waters during extreme weather events. The RS formulation requires a complex wave theory rather than the linear wave theory for the approximation of a vertical RS term to improve its performance under both breaking and non-breaking wave conditions.

The research work conducted on the southwestern part of the eastern Canadian shelf (ECS) focused on interactions between surface gravity waves and ocean currents during

three severe weather events using the coupled wave-circulation modelling system. The simulated significant wave heights (H_s) and peak wave periods were used to reveal the importance of WCIs during and after the storm. In the two fast-moving hurricane cases, the maximum H_s was found to reduce by more than 11% on the right-hand side of the storm track and increase by about 5% on the left-hand side due to different effects of WCIs on waves on two sides of the track. The dominant WCI mechanisms on surface waves (i.e., the effect of currents on waves, ECW) include the current-induced modification of wind energy input to the wave generation, and current-induced convergence and refraction. In the slow-moving winter storm case, the effect of WCIs was found to decrease the maximum H_s on both sides of the storm track due to the relatively small current gradient, which is affected by the storm size and translational speed. The simulated sea surface temperature (SST) cooling induced by hurricanes and SST warming induced by the winter storm are also enhanced (up to 1.2^{o}C) by the WCI mechanisms on circulation and hydrography. The 3D wave forces can affect water columns up to 200 m in all three storm cases. By comparison, the effect of breaking wave-induced mixing in the ocean upper layer is more important under strong stratification conditions in two hurricane cases than under weak stratification conditions in the winter storm case.

The study conducted in the Gulf of Maine (GoM) examined the tidal modulation in surface gravity waves over this region based on in-situ observations and numerical results produced by the coupled wave-circulation modelling system. Analysis of observational data demonstrated significant semidiurnal tidal modulations in the mean wave variables for swell-dominated waves in the region. The observed tidal modulation features significant spatial-temporal variabilities, with large magnitudes near the mouth of the GoM. Observations also demonstrated an unusual timing of the maximum H_s modulation in the following tidal currents. The coupled wave-circulation modelling system successfully reproduced the observed tidal modulation and associated spatial-temporal variabilities. Model results demonstrated that the maximum H_s modulations are first generated during the maximum flood or ebb tide near the mouth of the GoM, and then propagate onto the inner Gulf. Around the mouth of the GoM, tidal currents have strong spatial gradients, resulting in great effects of current-induced convergence, refraction, and wavenumber shift.

The tidal modulation in H_s generated by convergence (10-14%) is less affected by the wave propagation direction than the modulation generated by the wavenumber shift (6-10%) and refraction (4-20%). The latter varies significantly with the changes in the wave propagation direction. In addition, the current-enhanced dissipation becomes important during high winds by reducing at least half the H_s modulation during the study period. The observed unusual timing of the maximum H_s modulation in the following tidal currents can be mostly explained by the convergence and wavenumber shift associated with wave energy convergence and energy transfer from currents to waves in spatially deaccelerating currents.

The research work conducted on the central Scotian Shelf (ScS) adjacent to Halifax first examined the near-inertial oscillations (NIOs) over this region using observations, using a simple slab model and two operational shelf circulation models. The high-frequency (HF) radar and ADCP observations from December 2015 to February 2016 showed that individual NIO events forced by time-varying wind stress associated with the passage of storms typically lasted for three or four inertial periods. The NIOs with speeds exceeding 0.25 m/s were observed in the offshore part of the study region but their amplitudes decreased shoreward within ~40 km of the coast, consistent with the effect of decreasing water depth and increasing mixed layer depth as the coast is approached. The NIOs had spatial scales of ~80 km and ~40 km in the along and cross shore directions respectively. The NIO phases varied moving from west to east, consistent with typical movement of winter storms in this region. Evolving rotary spectral analysis reveals that the peak frequency (f_p) of the NIOs varied through time by ~7% of the local inertial frequency. The variation in f_p can be explained in part by local wind forcing as demonstrated by the slab model. The remaining variation of f_p can be mostly explained in terms of variations in the background vorticity associated with changes in the strength and position of the Nova Scotia Current, an unstable baroclinic boundary current that runs along the coast to the southwest. Two operational shelf circulation models are used to examine the above features in the HF-radar and ADCP observations. The models reproduce the spatial structure of the NIOs and, in a qualitative sense, the temporal variations in f_p.

The above-mentioned HF-radar data during a particular winter storm (Winter Storm

Echo) in December 2015 were used to further study the effects of surface gravity waves on ocean currents, with a special emphasis on the wave-induced vertical Reynolds stress ($\overline{\tilde{u}\tilde{w}}$). The analysis of the HF-radar data demonstrated the intense surface currents (up to 1.3 m/s) induced by this storm when strong winds blew offshore with the wind- and density-driven flow running nearly in the same direction over the inner ScS. The analyses of HF-radar observations also demonstrated intense NIOs (~0.27 m/s on average) associated with clockwise-rotating wind stress on the right side of the storm track. The coupled wave-circulation modelling system was used to simulate the surface waves and 3D circulations during Echo. The coupled model reproduced reasonably well the observed circulation features. The inclusion of the wave-related processes, particularly $\overline{\tilde{u}\tilde{w}}$, was found to significantly improves the model performance by reducing the surface currents during the storm and increasing the phase angles of currents over the offshore areas after the storm. The largest effects of $\overline{\tilde{u}\tilde{w}}$ were found to occur over the shallow banks, where $\overline{\tilde{u}\tilde{w}}$ substantially reduces the storm-induced vertical current shear by modifying the currents throughout the water column. The effects of $\overline{\tilde{u}\tilde{w}}$ can also strongly modify the storm-induced NIOs in terms of their magnitudes, phases, and vertical propagation. The model results indicate that, in addition to the turbulent Reynolds stress, the wave-induced Reynolds stress is another important process that transfers wind momentum to the water column.

The most important findings of my PhD research include:

- The inclusion of various WCI mechanisms in the coupled model significantly improves the model performance over coastal and shelf waters, particularly during extreme weather events, based on comparisons of model results with in-situ measurements made with buoys and ADCPs, and remote sensing data from satellites and HF radars.
- In comparison with the latest 3D radiation stress formulation, the vortex force formulation is a relatively better approach for the 3D wave force in simulating the 3D ocean currents over coastal waters under hurricane conditions.
- Analyses of observations and model results demonstrate significant semidiurnal tidal modulations in surface waves in the GoM, which can be mostly explained by

the effects of strong spatial variability of tidal currents on surface waves near the mouth of the Gulf.

- The peak frequency of the NIOs on the ScS can be modulated by the background vorticity associated with changes in the strength and position of the Nova Scotia Current.
- In addition to the turbulent Reynolds stress, the wave-induced vertical Reynolds stress $\overline{\tilde{u}\tilde{w}}$ (i.e., pressure-slope momentum transfer) is another important process that transfers wind momentum to the water column.

7.2 Future Work

Although significant achievements were made in this thesis on examining the effects of WCIs on the surface gravity waves and 3D ocean circulation over the eastern Canadian shelf, there are more scientific questions remaining to be addressed.

The VF formulation was found to be a relatively better approach than the RS formulation for applications over coastal waters in Chapter 2. The scientific debate between these two formulations, however, is still going on and no consensus has been reached so far (*Ardhuin et al.*, 2017; *Mellor,* 2017). Recently, attempts have been made to improve the RS formulation by *Xia* (2017) and *Ji et al.* (2017), which showed some improved performances of the modified RS formulation under non-breaking waves. Therefore, future improvements on the 3D wave force formulations, especially for the RS formulation, can be expected, and new formulations can be readily tested in idealized test cases and realistic applications discussed in Chapter 2.

In Chapter 4, the coupled wave-circulation modelling system was applied successfully to examine the semidiurnal tidal modulation in surface gravity waves in the GoM, particularly near the mouth of the GoM. The tidal modulation can also be significant over coastal areas of this region associated with strong tides and tidal currents, which, however, cannot be well resolved by the present setup of the coupled wave-circulation modelling system used in this study due to its relatively coarse spatial resolution. In the future, high resolution nested-grid modelling system can be developed over some socially and

economically important coastal waters of this region, such as the Saint John Harbor in the Bay of Fundy, to examine the tidal modulation in surface gravity waves in shallow water.

The HF-radar data presented in Chapter 5 demonstrated the strong time-varying coastal boundary current (i.e., Nova Scotia Current, NSC) on the ScS during winter months. The presence of the NSC can be expected to have strong influence on the surface wave field over this region through the current-induced wave convergence and refraction. Given the relatively good skill of the circulation model (DalCoast) in simulating the observed NSC by the HF-radar, the coupled model developed in this thesis is a good candidate to be used to further examine the effects of the NSC on surface gravity waves on the ScS. Moreover, the HF-radar unit located at Sandy Cove also provides continuous ocean surface wave measurements over a wide area on the ScS. After careful processing and quality-control, these wave measurements can provide a unique dataset to study the surface wave dynamics as well as the effect of WCIs on surface waves, together with the concurrently measured surface ocean currents over this region.

In Chapter 6, the important role of the wave-induced vertical Reynolds stress $\overline{\tilde{u}\tilde{w}}$ was examined in the case of a particular winter storm with moderate wind speeds (i.e., less than 30 m/s). However, the effects of $\overline{\tilde{u}\tilde{w}}$ on ocean currents during hurricane conditions with high wind speeds remain to be studied. Another interesting issue is how the effect of $\overline{\tilde{u}\tilde{w}}$ could affect the oceanic mixed layer development over a longer period.

Finally, although significant efforts were made to account for all important WCI mechanisms in this thesis, some mechanisms were not considered and left for future studies. For an example, the nonbreaking waves and the Langmuir circulation are recognized to be important processes that could strongly enhance the upper-ocean mixing. However, it is still an open scientific question on how to properly incorporate these two mechanisms, with many different parameterizations proposed for the nonbreaking wave-induced mixing (e.g., *Aijaz et al.*, 2017; *Pleskachevsky et al.*, 2011; *Qiao et al.*, 2004) and the Langmuir turbulence-induced mixing (e.g., *Ardhuin and Jenkins*, 2006; *Fan et al.*, 2014; *McWilliams and Sullivan et al.*, 2000) in the literature. The wave-induced bottom shear stress is another important mechanism that can strongly affect the nearshore circulation in very shallow

water and surf zone. It is also one of the most important parameters in modelling the coastal sediment transport. Future implementations of these mechanisms in the coupled model need to be carefully examined with available observations.

APPENDIX A

SENSITIVITY STUDY FOR THE STOKES DRIFT ESTIMATION

Accurate calculation of the Stokes drift velocity is important for the coupled wave-circulation modelling system to have satisfactory performances. For my thesis work, the horizontal Stokes drift velocity $\mathbf{U}_{\mathrm{s(2D)}}$ was calculated based on Eq. (2.7) from the 2D wave spectrum. In many applications, however, it is desirable to calculate the Stokes drift velocity $\mathbf{U}_{\mathrm{s(bulk)}}$ based on bulk wave parameters (e.g. significant wave height H_s, mean wave length L and mean wave direction θ_m) such as

$$(U_s, V_s) \cong \sqrt{\frac{2\pi}{L} g tanh(2\pi d/L)}\, \frac{2\pi}{L} \frac{H_s^2}{16} \frac{\cosh(4\pi(z+h)/L)}{\sinh^2(2\pi d/L)} (cos\theta_m, sin\theta_m) \qquad \text{(A.1)}$$

Since an ocean wave model such as WW3 and SWAN usually provides the calculation of these bulk wave parameters, the use of (A.1) makes a coupled modelling system to be computationally efficient by reducing the computing time and the amount of data transferred between wave and circulation models. Apparently, (A.1) and (2.7) are the same only when the wave variance density E is equally distributed in its frequency-direction bins. In practice, locally wind-generated ocean surface gravity waves are usually associated with large values of k and σ. The remotely generated swells, by comparison, are associated with small values of k and σ. Consequently, in (A.1), the contribution from locally generated waves is always underestimated, and the contribution from swell waves is overestimated. This error could become very large when the sea state is complicated under extreme weather events. To demonstrate this, we compute both $\boldsymbol{U}_{s(2D)}$ and $\boldsymbol{U}_{s(bulk)}$ in three storm events discussed in Chapter 3 (Fig. A.1). In comparison with those calculated from the 2D wave spectrum, the Stokes drift velocity calculated from the bulk

parameters are significantly underestimated by a factor of 2-3 for all three storm cases. Moreover, the use of (A.1) does not generate well the cyclonic pattern of the Stokes drift velocity in the fast-moving hurricane cases, since the contribution from locally generated waves is underestimated. The difference between directions of $\boldsymbol{U}_{s(2D)}$ and $\boldsymbol{U}_{s(bulk)}$ indicates although the wave fields are strongly affected by remotely generated swells under a fast-moving hurricane, the Stokes drift velocity is mainly determined by the locally generated waves. Therefore, under severe weather events, the Stokes drift velocity should be calculated from the 2D wave spectrum to ensure an accurate representation of the coupling between the wave and circulation models.

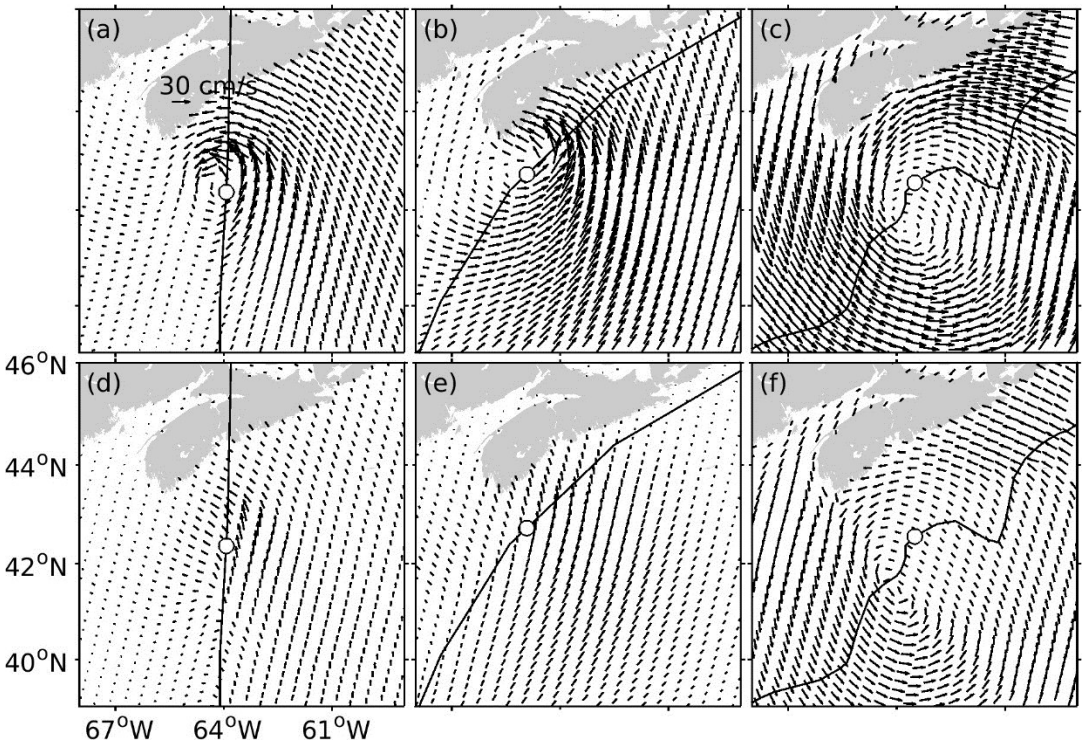

Figure A.1: Distributions of horizontal Stokes drift velocities calculated from (upper panels) the 2D wave spectrum and (lower panels) bulk wave parameters for cases of (a, d) Hurricane Juan, (b,e) Hurricane Bill, and (c,f) White Juan. The open circle at the storm track represents the current position of the storm center.

APPENDIX B

EFFECTIVE WIND SPEED IN THE PRESENCE OF CURRENT

For a mean wind speed U_r at a reference height z_r, drag coefficient $C_D(z_r)$ at this reference height, and the air density ρ_a, the surface wind stress is given by $\tau = \rho_a C_D(z_r) U_r^2$. In the absence of surface ocean currents, we can have an expression for τ using either the geostrophic winds (U_G) at the top of the planetary boundary layer ($z_r = G$) or winds at the 10 m height (U_{10}),

$$\tau = \rho_a C_D(G) U_G^2 = \rho_a C_D(10) U_{10}^2 \tag{B.1}$$

By introducing a surface ocean current velocity of U and assuming the geostrophic wind velocity does not adjust in the presence of the ocean currents, the geostrophic winds and the winds at the 10 m height relative to the currents are given as $(U_G - U)$ and U_{10r}, respectively. We have,

$$\tau_r = \rho_a C_D(G)(U_G - U) = \rho_a C_D(10) U_{10r}^2 \tag{B.2}$$

Combing (B.1) and (B.2) yields,

$$U_{10r} = U_{10} - \alpha U,\ \alpha = \sqrt{C_D(G)/C_D(10)} \tag{B.3}$$

The drag coefficient is a function of roughness length z_0, defined as,

$$C_D(z_r) = \left(\frac{\kappa}{\ln(z_r/z_0)}\right)^2 \tag{B.4}$$

where $\kappa = 0.4$ is the von Karman constant. The coefficient α is found be ~0.7 with a typical value of 1000 m for G and a typical value of 0.0002 m for z_0.

APPENDIX C

EOF ANALYSIS

A modified form of the empirical orthogonal function (EOF) analysis was used in my thesis work to quantify the near-inertial variability of the HF-radar observations and the simulations from DalCoast and GoMSS in Chapter 5. For simplicity of discussion, we assume the hourly current observations, or hourly simulations produced by a specific model, are defined at m grid points and denote the currents at a given grid point and time by (u, v).

To extract variations in the near-inertial band, a band-pass filter with cut-off periods of 20 and 15 hours is used to time series of each component at a given grid point. (Missing values in an observed time series are replaced by the mean of the legitimate values.) The band-pass filtered time series is denoted by $(\tilde{u}, \tilde{v})$ and the complexified time series is formed by $\tilde{u} + i\tilde{v}$ for each of the m grid points. The $m \times m$ covariance matrix is calculated from the complexified time series and its eigenvectors (the EOFs) and eigenvalues are denoted by φ_k and λ_k, respectively, where $k = 1, \ldots, m$. Each φ_k is scaled such that $\phi_k' \phi_k = 1$ and the phase of the mean of its elements is zero. Each eigenvector corresponds to a complex spatial pattern, or mode, defined over the grid. The time-varying complex amplitude (α_k) associated with each spatial pattern is calculated by projecting the m band-pass filtered currents for a given time onto φ_k. The covariance matrix is Hermitian and so, in accord with standard EOF analysis. All of the eigenvalues are real and the proportion of total variance (i.e., the trace of the covariance matrix) explained by the kth mode is $\frac{\lambda_k}{\sum \lambda_j}$.

APPENDIX D

NEAR-INERTIAL OSCILLATIONS OFF THE OREGON COAST

To examine the relevance of the study on the Scotian Shelf (Chapter 5) to other locations, we analyzed the HF-radar observations made off the coast of Oregon for a three month period in 2017. This region has a similar latitude (45-47^{o}N) to the Scotian Shelf (~44^{o}N) and also features a seasonally-varying, buoyancy-driven coastal boundary current (*Mazzini et al.*, 2014). Near-inertial oscillations (NIOs) have also been observed in this region (*Kim and Kosro*, 2013) similar to the Scotian Shelf.

Figure D.1a shows the mean surface current off Oregon from October to December 2017 based on hourly HF radar-observations. A northward surface buoyancy-driven flow, reaching peak speeds between about 0.1 to 0.2 m/s, is evident within ~25 km of the coast. Figure D.1b shows the spatial distribution of the amplitude of NIOs for the same period. In accord with the results of our study on the Scotian Shelf, the NIOs are suppressed within ~20 km of the Oregon coast. This is consistent with the study of *Kim and Kosro* (2013) based on an analysis of two years (2007-2008) of HF-radar observations. They term the suppression "coastal inhibition" (*Kundu et al.*, 1983).

We next selected two locations (O1 and O2, Fig. D.1a) associated with relatively strong background vorticity and NIOs in order to examine the effect of the background vorticity on the temporal changes of f_p. Again, we used the slab model driven by reanalysis winds to quantify the effect of local wind forcing on the temporal changes of f_p. In accord with the approach used for our study of the Scotian Shelf we selected decay timescales λ^{-1} based on visual examination of the time series of observed currents and the shape of the associated rotary spectra. This resulted in decay scales of 3.5 and 3 inertial periods at O1

and O2 respectively.

Rotary spectral analysis (Figs. D.2a-b and Figs. D.3a-b) shows reasonable agreement between the slab model simulations and the HF-radar observations in the near-inertial band at both locations. The evolutionary rotary spectra (ERS, Figs. D.2c-e and Figs. D.3c-e) show that the vorticity correction based on the background vorticity improves the f_p simulated by the slab model, particularly around (i) 12 October and 15 November at O1, and (ii) 20 October, 15 November, and 20 December at O2. This provides additional observational evidence for the relative vorticity correction given by Eq. (5.1).

Overall, the coastal suppression of NIOs and the modulation of f_p by the background vorticity found off the Oregon coast are consistent with our findings for the Scotian Shelf. This provides support for the relevance of the Scotian Shelf study to other locations.

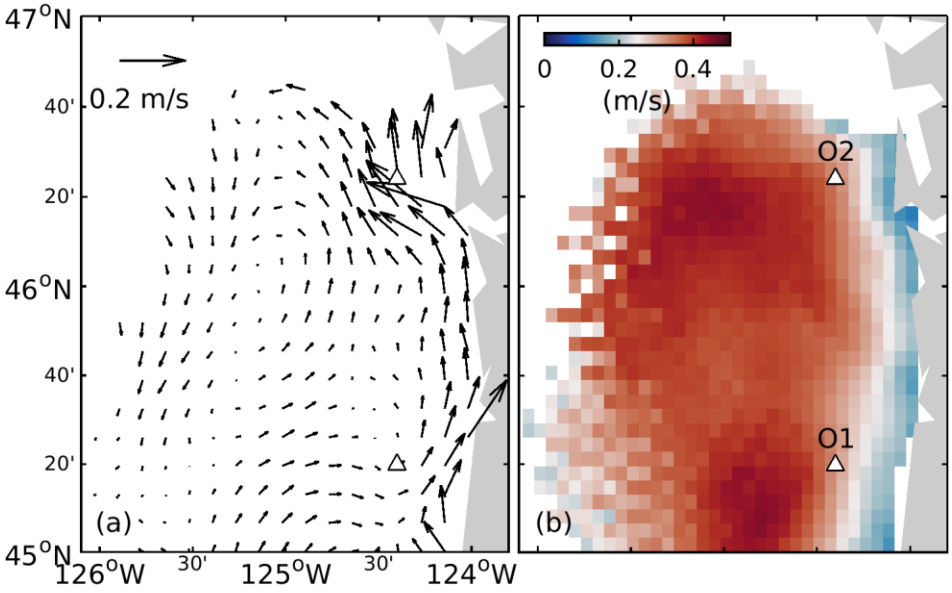

Figure D.1: (a) Mean surface current vectors, (b) and distributions of amplitudes of NIOs observed by the HF-radar off Oregon from October to December 2017.

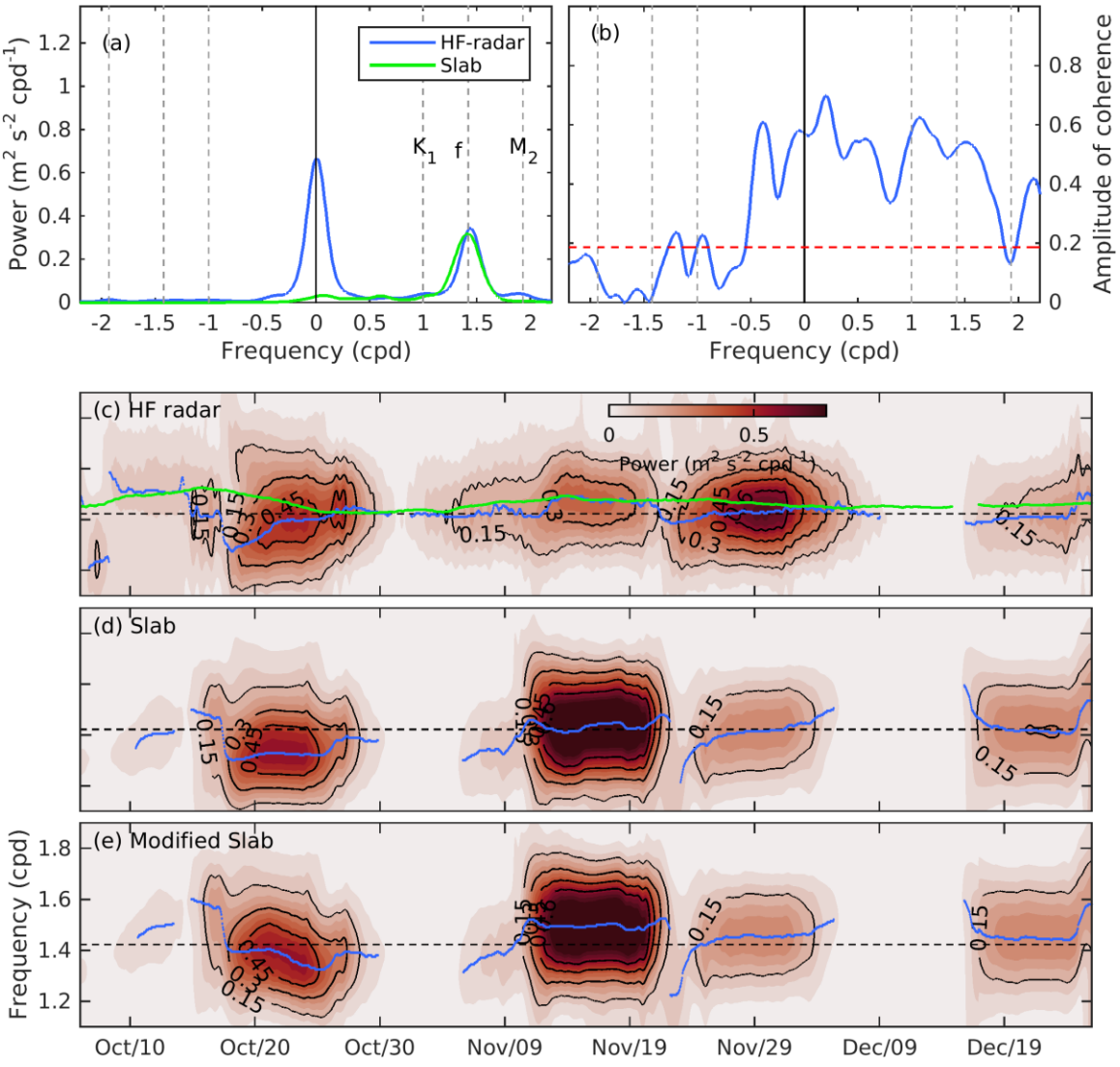

Figure D.2: Rotary spectral analysis of observed surface currents at O1 and simulations by the slab model. (a) Rotary spectra (b) magnitude of the coherence between the HF-radar and slab model simulations. The red dashed line in (b) is the 1% significance level. A Parzen spectral window of width 0.252 cpd was used to estimate (a) and (b). (c) The evolving rotary spectrum (ERS) of the HF-radar observations. The green line represents the effective inertial frequency $(f_e = f + \zeta/2)$ where ζ was estimated from current fields observed by the HF-radar. (d) ERS of slab model simulations. (e) Same (d) except that the ERS of the slab model simulations has been shifted at each frequency by $\zeta/2$. All ERS were calculated using a 10 d sliding window and a spectral window of width 0.379 cpd. The frequency axis is limited to the near-inertial band. The black dashed lines represent the local inertial frequency $(\omega = f)$ and the blue lines show the peak frequency f_p (plotted only for frequencies with relatively high near-inertial energy).

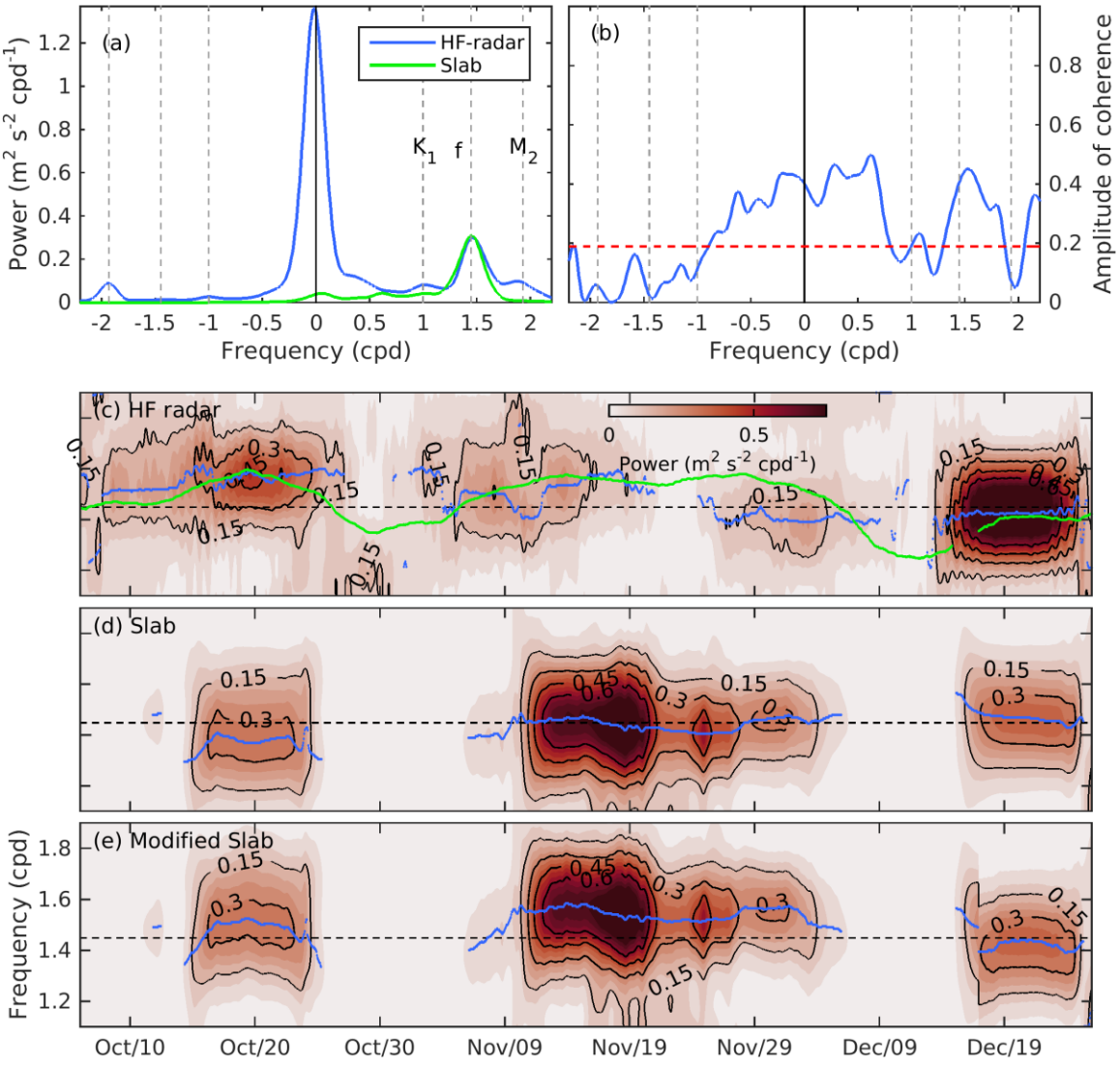

Figure D.3: Similar to Fig. D.2 but for location O2.

APPENDIX E

TYPICAL MODEL OUTPUT AND PRELIMINARY VALIDATION

Simulations of SST and current for a typical winter storm: A strong storm crossed the Scotian Shelf around December 16, 2015. (See Fig. 5.5 for time history of the wind at T2.) Snapshots of simulated surface currents and SST before, during and after the passage of the storm are shown in Fig. E.1.

Before the storm (Figs. E.1a and b), the surface currents simulated by both DalCoast and GoMSS are dominated by the strong tidal flow out of the Bay of Fundy and Gulf of Maine. Both model results also agree on the flow through the western side of Cabot Strait but differ on the outer shelf and adjacent deep waters. During the storm (Figs. E.1c and d), both models produce similar surface circulation on the Scotian Shelf. This is to be expected because they are forced by the same winds. After the passage of the storm (Fig. E.1e and f), the surface circulation is dominated by the tidal flow into the Bay of Fundy and Gulf of Maine. The NSC is also reinforced in both models but, further offshore, differences persist. The main reason for the above differences in these two model simulations is that DalCoast uses the spectral nudging and semi-prognostic methods to restore its density field to an observed seasonal climatology, while GoMSS is purely prognostic and simulates more variability in the large-scale circulation such as the Gulf Stream meanders and spin off eddies.

Validation using coastal sea level observations: The observed and simulated sea level for Halifax (see Fig. 5.1 for location) were first decomposed into tidal and non-tidal components using the analysis package of Pawlowicz et al. (2002). To quantify model

performance, we use the γ^2 statistic described in Eq. (2.18). The observed tides (Fig. E.2a) are predominantly semidiurnal and have a spring-neap variation of about 0.5 m. The observed non-tidal component (Fig. E.2b) includes several surges associated with winter storms. Both models reproduce reasonably well the tide and non-tidal component; γ^2 is 0.03 and 0.05 for tide and 0.17 for non-tidal component. These values are consistent with previous studies (e.g., *Shan et al*. 2016).

Validation using HF-radar current observations: Figure E.3 presents the horizontal distribution of γ^2 for the along-shore (left panels) and cross-shore (right panels) currents. The γ^2 distributions for the along-shore currents (Figs. E.3a and c) are similar for both models with the highest values in the vicinity of the NSC. The lowest γ^2 (below 0.4) are found close to the coast. The γ^2 distributions for the cross-shore currents (Fig. E.3b and d) are generally aligned with the cross-shore direction with the highest values near the edges of the grid. DalCoast performs better than GoMSS for this component of flow. Overall, for both models, there is similarity between the large-scale features in the distributions of γ^2 and the maps of GDOP for both flow components. This implies that observation errors have a significant effect on the assessment of model performance. Nevertheless, the γ^2 values are less than 0.6 over most of the grid indicating that both models have some skill in simulating the currents observed by the HF-radar.

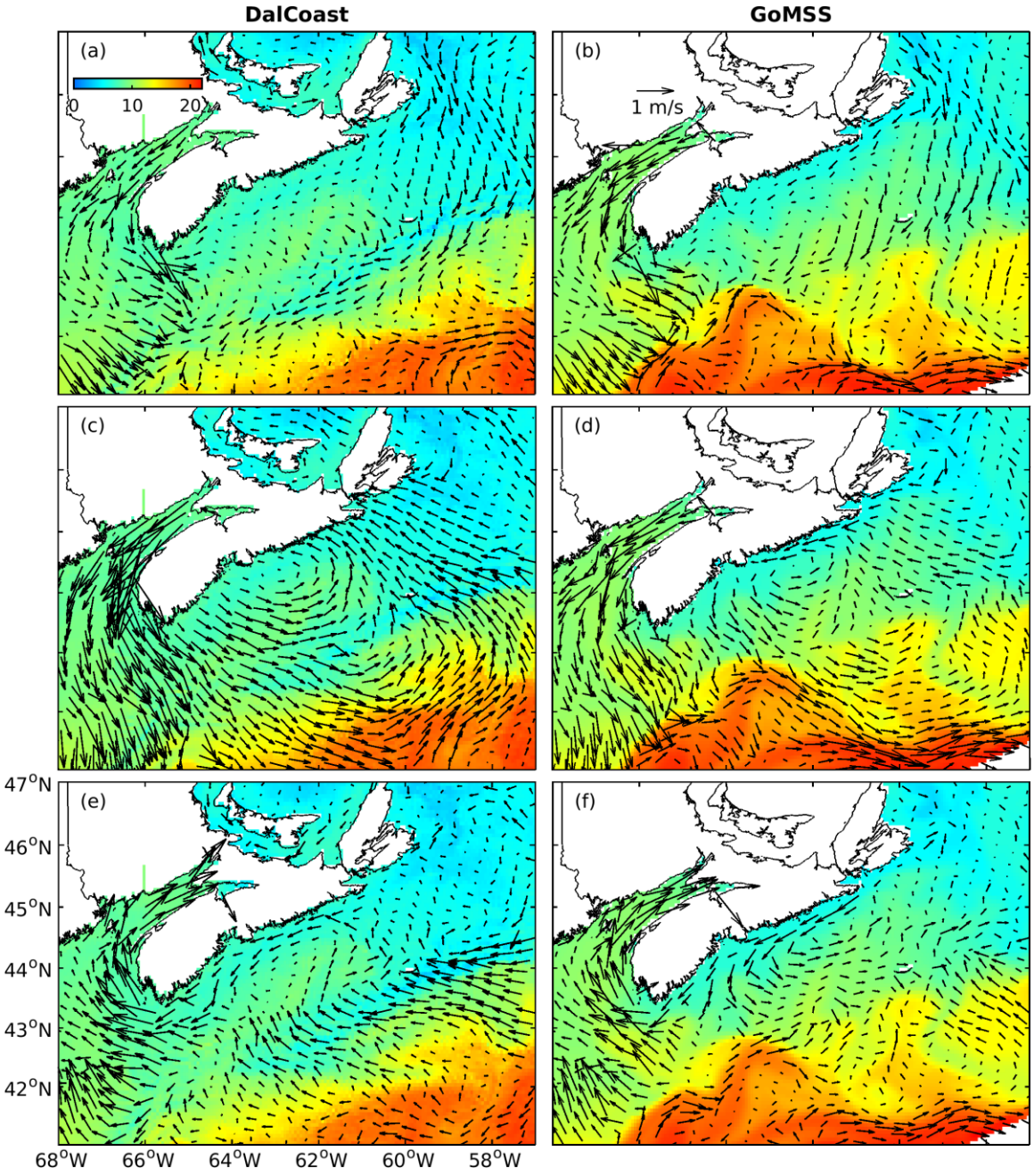

Figure E.1: Snapshots of simulated surface currents and SST (a, b) before, (c, d) during and (e, f) after the winter storm on 16 December. The left and right panels are for DalCoast and GoMSS respectively. The colorbar for SST is given in (a) and the velocity scale is given in (b).

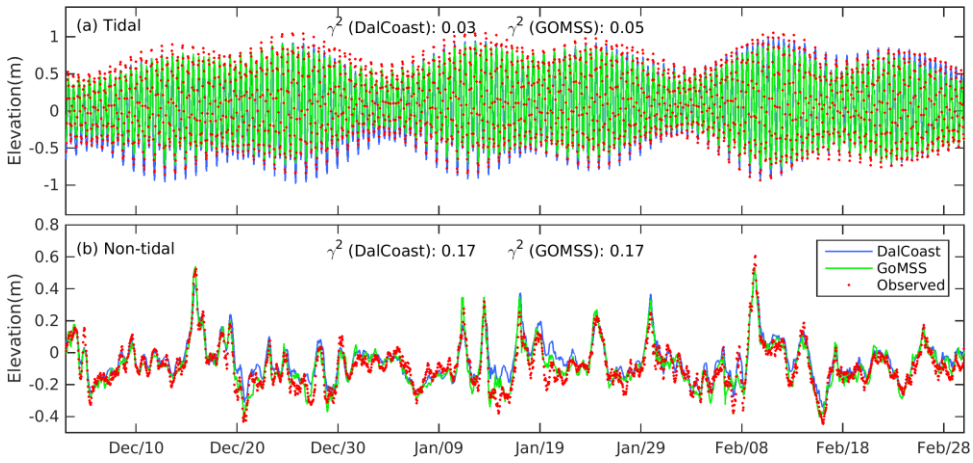

Figure E.2: Time series of observed and simulated (a) tidal and (b) non-tidal sea surface elevations at a tide gauge in Halifax Harbour. The observed and simulated sea surface elevations are decomposed into tidal and non-tidal components using the MATLAB package T_TIDE.

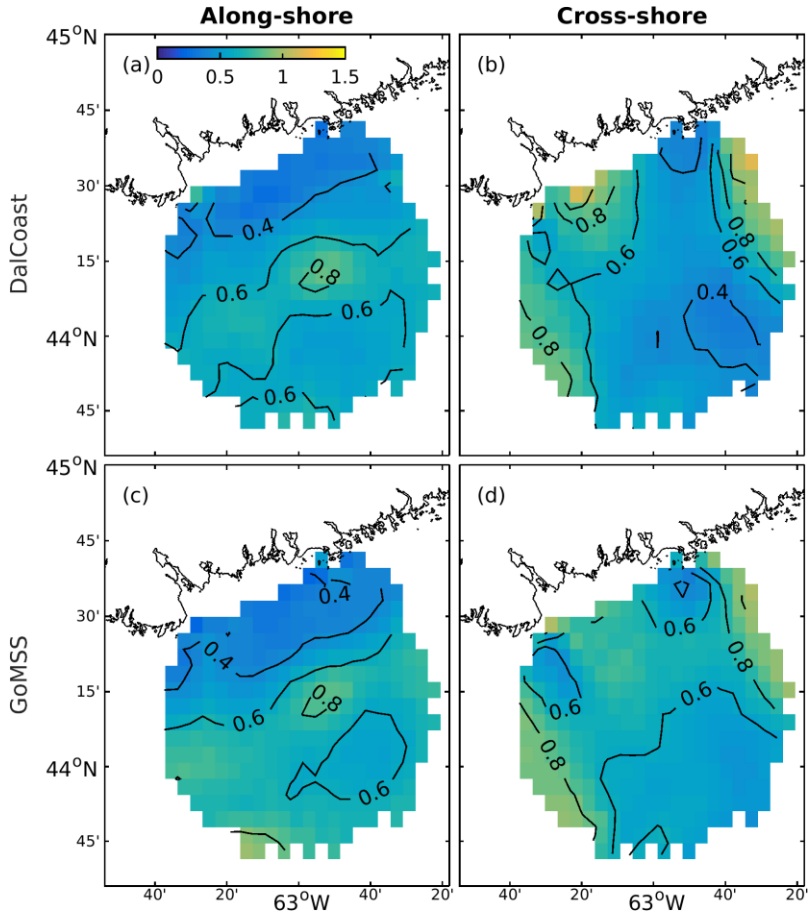

Figure E.3: Distributions of γ^2 for the along-shore (left) and cross-shore (right) currents produced by DalCoast and GoMSS, respectively.

APPENDIX F

COPYRIGHT PERMISSION

Title: Assessing the performance of formulations for nonlinear feedback of surface gravity waves on ocean currents over coastal waters

Author: Pengcheng Wang,Jinyu Sheng,Charles Hannah

Publication: Continental Shelf Research

Publisher: Elsevier

Date: 15 August 2017

LOGIN

If you're a copyright.com user, you can login to RightsLink using your copyright.com credentials. Already **a RightsLink user** or want to learn more?

Please note that, as the author of this Elsevier article, you retain the right to include it in a thesis or dissertation, provided it is not published commercially. Permission is not required, but please ensure that you reference the journal as the original source. For more information on this and on your other retained rights, please visit: https://www.elsevier.com/about/our-business/policies/copyright#Author-rights

BACK CLOSE WINDOW

Order Completed

Thank you for your order.

This Agreement between Pengcheng Wang ("You") and John Wiley and Sons ("John Wiley and Sons") consists of your license details and the terms and conditions provided by John Wiley and Sons and Copyright Clearance Center.

Your confirmation email will contain your order number for future reference.

printable details

License Number	4398230452012
License date	Jul 29, 2018
Licensed Content Publisher	John Wiley and Sons
Licensed Content Publication	Journal of Geophysical Research: Oceans
Licensed Content Title	A comparative study of wave-current interactions over the eastern Canadian shelf under severe weather conditions using a coupled wave-circulation model
Licensed Content Author	Pengcheng Wang, Jinyu Sheng
Licensed Content Date	Jul 31, 2016
Licensed Content Volume	121
Licensed Content Issue	7
Licensed Content Pages	30
Type of use	Dissertation/Thesis
Requestor type	Author of this Wiley article
Format	Electronic
Portion	Full article
Will you be translating?	No
Title of your thesis / dissertation	WAVE-CURRENT INERACTIONS IN THE EASTERN CANADIAN WATERS
Expected completion date	Oct 2018
Expected size (number of pages)	220
Requestor Location	Pengcheng Wang 1355 Oxford Street PO BOX 15000 Halifax, NS B3H 4R2 Canada Attn: Pengcheng Wang
Publisher Tax ID	EU826007151
Total	0.00 CAD

Perriello, Rebecca <rperriello@ametsoc.org>

Mon 2018-11-05 11:45 AM

To: Pengcheng Wang <Pengcheng.Wang@Dal.Ca>;

Cc: permissions@ametsoc.org <permissions@ametsoc.org>;

Dear Pengcheng,

This signed message constitutes permission to use the material requested below.

You may use your JPO article as part of your PhD thesis with the following conditions:

+ please include the complete bibliographic citation of the original source, and
+ please include the following statement with that citation: ©American Meteorological Society. Used with permission.

Thank you for your query. If you need any further information, please feel free to contact me.

Best regards,

Rebecca Perriello
Senior Peer Review Support Associate &
Permissions Specialist

American Meteorological Society
45 Beacon Street, Boston, MA 02108
permissions@ametsoc.org | ametsoc.org

On Mon, Nov 5, 2018 at 10:34 AM, Pengcheng Wang <Pengcheng.Wang@dal.ca> wrote:

> Dear Rebecca,
>
> Thank you for your quick response. Please find the information below,
>
> Article title: Tidal modulation of surface gravity waves in the Gulf of Maine
> Authors: Pengcheng Wang and Jinyu Sheng
> Name of the journal: Journal of Physical Oceanography

BIBLIOGRAPHY

Aijaz, S., M. Ghantous, A. V. Babanin, I. Ginis, B. Thomas, and G. Wake (2017). Nonbreaking wave–induced mixing in upper ocean during tropical cyclones using coupled hurricane-ocean-wave model. *J. Geophys. Res. Oceans*, 122(5), 3939-3963.

Alford, M. H., J. A. MacKinnon, H. L. Simmons, J. D. and Nash (2016). Near-Inertial Internal Gravity Waves in the Ocean. *Annu. Rev. Mar. Sci.*, 8, 95-123.

Anderson, C., and P. Smith (1989). Oceanographic observations on the Scotian Shelf during CASP. *Atmos. Ocean*, 27, 130-156, doi:10.1080/07055900.1989.9649331.

Andrews, D. and M. Mcintyre (1978). An exact theory of nonlinear waves on a Lagrangian-mean flow. *J. Fluid Mech.*, 89(04), 609, doi:10.1017/s0022112078002773.

Anderson, D. L. T., and A. E. Gill (1979). Beta dispersion of inertial waves. *J. Geophys. Res.*, 84, 1836-1842.

Ardhuin, F. (2018). Ocean waves in geosciences, doi:10.13140/RG.2.2.16019.78888/3.

Ardhuin, F., A. Jenkins, and K. Belibassakis (2008a). Comments on "The Three-Dimensional Current and Surface Wave Equations". *J. Phys. Oceanogr.*, 38(6).

Ardhuin, F., N. Rascle, and K. Belibassakis (2008b). Explicit wave-averaged primitive equations using a generalized Lagrangian mean. *Ocean Modell.*, 20, 35-60.

Ardhuin, F., A. Roland, F. Dumas, A. Bennis, A. Sentchev, P. Forget, J. Wolf, F. Girard, P. Osuna, and M. Benoit (2012). Numerical Wave Modelling in Conditions with Strong Currents: Dissipation, Refraction, and Relative Wind. *J. Phys. Oceanogr.*, 42, 2101-2120.

Ardhuin, F., N. Suzuki, J. C. McWilliams, and H. Aiki (2017). Comments on "A Combined Derivation of the Integrated and Vertically Resolved, Coupled Wave-Current Equations". *J. Phys. Oceanogr.*, 47(9), 2377-2385.

Balmforth, N. J., and W. R. Young (1999). Radiative damping of near-inertial oscillations in the mixed layer. *J. Mar. Res.*, 57, 561-584.

Bennis, A., F. Ardhuin, and F. Dumas (2011). On the coupling of wave and three-dimensional circulation models: Choice of theoretical framework, practical implementation and adiabatic tests. *Ocean Modell.*, 40, 260-272.

Bigelow, H. B. (1927). Physical oceanography of the Gulf of Maine. *Fish. Bull.,* 40*,* 511-1027.

Bolaños, R., J. M. Brown, and A. J. Souza (2014). Wave-current interactions in a tide dominated estuary. *Cont. Shelf Res.*, 87:109-123.

Bondur, V. G., K. D. Sabinin, and Y. V. Grebenyuk (2013). Anomalous variation of the ocean's inertial oscillations at the Hawaii shelf. *Dokl. Earth Sci.* 450, 526-530.

Booij, N., R. Ris, and L. Holthuijsen (1999). A third-generation wave model for coastal regions: 1. Model description and validation. *J. Geophys. Res.*, 104, 7649.

Boutin, J., Y. Quilfen, L. Merlivat, and J. Piolle (2009). Global average of air-sea CO_2 transfer velocity from QuikSCAT scatterometer wind speeds. *J. Geophys. Res.*, 114.

Bowyer, P., and A. MacAfee (2005). The Theory of Trapped-Fetch Waves with Tropical Cyclones-An Operational Perspective. *Wea. Forecasting*, 20, 229-244.

Chapman, R., L. Shay, H. Graber, J. Edson, A. Karachintsev, C. Trump, and D. Ross (1997). On the accuracy of HF radar surface current measurements: Intercomparisons with ship-based sensors. *J. Geophys. Res. Oceans*, 102(C8), 18737-18748.

Chen, Q., K. Hu, and A. Kennedy (2011). Numerical modelling of observed hurricane waves. *Int. Conf. Coastal. Eng.*, 1(32).

Craig, P., and M. Banner (1994). Modelling Wave-Enhanced Turbulence in the Ocean Surface Layer. *J. Phys. Oceanogr.*, 24, 2546-2559.

Craik, A. and S. Leibovich (1976). A rational model for Langmuir circulations. *J. Fluid Mech.*, 73(03), 401.

D'Asaro, E. A. (1985). The energy flux from the wind to near-inertial motions in the mixed layer. *J. Phys. Oceanogr.*, 15, 943-959.

Davidson, M. A., O'Hare, T. J., and K. J., George (2008). Tidal modulation of incident wave heights: fact or fiction? *J. Coast. Res.*, 2, 151-159.

Davies, A. M., and R. A. Flather (1987). Computing extreme meteorologically induced currents, with application to the northwest European continental shelf. *Cont. Shelf Res.,* 7, 643-683.

Deigaard, R., and J. Fredsøe (1989). Shear stress distribution in dissipative water waves. *Coast. Eng.*, 13(4), 357-378.

Deng, Z., L. Xie, T. Yu, S. Shi, J. Jin, and K. Wu (2013). Numerical Study of the Effects of Wave-Induced Forcing on Dynamics in Ocean Mixed Layer. *Adv. Meteor.*, 1-10.

Dever, M. (2017). Dynamics of the Nova Scotian Current and linkages with Atlantic salmon migration patterns over the Scotian Shelf, Doctoral dissertation, Dalhousie University, 196 pp.

Dever, M., D. Hebert, B. Greenan, J. Sheng, and P. Smith (2016). Hydrography and Coastal Circulation along the Halifax Line and the Connections with the Gulf of St. Lawrence. *Atmos. Ocean*, 54(3), 199-217.

Donelan, M. A., J. Hamilton, and W. Hui (1985). Directional spectra of wind-generated waves. *Philos. Trans. Roy. Soc. London, Ser. A*, 315, 509-562.

Donelan, M., Skafel, M., H. Graber, P. Liu, D. Schwab, and S. Venkatesh (1992). On the growth rate of wind−generated waves. *Atmos. Ocean*, *30*(3), 457-478.

Donelan, M. A., and coauthors (2004). On the limiting aerodynamic roughness of the ocean in very strong winds. *Geophys. Res. Lett.*, 31(18).

Egbert, G. D., and S. Y. Erofeeva (2002). Efficient inverse modelling of barotropic ocean tides. *J. Atmos. Oceanic Technol.*, 19(2), 183-204.

Elipot, S., R. Lumpkin, and G. Prieto (2010). Modification of inertial oscillations by the mesoscale eddy field. *J. Geophys. Res.*, 115(C9).

Fan, Y., I. Ginis, and T. Hara (2009a). The Effect of Wind-Wave-Current Interaction on Air-Sea Momentum Fluxes and Ocean Response in Tropical Cyclones. *J. Phys. Oceanogr.*, *39*, 1019-1034.

Fan, Y., I. Ginis, T. Hara, C. Wright, and E. Walsh (2009b). Numerical Simulations and Observations of Surface Wave Fields under an Extreme Tropical Cyclone. *J. Phys. Oceanogr.*, 39(9), 2097-2116.

Fan, Y., I. Ginis, and T. Hara (2010). Momentum flux budget across the air–sea interface under uniform and tropical cyclone winds. *J. Phys. Oceanogr.*, 40(10), 2221-2242.

Fan, Y., and S. M.Griffies (2014). Impacts of parameterized Langmuir turbulence and nonbreaking wave mixing in global climate simulations. *J. Clim.*, 27(12), 4752-4775.

Fogarty, C. (2003). *Hurricane Juan Storm Summary*, Can. Hurricane Cent., Environ. Can., Dartmouth, Canada.

Gao, G. D., and coauthors. (2018). Effects of Wave-Current Interactions on Suspended-Sediment Dynamics during Strong Wave Events in Jiaozhou Bay, Qingdao, China. *J. Phys. Oceanogr.*, *48*(5), 1053-1078.

Garrett C. (2001). What is the "near-inertial" band and why is it different from the rest of the internal wave spectrum? *J. Phys. Oceanogr.*, 31, 962-71.

Gemmrich, J., and C. Garrett (2012). The signature of inertial and tidal currents in offshore wave records. *J. Phys. Oceanogr.*, 42, 1051-1056.

Geshelin, Y., J. Sheng, and R.J. Greatbatch (1999). Monthly mean climatologies of temperatures and salinity in the western North Atlantic. *Can. Data Rep. of Hydrogr. Ocean Sci.*, 153.

Gill, A. E. (1984). On the behavior of internal waves in the wakes of storms. *J. Phys. Oceanogr.*, 14, 1129-1151.

Gonella, J. (1972). A rotary-component method for analysing meteorological and oceanographic vector time series. *Deep-Sea Res.*, 19(12), 833-846.

Greenberg, D. A. (1983). Modelling the mean barotropic circulation in the Bay of Fundy and Gulf of Maine. *J. Phys. Oceanogr.*, 13, 886-904.

Guillou, N., and G. Chapalain (2012). Effects of tide on waves in the outer Seine estuary and the harbor of Le Havre. *Coast. Eng. Proc.*, 1(33), 47.

Haas, K., and I. Svendsen (2002). Laboratory measurements of the vertical structure of rip currents. *J. Geophys. Res.*,107(C5), doi:10.1029/2001jc000911.

Haas, K., and J. Warner (2009). Comparing a quasi-3D to a full 3D nearshore circulation model: SHORECIRC and ROMS. *Ocean Modell.*, 26, 91-103.

Haller, M. (2002). Experimental study of nearshore dynamics on a barred beach with rip channels. *J. Geophys. Res.*, 107.

Hanley, K. E., S. E. Belcher, and P. P. Sullivan (2010). A global climatology of wind–wave interaction. *J. Phys. Oceanogr.*, 40, 1263-1282.

Hasegawa, D., J. Sheng, D. A. Greenberg, and K. R. Thompson (2011). Far-field effects of tidal energy extraction in the Minas Passage on tidal circulation in the Bay of Fundy and Gulf of Maine using a nested-grid coastal circulation model. *Ocean Dyn.*, 61, 1845-1868.

Hashemi, M., and S. Neill (2014). The role of tides in shelf-scale simulations of the wave energy resource. *Renew. Energ.*, 69, 300-310.

He, R., D. J. McGillicuddy, B. A. Keafer, and D. M. Anderson (2008). Gulf of Maine harmful algal bloom in summer 2005—Part 2: Coupled bio-physical numerical modeling. *J. Geophys. Res.* 113, C07040.

Huang, S., and L. Oey (2015). Right-side cooling and phytoplankton bloom in the wake of a tropical cyclone. *J. Geophys. Res. Oceans*, 120(8), 5735-5748.

Holland, G. (1980). An Analytic Model of the Wind and Pressure Profiles in Hurricanes. *Mon. Wea. Rev.*, *108*, 1212-1218.

Holthuijsen, L. H., M. D. Powell, and J. D. Pietrzak (2012). Wind and waves in extreme hurricanes. *J. Geophys. Res. Oceans*, *117*(C9).

Holthuijsen, L., and H. Tolman (1991). Effects of the Gulf Stream on ocean waves. *J. Geophys. Res.*, *96*(C7), 12755.

Holthuijsen, L., N. Booij, R. Ris, I. Haagsma, A. Kieften-burg, and E. Kriezi (2001). *SWAN Cycle III version 40.11 user manual*, Dep. of Civ. Eng., Delft Univ. of Technol., Delft, Netherlands.

Hu, K., Q. Chen, and S. Kimball (2011). Consistency in hurricane surface wind forecasting: an improved parametric model. *Nat. Hazards*, 61, 1029-1050.

Huang, Y., R. H. Weisberg, L. Zheng, and M. Zijlema (2013). Gulf of Mexico hurricane wave simulations using SWAN: Bulk formula-based drag coefficient sensitivity for Hurricane Ike. *J. Geophys. Res*., 118, 3916-3938.

Hwang, P. (2011). A Note on the Ocean Surface Roughness Spectrum. *J. Atmos. Oceanic Technol.*, *28*, 436-443.

Jing. Z., and L. Wu (2014). Intensified diapycnal mixing in the midlatitude western boundary current. *Sci. Rep.*, 4, 7412.

Jing, Z., L. Wu, and X. Ma (2017). Energy Exchange between the Mesoscale Oceanic Eddies and Wind-Forced Near-Inertial Oscillations. *J. Phys. Oceanogr.*, 47, 721-733.

Jochum, M., B. P. Briegleb, G. Danabasoglu, W. G. Large, N. J. Norton, S. R. Jayne, M. H. and F. O. Bryan (2013). The impact of oceanic near-inertial waves on climate. *J. Clim.*., 26(9), 2833-2844.

Johnson, C. L., and Coauthors (2011). Biodiversity and ecosystem function in the Gulf of Maine: pattern and role of zooplankton and pelagic nekton. *PLoS One*, 6, p.e16491.

Katavouta, A., and K. Thompson (2016). Downscaling ocean conditions with application to the Gulf of Maine, Scotian Shelf and adjacent deep ocean. *Ocean Modell.*, 104, 54-72.

Katavouta, A., K. Thompson, Y. Lu, and J. Loder (2016). Interaction between the Tidal and Seasonal Variability of the Gulf of Maine and Scotian Shelf Region. *J. Phys. Oceanogr.*, 46(11), 3279-3298.

Kim, S. Y., and P. M. Kosro (2013). Observations of near-inertial surface currents off Oregon: Decorrelation time and length scales. *J. Geophys. Res. Oceans*, 118, 3723-3736.

Kumar, N., G. Voulgaris, and J. Warner (2011). Implementation and modification of a three-dimensional radiation stress formulation for surf zone and rip-current applications. *Coast. Eng.*, *58*, 1097-1117.

Kumar, N., G. Voulgaris, J. Warner, and M. Olabarrieta (2012). Implementation of the vortex force formalism in the coupled ocean-atmosphere-wave-sediment transport (COAWST) modelling system for inner shelf and surf zone applications. *Ocean Modell.*, 47, 65-95.

Kundu, P. K., S.-Y. Chao, and J. P. McCreary (1983). Transient coastal currents and inertio-gravity waves. *Deep Sea Res.*, 30(10), 1059-1082.

Kundu, P.K. and R.E. Thomson (1985). Inertial Oscillations due to a Moving Front. *J. Phys. Oceanogr.*, 15, 1076-1084.

Kunze, E. (1985). Near-Inertial Wave Propagation In Geostrophic Shear. *J. Phys. Oceanogr.*, 15(5), 544-565.

Lane, E., J. Restrepo, and J. McWilliams (2007). Wave–Current Interaction: A Comparison of Radiation-Stress and Vortex-Force Representations. *J. Phys. Oceanogr.*, 37(5), 1122-1141.

Large, W., and S. Pond (1981). Open Ocean Momentum Flux Measurements in Moderate to Strong Winds. *J. Phys. Oceanogr.*, *11*, 324-336.

Levier, B., A. M. Treguier, G. Madec, and V. Garnier (2007). Free surface and variable volume in the NEMO code. MERSEA IP Rep. WP09-CNRS-STR-03-1A, 47 pp., IFREMER, Brest, France.

Li, Y., R. He, and D. J. McGillicuddy Jr. (2014). Seasonal and interannual variability in Gulf of Maine hydrodynamics: 2002-2011. *Deep-Sea Res.,* 11, 103, 210-222.

Liu, A., C. Peng, and J. Schumacher (1994). Wave-current interaction study in the Gulf of Alaska for detection of eddies by synthetic aperture radar. *J. Geophys. Res.*, *99*, 10075.

Longuet-Higgins, M. S., D. E. Cartwright, and N. D. Smith (1963). Observations of the directional spectrum of sea waves using the motions of a floating buoy. *Ocean Wave Spectrum*, Prentice-Hall, 111-136.

Longuet-Higgins, M. S., and R. W. Stewart (1961). The changes in amplitude of short gravity waves on steady non-uniform currents. *J. Fluid Mech.*, 10, 529-549.

Longuet-Higgins, M. S., and R. W. Stewart (1964). Radiation stresses in water waves; a physical discussion, with applications. *Deep Sea Res. Ocean. Abs.*, *11*, 529-562.

Lyard, F., F. Lefevre, T. Letellier, and O. Francis (2006). Modelling the global ocean tides: Modern insight from FES2004. *Ocean Dyn.*, 56, 394-415.

MacKinnon, J. A., and M. C. Gregg (2005). "Near-inertial waves on the New England shelf: The role of evolving stratification, turbulent dissipation, and bottom drag. *J. Phys. Oceanogr.*, 35, 2408-2424.

Masson, D. (1996). A case study of wave–current interaction in a strong tidal current. *J. Phys. Oceanogr.*, 26, 359-372.

Mazzini, P. L., J. A. Barth, R. K. Shearman, and A. Erofeev (2014). Buoyancy-driven coastal currents off Oregon during fall and winter. *J. Phys. Oceanogr.*, 44(11), 2854-2876.

McWilliams, J., J. Restrepo, and E. Lane (2004). An asymptotic theory for the interaction of waves and currents in coastal waters. *J. Fluid Mech.*, 511, 135-178.

Mellor, G. (2003). The three-dimensional current and surface wave equations. *J. Phys. Oceanogr.,* 33:1978-1989

Mellor, G., and T. Yamada (1982). Development of a turbulence closure model for geophysical fluid problems. *Rev. Geophys.*, *20*, 851.

Mellor, G. (2004). *Users Guide for a Three Dimensional, Primitive Equation, Numerical Ocean Model*, Program in Atmos. and Oceanic Sci., Princeton Univ. Princeton, N. J.

Mellor, G. (2008). The Depth-dependent current and wave interaction equations: A Revision. *J. Phys. Oceanogr.*, 38(11).

Mellor, G. (2011). Wave radiation stress, *Ocean Dyn.*, 61(5), 563-568.

Mellor, G. (2013). Pressure-slope momentum transfer in ocean surface boundary layers coupled with gravity waves. *J. Phys. Oceanogr.*, *43*(10), 2173-2184.

Mellor, G. (2015). A combined derivation of the integrated and vertically resolved, coupled wave–current equations. *J. Phys. Oceanogr.*, 45(6), 1453-1463.

Mellor, G. (2016). On theories dealing with the interaction of surface waves and ocean circulation. *J. Geophys. Res. Oceans,* 121(7), 4474-4486.

Mellor, G. (2017). Reply to "Comments on 'A Combined Derivation of the Integrated and Vertically Resolved, Coupled Wave-Current Equations'". *J. Phys. Oceanogr.*, *47*(9), 2387-2389.

Michaud, H., P. Marsaleix, Y. Leredde, C. Estournel, F. Bourrin, F. Lyard, C. Mayet, and F. Ardhuin (2012). Three-dimensional modelling of wave-induced current from the surf zone to the inner shelf. *Ocean Sci.*, *8*, 657-681.

Mihanović, H., C. Pattiaratchi, and F. Verspecht (2016). Diurnal Sea Breezes Force Near-Inertial Waves along Rottnest Continental Shelf, Southwestern Australia. *J. Phys. Oceanogr.*, 46, 3487-3508.

Molines, J. M., B. Barnier, T. Penduff, A. M. Treguier, and J. Le Sommer (2014). ORCA12.L46 climatological and interannual simulations forced with DFS4.4: GJM02 and MJM88. Drakkar Group Experiment Rep. GDRI-DRAKKAR-2014-03-19, 49 pp.

Moghimi, S., K. Klingbeil, U. Gräwe, and H. Burchard (2013). A direct comparison of a depth-dependent Radiation stress formulation and a Vortex force formulation within a three-dimensional coastal ocean model. *Ocean Modell.*, 70, 132-144.

Moon, I. J. (2005). Impact of a coupled ocean wave–tide–circulation system on coastal modelling. *Ocean Modell.*, *8*(3), 203-236.

Mooers, C. N. K. (1975). Several effects of a baroclinic current on the cross-stream propagation of inertial-internal waves, *Geophys. Fluid Dyn.*, 6, 245-275.

Müller, P. (1976). On the diffusion of momentum and mass by internal gravity waves. *J. Fluid Mech.*, 77, 789-823.

Mulligan, R., A. Hay, and A. Bowen (2008). Wave-driven circulation in a coastal bay during the landfall of a hurricane. *J. Geophys. Res.*, 113(C5).

Nagasawa M., Y. Niwa, T. Hibiya (2000). Spatial and temporal distribution of the wind-induced internal wave energy available for deep water mixing in the North Pacific. *J. Geophys. Res.*, 105, 13933-13943.

NDBC (2009). Handbook of automated data quality control checks and procedures, NDBC Tech. Doc. 09-02, 78 pp. https://www.ndbc.noaa.gov/NDBCHandbookofAutomatedDataQualityControl2009.pdf.

Ohashi, K., J. Sheng, K. Thompson, C. Hannah, and H. Ritchie (2009a). Effect of stratification on tidal circulation over the Scotian Shelf and Gulf of St. Lawrence: a numerical study using a three-dimensional shelf circulation model. *Ocean Dyn.*, *59*, 809-825.

Ohashi, K., J. Sheng, K. Thompson, C. Hannah, and H. Ritchie (2009b). Numerical study of three-dimensional shelf circulation on the Scotian Shelf using a shelf circulation model. *Cont. Shelf Res., 29*, 2138-2156.

Ohashi, K., and J. Sheng (2013). Influence of St. Lawrence River discharge on the circulation and hydrography in Canadian Atlantic waters. *Cont. Shelf Res., 58*, 32-49.

Ohashi, K., and J. Sheng (2015). Investigating the Effect of Oceanographic Conditions and Swimming Behaviours on the Movement of Particles in the Gulf of St. Lawrence Using an Individual-Based Numerical Model. *Atmos. Ocean*, 1-21.

Olabarrieta, M., J. C. Warner, B. Armstrong, J. B. Zambon, and R. He (2012). Ocean–atmosphere dynamics during Hurricane Ida and Nor'Ida: an application of the coupled ocean–atmosphere–wave–sediment transport (COAWST) modeling system. *Ocean Modell.*, *43*, 112-137.

Olfateh, M., P. Ware, D. P Callaghan, P. Nielsen, and T. E. Baldock (2017). Momentum transfer under laboratory wind waves. *Coast. Eng.*, *121*, 255-264.

Paduan, J. D., and H. C. Graber (1997). Introduction to high-frequency radar: reality and myth. *Oceanography*, 10, 36-39.

Paduan, J. D., R. A. Szoeke, and R. A. Weller (1989) Inertial oscillations in the upper ocean during the Mixed Layer Dynamics Experiment (MILDEX). *J. Geophys. Res. Oceans*, 94(C4), 4835-4842.

Park, J. J., K. Kim, and R. W. Schmitt (2009). Global distribution of the decay timescale of mixed layer inertial motions observed by satellite-tracked drifters. *J. Geophys. Res. Oceans*, 114(C11).

Pawlowicz, R., B. Beardsley, and S. Lentz (2002). Classical tidal harmonic analysis including error estimates in MATLAB using T_TIDE. *Comput. Geosci.*, 28(8), 929-937.

Perrie, W., C. L. Tang, Y. Hu, and B. M. DeTracy (2003). The impact of waves on surface currents. *J. Phys. Oceanogr.*, *33*(10), 2126-2140.

Petrie, B. (1987). Undulations of the Nova Scotia Current. *Atmos. Ocean*, 25, 1-9.

Phillips, O. M. (1977). The dynamics of the upper ocean. Cambridge University Press.

Pleskachevsky, A., M. Dobrynin, A. V. Babanin, H. Günther, and E. Stanev (2011). Turbulent mixing due to surface waves indicated by remote sensing of suspended particulate matter and its implementation into coupled modelling of waves, turbulence, and circulation. *J. Phys. Oceanogr.*, *41*(4), 708-724.

Pollard, R. T., and R. C. Millard (1970). Comparison between observed and simulated wind-generated inertial oscillations. *Deep-Sea Res.,* 17, 813-821.

Polton, J. A., D. M. Lewis, and S. E. Belcher (2005). The role of wave-induced Coriolis–Stokes forcing on the wind-driven mixed layer. *J. Phys. Oceanogr.*, *35*(4), 444-457.

Poulain, P., D. Luther, and W. Patzert (1992). Deriving inertial wave characteristics from surface drifter velocities: Frequency variability in the tropical Pacific. *J. Geophys. Res. Oceans*, 97(C11), 17947-17959.

Powell, M., P. Vickery, and T. Reinhold (2003). Reduced drag coefficient for high wind speeds in tropical cyclones. *Nature*, *422*, 279-283.

Price, J. (1981). Upper Ocean Response to a Hurricane. *J. Phys. Oceanogr.*, 11, 153-175.

Qiao, F. (2004). Wave-induced mixing in the upper ocean: Distribution and application to a global ocean circulation model. *Geophys. Res. Lett.*, *31*.

Saha, S. et al. (2010). The NCEP Climate Forecast System Reanalysis. *Bull. Amer. Meteor. Soc.*, *91*, 1015-1057.

Shan, S., J. Sheng, K. Ohashi, and M. Dever (2016). Assessing the performance of a multi-nested ocean circulation model using satellite remote sensing and in situ observations. *Satell. Oceanogr. Meteorol.,* 1(1).

Shearman, R. K. (2005). Observations of near-inertial current variability on the New England shelf. *J. Geophys. Res. Oceans*, 110 (C2).

Sheng, J., R. Greatbatch, and D. Wright (2001). Improving the utility of ocean circulation models through adjustment of the momentum balance. *J. Geophys. Res.*, 106, 16711.

Sheng, J., X. Zhai, and R. Greatbatch (2006). Numerical study of the storm-induced circulation on the Scotian Shelf during Hurricane Juan using a nested-grid ocean model. *Prog. Oceanogr.*, 70, 233-254.

Sheng, J., J. Zhao, and L. Zhai (2009). Examination of circulation, dispersion, and connectivity in Lunenburg Bay of Nova Scotia using a nested-grid circulation model. *J. Mar. Sys.*, 77(3), 350-365.

Sikirić, M. D., A. Roland, I. Tomaz, and I. Janeković (2012). Hindcasting the Adriatic Sea near−surface motions with a coupled wave−current model. *J. Geophys. Res. Oceans*, 117(C12).

Smith, P. (1989). Inertial oscillations near the coast of Nova Scotia during CASP. *Atmos. Ocean*, 27(1), 181-209.

Smith, P. C., N. R. Pettigrew, P. Yeats, D. W. Townsend, and G. Han (2012). Regime shift in the Gulf of Maine. *Am. Fish. Soc. Symp.*, 79, 185-203.

Staneva, J., K. Wahle, H. Günther, and E. Stanev (2016). Coupling of wave and circulation models in coastal–ocean predicting systems: a case study for the German Bight. *Ocean Sci.*, 12(3), 797-806.

Stewart, R., and J. Joy (1974). HF radio measurements of surface currents. *Deep-Sea Res.*, 21(12), 1039-1049.

Sun, Y., C. Chen, R. C. Beardsley, Q. Xu, J. Qi, H. Lin (2013). Impact of current-wave interaction on storm surge simulation: A case study for Hurricane Bob. *J. Geophys. Res. Oceans*, 118(5), 2685-2701.

Terray, E., M. Donelan, Y. Agrawal, W. Drennan, K. Kahma, A. Williams, P. Hwang, and S. Kitaigorodskii (1996). Estimates of Kinetic Energy Dissipation under Breaking Waves. *J. Phys. Oceanogr.*, *26*, 792-807.

Terray, E., W. Drennan, and M. Donelan (2000). The vertical structure of shear and dissipation in the ocean surface layer, in *Proc. Symp. on Air-Sea Interaction*, pp. 239-245.

Thompson, K., and J. Sheng (1997). Subtidal circulation on the Scotian Shelf: assessing the hindcast skill of a linear, barotropic model. *J. Geophys. Res.,* 102, 24987–25003.

Thompson, K., K. Ohashi, J. Sheng, J. Bobanovic, and J. Ou (2007). Suppressing bias and drift of coastal circulation models through the assimilation of seasonal climatologies of temperature and salinity. *Cont. Shelf Res.*, 27, 1303-1316.

Ting, F. C. K., and J. T. Kirby (1994). Observation of undertow and turbulence in a laboratory surf zone. *Coast. Eng.*, 24,51-80.

Tolman, H. (1990). The influence of unsteady, depths and currents of tides on wind-wave propagation in shelf seas. *J. Phys. Oceanogr.* 20, 1166-1174.

Tolman, H., and the WAVEWATCH-III Development Group (2014). *User Manual and system documentation of WAVEWATCH-III version 4.18*, Technical Note. 316, NOAA/NWS/NCEP/MMAB, College Park, U. S.

Uchiyama, Y., J. McWilliams, and A. Shchepetkin (2010). Wave-current interaction in an oceanic circulation model with a vortex-force formalism: Application to the surf zone. *Ocean Modell.*, *34*, 16-35.

Urrego-Blanco, J., and J. Sheng (2012). Interannual Variability of the Circulation over the Eastern Canadian Shelf. *Atmos. Ocean*, *50*, 277-300.

Vincent, C. E. (1979). The interaction of wind-generated sea waves with tidal currents. *J. Phys. Oceanogr.*, *9*(4), 748-755.

Wandres, M., E. M. S. Wijeratne, S. Cosoli, and C. Pattiaratchi (2017). The Effect of the Leeuwin Current on Offshore Surface Gravity Waves in Southwest Western Australia. *J. Geophys. Res. Oceans*, *122*(11), 9047-9067.

Wang, D., A. Liu, C. Peng, and E. Meindl (1994). Wave-current interaction near the Gulf Stream during the Surface Wave Dynamics Experiment, *J. Geophys. Res.*, *99*, 5065.

Wang, L., J. Sheng, A. Hay, and D. Schillinger (2007). Storm-Induced Circulation in Lunenburg Bay of Nova Scotia: Observations and Numerical Simulations. *J. Phys. Oceanogr.*, 37(4), 873-895.

Wang, P., and J. Sheng (2016). A comparative study of wave-current interactions over the eastern Canadian shelf under severe weather conditions using a coupled wave-circulation model. *J. Geophys. Res. Oceans*, 121.

Wang, P., J. Sheng, and C. Hannah (2017). Assessing the performance of formulations for nonlinear feedback of surface gravity waves on ocean currents over coastal waters. *Cont. Shelf Res.*, *146*, 102-117.

Wang, P. and J. Sheng (2018). Tidal modulation of surface gravity waves in the Gulf of Maine. *J. Phys. Oceanogr.*, 48, 2305-2323. ©American Meteorological Society. Used with permission.

Whitt, D. B., and L. N. Thomas (2015). Resonant generation and energetics of wind-forced near-inertial motions in a geostrophic flow. *J. Phys. Oceanogr.*, 45, 181-208.

Wright, D. G., K. R. Thompson and Y. Lu (2006). Assimilating long-term hydrographic information into an eddy-permitting model of the North Atlantic, *J. Geophys. Res.*, 111 (C9).

Wu, L., A. Rutgersson, and E. Sahlée (2015). Upper-ocean mixing due to surface gravity waves. *J. Geophys. Res.*, *120*, 8210-8228.

Xie, D., and Q. Zou (2017). Effect of wave-current interaction on waves and circulation over Georges Bank during storm events. *Coast. Eng. Proc.*, 1, 1-9.

Xue, H., F. Chai, and R. Pettgrew (2000). A model study of the seasonal circulation in the Gulf of Maine. *J. Phys. Oceanogr.,* 30, 1111-1130.

Xu, F., W. Perrie, B. Toulany, and P. Smith (2007). Wind-generated waves in Hurricane Juan. *Ocean Modell.*, *16*, 188-205.

Zervakis, V., and M. D. Levine (1995). Near-inertial energy propagation from the mixed layer: Theoretical considerations. *J. Phys. Oceanogr.*, 25, 2872-2889.

Zhai, L., J. Sheng, and R. J. Greatbatch (2007). Observations of the dynamical response of a coastal embayment to wind, tide and buoyancy forcing. *Cont. Shelf Res.,* 27, 2534-2555.

Zhai, X., R. J. Greatbatch, and J. Sheng, (2004). Advective spreading of storm-induced inertial oscillations in a model of the northwest Atlantic Ocean. *Geophys. Res. Lett.*, 31, L14315.

Zhai, X., R. J. Greatbatch, and J. Zhao (2005). Enhanced vertical propagation of storm-induced near-inertial energy in an eddying ocean channel model. *Geophys. Res. Lett.*, 32, L18602.

Zhai, X., R. J. Greatbatch, and C. Eden (2007). Spreading of near-inertial energy in a 1/28 model of the north Atlantic Ocean. *Geophys. Res. Lett.*, 34, L10609.

Zhai, X., R. J. Greatbatch, C. Eden, and T. Hibiya (2009). On the loss of wind-induced near-inertial energy to turbulent mixing in the upper ocean, *J. Phys. Oceanogr.*, 39, 917 3040-3045.

Zhang X., G. Han, D. Wang, W. Li, and Z. He (2011). Effect of surface wave breaking on the surface boundary layer of temperature in the Yellow Sea in summer. *Ocean Modell.*, *38*, 267-279.